Structural basis of antibacterial peptide export by ABC transporters

Kiran Bountra

Department of Life Sciences
Imperial College London

Thesis submitted for the degree of Doctor of Philosophy
2019

Abstract

Under conditions of nutrient starvation bacteria produce and release antibacterial peptides like the lasso peptide microcin J25 (MccJ25). Uptake of MccJ25 by other bacteria leads to RNA polymerase inhibition and subsequent cell death. MccJ25 is also toxic to the producing organism that utilises ATP-binding cassette (ABC) transporters to provide self-immunity. The ABC transporter McjD is responsible for the efflux of MccJ25. The general architecture of an ABC transporter comprises two nucleotide-binding domains (NBDs) and two transmembrane domains (TMDs). Previously, the structure of McjD from *Escherichia coli* was determined in complex with a non-hydrolysable ATP analogue (AMP-PNP), providing some insights into the transport cycle. However, the mechanistic basis for MccJ25 secretion remained elusive. In this work, the structure of McjD has been determined in a post-ATP hydrolysis intermediate state (ADP-VO_4). Using predictive cysteine cross-linking, cavity accessibility studies, transport assays and PELDOR measurements in lipid membranes, a novel mechanism for MccJ25 secretion is proposed requiring the transient opening of the McjD TMDs for substrate release. Unlike multidrug ABC exporters which display large conformational changes in the TMDs, the McjD TMDs exist in a predominantly occluded state which prevents MccJ25 reuptake upon efflux. These structural insights are complimented by the first single molecule FRET (smFRET) characterisation of an ABC exporter in a native-like environment. The smFRET findings report conformational changes in the NBDs and TMDs of McjD, demonstrating that opening of the TMDs is tightly coupled to the binding of both ATP and MccJ25. The NBDs display intrinsic conformational dynamics on the millisecond timescale whereas the TMDs do not show any dynamic behaviour. Finally, attempts are made to purify and functionally characterize two staphylococcal peptide ABC exporters Pmt and AbcA. These transporters secrete cytolytic α-helical peptides, phenol soluble modulins, that can evade the immune response.

Declaration

I declare that the content described in this thesis has been produced by myself, unless stated otherwise. All sources of information within this thesis have been acknowledged. The copyright of this thesis rests with the author. Unless otherwise indicated, its contents are licensed under a Creative Commons Attribution-Non Commercial 4.0 International Licence (CC BY-NC). Under this licence, you may copy and redistribute the material in any medium or format. You may also create and distribute modified versions of the work. This is on the condition that: you credit the author and do not use it, or any derivative works, for a commercial purpose. When reusing or sharing this work, ensure you make the licence terms clear to others by naming the licence and linking to the licence text. Where a work has been adapted, you should indicate that the work has been changed and describe those changes. Please seek permission from the copyright holder for uses of this work that are not included in this licence or permitted under UK Copyright Law.

Table of Contents

Abstract **2**

Declaration **3**

Table of Contents **4**

Figure list **8**

Table list **11**

Abbreviations **12**

Acknowledgements **15**

Chapter 1: Introduction **16**

1.1. ABC transporters **17**

1.1.1. Membrane transport proteins 17-18

1.1.2. Why study ABC transporters? 19-20

1.1.3. Structural features of ABC transporters 20-21

1.1.4. Architecture of the NBDs 22-23

1.1.5. Architecture of the TMDs 24-25

1.1.6. Structures and mechanisms of ABC importers 25-31

1.1.7. Structures and mechanisms of ABC exporters 32-40

1.1.8. How do ABC exporters recognise their substrates? 40-43

1.1.9. PELDOR studies of ABC transporters 44

1.1.10. Principle of single-molecule FRET 45-47

1.1.11. Single-molecule FRET studies of ABC transporters 47-50

1.1.12. Peptide ABC transporters 51

1.2. McjD **52**

1.2.1. Microcins 52-56

1.2.2. Biosynthesis and export of MccJ25 57-59

1.2.3. Mechanism of MccJ25 import 60-62

1.2.4. Mechanism of MccJ25 inhibition 63-64

1.2.5. Therapeutic potential of MccJ25 65

1.2.6. McjD is a microcin immunity protein 66

1.2.7. Structure of McjD-AMP-PNP 66-67

1.2.8. Comparison of McjD structure with other ABC exporters 68-69

1.2.9. McjD is modulated by specific lipids 69
1.2.10. Current model for MccJ25 export 70-71
1.2.11. Aims 72-73
Chapter 2: McjD structure and mechanism 74
2.1. Introduction 75
2.1.1. Approach to define McjD transport mechanism 75
2.2. Materials and Methods 76
2.2.1. Protein expression 76-77
2.2.2. Preparation of membranes 77
2.2.3. Protein purification 78-79
2.2.4. Crystallisation of McjD-ADP-VO_4 79
2.2.5. Data collection and processing 79-80
2.2.6. Structure solution and refinement 80-82
2.2.7. Site-directed mutagenesis 83-84
2.2.8. Predictive cysteine cross-linking 85-86
2.2.9. PEGylation cavity accessibility assays 86-87
2.2.10. Preparation of labelled McjD mutants for PELDOR 87
2.2.11. ATPase assays 88
2.2.12. Liposome reconstitution 89
2.2.13. Transport assays 89-91
2.3. Results 92
2.3.1. Structure of McjD-ADP-VO_4 92-99
2.3.2. Coordination of ADP-VO_4 in the NBDs 100-102
2.3.3. Structure of Mcjd *apo* 103-105
2.3.4. Comparison of McjD structures with other ABC exporters 106-107
2.3.5. Predictive cysteine cross-linking 108-114
2.3.6. PEGylation cavity accessibility 115-120
2.3.7. PELDOR measurements 121-125
2.3.8. Fluorescence transport assays 126-130
2.4. Discussion 131
2.4.1. McjD-ADP-VO_4 structure defines a new intermediate state 131

2.4.2. The McjD TMDs are predominantly occluded 131-132
2.4.3. MccJ25 can enter the McjD TMDs from the cytoplasm 132
2.4.4. McjD can adopt a transient outward-open state 132-133
2.4.5. The apo McjD NBDs are closely separated 133
2.4.6. MccJ25 export cycle 134-135
2.4.7. Mechanism for antibacterial self-immunity 136
Chapter 3: McjD dynamics 137
3.1. Introduction 138
3.1.1. Application of smFRET to McjD 138-139
3.2. Materials and Methods 140
3.2.1. Design of smFRET mutants 141-141
3.2.2. Site-directed mutagenesis 141-142
3.2.3. Preparation of McjD FRET mutants 142-143
3.2.4. Protein labelling 143
3.2.5. Preparation of biotinylated lipids 143-144
3.2.6. Liposome incorporation 144
3.2.7. Orientation of McjD in liposomes 145
3.2.8. ATPase assays 145
3.2.9. Transport assays 146
3.2.10. Single-molecule FRET using ALEX 146
3.2.11. Confocal scanning microcopy and data analysis 146
3.3. Results 147
3.3.1. Purification and labelling of McjD mutants 147-151
3.3.2. Functional characterization of labelled mutants 152-154
3.3.3. Visualization of McjD mutants in detergent by ALEX 155-156
3.3.4. FRET observations of McjD C547 in detergent 157-160
3.3.5. FRET observations of McjD Y64C and L67C in detergent 161-164
3.3.6. Orientation of McjD in proteoliposomes 165-166
3.3.7. Optimization of McjD reconstitution in liposomes 167-169
3.3.8. FRET observations of McjD C547 in liposomes 170-172
3.3.9. FRET observations of McjD Y64C and L67C in liposomes 172-173
3.4. Discussion 174

3.4.1. McjD displays conformational dynamics in the NBDs 174-175
3.4.2. NBD dynamics are a common feature of ABC transporters 175
3.4.3. Comparison between McjD and MsbA 176-177
3.4.4. The McjD TMDs are tightly coupled to ATP and MccJ25 177-178
3.4.5. Refined transport model for McjD based on smFRET 179
Chapter 4: Staphylococcal peptide ABC exporters 180
4.1. Introduction 181
4.1.1. *Staphylococcus aureus* toxins 181
4.1.2. Phenol soluble modulin classes 182-183
4.1.3. Phenol soluble modulin functions 184-185
4.1.4. Pmt 186-187
4.1.5. AbcA 188
4.1.6. Aims 189
4.2. Materials and Methods 190
4.2.1. Cloning of Pmt 190
4.2.2. Cloning of AbcA 191
4.2.3. Protein expression and membrane preparation 191
4.2.4. FSEC 192
4.2.5. Purification of Pmt-GFP-His 193
4.2.6. Purification of Pmt-His 193
4.2.7. Purification of AbcA-GFP-His 194-195
4.2.8. Crystallisation trials of AbcA-GFP-His 195
4.2.9. Liposome incorporation of AbcA 195-196
4.2.10. ATPase assays 196
4.3. Results 197
4.3.1. FSEC screening of Pmt-GFP-His 197-198
4.3.2. Purification of Pmt-GFP-His 199-201
4.3.3. Purification of Pmt-His 202-203
4.3.4. FSEC screening of AbcA-GFP-His 204-205
4.3.5. Purification and characterisation of AbcA-GFP-His 206-209
4.4. Discussion 210
References 212

Figure list

Figure 1.	Major classes of membrane transport protein	18
Figure 2.	Domain arrangement of ABC transporters	21
Figure 3.	Conserved architecture in the NBDs	23
Figure 4.	Mode of substrate recognition by SBPs	28
Figure 5.	Transport mechanism for the type I ABC importer $MalFGK_2$	29
Figure 6.	Architecture of type II and type III ABC importers	31
Figure 7.	Structures of the type IV ABC transporter MsbA	35
Figure 8.	Structures of the type IV ABC transporter PCAT1	36
Figure 9.	Architecture of type IV-VII ABC transporters	39
Figure 10.	Ligand recognition in MsbA	41
Figure 11.	Cryo-EM structure of P-glycoprotein in complex with zosuquidar	43
Figure 12.	Equation to calculate FRET efficiency	45
Figure 13.	Principle of FRET	46
Figure 14.	Experimental design for smFRET of BtuCD	49
Figure 15.	Comparison between different classes of microcin	53
Figure 16.	Genetic organisation of class I and class II microcins	54
Figure 17.	Biosynthesis of MccJ25	58
Figure 18.	Structure of FhuA in complex with MccJ25	61
Figure 19.	Uptake of MccJ25 into cells	62
Figure 20.	MccJ25 inhibits RNA polymerase	64
Figure 21.	Structure of McjD-AMP-PNP	67
Figure 22.	Comparison between TMDs in McjD and Sav1866	68
Figure 23.	Proposed alternating access model for MccJ25 export	71
Figure 24.	Schematic representation of McjD-GFP-His construct	76
Figure 25.	Equation to calculate GFP and McjD concentration	77
Figure 26.	Final electron density map for McjD-ADP-VO_4	81
Figure 27.	Equations for calculation of McjD ATPase activity	88
Figure 28.	Hoechst 33342 uptake assay in liposomes	90
Figure 29.	The stereochemistry of ATP during hydrolysis	93
Figure 30.	Purification and crystallisation of McjD	95
Figure 31.	Structure of McjD ADP-VO_4	97

Figure 32.	Electron density and anomalous difference maps for McjD-ADP-VO_4	98
Figure 33.	Comparison of McjD-ADP-VO_4 structure with McjD-AMP-PNP	99
Figure 34.	Coordination of ADP, VO_4 and Mg^{2+} in the McjD NBDs	101
Figure 35.	Comparison between the McjD ground state and transition state	102
Figure 36.	Comparison of McjD-ADP-VO_4 structure with McjD *apo*	104
Figure 37.	Comparison of McjD structures in distinct conformational states	105
Figure 38.	Structural comparison of McjD and MsbA	107
Figure 39.	Positions of cysteine mutations for predictive cross-linking	109
Figure 40.	Predictive cysteine cross-linking of the McjD periplasmic TMDs	110
Figure 41.	Predictive cysteine cross-linking of the McjD cytoplasmic TMDs	112
Figure 42.	Predictive cysteine cross-linking of the McjD NBDs	114
Figure 43.	McjD cavity accessibility assay design	116
Figure 44.	PEGylation of McjD at pH 7.5	118
Figure 45.	PEGylation of McjD at pH 9.0	119
Figure 46.	Competition PEGylation assay with MccJ25	120
Figure 47.	Positions of McjD mutations for the attachment of spin labels	122
Figure 48.	Characterisation of McjD-L52C and McjD-C547	123
Figure 49.	PELDOR analysis of McjD	125
Figure 50.	Competition transport assay with MccJ25	127
Figure 51.	McjD-L53C transport assay	129
Figure 52.	SDS-PAGE to show efficiency of McjD-L53C crosslinking	130
Figure 53.	Mechanism of antibacterial peptide export by McjD	135
Figure 54.	Positions of cysteine mutations for smFRET	141
Figure 55.	Generation of smFRET mutants	142
Figure 56.	Purification of McjD-Y64C using a Superdex S200 column	148
Figure 57.	Optimised gel filtration profiles of McjD FRET mutants	149
Figure 58.	SDS-PAGE of McjD FRET mutants	150
Figure 59.	SDS-PAGE of labelled McjD-C547 reconstituted in proteoliposomes	152
Figure 60.	ATPase activity of labelled McjD FRET mutants in liposomes	153
Figure 61.	Hoechst uptake of labelled McjD 547C compared to wild-type protein	155
Figure 62.	Schematic of smFRET using ALEX	156
Figure 63.	Optimisation of McjD-C547 visualisation by ALEX	158
Figure 64.	Conformational changes in the NBDs correlate with McjD structures	159
Figure 65.	FRET efficiency values in the McjD NBDs	160

Figure 66. Distinct FRET populations observed for McjD-Y64C and McjD-L67C 162
Figure 67. FRET population shifts in the TMDs upon ATP/MccJ25 treatment 163
Figure 68. FRET efficiency values in the McjD TMDs 164
Figure 69. McjD orientiation in proteoliposomes 166
Figure 70. Experimental setup for McjD immobilised to the surface 167
Figure 71. Optimisation of McjD liposome reconstitution for surface-immobilisation 169
Figure 72. Conformational states of McjD-C547 in liposomes 171
Figure 73. Conformational states of the McjD TMD mutants in liposomes 173
Figure 74. Conformational dynamics of the McjD NBDs 175
Figure 75. Sequences of gene-encoded PSMs in *S. aureus* and *S. epidermis* 183
Figure 76. Summary of PSM functions in pathogenesis 185
Figure 77. Gene organisation and arrangement of Pmt 187
Figure 78. Schematic representation of Pmt constructs 190
Figure 79. Schematic representation of AbA-GFP-His construct 191
Figure 80. FSEC profile of Pmt-GFP-His in different detergents 198
Figure 81. Nickel affinity purification of Pmt-GFP-His 200
Figure 82. Gel filtration of uncleaved Pmt-GFP-His 201
Figure 83. Purification of Pmt-His 203
Figure 84. FSEC profile of AbcA-GFP-His in different detergents 205
Figure 85. Purification of AbcA in DDM 207
Figure 86. ATPase activity assay for AbcA in DDM 208
Figure 87. Gel filtration profiles for AbcA purified in different detergents 209

Table list

Table 1.	Comparison between different classes of ABC importer	26
Table 2.	Comparison between different classes of ABC exporter	33
Table 3.	Structural features and intracellular targets of microcins	56
Table 4.	McjD purification table	79
Table 5.	Data collection and refinement statistics for McjD-ADP-VO_4	82
Table 6.	McjD mutant primer sequences for cysteine mutations	84
Table 7.	Mechanistic comparison between McjD and MsbA	178
Table 8.	List of detergents used for FSEC screening of Pmt and AbcA	192
Table 9.	AbcA purification table	195
Table 10.	Detergent extraction efficiencies for AbcA-GFP-His	204

Abbreviations

Å	Angstrom
ABC	Adenosine 5'-triphosphate-binding cassette
ADP	Adenosine 5'-diphosphate
ALEX	Alternating laser excitation
AMP-PNP	Adenosine 5'-(β,γ-imido) triphosphate
ATP	Adenosine 5'-triphosphate
BCA	Bicinchoninic acid
BSA	Bovine serum albumin
C12E8	Octaethylene glycol monododecyl ether
CFTR	Cystic fibrosis transmembrane regulator
CLD	Cross-linked dimer
CPM	7-Diethylamino-3-(4'-Maleimidylphenyl)-4-Methylcoumarin
CV	Column volume
Cymal-6	6-Cyclohexyl-1-Hexyl-β-D-Maltoside
DDM	n-Dodecyl β-D-Maltopyranoside
DM	n-Decyl-β-D-Maltopyranoside
DMSO	Dimethyl sulfoxide
DNA	Deoxyribonucleic acid
DOPA	1,2-Dioleoyl-sn-glycero-3-phosphate
DOPE	1,2-Dioleoyl-sn-glycero-3-phosphoethanolamine
DOPG	1,2-Dioleoyl-sn-glycero-3-phospho-(19-rac-glycerol)
ECF	Energy-coupling factor
ECL	Extracellular loop
EPR	Electron paramagnetic resonance
FPR2	Formyl peptide receptor 2
FRET	Förster resonance energy transfer
FSEC	Fluorescence-detection size-exclusion chromatography
g	9.81 ms^{-2}
GFP	Green fluorescent protein
GPCR	G-protein coupled receptor
ICL	Intracellular loop

IMAC	Immobilised metal affinity chromatography
IPTG	Isopropyl β-D-1-thiogalactopyranoside
ISOV	Inside-out vesicle
kDa	kiloDalton
kpsi	kilo-pound per square inch.
HDX	Hydrogen/deuterium exchange
LB	Luria broth
LDAO	n-Dodecyl-N,N-Dimethylamine-N-oxide
LDS	Lithium dodecyl sulphate
LLO	Lipid-linked oligosaccharide
LMNG	Lauryl maltose neopentyl glycol
LPS	Lipolysaccharide
MBP	Maltose-binding protein
MGE	Mobile genetic element
MESG	2-amino-6-mercapto-7-methylpurine riboside
MIC	Minimal inhibitory concentration
mM	Millimolar
M_n	Number average molecular weight
mPEG	Methoxypolyethylene glycol
MRSA	Methicillin-resistant *Staphylococcus aureus*
MST	Microscale thermophoresis
MW	Molecular weight
NBD	Nucleotide binding domain
NTA	Nitrilotriacetic acid
NMR	Nuclear magnetic resonance
OD	Optical density
OG	Octyl-β-glucoside
OM	n-Octyl-β-D-Maltoside
P-gp	P-glycoprotein
PBS	Phosphate buffered saline
PCAT	Peptidase-containing adenosine 5'-triphosphate-binding cassette
PCR	Polymerase chain reaction
PE	Phosphatidylethanolamine
PEG	Poly(ethylene) glycol

PELDOR	Pulsed electron-electron double resonance
P_i	Inorganic phosphate
PLD	Periplasmic domain
PNP	Purine nucleoside phosphorylase
PSM	Phenol soluble modulin
RFU	Relative fluorescence unit
RNA	Ribonucleic acid
RNAP	Ribonucleic acid polymerase
ROS	Reactive oxygen species
SBP	Substrate-binding protein
SDS-PAGE	Sodium dodecyl sulfate polyacrylamide gel electrophoresis
SEC	Size exclusion chromatography
smFRET	Single-molecule Förster resonance energy transfer
TAP	Transporter associated with antigen
TCDB	Transporter classification database
TEV	Tobacco etch virus
TM	Transmembrane
TMD	Transmembrane domain
tRNA	Transfer ribonucleic acid
TSS	Toxic shock syndrome

Acknowledgements

I would first like to thank my supervisor Dr Konstantinos Beis for the opportunity to undertake a PhD in his laboratory. The mentoring and guidance I have received from him have led me to become a better scientist. I would like to offer a special thanks to my fellow PhD student Feng who has accompanied me on this journey from the beginning. I would also like to thank my fellow researchers Maria, Indran and Jason. You have provided me with great technical advice, along with excellent conversation and much needed coffee breaks. I also wish to thank Florence and Thorben for a successful collaboration and for allowing me to spend time in Groningen to do experiments. Finally, I would like to pass on my regards to all the people at RCaH who helped to create a productive and relaxing environment to come to work every day.

Chapter 1: Introduction

1.1. ABC transporters

1.1.1. Membrane transport proteins

The lipid bilayer acts as a hydrophobic barrier that shields cellular components and organelles from the exterior environment (Singer and Nicolson, 1972). Membrane transport proteins mediate the exchange of chemicals and signals across the plasma membrane (Mitchell, 1957). Although some low molecular weight species can pass directly through the membrane, the majority of hydrophilic chemicals such as sugars, amino acids, ions and drugs require specific transport proteins to ensure selective permeability. As such, there are three major types of membrane transporter to fulfil this essential role: (i) uniporters, (ii) primary active transporters and (iii) secondary active transporters (Figure 1) (Saier Jr, 2000).

The least complex of the transporters are uniporters which facilitate the movement of their substrates down a concentration gradient by passive diffusion (Wolfersberger, 1994). They can be subdivided into ion channels and carrier proteins. Channels open in response to chemical or electrophysiological stimuli (Neher and Sakmann, 1976) and typically permit the passage of inorganic ions of appropriate size and charge (Doyle *et al*., 1998). Uniporter carrier proteins operate by binding to one molecule of substrate at a time and transporting the substrate along its concentration gradient (Wolfersberger, 1994).

Primary active transporters directly utilise the energy supplied by ATP hydrolysis in order to translocate ions or small molecules against the concentration gradient (Higgins *et al*., 1986; Hyde *et al*., 1990). Secondary active transporters by contrast exploit the energy stored in ion electrochemical gradients by coupling thermodynamically downhill movements of those ions to drive the uphill transport of another substrate (Ramos *et al*., 1976). In secondary active transport, the two molecules being transported may move either in the same direction or in

opposite directions across the membrane. When they move in the same direction, the protein that transports them is called a symporter, while if they move in opposite directions, the protein is called an antiporter. The Transporter Classification Database (TCDB), which groups membrane transport proteins according to their functional roles and phylogenetic relationships, currently contains more than 1000 families, highlighting the diversity of these systems (Saier Jr *et al*., 2016).

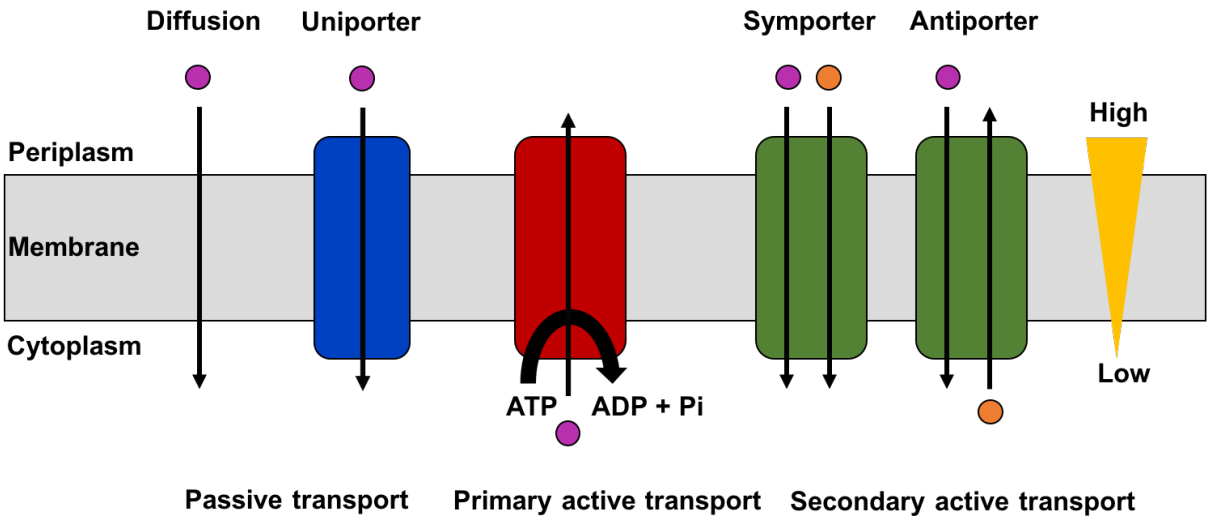


Figure 1. Major classes of membrane transport protein. The transported substrate is indicated by the pink circle and the transmembrane electrochemical gradient is shown as a yellow triangle. While some small molecules can diffuse directly across the membrane, passive transport can also occur by facilitated diffusion. A representative example of a uniporter carrier protein is shown transporting a substrate along its concentration gradient. Primary active transporters are driven by ATP hydrolysis to translocate substrates against the concentration gradient. Secondary active transporters are driven by the energy stored in ion concentration gradients. In secondary active transport, the two molecules being transported may be moved either in the same direction (symporters) or in opposite directions (antiporters) across the membrane.

1.1.2. Why study ABC transporters?

Among the class of primary active transporters, ATP-binding cassette (ABC) transporters couple the energy of ATP hydrolysis to the movement of substrates across the plasma membrane (Hyde *et al*., 1990). They can be subdivided into importers, which mediate the uptake of molecules into the cell and exporters, which transport molecules out of the cell. While ABC exporters are ubiquitously present in all domains of life (archaea, bacteria and eukaryotes), importers are found predominantly in bacteria (Davidson *et al*., 2008).

ABC transporters are responsible for the translocation of a wide range of substrates including amino acids, lipids, ions, proteins and carbohydrates (Beis, 2015). Bacterial ABC transporters are involved in fundamental biochemical processes such as the uptake of nutrients for cell growth (Cui and Davidson, 2011), export of cell wall assembly components (Cuthbertson *et al*., 2010), and efflux of antibiotics (Seeger and Van Veen, 2009). In addition, pathogenic bacteria that invade host cells during their infection cycle utilise ABC transporters to mediate virulence (Kobayashi *et al*., 2001; Chatterjee *et al*., 2013). As such, they represent important targets for therapeutic intervention.

There are 48 ABC transporters in humans and mutations in these proteins result in genetic disorders of the liver (Nicolaou *et al*., 2012), eye (Martinez-Mir *et al*., 1998) and blood (Albrecht *et al*., 2005). A number of multidrug ABC transporters are overexpressed in the gut, liver and kidneys where they restrict the bioavailability of administered drugs and contribute to multidrug resistance in cancer (Glavinas *et al*., 2004). Other clinically important members include the transporter of antigenic peptides (TAP) which plays an important role in the onset of adaptive immunity (Abele and Tampé, 2011). Some human ABC transporters have roles other than translocation such as the sulfonylurea receptor, which is part of an ATP-sensitive potassium channel involved in insulin secretion (Aittoniemi *et al*., 2009). Another example is

the cystic fibrosis transmembrane regulator (CFTR), an ATP-gated chloride channel containing > 1000 disease mutations responsible for cystic fibrosis (Riordan, 2008).

1.1.3. Structural features of ABC transporters

The core arrangement of an ABC transporter consists of two transmembrane domains (TMDs) that contain the substrate-binding site and two nucleotide-binding domains (NBDs) for ATP binding and hydrolysis (Figure 2) (Beis, 2015). The NBDs and TMDs of ABC importers are encoded by distinct genes, whereas ABC exporters can either exist as homodimers, where the NBDs and TMDs are encoded by a single polypeptide, or as heterodimers, where each half of the transporter is encoded by distinct genes. ABC importers are distinct in utilising an additional substrate-binding protein (SBP) for the recruitment of substrates to the TMDs (Figure 2) (Berntsson *et al*., 2010). The NBDs are highly conserved and contain a variety of motifs for ATP turnover whilst the TMDs differ in terms of sequence and topology to ensure substrate selectivity (Beis, 2015). Conformational changes between the NBDs and TMDs are transmitted through a pair of coupling helices.

Structural and biophysical studies have revealed that ABC transporters switch between inward and outward-facing states, exposing the substrate-binding site to either the inside or outside of the membrane (Locher, 2016). This model is known as the 'alternating access' mechanism, first proposed for membrane transport proteins over 50 years ago (Jardetzky, 1966). While the majority of ABC transporters follow the alternating access model, a number of members display novel and unconventional mechanisms that differ from this mode of translocation (Ford and Beis, 2019). Until recently, our knowledge of eukaryotic ABC transporters was predominantly based on the crystal structure of the multidrug ABC exporter P-glycoprotein (Aller *et al*., 2009; Jin *et al*., 2012). However, recent advances in cryo-electron microscopy

have enabled structure determination of eukaryotic ABC transporters from different classes (Zhang and Chen, 2016; Johnson and Chen, 2017; Qian *et al*., 2017; Taylor *et al*., 2017).

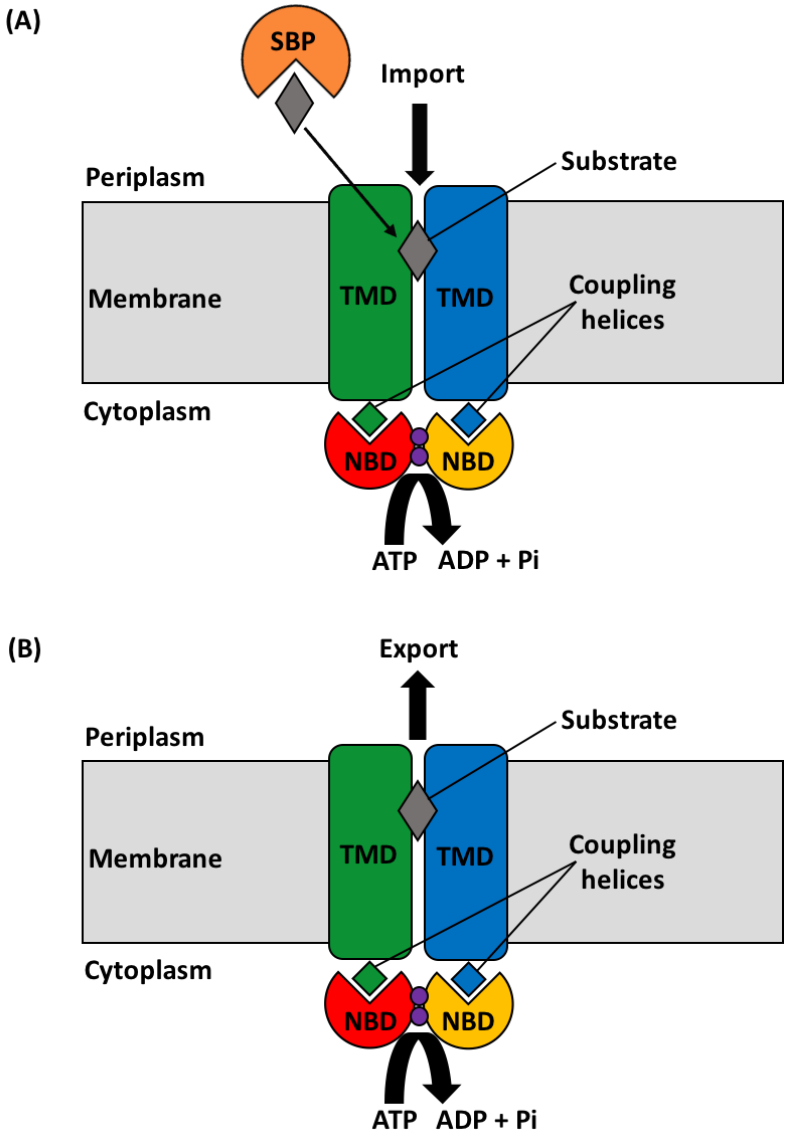


Figure 2. Domain arrangement of ABC transporters. Purple circles depict molecules of bound ATP at the NBD interface. (A) ABC importers require substrate-binding proteins (SBPs) to deliver substrates to the TMDs. The minimal arrangement of an ABC importer comprises two NBDs and two TMDs. A pair of coupling helices transmits conformational changes between the NBDs and TMDs. ABC importers use the energy of ATP hydrolysis to translocate substrates across the plasma membrane from the periplasm to the cytoplasm. (B) ABC exporters have a similar domain arrangement to ABC importers but do not utilise SBPs for substrate recruitment. ABC exporters harness the energy of ATP hydrolysis to expel substrates from the cytoplasm to the periplasm. Adapted from (Locher, 2016).

1.1.4. Architecture of the NBDs

The nucleotide-binding domains of ABC transporters possess a head-to-tail arrangement that upon dimerisation allows formation of the composite ATP-binding site. Each NBD is divided into a catalytic core and an α-helical subdomain that are characterised by a network of seven conserved motifs important for binding and hydrolysing ATP (Figure 3) (Schneider and Hunke, 1998; ter Beek *et al*., 2014).

(1) The A-loop contains a conserved aromatic residue which positions ATP by packing against and stabilising the adenine ring.

(2) The P-loop or Walker A motif (GXXGXGK(S/T) contains a highly conserved lysine residue which interacts with the α and β-phosphate groups of ATP.

(3) The Walker B motif (ϕϕϕϕDE where ϕ represents a hydrophobic residue) contains an aspartate immediately followed by a glutamate residue. The aspartate enables coordination of the magnesium ion and the catalytic glutamate acts as a general base to activate water molecules for nucleophilic attack on the γ -phosphate of ATP.

(4) The D-loop modulates formation of the ATP hydrolysis competent state by contacting the adjacent D-loop at the dimer interface.

(5) The H-loop or switch histidine forms a flexible hinge region that stabilises transition state geometry in the active site.

(6) The Q-loop forms direct contacts with the coupling helices and therefore mediates transmission of signals from the NBDs to the TMDs.

(7) The ABC signature motif (LSGGQ) forms an electrostatic interaction with the γ -phosphate of ATP, correctly positioning the nucleotide for hydrolysis.

In homodimeric ABC transporters, both NBDs contain consensus ATP-binding sites where ATP hydrolysis proceeds in a cooperative manner (Davidson *et al*., 1996). The NBDs of homodimeric ABC transporters can hydrolyse ATP even in the absence of transport substrates, resulting in futile cycles of ATP hydrolysis (Choudhury *et al*., 2014). In some heterodimeric ABC transporters, the presence of non-identical NBDs results in one consensus and one degenerate nucleotide binding site (Ernst *et al*., 2008). The degenerate ATP-binding site contains non-canonical residues that deviate from the consensus sequence, notably in the Walker B motif and switch histidine (both essential for ATP hydrolysis) as well as the ABC-signature motif. As such, the degenerate binding site is catalytically impaired and the rate of ATP hydrolysis is significantly slower in the corresponding NBD (Ernst *et al*., 2008).

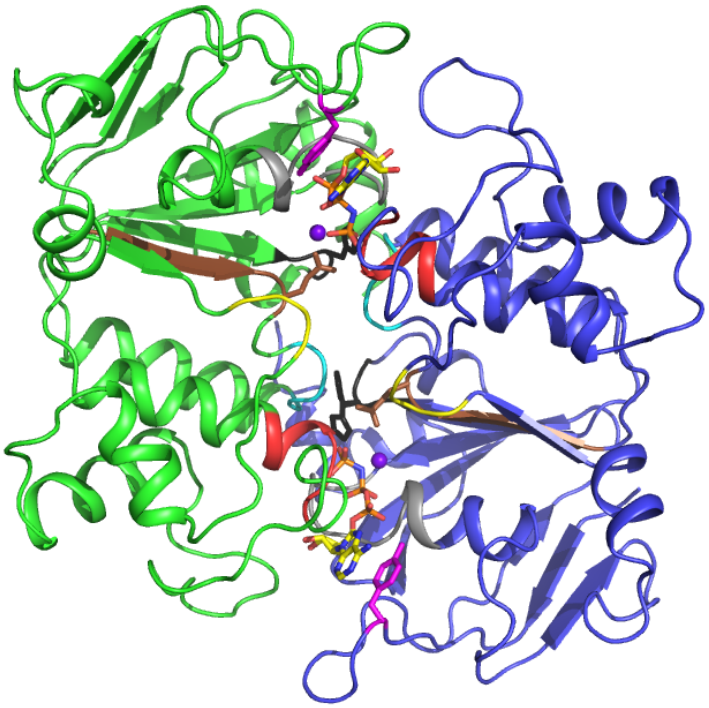


Figure 3. Conserved architecture in the NBDs. The structure of the NBDs from the bacterial ABC exporter McjD in complex with the non-hydrolysable ATP analogue AMP-PNP (PDB: 4PL0) is shown (Choudhury *et al*., 2014). The NBD monomers are coloured green and blue respectively. Two AMP-PNP molecules are depicted in yellow stick format and the Mg^{2+} ions are shown as purple spheres. Conserved motifs in the NBDs are coloured as follows: ABC-sigature motif (red), Walker A motif (grey), Walker B motif (brown), A-loop (magenta), D-loop (cyan), H-loop (black) and Q-loop (yellow).

1.1.5. Architecture of the TMDs

The TMDs of ABC transporters are phylogenetically diverse, which distinguishes them from the conserved nature of the NBDs and accounts for the broad range of substrates recognised (Beis, 2015). The mechanisms by which the TMDs of ABC transporters recognise their substrates will be discussed in section 1.1.8. The TM helices in each TMD are linked together by intracellular and extracellular loops. The N-terminus of the TMDs starts with an amphipathic elbow helix which is parallel to and partially inserted into the membrane from the intracellular side (Dawson and Locher, 2006). The elbow helix can also interact with potential substrates to facilitate access to the TMDs (Smriti *et al*., 2009). The cytoplasmic end of the TMDs contain a pair of coupling helices to mediate cross-talk with the grooves of the NBDs (Dawson and Locher, 2006).

ABC transporters can be divided into a total of seven classes on the basis of sequence and structural homology in the TMDs. Types I-III function as importers, types IV/V as exporters, type VI as extractors and type VII transporters assemble as part of multicomponent efflux pumps (Thomas and Tampé, 2018). Type I and II importers differ in the number of TM helices in each TMD (Lewinson and Livnat-Levanon, 2017), whereas type III importers, also known as ECF (energy-coupling factor) transporters, have a distinct organisation and lack conventional TMDs (Xu *et al*., 2013). Type IV-VII ABC transporters differ in both the number of TM helices in each half of the transporter and the type of fold exhibited (Thomas and Tampé, 2018). The precise TMD arrangement of each class of ABC transporter will be discussed in sections 1.1.6 and 1.1.7.

Human ABC transporters can be further grouped into seven subfamilies, ABCA to ABCG, according to their domain organisation and auxiliary domains (Dean and Annilo, 2005). The presence of auxiliary domains confers additional functions that are critical for the processing

of transport substrates. Representatives of subfamilies B, C and D adopt the same overall fold as type IV transporters, Members of the ABCA and ABCG subfamilies possess a type V fold, whereas ABCE and ABCF proteins do not function as transporters since they lack any TMDs (Thomas and Tampé, 2018). It is worth noting that the gene products of human ABC transporters encode proteins that may differ in nomenclature depending on the member (*e.g.* ABCA1 is commonly referred to as P-glycoprotein and ABCC1 is known as MRP1).

1.1.6. Structures and mechanisms of ABC importers

ABC importers are responsible for the translocation of substrates from the outside of the membrane to the inside of the cell (Beis, 2015). Type I ABC importers typically import metabolites such as sugars, solutes, amino acids and peptides (Lewinson and Livnat-Levanon, 2017). The best studied example of a type I ABC importer is the maltose importer $MalFGK_2$ from *Escherichia coli* which has been structurally characterised at each step of the transport cycle (Chen, 2013). The substrates of type II ABC importers are typically larger, hydrophobic molecules such as heme and vitamin B_{12} (Köster, 2001). Type III ABC importers are responsible for the translocation of a diverse range of compounds including micronutrients. However, their transport mechanisms are less well-defined owing to their recent identification (Rempel *et al*., 2019). Table 1 compares the architectures and mechanisms of ABC importers from different classes.

Class	Type I	Type II	Type III
Examples	$MalFGK_2$ (maltose)	BtuCD (vitamin B_{12})	HmpT (vitamin B_6)
TMD organisation	TMDs can either be identical or different with variable numbers of TM helices in each TMD	10 TM helices in each TMD	Lack TMDs. Instead contains TM coupling protein (5 TM helices plus 3 cytoplasmic α-helices)
Substrate capture	SBP contains flexible hinge. Large conformational changes upon substrate binding.	SBP contains rigid α-helix. Limited conformational changes upon substrate binding.	Lacks SBP. Instead contain membrane embedded S-components for substrate capture.
Substrate affinity to SBP/S-component	Variable, nanomolar to low micromolar	Nanomolar	Nanomolar
Substrate-transporter interaction	Substrate binding by SBP promotes its association with the TMDs	High substrate concentrations inhibit SBP-transporter interaction	Unknown
ATPase activity	Low basal, high stimulation by substrates	High basal, low stimulation by substrates	Unknown
Transport mechanism	ATP binding stabilises SBP-transporter interaction. Substrate released from SBP binds TMDs. Transporter transitions from inward to outward-facing state.	ATP binding destabilises SBP-transporter interaction. Transporter transitions from outward to inward-facing state. ATP hydrolysis stimulates substrate release.	ATP binding to the NBDs exposes S-component binding site to the periplasm for substrate capture. ATP hydrolysis causes toppling of the S-component and release of substrate in the cytoplasm.

Table 1. Comparison between different classes of ABC importer.

Type I and II ABC importers require periplasmic substrate-binding proteins (SBPs) to capture substrates at the extracellular side of the membrane and deliver them to the TMDs (Berntsson *et al*., 2010). There is considerable variation in the binding affinities of type I SBPs for their substrates, varying between tens of nanomolar to several micromolar (Lewinson and Livnat-Levanon, 2017). SBPs associated with type II ABC importers typically bind their substrates with nanomolar affinities. SBPs share a common core architecture consisting of two α/β domains connected together by a hinge region (Quiocho and Ledvina, 1996). Substrate binding at the interface of the two domains occurs by a 'Venus-Fly trap' mechanism of capture (Figure 4). SBPs associated with type I ABC importers contain a flexible hinge region and therefore undergo large conformational changes upon interaction with the substrate (Berntsson *et al*., 2010). SBPs associated with type II ABC importers possess a rigid α-helix between the two domains that limits the extent of rotation upon substrate binding. Type III ABC importers do not utilise SBPs for substrate delivery and instead employ membrane-embedded S-components to perform this function (Rodionov *et al*., 2009). Within the S-components, the substrate-binding site is located near the extracellular surface, capturing substrates with high affinity (nanomolar K_D range) and specificity (Zhang *et al*., 2010; Erkens *et al*., 2011).

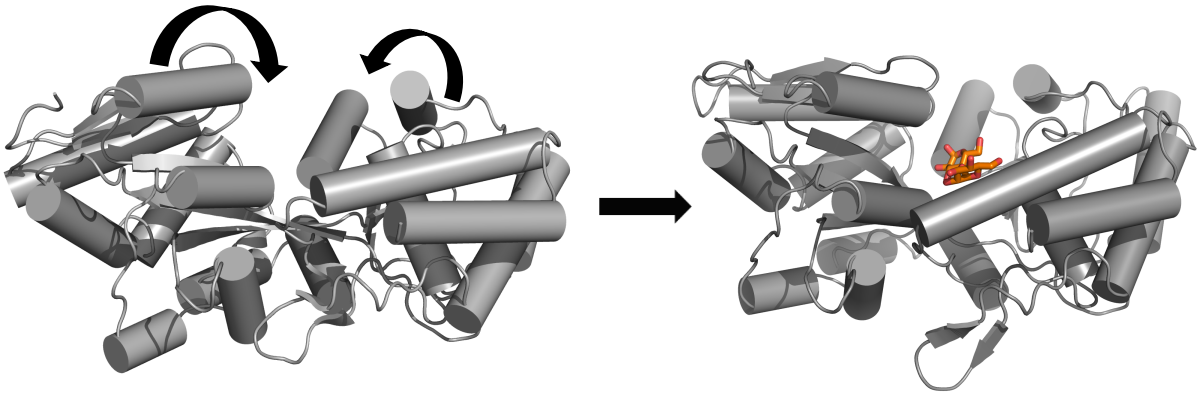


Figure 4. Mode of substrate recognition by SBPs. The left hand panel shows the structure of the type 1 associated SBP maltose-binding protein (MBP) (PDB ID: 1EZ9) (Sharff *et al*., 1992). The right hand panel shows the structure of MBP in complex with maltose (PDB ID: 1AN4) (Spurlino *et al*., 1991). MBP is coloured grey and maltose is depicted in orange stick format. In the substrate-free form the cavity between the two lobes connected by the hinge is accessible. Upon binding of maltose, the cavity undergoes a 'Venus-Fly trap' closure.

The two TMDs of type I ABC importers are structurally diverse and can exist as either homodimers (*e.g.* MetNI) (Kadaba *et al*., 2008) or heterodimers (*e.g.* $MalFGK_2$) (Oldham *et al*., 2007). The TMDs of the methionine importer, MetNI, each contain 5 TM helices (Kadaba *et al*., 2008) whereas the TMDs of maltose importer $MalFGK_2$ are distinct, containing 6 and 8 TM helices respectively (Oldham *et al*., 2007). The TMDs of type II ABC importers are identical, each composed of 10 TM helices, resulting in an arrangement of 20 TM helices in the complete transporter (Locher *et al*., 2002). In contrast, type III ABC importers are lack TMDs and instead contain transmembrane coupling proteins that interact with their cognate S-components during transport (Xu *et al*., 2013; Wang *et al*., 2013).

Type I ABC importers such as $MalFGK_2$ deploy the alternating access mechanism in order to translocate substrates from the periplasm to cytoplasm (Figure 5) (Chen, 2013). The resting state of type I importers is an inward-facing conformation containing open NBDs (Khare *et al*., 2009). Docking of the substrate-loaded SBP at the TMDs generates a pre-translocation state characterised by partial closure of the NBDs and rotation of the TMDs (Oldham and Chen,

2011a). In $MalFGK_2$, interactions between the SBP and TMDs are mediated by a large, periplasmic P2 loop in the MalF subunit. Following ATP binding to the NBDs, the transporter switches to an outward-facing conformation characterised by further closure of the NBDs and TMDs (Oldham *et al*., 2007). This change in conformation distorts the SBP binding pocket, and enables substrate transfer from the SBP to the TMDs. ATP hydrolysis then promotes opening of the NBDs, leading to substrate release in the cytoplasm (Oldham and Chen, 2011b). In $MalFGK_2$, the substrate-induced changes lead to a 1000-fold stimulation of the transporter ATPase activity (Khare *et al*., 2009).

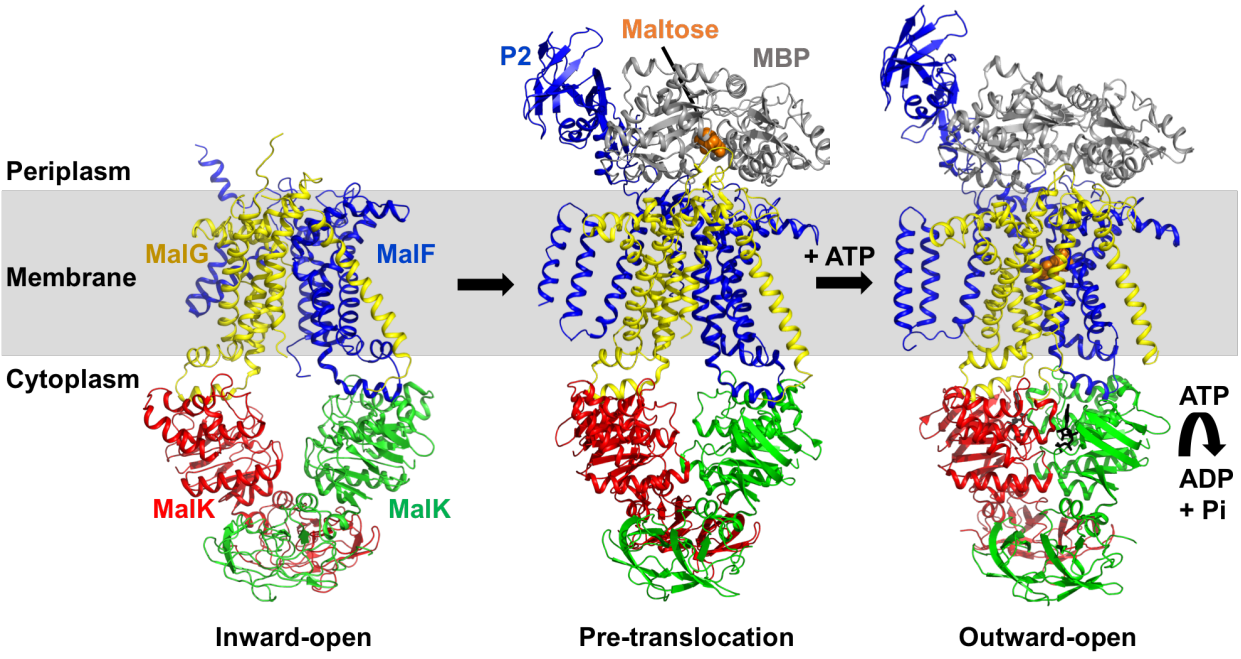


Figure 5. Transport mechanism for the type I ABC importer $MalFGK_2$. The $MalFGK_2$ subunits are coloured blue (MalF), yellow (MalG), red and green (MalK). MBP is coloured grey, maltose is shown as orange spheres and ATP in black stick format. The resting state of $MalFGK_2$ is an inward-open conformation (PDB: 3FH6). Association of substrate-bound MBP promotes reorientation of the TMDs, resulting in a closed $MalFGK_2$ conformation (pre-translocation state) where the NBDs adopt a semi-open dimer (PDB:2R6G). The P2 loop of MalF stabilises the transporter-SBP interaction. ATP binding leads to formation of the outward-open state (PDB: 3RLF), resulting in the transfer of maltose from MBP to the TMDs, complete closure of the NBDs and ATP hydrolysis. The dissociation of nucleotide and MBP restores the inward-facing state.

Type II ABC importers possess a more complex mechanism of transport. Unlike type I importers, they have high basal rates of ATP hydrolysis that are only weakly stimulated by SBPs (Borths *et al*., 2005). The best characterised type II importer is the vitamin B_{12} importer BtuCD from *E. coli* (Korkhov *et al*., 2014). Unlike type I importers, the resting conformation of type II importers is outward-facing and ATP-bound (Figure 6A) (Korkhov *et al*., 2014). Docking of the substrate-bound SBP to the TMDs promotes substrate release into the cavity, promoting conformational changes in the TMDs (Korkhov *et al*., 2012). Unlike type I importers, the TMDs of type II importers have little or no affinity to their substrates. ATP hydrolysis then induces opening of the NBD dimer, formation of an inward-facing state and release of the substrate into the cytoplasm (Pinkett *et al*., 2007). Following substrate dissociation, type II importers transition to an asymmetric conformation which may be involved in preventing solute leakage as the system resets for a new cycle (Hvorup *et al*., 2007). At high substrate concentrations, the interaction between the SBP and transporter is inhibited (Gerber *et al*., 2008).

Type III ABC importers are often referred to as energy coupling factor (ECF) transporters. One of he best characterised examples at the structural level is the vitamin B_6 ABC importer HmpT from *Lactobacillus brevis* (Figure 6B) (Wang *et al*., 2013). Type III members are thought to adopt a toppling mechanism where the S-component rotates in the lipid bilayer to expose its binding site alternately to the cytoplasm and periplasm (Xu *et al*., 2013; Wang *et al*., 2013; Zhang *et al*., 2014; Swier *et al*., 2016). ATP binding to the NBDs disrupts the hydrophobic interface of the transmembrane coupling protein, resulting in dissociation of the S-component. The S-component then adopts an upright conformation in the membrane where it can capture substrates from the periplasm. Upon ATP hydrolysis, the substrate-bound S-component topples over and clicks back onto the transmembrane coupling protein, releasing the substrate into the cytoplasm (Rempel *et al*., 2019).

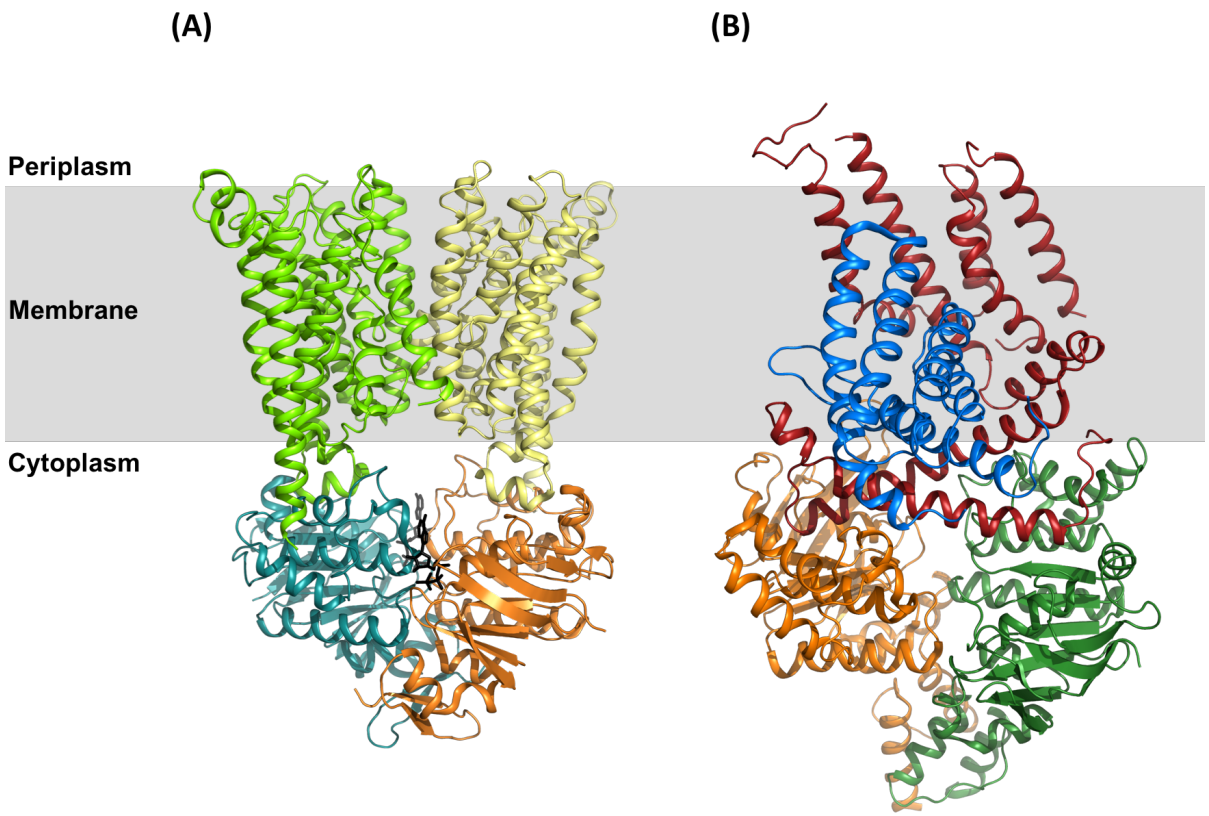


Figure 6. Architecture of type II and type III ABC importers. (A) Structure of the type II ABC importer BtuCD. The BtuCD subunits are coloured green/yellow (BtuC) and teal/orange (BtuD). The substrate-binding protein BtuF is coloured red and the ATP analogue AMP-PNP is shown in black stick format. BtuCD adopts an outward-open ATP-bound state under resting conditions (PDB: 4RNU). (B) Structure of the type III ABC importer HmpT. The transmembrane coupling protein is coloured red and the S-component is coloured blue. The NBDs are coloured green and orange respectively. HmpT is shown in the nucleotide free state (PDB: 4HZU) (Wang *et al*., 2013). The S-component adopts a 'toppled' conformation in the membrane.

1.1.7. Structures and mechanisms of ABC exporters

ABC exporters are responsible for the translocation of substrates from the inside of the membrane to the outside of the cell (Beis, 2015). The substrates of ABC exporters are diverse and involved in critical biological processes. For example, assembly of the potent immune stimulant lipopolysaccharide (LPS) in the outer membrane is coordinated by three ABC exporters from different classes. The LPS precursor, lipid A-core oligosaccharide (rough LPS), is synthesised in the cytoplasmic leaflet of the inner membrane and flipped to the periplasmic leaflet by the type IV ABC transporter MsbA (Zhou *et al*., 1998). The third component of LPS, O-antigen polysaccharide, is translocated from the cytoplasmic to the periplasmic leaflet using the type V ABC transporter, Wzm-Wzt, where it is ligated to the lipid A-core forming mature LPS (Greenfield and Whitfield, 2012). The type VI ABC transporter $LptB_2FG$ subsequently extracts LPS from the periplasmic leaflet (Ruiz *et al*., 2008). Following extraction, LPS is delivered across the periplasm by other components of the Lpt system that bridge together and insert LPS in the outer membrane (Sherman *et al*., 2018).

ABC exporters also participate in antibiotic resistance. The type VII ABC transporter MacB forms part of a tripartite efflux pump (TEP), allowing macrolide antibiotics to bypass the periplasm during transport across the inner and outer membranes of Gram-negative bacteria (Kobayashi *et al*., 2001). In addition to its role as a lipid flippase, the type IV ABC transporter MsbA also functions as a multidrug efflux pump responsible for the secretion of a large number of amphipathic and hydrophobic molecules (Woebking *et al*., 2005). Table 2 compares the architectures and mechanisms of ABC exporters from different classes.

Class	Type IV	Type V	Type VI	Type VII
Examples	MsbA (LPS flipping, drugs), PCAT (peptides), PglK (LLOs)	Wzm-Wzt (O-antigen)	$LptB_2FG$ (LPS extraction)	MacB (macrolide antibiotics)
Topology	N-terminal TMD, C-terminal NBD	N-terminal NBD, C-terminal TMD	N-terminal NBD, C-terminal TMD	N-terminal NBD, C-terminal TMD
TMD organisation	6 TM helices in each TMD. TM helices may intertwine with the opposite monomer.	6 TM helices in each TMD, shorter than type IV. Unique interface with the NBDs and no crossover helices.	6 TM helices in each TMD containing additional β-jellyroll-like subdomains.	4 TM helices in each TMD containing additional periplasmic subdomains.
Substrate-transporter interaction	Large central cavity. Substrates recruited either from cytoplasm or membrane.	Central cavity between the TMDs.	Large outward-facing V-shaped cavity.	Lacks central cavity. Substrates recruited directly from periplasm.
Transport mechanism	Variable. Alternating access model for MsbA but outward-only model for PglK. May require occluded states.	Processive threading of polymeric substrates through Wzm-Wzt driven by multiple cycles of ATP binding and hydrolysis.	Outward-only mechanism for $LptB_2FG$, where the V-shaped cavity opens laterally in response to ATP binding.	Molecular bellows mechanism where ATP binding to the NBDs triggers closure of the PLDs and expulsion of the substrate.

Table 2. Comparison between different classes of ABC exporter.

Type IV ABC transporters are composed of an N-terminal TMD and a C-terminal NBD. They exist as either homodimers or heterodimers, with a common arrangement of 6 TM helices in each TMD. The TM helices in each hexahelical bundle are connected to one another by an arrangement of long intracellular and extracellular loops (Dawson and Locher, 2006). Structures of some homodimeric members (*e.g.* Sav1866 from *Staphylococcus aureus*, MsbA from *Vibrio cholerae* and *Salmonella typhimurium*) display domain swapping, otherwise known as 'inter-domain twining', a phenomenon where TM helices from one half of the transporter cross over and interact with TM helices from the opposite monomer (Dawson and Locher, 2006; Ward *et al*., 2007). These ABC exporters adopt an inward-open state in the absence of nucleotides. The inward-open conformation contains TMDs open to the cytoplasmic side of the membrane and separated NBDs (Ward *et al*., 2007). The large transmembrane cavity of MsbA is open to substrate binding from either the cytoplasm or membrane (Ward *et al*., 2007) but for Sav1866, the translocation pathway is completely shielded from the inner membrane leaflet (Dawson and Locher, 2006). The alternating access transport mechanism for MsbA is shown in Figure 7. ATP binding causes the NBDs to dimerise and triggers formation of the outward-open state, where the TMDs are open to the extracellular side. Transport may be further aided by the transmembrane electrochemical proton gradient which has been shown to enhance drug efflux by MsbA (Singh *et al*., 2016). Following substrate release, ATP hydrolysis enables dissociation of the NBD dimer to reset the transport cycle (*i.e.* restore the inward-facing state).

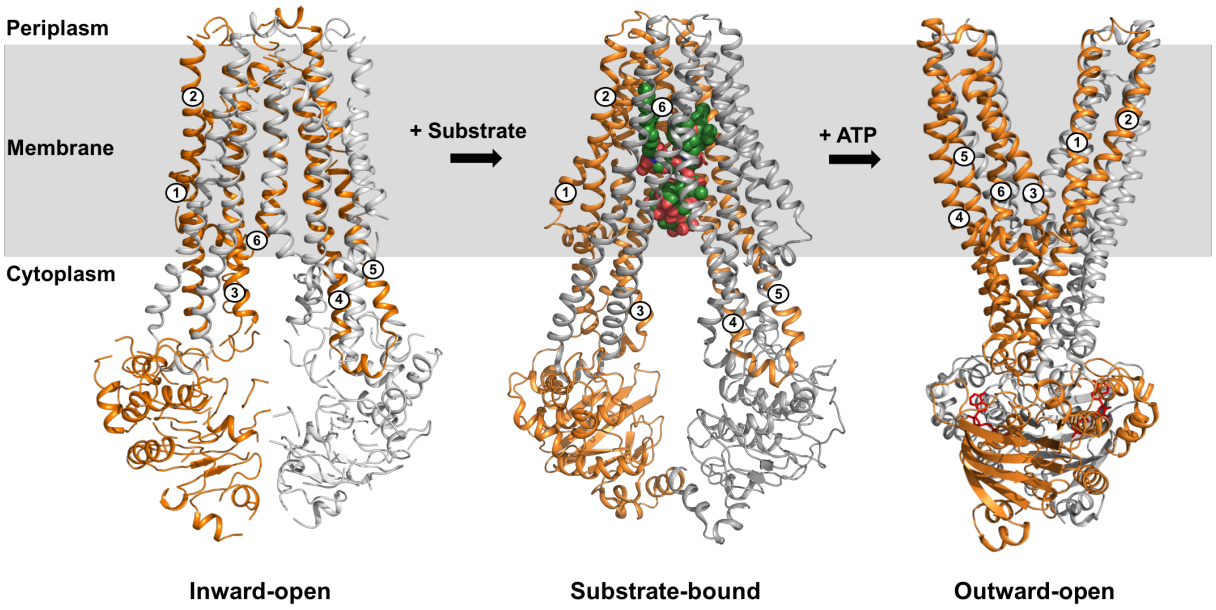


Figure 7. Structures of the type IV ABC transporter MsbA. The MsbA monomers are coloured orange and grey. AMP-PNP is depicted in red stick format. LPS is shown as green spheres. The left panel shows the structure of MsbA in the nucleotide free inward-open state (PDB: 3B5X) (Ward *et al*., 2007). The NBDs have disengaged and the TMDs have diverged to the cytoplasm owing to inter-subunit twining between TM4 and TM5 with TMs 1-3 and 6 of the opposite subunit. The middle panel shows the structure of MsbA in complex with LPS (PDB: 5TV4) (Mi *et al*., 2017). The right panel shows the structure of MsbA-AMP-PNP in the outward-open state (PDB: 3B60) (Ward *et al*., 2007). The NBDs are dimerised and the TMDs have diverged to the periplasm due to inter-subunit twining of TM1 and TM2 with TM3-6 of the opposite monomer.

Importantly, not all type IV ABC transporters follow the same mechanism. For example, structures of the homodimeric type IV peptide ABC transporters McjD from *E. coli* (Choudhury *et al*., 2014) and PCAT from *Clostridium thermocellum* (Lin *et al*., 2015) adopt nucleotide bound occluded conformations along the transport cycle where the TMDs are inaccessible from both sides of the membrane. PCAT contains auxiliary C39 peptidase domains that cleave peptides before transferring them to the TMDs (Figure 8). Upon ATP binding, the C39 peptidase domains become disengaged from the transporter giving rise to the

occluded state. The occluded state is then likely to open up to the extracellular side to release the bound peptide (Lin *et al*., 2015). Another example is the homodimeric type IV LLO (lipid-linked oligosaccharide) flippase, PglK, from *Campylobacter jejuni* which utilises an 'outward-only' mechanism distinct from the alternating access model (Perez *et al*., 2015). For PglK, the inward-open conformation is not required for flippase activity and LLOs directly enter the outward-facing cavity *via* a lateral opening in the cell membrane.

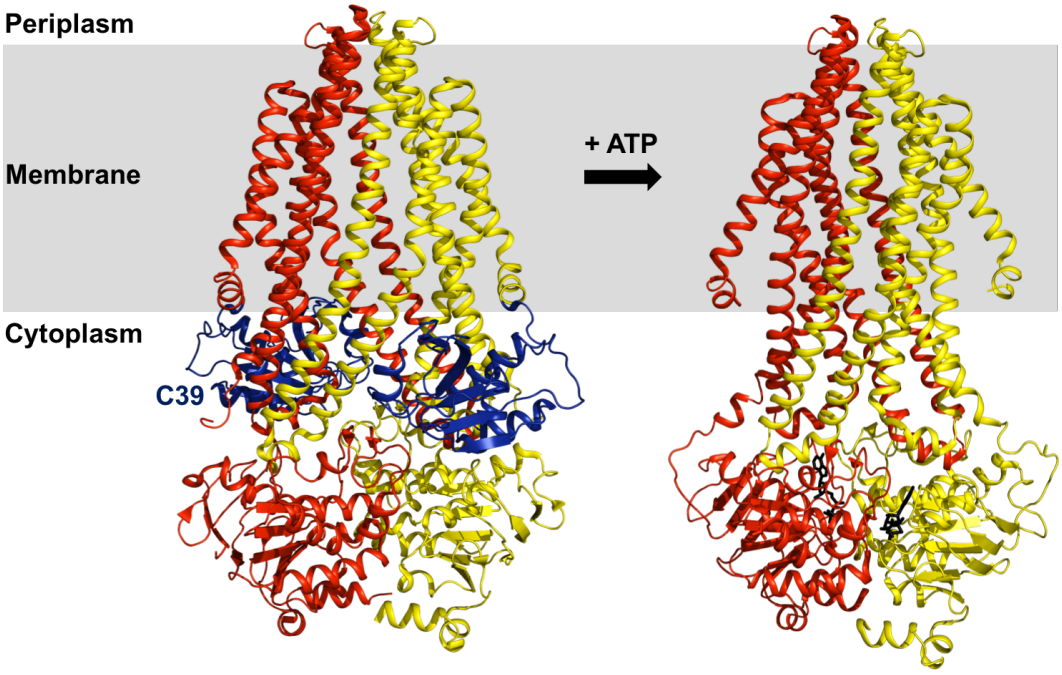


Figure 8. Structures of the type IV ABC transporter PCAT. The PCAT monomers are coloured red and yellow with the C39 peptidase domain highlighted in green. The ATP analogue ATPγS is shown in black stick format. The left panel shows the nucleotide free structure of PCAT in an inward-open conformation (PDB: 4RY2) (Lin *et al*., 2015). The C39 peptidase domains interact with the open TMDs and facilitate substrate binding within the cavity upon processing. The right panel shows the ATPγS-bound structure of PCAT (PDB: 4S0F) in an outward-occluded conformation. The C39 peptidase domains dissociate following nucleotide binding.

Type V ABC transporters contain a different transmembrane organisation to type IV members. Each half of the transporter is composed of an N-terminal NBD fused to a C-terminal TMD containing 6 TM helices. The TM helices and intracellular loops are shorter in type V ABC transporters, resulting in a smaller distance between the NBDs and membrane (Taylor *et al*., 2017; Bi *et al*., 2018). In addition, they also lack crossover helices between the two TMDs. The compact arrangement of the type V TMDs resembles that found in type I and II ABC importers (Locher *et al*., 2002). The structure of the heterodimeric O-antigen polysaccharide transporter Wzm-Wzt from *Aquifex aeolicus* contains a type V fold (Figure 9A). The TMD subunits (Wzm) assemble into a continuous transmembrane channel. The NBDs (Wzm) are closely separated and contain gate helices that pack against the TMDs, serving as a substrate entry point (Bi *et al*., 2018). Wzm-Wzt operates using a mechanism distinct from the alternating access model, where processive cycles of ATP binding and hydrolysis drive translocation of the polymer across the channel.

Type VI ABC transporters contain a unique TMD fold as revealed by structures of $LptB_2FG$ from *Pseudomonas aeruginosa* (Luo *et al*., 2017) (Figure 9B) and *Klebsiella pneumoniae* (Dong *et al*., 2017). The heterodimeric TMDs (LptF and LptG), each contain 6 TM helices, and form a large outward-facing V-shaped central cavity, lacking crossover helices between the two domains. Unlike other ABC transporter classes, the TMDs contain β-jellyroll-like subdomains composed of 7 and 9 β-strands respectively. $LptB_2FG$ is proposed to transport LPS using an outward-only mechanism similar to that of PglK (Perez *et al*., 2015). ATP binding to LptB drives closure of the NBDs and is thought to trigger opening of the lateral gates for substrate entry. Following ATP hydrolysis, LPS is transferred to the TMDs *via* their β-jellyroll-like subdomains before dissociation of the nucleotide restores the resting state (Luo *et al*., 2017; Dong *et al*., 2017). To date, $LptB_2FG$ is the only type VI ABC transporter to be structurally characterised.

Type VII ABC transporters represent the most recently identified class in the subfamily. Structures of the homodimeric ABC transporter MacB from *Aggregatibacter actinomycetemcomitans* (Crow *et al*., 2017) and *Acinetobacter baumannii* (Okada *et al*., 2017) have revealed novel features in the type VII fold that differ to other classes. MacB is coupled to the hexameric adapter protein MacA and the trimeric TolC exit duct, forming a continuous pathway across the inner and outer membranes (Fitzpatrick *et al*., 2017). Unlike the TMDs of type IV-VII ABC transporters, MacB has only 4 TM helices in each TMD monomer (lacking inter-subunit twining) and contains a large periplasmic domain (PLD) (Crow *et al*., 2017; Okada *et al*., 2017). The TMD dimer interface is composed of TM1 and TM2 from each monomer, both of which extend beyond the height of the periplasmic leaflet, forming a stalk that contacts the TMDs (Figure 9C). Unlike other classes of ABC transporter, MacB lacks a central cavity through which substrates can enter. Instead, MacB recruits substrates directly from the periplasm where they can enter an open V-shaped cavity. ATP binding closes the stalk and PLDs, leading to a reduction in the volume of the cavity and expelling substrates into the MacA gating ring and subsequently through TolC (Crow *et al*., 2017).

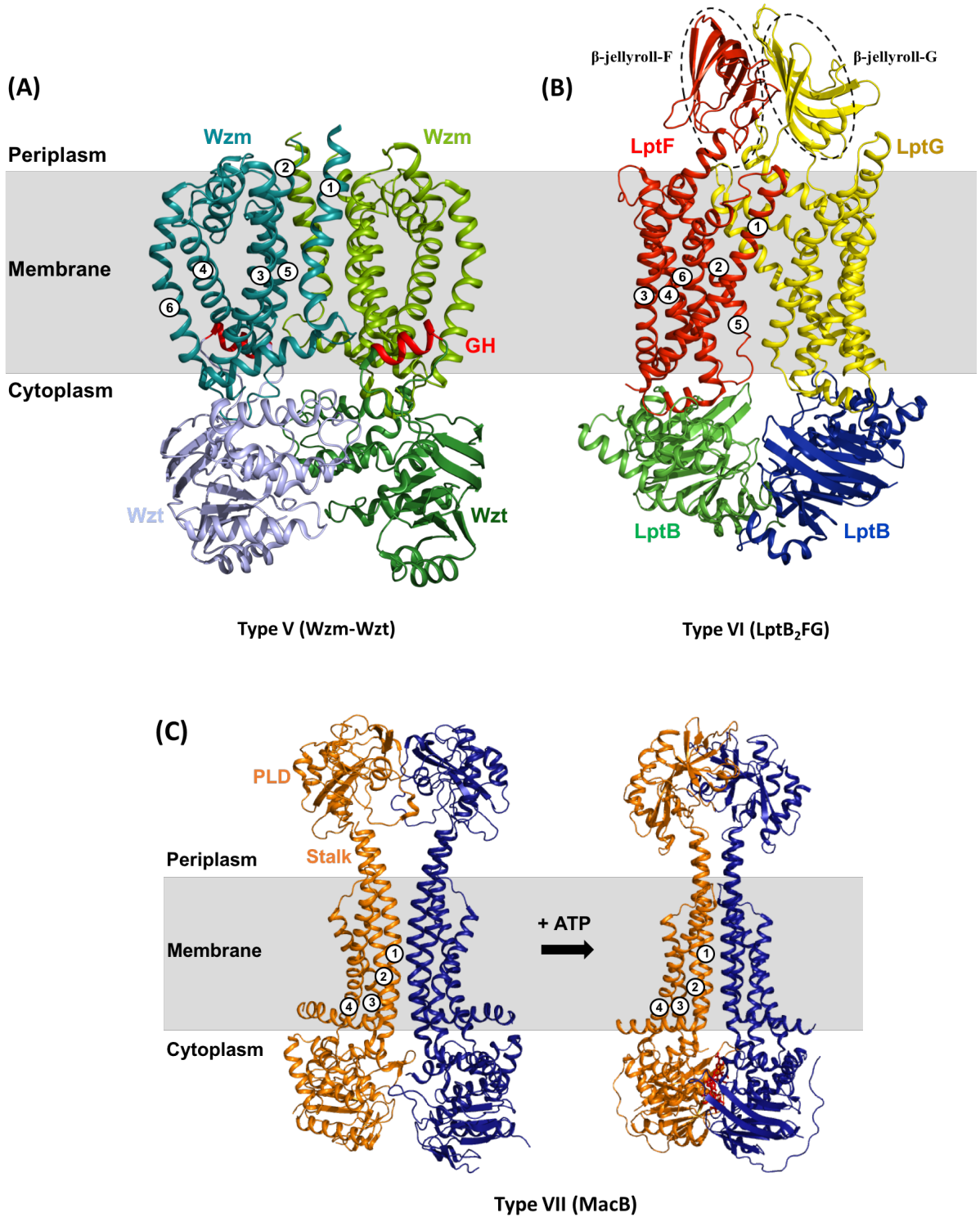


Figure 9. Architecture of type IV-VII ABC transporters. The TM helices are numbered in one TMD of each monomer. (A) Structure of the type V ABC transporter Wzm-Wzt in the nucleotide free state (PDB: 6ANZ) (Bi *et al*., 2018). The NBDs (Wzm) are coloured teal and light green. The TMDs (Wzt) are coloured grey and forest green. Gate helices (GH) are highlighted in red. Wzm-Wzt contains a compact NBD-TMD interface characteristic of type V ABC transporters. (B) Structure of the type VI ABC transporter $LptB_2FG$ in the nucleotide

free state (PDB: 5X5Y) (Luo *et al*., 2017). The NBDs (LptB) are coloured green and blue. The TMDs are coloured red (LptF) and yellow (LptG). Positions of the β-jellyroll-like subdomains are highlighted in black circles and represent the most striking feature of type VI ABC transporters. (C) Structures of the type VII ABC transporter MacB in the nucleotide free state (PDB: 5NIK) (Fitzpatrick *et al*., 2017) and ATP-bound state (PDB: 5L57) (Crow *et al*., 2017). The MacB monomers are coloured orange and blue. ATP is depicted in red stick format. MacB contains 4 TM helices characteristic of type VI ABC transporters. TM1 and TM2 extend into the periplasm *via* a stalk which is linked to a large periplasmic domain (PLD). ATP binding induces conformational changes across the transporter, resulting in closure of the NBDs, TMDs and PLDs.

1.1.8. How do ABC exporters recognise their substrates?

In recent years, structure determination of ABC exporters in complex with substrates and inhibitors has revealed important insights into the principles that govern ligand recognition. The cryo-EM structure of MsbA in complex with rough LPS captures a state where LPS has traversed the lipid bilayer but remains 'unflipped' in the TMDs (Figure 10A) (Mi *et al*., 2017). The MsbA inner space is subdivided into a hydrophilic cavity and a hydrophobic pocket. The hydrophilic cavity contains a cluster of positively charged residues that form a ring of interactions with the phosphorylated glucosamine head groups of lipid A (Figure 10B). The hydrophobic pocket houses the acyl chains of LPS which orient towards the periplasmic side of the TMDs. The authors define a lateral entry point for LPS between TM4 and TM6. The structure of LPS-bound MsbA has also been determined in the presence of the selective small molecule quinolone antagonist G907 (Ho *et al*., 2018). The inhibitor locks MsbA in an inward-facing conformation, wedging between the TMDs at the interface of TM4 and TM6 (Figure 10C). The presence of G907 in the cavity causes a 4 Å shift of TM4. The NBDs also adopt an asymmetric conformation where they are no longer primed for ATP binding and hydrolysis (Ho *et al*., 2018).

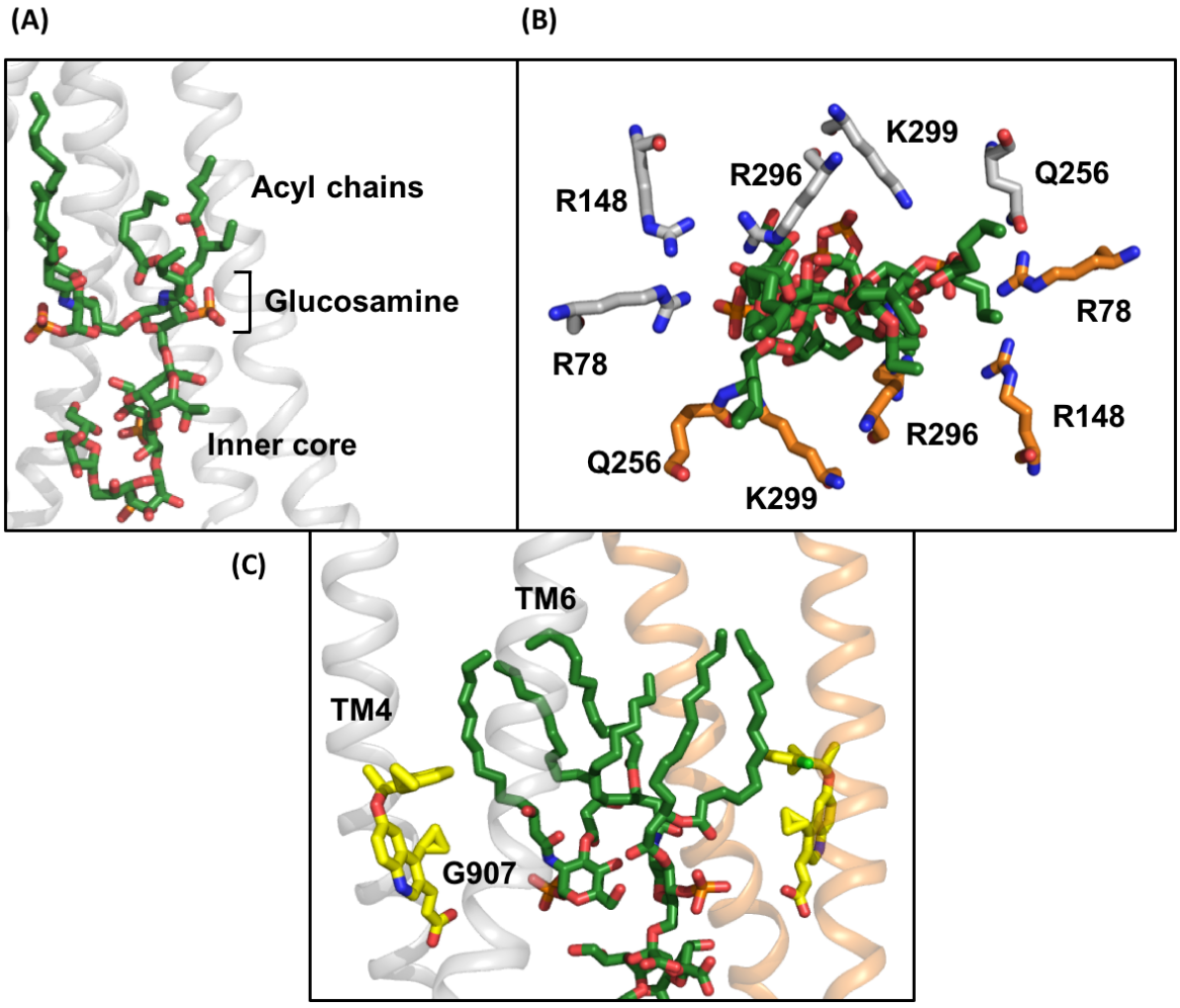


Figure 10. Ligand recognition in MsbA. LPS is shown in green stick format with phosphate groups coloured orange. (A) Orientation of LPS in the MsbA binding pocket (PDB: 5TV4) (Mi *et al*., 2017). The acyl chains are located towards the periplasmic side of the TMDs. (B) Coordination of LPS in the MsbA binding pocket. Charged residues in the MsbA monomers are shown in grey or orange stick format depending on the monomer from which they are derived. The conserved positively charged residues R78, R148 and K299 are most important in stabilising the phosphorylated glucosamine group of LPS. (C) Binding pocket of MsbA-LPS in the presence of the inhibitor G907 (Ho *et al*., 2018) (PDB: 6BPL). G907 is shown in yellow stick format. G907 binds to MsbA at the interface of TM4 and TM6 *via* an induced-fit mechanism.

Structures of the homodimeric type IV ABC transporter P-glycoprotein reveal how multidrug ABC exporters can recognise such a broad range of substrates. The substrate translocation pathway of P-glycoprotein is continuous with the membrane inner leaflet, enabling drugs to be recruited directly from the membrane (Aller *et al*., 2009). The structure of P-gp from *C. elegans* contains discontinuous TM helices lining the lateral opening of the TMDs (Jin *et al*., 2012). The presence of these disordered loop regions enhances the propensity for transporter-drug interactions and provides flexible hinges to gate the translocation pathway. The structure of P-gp in complex with the inhibitor zosuquidar has also been determined (Figure 11) (Alam *et al*., 2018). The two bound zosuquidar molecules are wrapped around each other in a defined binding pose and display pseudo two-fold symmetry. The binding pocket is lined with residues from all 12 TM helices while residues from 8 TM helices exhibit direct interactions with zosuquidar. The presence of many aromatic amino acids confers adaptive plasticity to the pocket, enabling recognition of structurally diverse compounds (Loo *et al*., 2003).

The recently determined structure of P-gp in complex with the substrate Taxol, demonstrates how ABC exporters can discriminate between substrates and inhibitors (Alam *et al*., 2019). Interestingly, zosuquidar and Taxol share the same binding pocket, and the residues involved in drug binding are largely similar. The authors go on to demonstrate that competitive inhibitors such as zosuquidar function by restricting access to the substrate-binding pocket, preventing NBD closure and preventing transition to the outward-open state. In contrast, transport substrates like Taxol fill the binding pocket less completely than inhibitors, suggesting that shape complementarity and the strength of contacts, are key determinants distinguishing substrates from inhibitors (Alam *et al*., 2019).

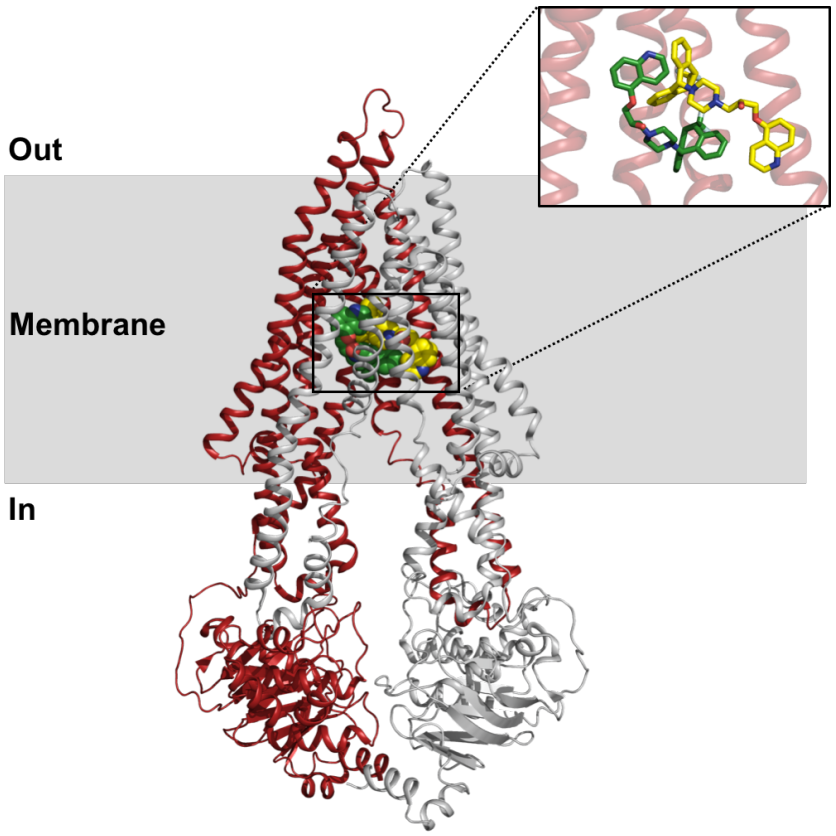


Figure 11. Cryo-EM structure of P-glycoprotein in complex with zosuquidar. The P-glycoprotein monomers are coloured red and grey. Two molecules of zosuquidar are depicted in stick format, coloured green and yellow respectively. The zosuquidar molecules are wrapped around each other and display pseudo two-fold symmetry (PDB: 6FN1) (Alam *et al*., 2018).

The structure of the homodimeric type IV ABC transporter MRP1 in complex with leukotriene explains how substrate binding stimulates the ATPase activity of the transporter (Johnson and Chen, 2017). Comparison between the *apo* and leukotriene bound structures reveals that substrate binding brings the NBDs 12 Å closer together in a manner that primes MRP1 for ATP binding and hydrolysis. Unlike P-gp, the translocation pathway of MRP1 is completely shielded from the membrane, indicating that substrates are directly recruited from the cytoplasm. In addition, the TM helices are well-ordered and lack the helical breaks observed in the P-gp structures (Johnson and Chen, 2017). These differences highlight how ABC exporters have evolved distinct mechanisms to enable substrate recognition.

1.1.9. PELDOR studies of ABC transporters

Although there are numerous structures of ABC transporters now available from X-ray crystallography, these structures only represent static snapshots locked in specific conformations (Locher, 2016; Thomas and Tampé, 2018). To complement structure determination, a range of additional techniques have been used to probe conformational changes in ABC exporters. PELDOR (pulsed electron-electron double resonance) is a commonly used method to infer site-specific distance changes in membrane proteins (Glaenzer *et al*., 2018). The technique is based on EPR (electron paramagnetic resonance) spectroscopy and involves introducing spin labels carrying unpaired electrons to the protein (Reginsson and Schiemann, 2011). Typically, these labels are nitroxides such as MTSSL that react with sulfhydryl groups on cysteine residues (Berliner *et al*., 1982). The spin-labelled proteins can then be irradiated with specific pulses of microwaves, enabling measurements of dipolar electron-electron coupling distances in the range of 1.5 - 8 nm (Reginsson and Schiemann, 2011). Inter-distance changes between the spin labels alter the frequency of oscillations that occur within the dipolar couplings (Jeschke and Polyhach, 2007).

The structures of MsbA have been extensively verified by EPR spectroscopy. Previous studies have predicted a large change in the aqueous accessibility of the intracellular cavity upon nucleotide binding, consistent with transitions between the inward-open and outward-open states (Dong *et al*., 2005). More recently, PELDOR measurements in liposomes have revealed a significant degree of conformational motion in the NBDs of MsbA and a comparatively rigid outward-open state (Borbat *et al*., 2007; Zou *et al*., 2009). Additional PELDOR studies have been performed for P-gp (Wen *et al*., 2013; Verhalen *et al*., 2012) and the type IV heterodimeric ABC transporters TmrAB (Nöll *et al*., 2017; Barth *et al*., 2018), TM287-288 (Timachi *et al*., 2017) and BmrCD (Misha *et al*., 2014).

1.1.10. Principle of single-molecule FRET

Single-molecule Förster resonance energy transfer (smFRET) analyses the conformational states of proteins by visualising individual molecules one at a time. Unlike ensemble methods such as PELDOR, smFRET can unravel the dynamics of single molecules, enabling the detection of heterogeneity in complex systems (Husada *et al*., 2015). In recent years, smFRET has been applied to study the conformational dynamics of different classes of membrane transporter (Dyla *et al*., 2017; Zhao *et al*., 2010; Zhao *et al*., 2011; Akyuz *et al*., 2013; Erkens *et al*., 2013). There are also a number of emerging smFRET studies that probe the architecture of ABC transporters which will be discussed in section 1.1.11.

FRET measures the efficiency of energy transfer between two spectrally distinct fluorophores in the range of 2-10 nm (Hohlbein *et al*., 2014). The fluorophores can be denoted as the donor (D) and the acceptor (A) dyes. Upon excitation of the donor fluorophore, a fraction of its energy can be transferred to the acceptor fluorophore with an efficiency that depends on the sixth power of the distance between the dyes (R). Proteins can be labelled at specific positions with a donor-acceptor dye pair. FRET efficiency (E*) represents the proximity between the two fluorophores and can be estimated from the ratio of acceptor to total emission intensity. The following equation can be used to calculate FRET efficiency in a typical protein system:

$$E^* = \frac{F(DA)}{F(DD) + F(DA)}$$

Figure 12. Equation to calculate FRET efficiency. The equation is applicable to proteins labelled with a donor-acceptor pair. E* represents the FRET efficiency and can be determined from the ratio of acceptor fluorescence (F(DA)), to fluorescence from both the donor (F(DD)) and acceptor (F(DA)) after donor excitation. (Lerner *et al*., 2018).

The Förster radius (R_0) represents the inter-dye distance that gives rise to E* values of 0.5. A protein molecule labelled correctly with a single donor and acceptor fluorophore, exhibits high FRET values when the inter-probe dye distance R is smaller than R_0 and low FRET values when R is greater than R_0 (Figure 13).

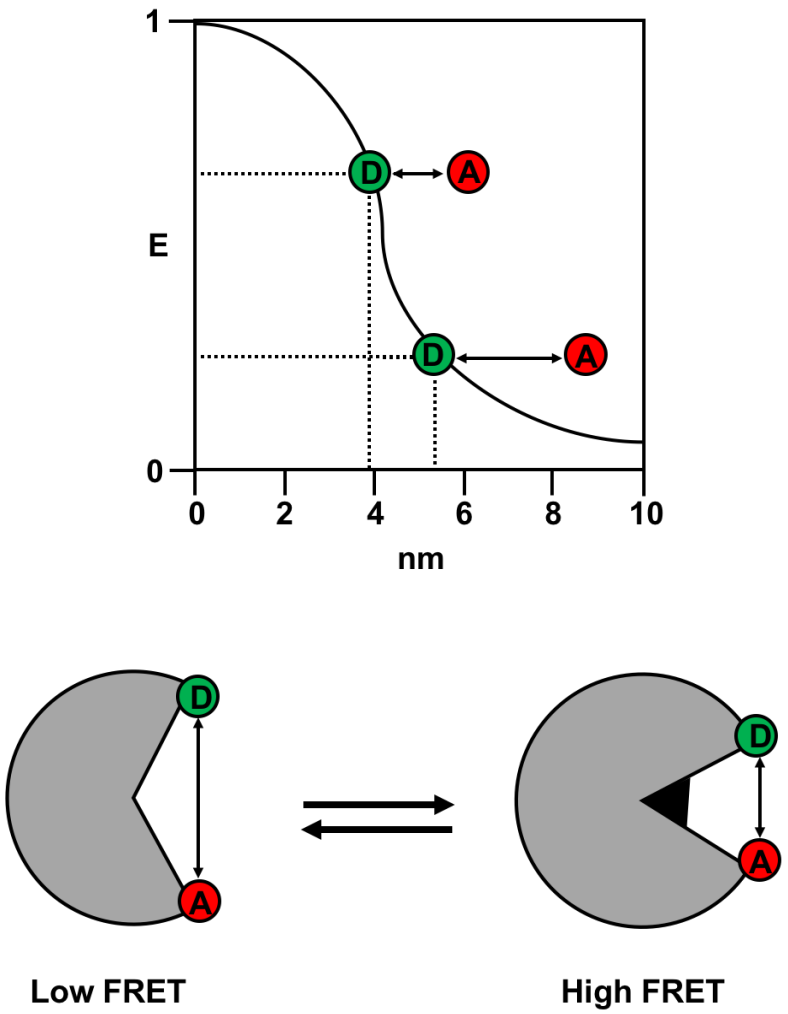


Figure 13. Principle of FRET. The top panel shows how FRET efficiency (E*) is related to the distance between the donor and acceptor fluorophores. The lower panel shows a typical example of a protein molecule labelled with a donor-acceptor dye pair undergoing a conformational change. The protein exhibits 'low FRET' values when the distance between the two fluorophores is further apart and a 'high FRET' value when the labelled positions move closer together. Adapted from Lerner *et al*. (2018).

Single-molecule FRET can be performed with labelled proteins that are either freely diffusing in solution or immobilised to a surface. ALEX (alternating laser excitation) is a technique that measures the FRET efficiency values (E*) and labelling stoichiometry (S) of freely diffusing molecules as they pass through the excitation volume of a confocal microscope (Kapanidis *et al*., 2004; Hohlbein *et al*., 2014). Individual molecules can be sorted based on their labelling stoichiometry, which enables filtering out of unwanted molecules labelled with either two donor or two acceptor fluorophores. Molecules labelled 'correctly' with one donor and one acceptor fluorophore can be further sorted into distinct populations depending on their E* values. The E* values can be plotted in the form of histograms showing the relative distributions and frequencies of each population (conformational state) (Kapanidis *et al*., 2004; Hohlbein *et al*., 2014). In surface-immobilised smFRET experiments, single labelled molecules are bound to the surface of a cover slide and visualised by a confocal scanning microscope. These measurements have the added benefit of being able to track dynamic changes in the E* values of individual molecules with time as they transition between different conformational states.

1.1.11. Single-molecule FRET studies of ABC transporters

The first smFRET studies of ABC transporters focused on the substrate-binding proteins (SBPs) of type I importers. The interaction between maltose and maltose-binding protein (MBP) which initiates the transport cycle of $MalFGK_2$, has been extensively probed by smFRET. MBP was shown to display intrinsic conformational dynamics, suggesting that maltose binding occurs *via* an induced-fit mechanism (Kim *et al*., 2013). The same authors later designed mutations in the hinge region of MBP and showed that the intrinsic opening rate of MBP dictates the binding affinity of maltose (Seo *et al*., 2014). The SBPs from the glutamine ABC importer GlnPQ have

also been investigated by smFRET (Gouridis *et al*., 2015). The authors demonstrated that the lifetime of the closed state controls both SBP docking to the translocator and substrate dissociation (Gouridis *et al*., 2015).

To date, the only ABC importer whose core architecture has been probed by smFRET is the type II importer BtuCD (Goudsmits *et al*., 2017; Yang *et al*., 2018). The smFRET experimental design by Yang *et al*. (2014) is described in Figure 14. Briefly, cysteine mutations were incorporated at the periplasmic end of the TMDs, the cytoplasmic end of the TMDs and the NBDs. The selected positions reflect regions that undergo conformational changes following ATP binding and docking of the SBP BtuF. Following site-specific fluorophore labelling, BtuCD was reconstituted into nanodiscs and then immobilised to a streptavidin-treated, PEG-coated surface *via* biotin-PE for smFRET measurements (Figure 66B) (Yang *et al*., 2018). The authors demonstrated that BtuCD forms a stable complex with the cognate SBP BtuF, even in the absence of ATP and vitamin B_{12}. The lifetime for vitamin B_{12} binding to the complex was measured in the tens of seconds timescale and associated with multiple cycles of ATP hydrolysis (Goudsmits *et al*., 2017). However, BtuCD-F did not display spontaneous conformational dynamics in the NBDs or TMDs, suggesting a mechanism of tight coupling to the binding of vitamin B_{12} (Yang *et al*., 2018).

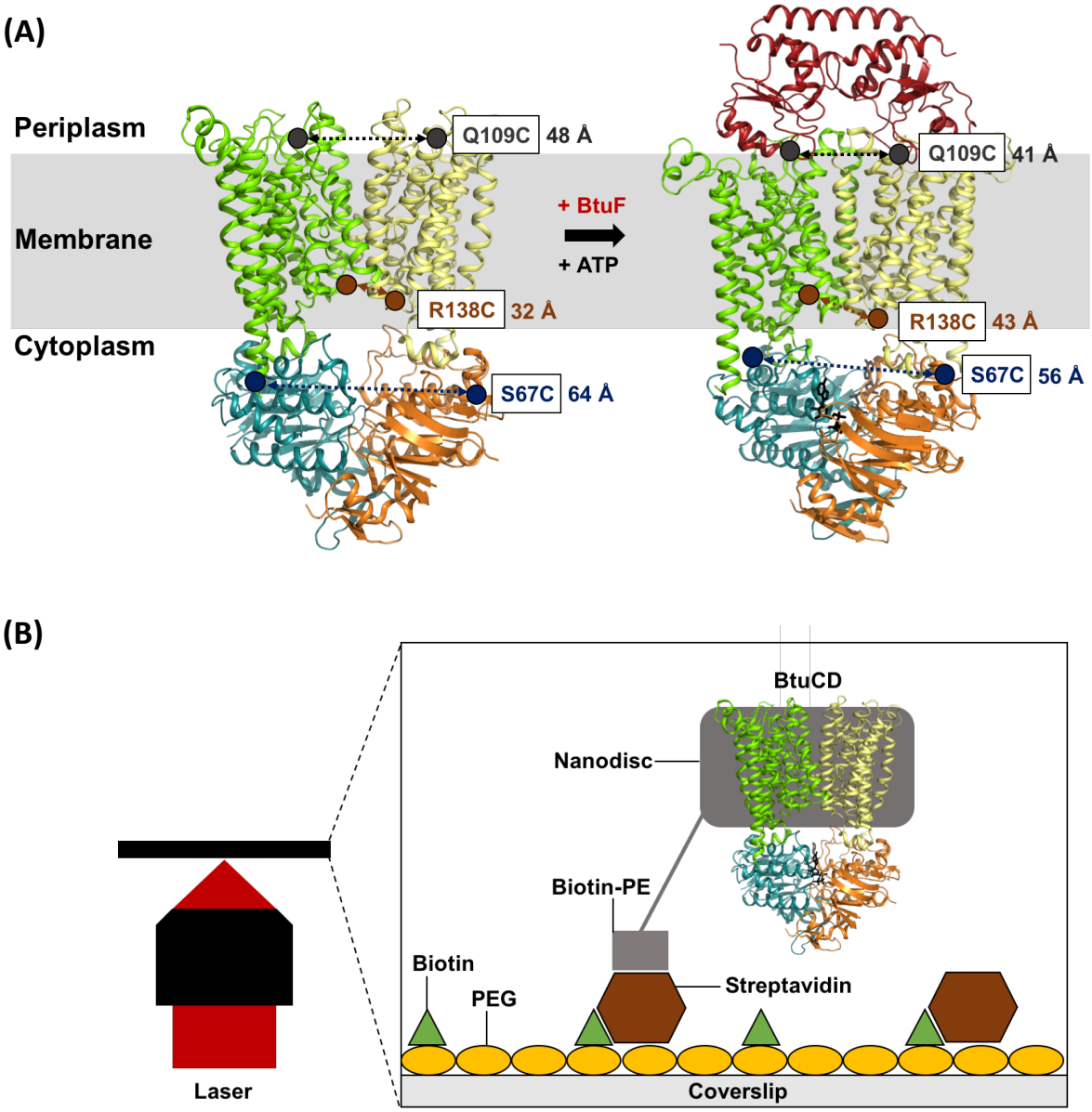


Figure 14. Experimental design for smFRET of BtuCD. (A) The structures of *apo* BtuCD (PDB: 1L7V) and AMP-PNP bound BtuCD-F (PDB: 4FI3) are shown. The BtuCD subunits are coloured green/yellow (BtuC) and teal/orange (BtuD). The substrate-binding protein BtuF is coloured red. AMP-PNP is shown in black stick format. Cysteine mutations designed at the periplasmic side of the TMDs (Q109C), cytoplasmic side of the TMDs (R138C) and NBDs (S67C), are depicted in grey, brown and blue respectively. Also shown are the distances between the two labelling positions in the homodimer which differ between the crystal structures and can be distinguished by changes in FRET efficiency. (B) Fluorophore labelled BtuCD was reconstituted into nanodiscs and immobilised to a streptavidin-treated, PEG-coated surface *via* biotin-PE. Adapted from Yang *et al*. (2018).

The first smFRET investigation of an ABC exporter reported conformational changes in the NBDs of liposome incorporated P-glycoprotein (Verhalen *et al*., 2012). P-glycoprotein was shown to adopt a broad range of NBD distance distributions in the presence of nucleotides, substrates and inhibitors. Single P-glycoprotein molecules displayed rapid fluctuations, indicative of rapid movements in the NBDs on the timescale of 10-100 ns. Analysis of the dwell times for each FRET state support the notion of drug-dependent changes in NBD dynamics (Verhalen *et al*., 2012).

Until recently, there were no smFRET studies of an ABC exporter that monitor conformational changes in both the NBDs and TMDs. However, the conformational states and dynamics of the ABC exporter MsbA have since been probed by smFRET in detergent micelles, liposomes and nanodiscs (Liu *et al*., 2018). MsbA was labelled with fluorophores in the NBDs and at the periplasmic end of the TMDs. In detergent and liposomes, large amplitude separations were observed in the nucleotide free state of the NBDs indicating a high level of mobility. By contrast, the addition of nucleotides resulted in high FRET values indicating formation of the closed NBD dimer. Interestingly, the FRET population distributions were more restricted for MsbA in nanodiscs than in either liposomes or detergent micelles. At the periplasmic side of the TMDs, there was a transition from a high FRET state to a lower FRET state in the presence of nucleotides. The periplasmic opening of the TMDs detected in detergent micelles was significantly wider compared to liposomes and nanodiscs. However, the absence of substrate-induced measurements from the MsbA smFRET study limits observations to conformational changes in the futile ATP hydrolysis cycle. As such, the authors are unable to address how the binding of substrate triggers ATP hydrolysis in a productive transport cycle (Liu *et al*., 2018).

1.1.12. Peptide ABC transporters

Peptide ABC exporters are important members of the ABC superfamily whose mechanisms are poorly understood. For these systems, processing of transport substrates is often a necessary first step in initiating the export cycle (Choudhury *et al*., 2014; Lin *et al*., 2015). Peptide ABC transporters contain a number of novel features that distinguishes them from other classes. Firstly, structural studies indicate they can adopt occluded conformations where the TMDs are sealed from both sides of the membrane (Choudhury *et al*., 2014; Lin *et al*., 2015; Morgan *et al*., 2017). Secondly, ATP binding to the NBDs of peptide ABC exporters is insufficient to drive opening of the TMDs. Thirdly, unlike ABC transporters that demonstrate substrate promiscuity, peptide ABC exporters may display a high level of specificity for their substrates (Romano *et al*., 2018). In light of these differences, deciphering the mechanisms of peptide ABC systems will provide new insights into how they evolved distinct biological functions.

In section 1.2, the antibacterial peptide ABC exporter McjD will be introduced. McjD exports MccJ25, a lasso peptide belonging to the family of microcins. The structure of McjD from *E. coli* was previously determined in complex with the non-hydrolysable ATP analogue AMP-PNP (Choudhury *et al*., 2014). While some initial work has been done to characterise the transporter, the conformational changes that govern MccJ25 recognition and coupling between the NBDs and TMDs have yet to be elucidated. As such, the existing model for MccJ25 efflux by McjD is based on studies of other ABC exporters and requires further investigation. In chapter 4, the peptide ABC exporters Pmt and AbcA from *Staphylococcus aureus* will be introduced. Pmt and AbcA release a class of α-helical peptides called phenol soluble modulins (PSMs) that lyse red blood cells and neutrophils (Peschel and Otto, 2013). These ABC exporters represent attractive targets against staphylococcal infections but are yet to be characterised at the biochemical or structural level.

1.2. McjD

1.2.1. Microcins

Microcins are gene-encoded antibacterial peptides with sizes below 10 kDa secreted by *Enterobacteriaceae* against phylogenetically related species (Baquero *et al*., 1978; Duquesne *et al*., 2007). They are often hydrophobic molecules characterized by their remarkable stability which enables resistance to heat, pH and proteases (Duquesne *et al*., 2007). Microcins are produced under conditions of stress or nutrient starvation, and can be strongly activated during the stationary phase of the growth cycle (Connell *et al*., 1987; Chiuchiolo *et al*., 2001; Fomenko *et al*., 2001). They belong to the wider class of toxins known as bacteriocins, which also includes colicins (Cotter *et al*., 2013). Colicins are high molecular weight toxins between 25-80 kDa in size and unlike microcins, they are induced in response to activation of the SOS system (Housden and Kleanthous, 2012). Induction of colicins is lethal to the producing cell, resulting in a suicide process where the producing cells actively participate in their own death while killing neighbouring sensitive cells. Microcins and colicins demonstrate highly potent antibacterial activity with nanomolar minimum inhibitory concentrations (MICs). However, unlike colicin-producing cells, microcins are secreted continuously without the loss of cell viability. This capability is conferred by the presence of dedicated transport systems that maintain self-immunity to the producer strain (Duquesne *et al*., 2007).

To date, at least 16 different microcins have been identified (Zhao *et al*., 2017). They are either plasmid or chromosomally encoded in gene clusters with an arrangement consisting of four key components; (i) a precursor molecule, (ii) enzymes for post-translational modifications, (iii) proteins that ensure self-immunity and (iv) export machinery. Microcins can be divided into two classes on the basis of their size, gene organisation and presence of post-translational modifications (Duquesne *et al*., 2007).

Class I microcin gene clusters are plasmid-encoded and the self-immunity gene is located furthest away from the structural gene (Figure 15). Two further genes are positioned adjacent to the structural gene and their products are responsible for catalysing the extensive peptide backbone modifications present in these microcins (Duquesne *et al*., 2007). Class IIa microcin gene clusters have an arrangement of four plasmid-encoded genes distributed in two operons. Class IIb microcin clusters by contrast are chromosomally encoded and contain more complex gene organisations distributed across multiple operons (Duquesne *et al*., 2007). The precise roles of some gene components of class IIb microcins however have yet to be elucidated.

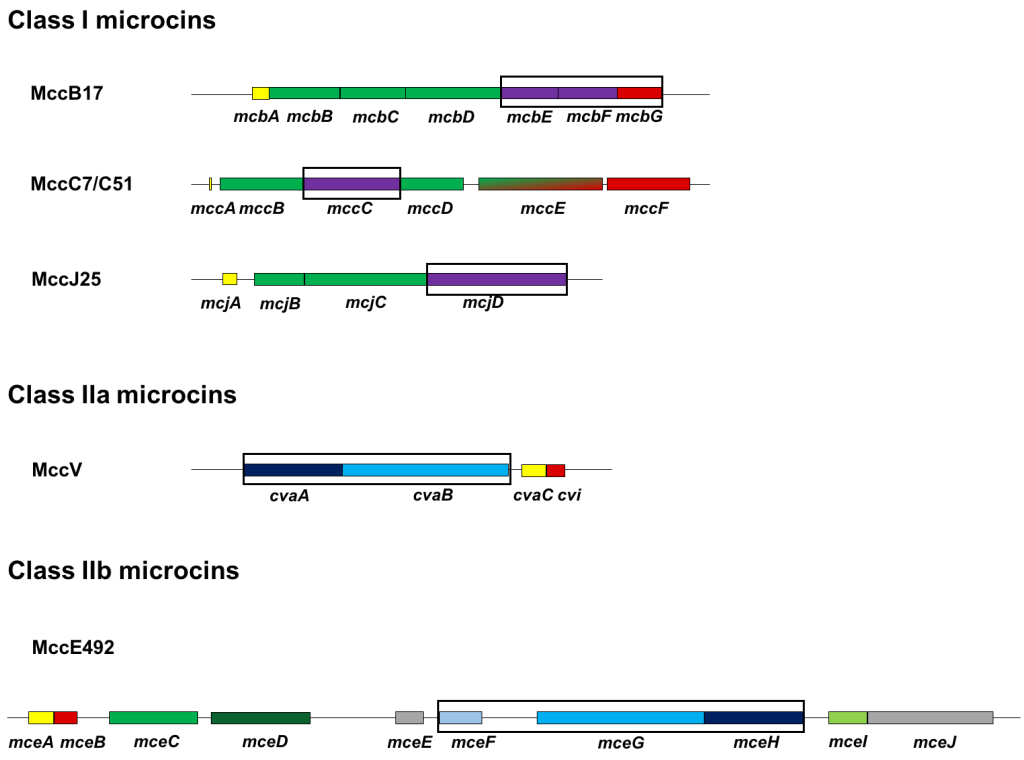


Figure 15. Genetic organisation of class I and class II microcins. Representative examples of different classes of microcins are shown. The genes are coloured according to their function within the clusters; structural precursor (yellow), post-translational modifications (green), export (blue), and self-immunity (red). Genes responsible for both export and self-immunity are coloured purple and genes with unknown function are coloured grey. Genes involved in export are highlighted in black boxes for clarity. Adapted from Duquesne *et al*. (2007)

Class I microcins are below 5 kDa in size and all contain post-translational modifications. Class II microcins have molecular masses between 5-10 kDa and can be further subdivided into class IIa (contain disulphide bonds but no post-translational modifications) and class IIb (may contain C-terminal modifications) (Figure 16) (Duquesne *et al*., 2007).

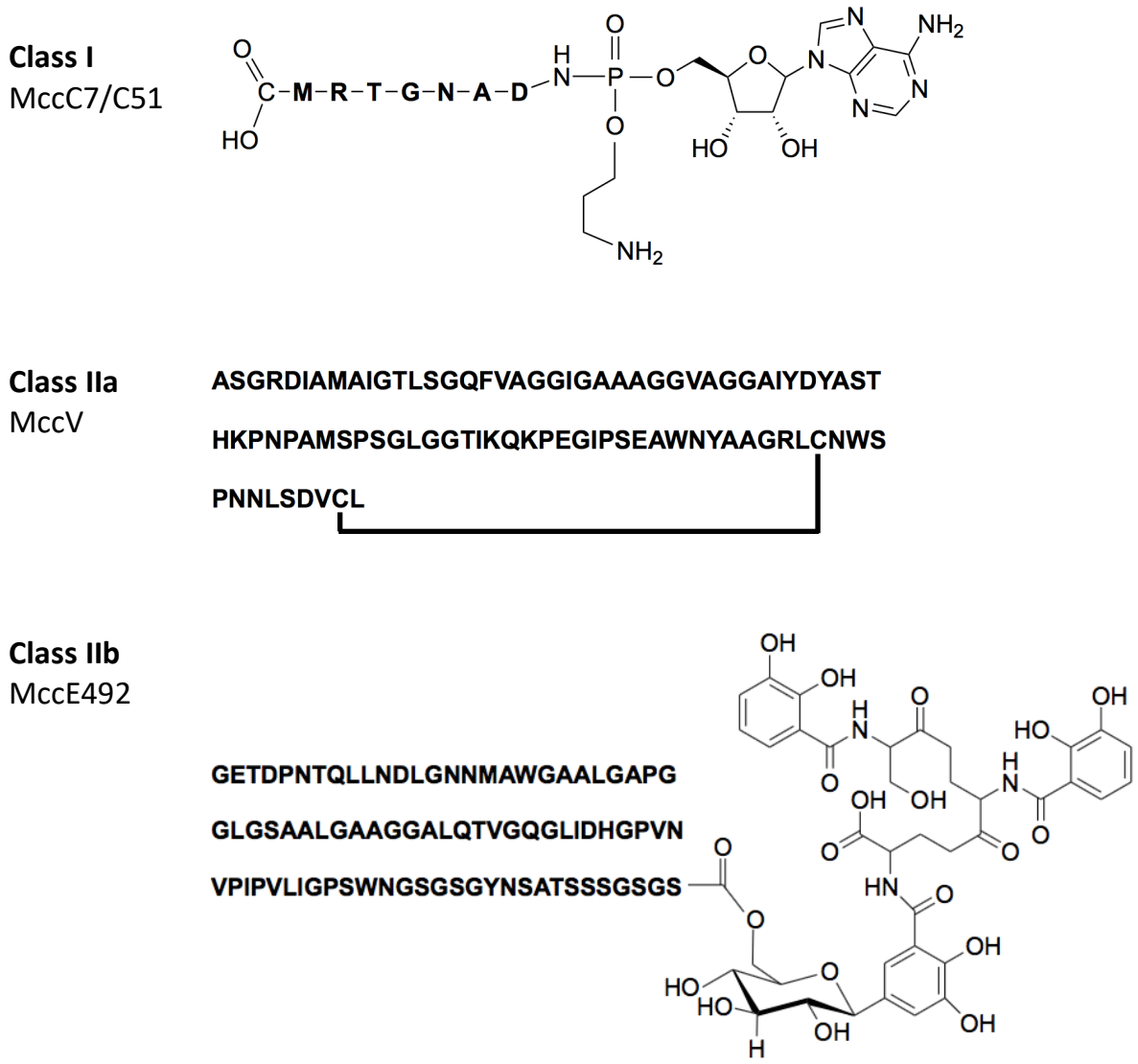


Figure 16. Comparison between different classes of microcin. Representative examples of each microcin class are shown. Class I microcins (*e.g.* MccC7/C51) have molecular masses below 5 kDa and contain extensive backbone post-translational modifications. Class II microcins have molecular masses between 5-10 kDa. Class IIa members (*e.g.* MccV) lack post-translational modifications but contain disulphide bonds as indicated by the black line. Class IIb members (*e.g.* MccE492) carry C-terminal post-translational modifications involving the addition of catechol-type siderophores.

Class I microcins comprise three structurally unrelated members in *Escherichia coli* that have each been biochemically and structurally characterised (MccB17, MccC7/51 and MccJ25) (Duquesne *et al*., 2007). MccB17 is a 43 amino acid heterocyclic peptide containing four oxazole and four thiazole rings (Li *et al*., 1996). MccC7/C51 is the shortest known microcin, consisting of a heptapeptide sequence with a C-terminal modified adenosine monophosphate moiety (Guijarro *et al*., 1995). MccC7/C51 is unique amongst microcins in that the precursor sequence does not undergo cleavage prior to secretion (Garcia-Bustos *et al*., 1985). MccJ25 is a 21 amino acid peptide characterised by an unusual lasso type fold structure (Solbiati *et al*., 1996). Class II microcins are characterised by their requirement for the outer membrane protein TolC to mediate secretion (Braun *et al*., 2002). MccV (formerly known as ColV) represents the best studied class IIa microcin, consisting of a linear 88 amino acid peptide containing a disulphide linkage. Class IIb microcins contain serine-rich C-terminal regions and can be post-translationally modified by the addition of catechol-type siderophores (Lagos *et al*., 2009). The class IIb microcin MccE492 from *Klebsiella pneumoniae* contains a C-terminal serine which is covalently linked to a glucosylated trimer of 2,3-dihydrobenzolserine.

Once microcins have been exported from the producer cell, they utilise specific transporters for uptake into the target cell. Following internalisation, microcins deploy a variety of mechanisms to inhibit bacterial growth in either the cytoplasm or inner membrane (Table 3) (Duquesne *et al*., 2007). Within the cytoplasm, type I microcins target intracellular enzymes involved in DNA and protein synthesis. MccB17 inhibits DNA replication by altering the activity of DNA gyrase (Vizán *et al*., 1991). Specifically, MccB17 slows down the steps of supercoiling and relaxation by trapping a DNA gyrase-cleavage intermediate (Pierrat and Maxwell, 2003). MccC7/C51 inhibits translation by arresting the synthesis of aminoacylated $tRNA^{Asp}$ by aspartyl tRNA synthetase (Metlitskaya *et al*., 2006). The mechanism for MccJ25 mediated RNA polymerase (RNAP) inhibition (Adelman *et al*., 2004; Mukhopadhyay *et al*.,

2004) will be discussed extensively in section 1.2.4. Among microcins that target the inner membrane, MccV has been shown to disrupt the membrane potential (Yang and Konisky, 1984) and MccE492 interferes with membrane depolarisation by inhibiting the ManYZ components of the mannose permease complex (Bieler *et al*., 2006). Furthermore, the type IIb microcin MccH47 appears to exert antibacterial activity against the F_o membrane subunit of ATP synthase (Trujillo *et al*., 2001; Rodríguez and Laviña, 2003).

Microcin	Class	Mass (Da)	Features	Target
MccB17	I	3093	Heterocycles but no other modifications	DNA gyrase
MccC7/C51	I	1177	Covalently attached to a C-terminal aspartic acid	Aspartyl-tRNA synthetase
MccJ25	I	2107	Lasso type structure	RNA polymerase
MccV	IIa	8733	Unmodified, linear, single peptide	Unknown inner membrane protein
MccE492	IIb	8717	Serine-rich C-terminal region with a siderophore	Mannose permease
MccH47	IIb	4865	Serine-rich C-terminal region with a siderophore	ATP synthase

Table 3. Structural features and intracellular targets of microcins.

1.2.2. Biosynthesis and export of MccJ25

The class I microcin MccJ25 is a ribosomally synthesised and plasmid encoded antibacterial peptide (Salomon and Farias, 1992). The biosynthesis and export of MccJ25 are coordinated by the products of four genes (*mcjA-D)* organised within two operons (Figure 17) (Solbiati *et al*., 1996). The arrangement ensures that production and export of MccJ25 are very efficient and prevents toxic level build up in the cell. In accordance with other microcin family members, the four gene elements within the cluster consist of a precursor gene (*mcjA*), post-translational modification genes (*mcjB, mcjC*) and a gene responsible for immunity and export (*mcjD*).

The *mcjA* gene encodes a linear 58 amino acid precursor sequence (Solbiati *et al*., 1996). The *mcjB* gene product encodes a cysteine protease which removes the 37 amino acid N-terminal leader sequence from McjA (Yan *et al*., 2012). Only the eight leader amino acids preceding the start of the 21 amino acid MccJ25 sequence are necessary for the proteolytic activity of McjB (Cheung *et al*., 2010). The *mcjC* gene encodes a lactam synthetase (Yan *et al*., 2012) which catalyses a cyclisation reaction between the α-amino group of Gly^{1} and the γ-carboxyl group of Glu^{8}, resulting in formation of an N-terminal macrolactam ring. The 13 amino acid C-terminal tail is oriented perpendicular to the ring, with the aromatic side chains Phe^{19} and Tyr^{20} positioned either side of the ring, causing the tail to become sterically trapped inside (Figure 17). The resulting 3D lasso type structure of MccJ25 has been determined by NMR spectroscopy (Bayro *et al*., 2003; Rosengren *et al*., 2003; Wilson *et al*., 2003). The rigid, compact nature of the lariat-protoknot structure enables it to withstand conditions of extreme temperature and mediates resistance to denaturation by chaotropes and organic solvents (Rosengren *et al*., 2004). Pre-folding of the MccJ25 structure is necessary for correct formation of the lasso fold, since the bulky aromatic side chains in the tail cannot pass through the ring once it is formed (Ferguson *et al*., 2010).

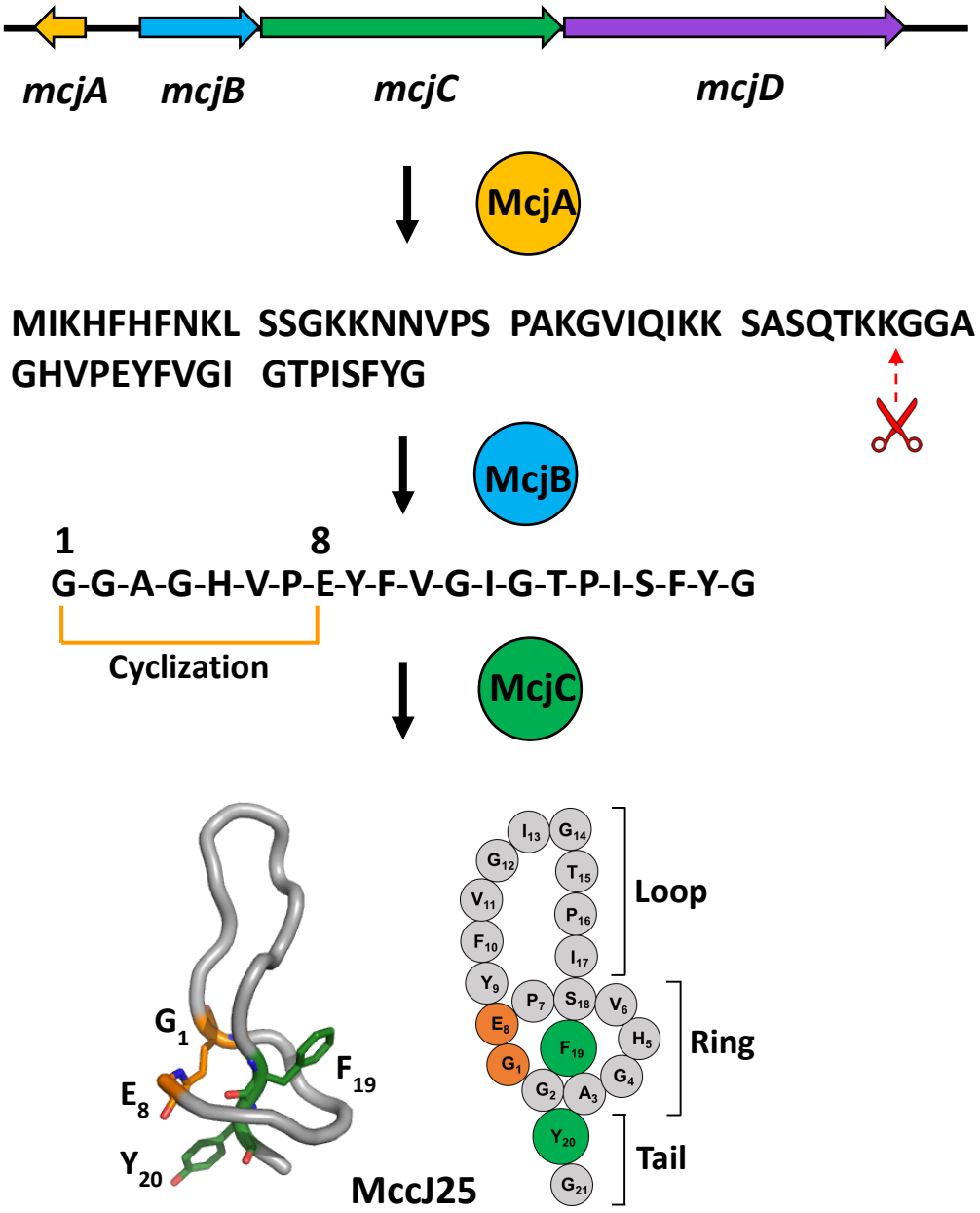


Figure 17. Biosynthesis of MccJ25. The four genes required for MccJ25 production and export are arranged in the same operon. McjA encodes a linear 58 amino acid precursor molecule. McjA undergoes cleavage by McjB, resulting in removal of the upstream 37 residue N-terminal leader sequence, followed by cyclisation by McjC and formation of the mature MccJ25 peptide. The 3D lasso type structure of MccJ25 is shown (Bayro *et al.*, 2003). Cyclisation results from a linkage between the N-terminal Gly 1 amino group and the Glu 8 side chain carboxylate, giving rise to a small ring. The C-terminal tail of MccJ25 becomes sterically entrapped within the ring, locked in place by two bulky hydrophobic residues (green).

The *mcjD* gene encodes an ATP-binding cassette transporter responsible for the export of endogenous MccJ25 from the cytoplasm to the periplasm (Solbiati *et al*., 1999) and also for the export of exogenous MccJ25 which may enter the producing bacteria (Solbiati *et al*., 1996). The ABC transporter YojI can also confer resistance to MccJ25 in a TolC-dependent manner (Delgado *et al*., 2005). Mutagenesis of each residue in the 21 amino acid sequence of MccJ25 revealed that three residues in the ring (Gly^{1}, Gly^{2}, Glu^{8}) and one residue in the tail (Tyr^{20}) are essential for the production and stability of the peptide (Pavlova *et al*., 2008). MccJ25 is remarkably resistant to proteases but digestion with thermolysin results in cleavage of the Phe^{10}-Val^{11} amide bond (Rosengren *et al*., 2004) and acid hydrolysis results in deletion of the loop spanning residues 13-17 (Blond *et al*., 2002). Both modifications give rise to two polypeptide chains but importantly, the lasso type structure is maintained through Phe^{19}-Tyr^{20} anchoring of the tail to the ring.

Lasso peptides can be divided into three different classes. Classes I and III comprise peptides stabilised by two and one disulphide bonds respectively, whereas class II members such as MccJ25 lack any disulphide bonds (Hegemann *et al*., 2015). MccJ25 displays a similar 3D structure to the type I lasso peptide RP71955 (aborycin) from *Streptomyces* with the addition of two disulphide bonds that confer additional stability to the lasso fold (Fréchet *et al*., 1994). Genome mining has identified a gene cluster in *Burkholderia thailandensis* E264 that contains four genes homologous to *mcjA-D.* The *capABCD* gene cluster is responsible for production, modification and export of the 19 residue type II antibacterial lasso peptide capistruin (Knappe *et al*., 2008). The overall structure of capistruin shows similarities to MccJ25 with an N-terminal ring of 9 amino acids and a C-terminal tail threaded through the ring (Knappe *et al*., 2008). However, unlike MccJ25, capistruin contains a shorter loop region and a longer C-terminal tail. Interestingly, MccJ25 and capistruin both share the same intracellular target (RNA polymerase) (Kuznedelov *et al*., 2011).

1.2.3. Mechanism of MccJ25 import

The uptake of MccJ25 into target cells is mediated by three components: (i) the outer membrane protein FhuA, (ii) the TonB/ExbB/ExbD complex and (iii) the inner membrane protein SbmA (Duquesne *et al*., 2007). The physiological role of FhuA is uptake of the siderophore ferrichrome to ensure iron availability for bacteria (Coulton *et al*., 1983). FhuA is a monomeric β-barrel protein containing 22 antiparallel β-strands and a plug domain folded inside the barrel (Locher *et al*., 1998). In addition to its role in iron uptake, FhuA can be hijacked by MccJ25 as a mechanism for entering the periplasmic space (Salomon and Farias, 1993). The high resolution structure of FhuA has been determined in complex with MccJ25 (Figure 18) (Mathavan *et al*., 2014). Binding of MccJ25 occurs at the outer surface of the β-barrel with the macrolactam ring (residues 1-8) positioned vertically inside the cavity. Three amino acids (Ala^3, His^5, Val^6) contact the plug domain through a network of hydrogen bonds. The peptide loop region (residues 9-18) of MccJ25 becomes distorted upon binding, resulting in a wider, less structured conformation (Mathavan *et al*., 2014). The uptake mechanism of MccJ5 into target cells is described in Figure 31. Transport of MccJ25 by FhuA is energised by the TonB/ExB/ExbD complex which supplies a proton motive force from the inner membrane (Figure 19) (Dupuy *et al*., 2009). The assembled complex comprises a pentamer of ExbB, a dimer of ExbD and a minimum of one TonB molecule (Celia *et al*., 2016). A switch helix located at the N-terminus of the FhuA plug domain contains a five amino acid conserved sequence (TonB box) that transduces the signal to TonB (Killmann *et al*., 2002).

Following uptake into the periplasm, MccJ25 can enter the cytoplasm using the inner membrane protein Sbma (Figure 19) (Salomon and Farias, 1995). The structure of SbmA is currently unknown but the protein contains 8 TM helices and can form homodimers (Corbalan *et al*., 2013). On the basis of sequence analysis, SbmA was previously thought to resemble the

membrane-spanning region (TMDs) of ABC transporters (LeVier and Walker, 2001). However, a bacterial two-hybrid screen was unable to identify potential NBD interacting partners (Runti *et al*., 2013) and the authors of the same study demonstrated that SbmA-dependent transport requires an electrochemical proton gradient. The interaction between SbmA and MccJ25 is dependent on His^5 which is positioned in the lariat ring of the peptide (de Cristobal *et al*., 2006). SbmA is also responsible for uptake of the structurally unrelated microcin MccB17 (Laviña *et al*., 1986), the antibiotic bleomycin (Yorgey *et al*., 1994), the proline-rich eukaryotic peptides Bac7 (Mattiuzo *et al*., 2007) and PR39 (Pranting *et al*., 2008), and peptide nucleic acids (PNAs) (Ghosal *et al*., 2013).



Figure 18. Structure of FhuA in complex with MccJ25. The FhuA β-barrel is shown in orange cartoon format and MccJ25 is shown as green sticks. The plug domain labelled black spans the interior of the barrel and forms contacts with MccJ25. The peptide is bound at the apex of the barrel with the loop region of MccJ25 undergoing conformational changes (PDB: 4CU4) (Mathavan *et al*., 2014).

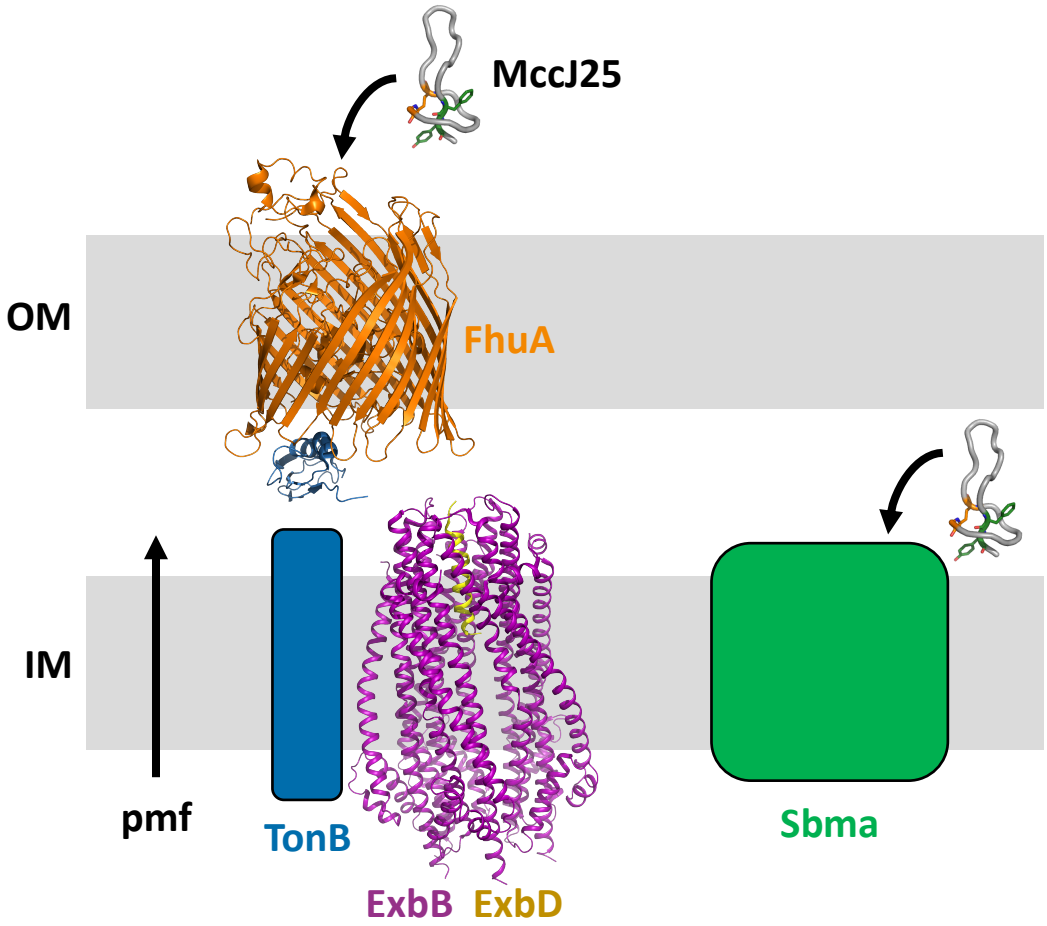


Figure 19. Uptake of MccJ25 into cells. MccJ25 is recognised by the β-barrel outer membrane receptor FhuA at the outer membrane. The structure of FhuA in complex with the C-terminal domain of TonB is shown (PDB: 2GRX) (Pawelek *et al*., 2006). Translocation by FhuA requires an electrochemical ΔΨ gradient transduced by the TonB/ExbB/ExbD complex in the inner membrane. The structure of the ExbB/ExbD complex (PDB: 5SV0) comprises a pentameric core of ExbB and a dimer of ExbD linked in a minimum of one TonB subunit (Celia *et al*., 2016). Following MccJ25 entry in the periplasm, the dimeric inner membrane protein Sbma transports the peptide into the cytoplasm.

1.2.4. Mechanism of MccJ25 inhibition

Upon internalisation, MccJ25 disrupts the activity of RNA polymerase. MccJ25 inhibits transcription by constricting the RNA polymerase (RNAP) secondary channel, thus preventing incoming nucleotide triphosphates (NTPs) from trafficking through the enzyme (Adelman *et al*., 2004; Mukhopadhyay *et al*., 2004). The secondary channel forms the only solvent accessible pathway in RNAP and provides an entrance cleft to the active site. MccJ25 binds to RNAP with a K_D of 0.5 μM (Adelman *et al*., 2004) and seals the channel in a manner analogous to a cork-in-a-bottle (Mukhopadhyay *et al*., 2004). The interaction between MccJ25 and RNAP causes long pauses in the rate of transcription elongation as a consequence of reduced accessibility to NTPs (Adelman *et al*., 2004). Interestingly, RNAP resistance mutations to MccJ25 are clustered within the secondary channel (Yuzenkova *et al*., 2002). The recently determined cryo-EM structure of RNAP in complex with MccJ25 validates the mechanism for inhibition (Braffman *et al*., 2019). MccJ25 binds deep within the RNAP channel, burying a total surface area of 960 $Å^2$ (Figure 20). Within MccJ25, Tyr^9 makes the most extensive interactions with RNAP, in agreement with previous biochemical data suggesting that Tyr^9 is indispensable for antibacterial activity (Pavlova *et al*., 2008)

A second independent mode of action for MccJ25 has been proposed where the peptide inhibits components in the bacterial respiratory chain leading to an increase in reactive oxygen species (ROS) production (Bellomio *et al*., 2007). Recent work has identified cytochromes bd-I and bo_3 as the sites targeted by MccJ25 during inhibition (Galván *et al*., 2018). However, further experiments will be required to define the precise roles of these cytochromes in mediating MccJ25 resistance.

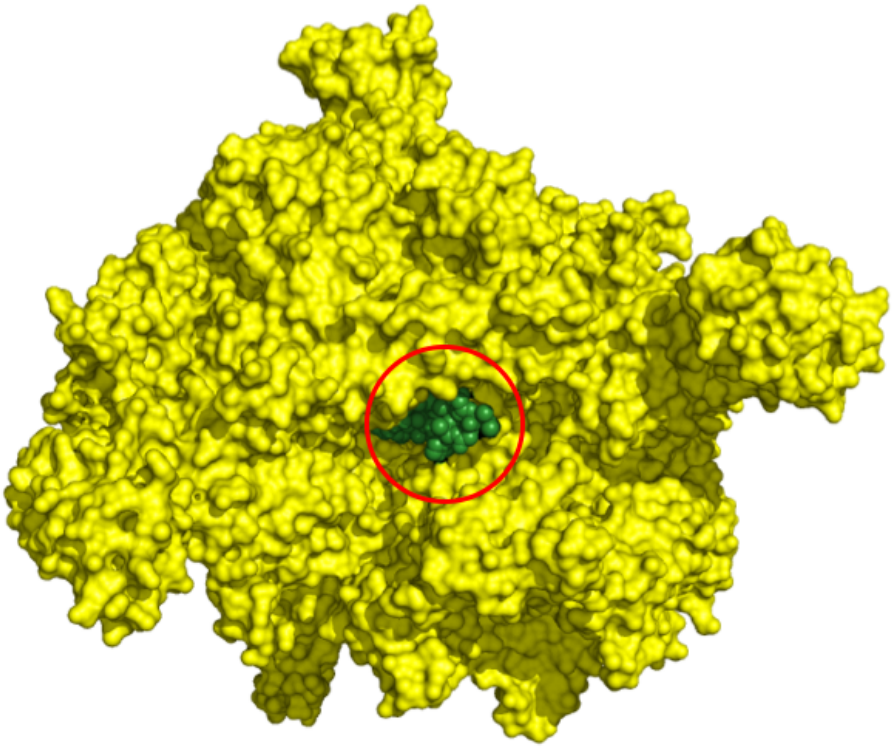


Figure 20. MccJ25 inhibits RNA polymerase. The structure of RNA polymerase in complex with MccJ25 is shown (PDB:6N60) (Braffman *et al*., 2019). RNAP is shown in yellow surface representation and MccJ25 is depicted by the green spheres. The red circle indicates the location of the RNAP secondary channel. Upon internalisation into the target cell, MccJ25 inhibits the activity of RNAP by blocking the secondary channel and preventing incoming nucleotide triphosphates from trafficking through the enzyme.

1.2.5. Therapeutic potential of MccJ25

The potency of MccJ25 coupled with its high stability and narrow spectrum of activity against certain bacterial strains (Delgado *et al*., 2001) makes this microcin a potentially viable alternative to conventional antibiotics. Following treatment with MccJ25, a mouse model infected with *Salmonella enterica* contained reduced pathogen numbers in the liver and spleen when compared to levels in control mice (Lopez *et al*., 2007). The effectiveness of MccJ25 as a therapeutic agent may be enhanced in combination with other antibacterial compounds. A study has demonstrated that the membrane permeabilising peptide $(KFF)_3K$ is able to induce sensitisation of MccJ25-resistant strains to MccJ25 (Pomares *et al*., 2010).

MccJ25 can also act as a molecular scaffold for the introduction of peptide epitopes. A modified variant of MccJ25 containing a substituted integrin binding motif has been shown to modulate capillary formation in endothelial cells (Knappe *et al*., 2011). MccJ25 variants have been further engineered containing 5-fold higher potency against *E. coli* and *Salmonella* species (Pan and Link, 2011). The authors demonstrated that MccJ25 is remarkably tolerant to diverse and widespread mutations in the tail region of the peptide, providing scope for enhancement of function.

Another study has demonstrated that a variant of MccJ25 containing a Gly^{12} to Tyr substitution has the potential to be used as a next generation food preservative in dairy products (Pomares *et al*., 2009). The mutant retains the antibacterial activity of wild-type MccJ25 but importantly can be cleaved and inactivated by proteases in the gastric tract, thus preventing interference with commensal microbiota. These findings are particularly intriguing since the commonly used bacteriocin food preservative, nisin, is only effective against Gram-positive bacteria (Bauer and Dicks, 2005).

1.2.6. McjD is a microcin immunity protein

Microcin immunity proteins form an essential component of the machinery required to confer cellular resistance against the toxic effects of microcins (Duquesne *et al*., 2007). Microcin immunity proteins can be either cytoplasmic enzymes involved in detoxification or membrane transport proteins that expel microcins from the producer cell. The export systems typically belong to the ABC transporter superfamily, with the exception of the MccC7/C51 export protein MccC which is a member of the major-facilitator superfamily (MFS) (Duquesne *et al*., 2007). McjD is a homodimeric ABC transporter responsible for the export of endogenously and exogenously produced MccJ25 (Solbiati *et al*., 1996; Solbiati *et al*., 1999). Export of MccJ25 by McjD prevents toxic levels of MccJ25 from building up inside the producer cell and therefore provides it with self-immunity to the peptide. However, despite being a critical step biological process, the mechanism of MccJ25 efflux by McjD has not been resolved at the molecular level.

1.2.7. Structure of McjD-AMP-PNP

McjD is a type IV ABC transporter with an N-terminal TMD containing six TM helices and a C-terminal NBD (Solbiati *et al*., 1999). The structure of McjD from *Escherichia coli* was previously determined in complex with the non-hydrolysable ATP analogue AMP-PNP which mimics the ATP-bound state (Figure 21) (Choudhury *et al*., 2014). The TMDs are occluded from both sides of the membrane while the NBDs adopt a dimerised state where the bound nucleotide is sandwiched between the P-loop and ABC signature motifs. The outward-occluded state is proposed to be an intermediate state between the inward-open and outward-open states of ABC exporters. The McjD TMD dimer interface is formed between TM2 and TM5-6 from

one subunit along with the equivalent TM helices from the opposite subunit. This gives rise to a well-defined cavity with a volume of ~5900 Å^3 that is sufficiently large to accommodate a molecule of MccJ25. Although a structure of McjD in complex with MccJ25 is not available, site-directed mutagenesis has revealed residues in the cavity important for peptide recognition. Within the TMDs, there is a network of salt bridges important for stabilising the interaction between TM2 and TM6' of the opposite monomer. Choudhury *et al*. (2014) propose that protonation of carboxylate groups in these residues may disrupt salt bridge formation, but there is currently no direct evidence for how ATP binding and hydrolysis are linked to opening of the McjD TMDs.

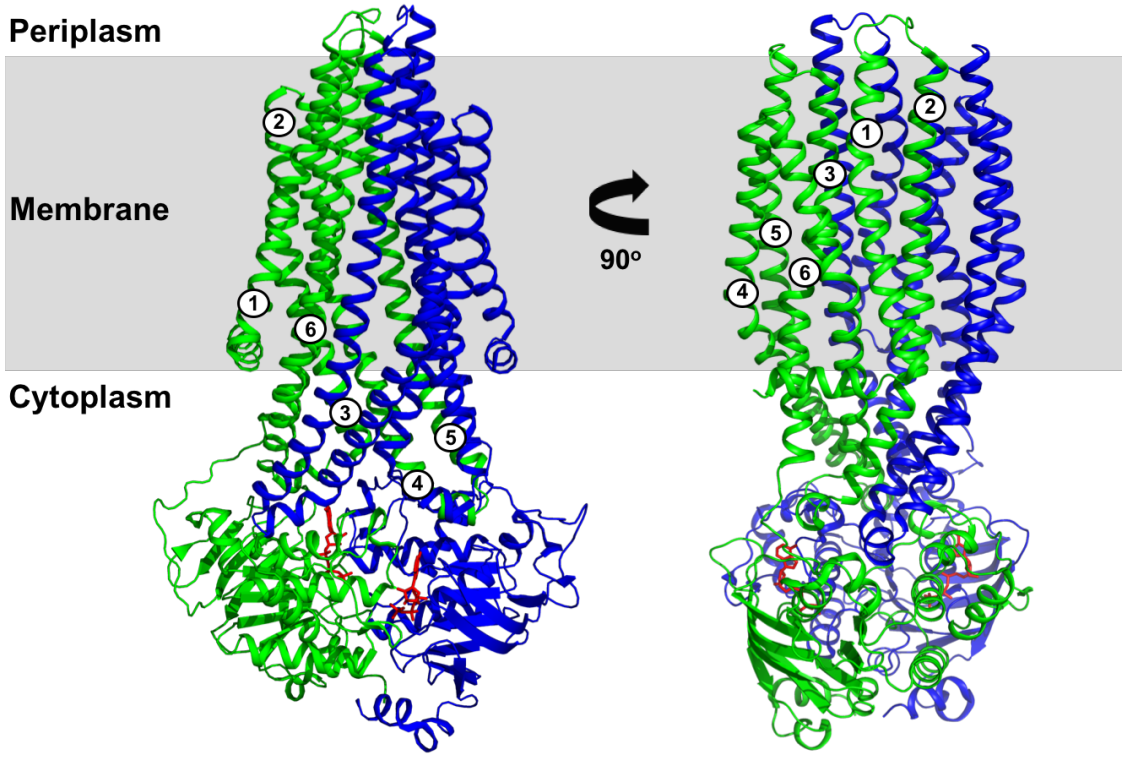


Figure 21. Structure of McjD-AMP-PNP. The McjD monomers are coloured green and blue respectively. The McjD-AMP-PNP structure is outward-occluded with TMDs inaccessible from both sides of the membrane (PDB: 4PL0) (Choudhury *et al*., 2014). The transporter lacks inter-subunit twining at the TMDs. The TMD dimer interface is formed between TM2 and TM5-6 from one subunit along with the equivalent TM helices from the opposite subunit.

1.2.8. Comparison of McjD structure with other ABC exporters

Unlike the nucleotide bound structures of MsbA and Sav1866, that both contain TMDs open to the periplasm, the structure of McjD-AMP-PNP is occluded at the TMDs (Choudhury *et al*., 2014). This can be explained by the absence of inter-subunit twining in the McjD TMDs, a feature that is present in the outward-open states of ABC exporters. In McjD, the occluded state is formed by rotation of TMs 1 and 2 towards the equivalent TMs of the opposite subunit, whereas in Sav1866 and MsbA, the equivalent TM helices intertwine with TMs 3-6 of the opposite monomer (Figure 22) (Dawson and Locher, 2006; Ward *et al*., 2007). In McjD, TMs 1 and 2 have rotated by 26° and shifted by 6 Å at extracellular loop 1 relative to Sav1866, leading to a loss of intertwining (Choudhury *et al*., 2014).

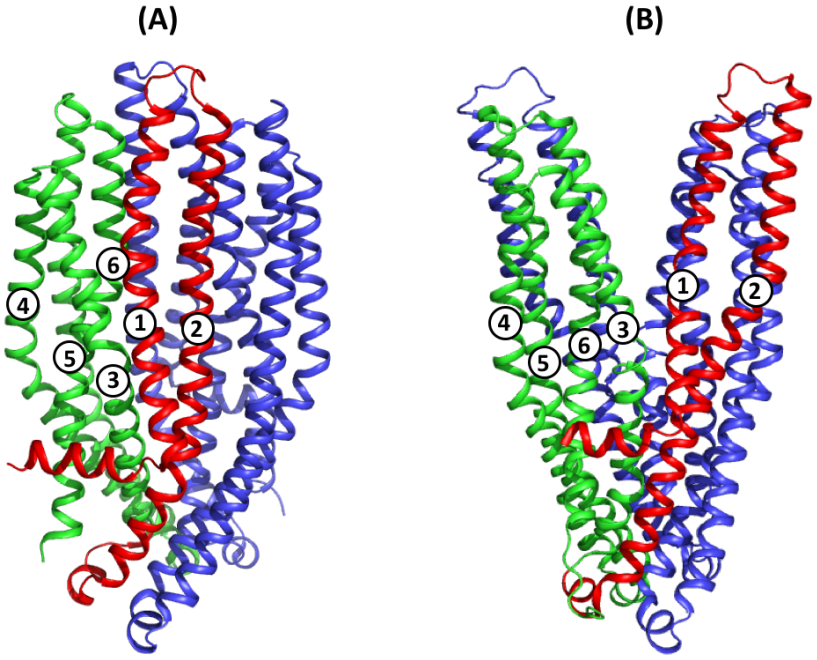


Figure 22. Comparison between TMDs in McjD and Sav1866. The TMD monomers are coloured green and blue for both McjD and Sav1866. TM1 and TM2 are highlighted red in one monomer for clarity. (A) In the McjD-AMP-PNP structure, the TMDs lack inter-domain twining. TM1 and TM2 rotate away from the opposite half of the transporter resulting in an outward-occluded cavity to the periplasm. (B) In the outward-open Sav1866 structure, TM1 and TM2 intertwine with TM3-6 in the opposite half of the transporter.

By contrast, structures of the type IV nucleotide bound peptide ABC transporters PCAT (Lin *et al*., 2005) and PrtD (Morgan *et al*., 2017) both contain occluded cavities similar to McjD. PCAT and PrtD do not have domain intertwining but display minor differences in their TM organisation. While TM3 and TM6 in the McjD structure shift outwards to create a spacious cavity (Choudhury *et al*., 2014), the equivalent TMs in the PrtD structure contain sharp kinks causing them to orient inwards (Morgan *et al*., 2017). In PCAT, TM3 and TM6 follow the same path as PrtD but the kinks are less pronounced (Lin *et al*., 2015). Interestingly, a recent structure of the type IV heterodimeric ABC exporter ABCG5/G8 also displays similarities to McjD. ABCG5/G8 contains an occluded TMD interface lacking TM swapping, but unlike McjD, the structure was determined in a nucleotide free state (Lee *et al*., 2016).

1.2.9. McjD is modulated by specific lipids

Mass spectrometry has demonstrated how the activity of McjD can be modulated by specific classes of membrane lipid (Mehmood *et al*., 2016). McjD in complex with MccJ25 was shown to survive the gas phase, while partial delipidation led to a reduction in both the measured ATPase activity and thermostability of the transporter. The authors further revealed how negatively charged lipids are required for the function of McjD and zwitterionic lipids provide structural stability. A phosphatidyl glycerol lipid molecule could be resolved in the structure of McjD-AMP-PNP (Mehmood *et al*., 2016). These data support the notion that McjD should be studied in its native lipid environment. The importance of preferential lipid association has also been demonstrated for flippase activity in the type IV ABC transporter TmrAB (Bechara *et al*., 2015). In addition, a clear inter-dependence of lipid and ligand binding has been reported for P-glycoprotein (Marcoux *et al*., 2013).

1.2.10. Current model for MccJ25 export

McjD has been shown to demonstrate a high level of specificity for MccJ25 since structurally distinct drugs and peptides are unable to stimulate the ATPase activity of the transporter (Romano *et al*., 2018). The current model for MccJ25 export by McjD is based on a modified version of the alternating access mechanism (Figure 23). In the absence of substrate, ATP binding to the McjD NBDs triggers a futile ATP hydrolysis cycle. The requirement for a functionally relevant inward-open conformation (state 1) cannot be confirmed in the absence of a resolved structure and/or biophysical evidence. As such, it remains to be determined whether McjD accepts MccJ25 from the cytoplasm, or receives MccJ25 *via* a lateral entrance in the cell membrane using the outward-only mechanism proposed for PglK (Perez *et al*., 2015). Following substrate binding to the TMDs, two molecules of ATP bind to the NBDs resulting in a closed NBD dimer (state 2). This step is presumably followed by inter-subunit twining in the TM helices, causing the TMDs to diverge and form the outward-open state (state 3). A molecular dynamics study has indicated that McjD only requires a small opening at the periplasmic side of the TMDs for MccJ25 release (Gu *et al*., 2014). However, there is currently no direct evidence for formation of the outward-open state and the roles of ATP binding and hydrolysis in inducing TMD opening have yet to be elucidated. Following export of MccJ25, McjD returns to the outward occluded state (current McjD structure). ATP hydrolysis then disrupts the NBD dimer interface, presumably leading to restoration of the inward-facing conformation. The degree of opening in the McjD NBDs upon nucleotide dissociation is currently unknown and requires further investigation.

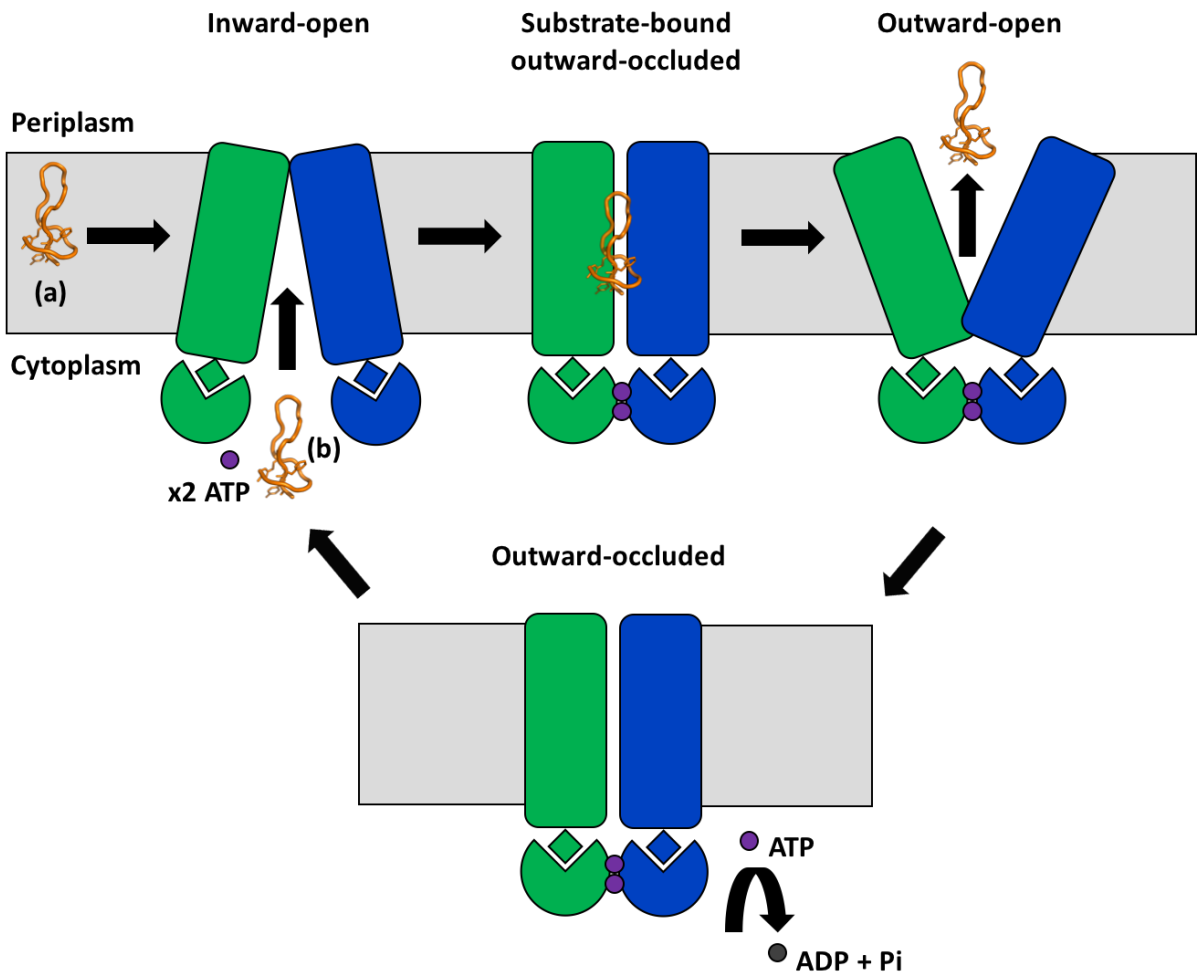


Figure 23. Proposed alternating access model for MccJ25 export. The McjD monomers are labelled green and blue. MccJ25 is shown in cartoon format and coloured orange. ATP and ADP are shown as purple and grey circles respectively. It is currently unknown whether MccJ25 enters the TMDs (a) laterally from the membrane or (b) directly from the cytoplasm. ATP binding induces dimerisation at the NBDs, switching the transporter to a substrate-bound occluded conformation. Inter-subunit twining in the TMDs generates a cavity open to the periplasm for substrate release before McjD returns to the occluded state (current McjD structure). ATP hydrolysis then resets the transporter back to the inward-facing conformation for a new transport cycle. Adapted from Choudhury *et al*. (2014).

1.2.11. Aims

While structural and biochemical studies to date have provided some valuable insights into McjD, the reported findings have been insufficient to define a complete transport mechanism for MccJ25. The purpose of this research is to address how McjD, a substrate-specific ABC transporter can efflux antibacterial peptides. Specifically, I aim to answer the following mechanistic questions.

(1) What is the functional relevance of the occluded state observed in the McjD structure?

(2) Is there any direct evidence for McjD adopting inward-open and outward-open conformations along the transport cycle?

(3) Does MccJ25 enter the McjD cavity from the cytoplasm or through a lateral entrance in the cell membrane?

(4) What is the degree of separation in the McjD NBDs in the absence of nucleotides?

(5) How are ATP binding and hydrolysis linked to opening of the McjD TMDs and are these changes substrate-dependent?

(6) Does McjD display conformational dynamics and if so, on what timescales do they occur?

(7) Why does McjD display a low level of substrate-induced ATPase activity compared to other ABC transporters?

(8) How does McjD provide producer cells with self-immunity to MccJ25?

(9) How do the translocation mechanisms of antibacterial peptide ABC transporters differ to models proposed for multidrug ABC transporters?

In order to answer these questions, attempts will be made to crystallise McjD in different conformational states and to determine whether these structures can be adopted in the native cell membrane (chapter 2). To investigate the existence of the inward- and outward-open states, functional assays will be performed that test both the transport activity of McjD and accessibility of the binding pocket to substrates (chapter 2). The ability of McjD to export MccJ25 whilst preventing reuptake of the peptide and ensuring self-immunity to the producer stain will also be evaluated. These mechanistic insights will be highly relevant to other antibacterial peptide ABC transporters that contain occluded TMDs in the presence of bound nucleotides (Lin *et al*., 2015; Morgan *et al*., 2017). In addition, it remains to be established whether the large conformational changes proposed for multidrug ABC transporters such as MsbA are required by McjD for MccJ25 efflux (Ward *et al*., 2007).

Conformational changes in the McjD NBDs and TMDs will be examined using a combination of PELDOR (chapter 2) and smFRET (chapter 3) measurements. While both techniques can be applied to investigate distance changes along the transporter, smFRET has the added advantage of being able to probe whether McjD displays conformational dynamics. Key to these experiments is the design of spin/fluorophore labelled McjD variants that retain their functional activity after labelling. Moreover, defining whether the observed conformational changes differ in detergent solution and native conditions (bicelles or liposomes) enables assessment of their physiological relevance. To date, there is no available smFRET investigation of an ABC exporter that monitors coupling of the NBDs to the TMDs in the presence of a substrate. As such, McjD has the potential to be a model system for smFRET that can be applied to other ABC exporters and facilitate complete understanding of their translocation cycles.

Chapter 2: McjD structure and mechanism

The work presented in this chapter is published in:

Bountra, K[#]., Hagelueken, G[#]., Choudhury, H. G[#]., Corradi, V., El Omari, K., Wagner, A., Mathavan, I., Zirah, S., Yuan Wahlgren, W., Tieleman, D. P., Schiemann, O., Rebuffat, S. & Beis, K. 2017. Structural basis for antibacterial peptide self-immunity by the bacterial ABC transporter McjD. *The EMBO Journal*. **36**, 3062-79.

[#] these authors contributed equally

2.1. Introduction

2.1.1. Approach to define the McjD transport mechanism

Structures of ABC exporters have been reported in a variety of conformational states (section 1.1.7), but in most cases, structural information is only available at certain stages of the transport cycle (Beis, 2015). Therefore, being able to trap different conformations of the same ABC exporter is necessary to fully understand how they operate at the molecular level. McjD is thought to differ from conventional type IV ABC transporters such as MsbA by using a variation on the alternating access model (section 1.2.10). While the existing McjD structure mimics the ATP-bound state of the transporter, it cannot explain how the NBDs open up in the absence of nucleotides or whether ATP hydrolysis induces an opening of the TMDs to release MccJ25 (Choudhury *et al*., 2014). The purpose of this chapter will be to determine structures of McjD in the nucleotide free (*apo*) and post-ATP hydrolysis intermediate states, thus providing snapshots of the transporter at sequential stages of the catalytic cycle.

Structure elucidation of McjD in distinct conformational states provides a framework for in-depth mechanistic analysis of the transporter. Cysteine mutations will be strategically incorporated in the McjD NBDs and TMDs to facilitate (1) predictive cross-linking experiments, (2) PEGylation of the binding pocket, (3) transport measurements in liposomes and (4) spin labelling of the transporter for PELDOR analysis. These methods will seek to answer whether the structures obtained for McjD can be sampled in the native cell membrane, whether the occluded state is a stable feature of the McjD cavity, how MccJ25 can access the McjD TMDs and what set of conditions can give rise to the outward-open state. Taken together, the goal of this chapter will be to assemble a detailed transport model for MccJ25 export by McjD, and to address the mechanistic questions raised in section 1.2.11.

2.2. Materials and Methods

2.2.1. Protein expression

The full length *mcjD* gene (accession number: Q9X2W0, residues 1-580) was subcloned from the *E. coli* pTUC202 vector into the pWaldo-GFPd vector (Drew *et al*., 2006) by Dr Konstantinos Beis. This generated a C-terminal GFP-His_8 tagged protein containing a TEV (tobacco etch virus) cleavage site. The DNA was transformed into the C43 (DE3) strain of *E. coli* and cells were grown on LB-agar plates containing kanamycin (34 μg/mL).



Figure 24. Schematic representation of McjD-GFP-His construct.

A single colony was transferred to a volume of 250 mL LB (Luria broth) and grown overnight at 37° C in the presence of kanamycin (34 μg/mL). 10 mL of starter culture was added to baffled flasks, each containing 1 L LB and supplemented with antibiotic. The flasks were incubated at 37° C, shaking until an OD_{600} of 0.4 - 0.5 was reached. The temperature of the incubator was then lowered to 25° C and protein expression was induced by addition of 1 mM IPTG (Isopropyl β-D-1-thiogalactopyranoside) for 17 h. The presence of a GFP tag allows McjD expression levels in whole cells to be quantified following overnight induction. To measure protein expression, a 1 mL aliquot of culture was centrifuged at 15,000 *g* for 2 min. The cell pellet was resuspended in 200 μl of 1 X PBS (phosphate buffered saline) (pH 7.4) and

100 µl of the resuspension was loaded on a Nunc optical bottom 96 well plate (Thermo Fisher Scientific). A SpectraMax microplate reader (Molecular Devices) was set to measure GFP emission at 512 nm and excitation at 485 nm, using the option 'bottom read' to maximise sensitivity. The equation below demonstrates conversion of this value (sample fluorescent counts) to estimate the amount of McjD expressed. This calculation is used in subsequent steps of the purification where indicated.

$$\frac{\text{Sample fluorescent counts}}{\text{Fluorescent counts of pure GFP } (0.03\frac{\text{mg}}{\text{mL}})} * 0.03\frac{\text{mg}}{\text{mL}} = c_{GFP}$$

$$\frac{M_w \text{ of McjD } (65425\frac{\text{g}}{\text{mol}})}{M_w \text{ of GFP } (26866\frac{\text{g}}{\text{mol}})} * c_{GFP} = c_{McjD}$$

Figure 25. Equation to calculate GFP and McjD concentration.

2.2.2. Preparation of membranes

Cells from the large scale culture were harvested by centrifugation at 10,000 *g* for 10 min. The collected pellet was resuspended in a volume of 300 mL 1 X PBS (pH 7.4), containing DNAse (Sigma Aldrich), Pefabloc (Sigma Aldrich) and 5 mM $MgCl_2$. All subsequent steps were performed at 4° C. The resuspension was then passed through a cell disrupter (Constant Systems) set at 22 kpsi for the first cycle and increased to 25 kpsi for the second cycle. To remove cellular debris and unbroken cells, the sample was centrifuged at 15,000 *g* for 10 min. The supernatant was then spun in an ultracentrifuge at 120,000 *g* for 1 h in order to pellet the membranes. The membrane pellet was resuspended in 1 X PBS using a glass homogeniser to make inside-out vesicles (ISOVs) and the fluorescent counts were recorded.

2.2.3. Protein purification

Inside-out vesicles were brought to a total volume of 360 mL 1 X PBS and solubilised in 1% (w/v) n-Dodecyl β-D-maltoside (DDM) (Anatrace) for 1 h. Unsolubilised material was removed by ultracentrifugation at 120, 000 *g* for 30 min. The efficiency of solubilisation was calculated by dividing fluorescent counts in the supernatant by the value taken before DDM addition. The supernatant was brought to 20 mM imidazole (pH 7.5) and incubated with nickel-NTA superflow resin (Qiagen) (1 mL resin per 1 mg of GFP), stirring for 4 h. The slurry was loaded onto a glass Econo-column (Biorad) and washed with 10 X CV of 1 X PBS containing 30 mM imidazole and 0.1% DDM. McjD-His_8-GFP was then eluted in a buffer of 1 X PBS containing 250 mM imidazole and 0.1% DDM. The eluted protein was treated with TEV protease (1 mg of TEV per 1 mg GFP) and dialysed overnight in 2 L of buffer (20 mM Tris (pH 7.5), 150 mM NaCl, 0.03% DDM). The dialysed sample was then passed through a 5 mL His Trap HP column (GE Healthcare) equilibrated in the same buffer. The reverse nickel step was required to remove uncleaved McjD, His_8-GFP and TEV-His_6 which remained bound to the resin. The flow through containing cleaved McjD was concentrated to a final volume of < 500 µl using a 100 kDa cut-off concentrator (Sigma Aldrich) and injected onto a Superdex S200 10/300 gel filtration column (GE Healthcare) equilibrated in the dialysis buffer. The absorbance at 280 nm was monitored using the Äkta prime system and fractions were collected at a volume of 200 µl. Fractions corresponding to McjD at an elution volume of ~11.5 mL were pooled together and concentrated to 12 mg/mL for crystallisation or biochemical assays.

Purification step	Amount of McjD
Protein expression	40 mg
Cell disruption	20 mg
Membrane preparation	18 mg
Detergent solubilisation	14 mg
Nickel IMAC elution	6.5 mg
Reverse IMAC elution	5 mg
Gel filtration	3.5 mg
Concentration to 12 mg/mL	2.5 mg

Table 4. McjD purification table. The amount of wild-type McjD recovered at each step of purification from a typical 12 L expression is shown. Values shown up until the nickel IMAC elution step were derived by first calculating the total GFP concentration. Thereafter, the McjD concentration was estimated by measuring the absorbance at 280 nm ($\varepsilon = 8.3\ M^{-1}\ cm^{-1}$).

2.2.4. Crystallisation of McjD-ADP-VO_4

Prior to crystallisation, McjD (12 mg/mL) was treated with 2 mM ATP, 2 mM sodium orthovanadate and 2.5 mM $MgCl_2$ at room temperature for 1 h. Crystals grew overnight at 20° C using the hanging-drop vapour diffusion method by mixing protein and reservoir solution at a ratio of 1:1. Crystals were grown from a mother liquor containing 10% PEG 4000 supplemented by 0.1 M ammonium sulphate, 0.1 M HEPES (pH 7.5) and 22% glycerol. They reached maximum size after 4 d. The crystals were directly frozen in liquid N_2 and data collection was performed at the Diamond Light Source (I23 beamline).

2.2.5. Data collection and processing

McjD-ADP-VO_4 diffraction data were collected at ~60 K on I23, the long wavelength Beamline at the Diamond Light Source (Wagner *et al*., 2016) close to the vanadium K-edge,

λ= 2.26 Å. In total 360º of data were recorded using the inverse-beam method (20º wedges). Images from a Pilatus 12M detector were processed using autoPROC (Vonrhein *et al*., 2011) and the STARANISO server (http://staraniso.globalphasing.org/cgi-bin/staraniso.cgi). Further processing was performed using the CCP4 suite (Winn *et al*., 2011). Due to high anisotropy, the resolution limit was restricted to 3.4 Å in the refinement stage. The space group was determined to be C2 with two copies of McjD in the asymmetric unit.

2.2.6. Structure solution and refinement

The McjD-ADP-VO_4 structure was determined by molecular replacement in Phaser (McCoy *et al*., 2007) using the previously published McjD-AMP-PNP structure (PDB ID: 4PL0) (Choudhury *et al*., 2014) as a search model. Initial refinement to 3.4 Å was carried out in REFMAC5 (Murshudov *et al.,* 2011) and at later stages in Buster (Blanc *et al*., 2004). The structure was refined with restraints against the high-resolution structure 4PL0 (Figure 26). After rigid body and restrained refinement, extra electron density corresponding to two ADP-VO_4 molecules and two $MgCl_2$ ions were identified, allowing these molecules to be built in and refined. To verify the presence of ADP-VO_4 anomalous difference maps were calculated in CCP4. Strong electron density could be observed up to 10 σ at the vanadium position at both NBDs. Due to the medium resolution of the data, placement of the VO_4^{3-} was guided by the anomalous difference maps. The final model has an R_{work} of 25.9% and an R_{free} of 26.1% (Table 5). The McjD-ADP-VO_4 structure has 93.3% of the residues in the favoured Ramachandran region and has 7 outliers as calculated by MolProbity (Chen *et al*., 2010). The existence of these outliers is due to the presence of weak electron density in certain parts of the model, particularly in the loop connecting the NBDs and TMDs.

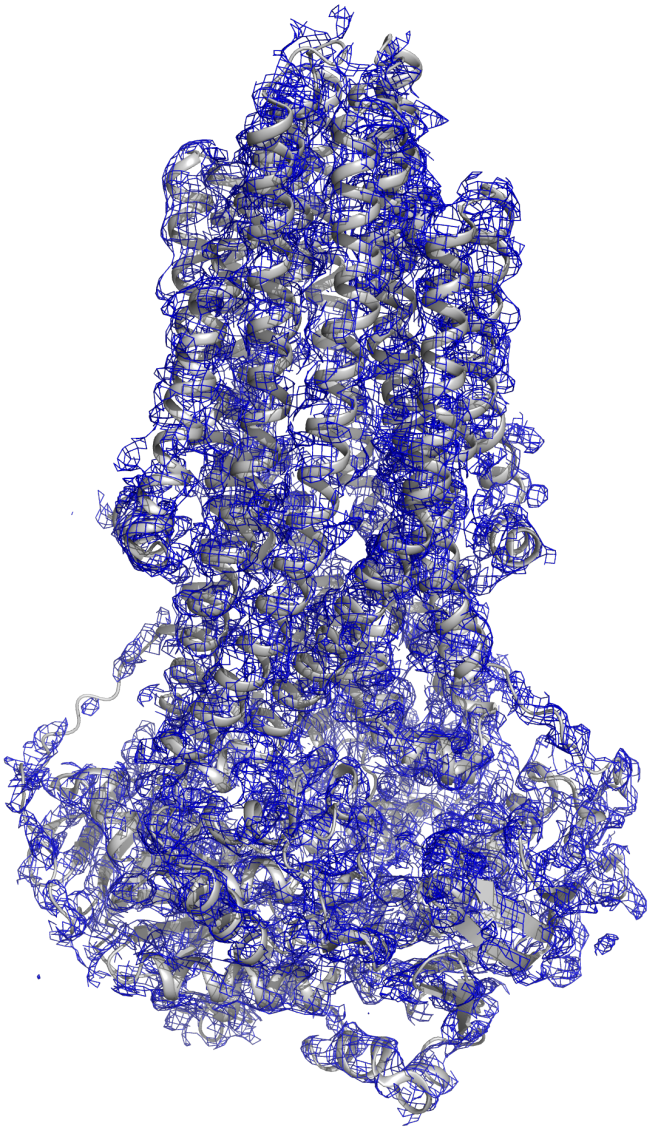


Figure 26. Final electron density map for McjD-ADP-VO_4. $2F_o$-F_c electron density map (blue mesh contoured at 1 σ) showing good quality electron density overall in both the McjD NBDs and TMDs after refinement of the structure.

Data collection statistics	**McjD-ADP-VO_4**
Beamline	DLS-I23
Wavelength (Å)	2.26
Resolution (Å)	77.3 -3.40 (3.40 – 3.40)
Space group	C2
Cell Dimensions	a = 235.3, b = 105.0, c = 117.4, β = 105.6
Number of reflections	143753 (2852)
Number of unique reflections	22352 (437)
Completeness (%) *spherical*[#]	58.6 (23.2)
Completeness (%) *ellipsoidal*[#]	94.2 (87.2)
Redundancy	6.4 (6.5)
Rmerge (%)	5.5 (63.5)
Mean (I)	18.1 (2.6)
$CC_{1/2}$	0.99 (0.86)
Refinement statistics	
R_{work} (%)	25.9
R_{free} (%)	26.1
Average B-factors (Å^2)	104
Rms deviations from ideal values	
Bonds (Å)	0.01
Angle (°)	6.9
Ramachandran plot outliers (%)	0.61

Table 5. Data collection and refinement statistics for the McjD ADP-VO_4. Values in brackets refer to data in the highest resolution shell.

2.2.7. Site-directed mutagenesis

Mutants were derived from a Cys-less variant of either McjD-His_8 (cross-linking, PEGylation) or McjD-GFP-His_8 (PELDOR), using the QuikChange Site-Directed Mutagenesis Kit (Agilent Technologies) to insert cysteines at specific positions. Mutagenic primer sequences were generated using the QuikChange Primer Design tool (Table 6). The Cys-less McjD template was generated Dr Konstantinos Beis by removing four native cysteine residues and replacing them with alanine. The resulting Cys-less McjD displays a similar basal ATPase activity to wild-type protein (Choudhury *et al*., 2014). The positions of the mutations were selected based on inspection of the McjD structure in COOT (Emsley and Cowtan, 2004). The primers designed for mutagenesis are shown in Table 1. Reactions were carried out using a MyCycler thermal system (Bio-Rad) according to manufacturer's instructions. Positive clones were miniprepped using the Wizard Plus DNA Purification System (Promega) and verified by sequencing (Source Bioscience, UK).

Mutation	Forward primer	Reverse primer	Application (position)
L52C	5’AATTTGACAATGAGCCAGACAG GCAATCTGTAATCTTTGCAAGAAT CAATG-3’	5’CATTGATTCTTGCAAAGATTA CAGATTGCCTGTCTGCATTGTCA-3’	PELDOR (periplasmic TMDs)
L53C	5’-AAATTTGACAATGAGCCAGA GCATAAATCTGTAATCTTGCAA GAATCAATGGTG AAATAGA-3'	5'-TCTATTTCACCATTGATTCTT GCAAAGATTACAGATTTATGC TCTGGCTCATTGTCAAATTT-3'	Cross-linking (periplasmic TMDs)
A122C	5’-AGACTTTGCGTTGTATAATAT CCACAATTATTTTTACTCAAGTTA GTTATATTTTCGTTATACAATT-3’	5’-AATTGTATAACGAAAATATA ACTAACTTGAGTAAAAATAATT GTGGATATACAACGCAAAGTCT-3’	Cross-linking (cytoplasmic TMDs)
R134C	5’-TCTCACAAGAATATAAATGTC ACATGAACCCTGGTTAAGACTTT GCGTTG-3’	5'-CAACGCAAAGTCTTAACCAG GCTTCATGTGACATTTATATTCT TGTGAGA-3’	PEGylation (cytoplasmic TMDs)
I138C	5’-AAGTCTTAACCAGGCTTCAAA TGACATTTATTGTCTTGTGAGAA ATCTTTCC-3’	5’-GGAAACATTTCTCACAAGAC AATAAATGTCATTTGAAGCCTG GTTAAGACTT-3’	PEGylation (cytoplasmic TMDs)
I287C	5’-AAGAATGATATATGATGTAAT CATACAGAAGTGGCCGATACTAA CTACACC-3’	5’-GGTGTAGTTAGTATCGGCCA CTTCTGTATGATTACATCATATA TCATTCTT-3’	PEGylation (periplasmic TMDs)
T298C	5’-CCCCTATATTTTCCACTGGACA TGAAAGAAGAATGAATATATGA TGTAATCATAATGAAC-3’	5’-CTTCATTATGATTACATCATA TATCATTCTTCTTTCATGTCCAG TGGAAAATATAGGGG-3’	PEGylation (periplasmic TMDs)
S509C	5’-GCTCTCTTATGGACAGGTTTAA CATTCGCTCCATGTTGAGAAAAG G -3’	5’-CCTTTTCTCAACATGGAGCG AATGTTAAACCTGTCCATAAGA GAGC-3’	Cross-linking (NBDs)
C547	5’-CTTCATTCAATACATAAACACA ATCGGAAGACTCCAGAAGATTTA TT-3’	5’-AATAAATCTTCTGGAGTCTTC CGATTGTGTTTATGTATTGAATG AAG-3’	PELDOR (NBDs)

Table 6. McjD mutant primer sequences for cysteine mutations.

2.2.8. Predictive cysteine cross-linking

Cysteine mutations for cross-linking were incorporated at the periplasmic side of the TMDs (L53C), the cytoplasmic side of the TMDs (A122C) and in the NBDs (S509C). ISOVs were prepared using the methods described in section 2.2.2 with the following modification. After the ultracentrifugation step, the membrane pellet was resuspended using a glass homogeniser in a buffer containing 50 mM HEPES (pH 7.5) and 150 mM NaCl. The protein concentration of the ISOVs was determined using the Bicinchoninic acid assay (BCA) kit (Thermo Fisher Scientific). ISOVs of each McjD mutant were adjusted to a total protein concentration of 10 µg/µl in the resuspension buffer. All cross-linking reactions were performed in triplicate. ISOVs containing the S509C mutation were pre-treated with 1 mM DTT at 25° C for 1 h to limit the degree of pre-formed cross-linked dimer. Where appropriate, ISOVs were incubated with 3 mM nucleotides (AMP-PNP or ATP/sodium orthovanadate) and 3 mM $MgCl_2$ at 37° C for 30 min. To test the ability of MccJ25 to induce cysteine cross-links of A122C, 1 mM MccJ25 was added to A122C ISOVs. The cross-linking reactions were initiated by the addition of 2 mM $CuCl_2$, which was freshly prepared, followed by incubation at 25° C for 1 h. The reaction mixtures were then quenched by adding 2 mM *N*-ethylmaleimide, and diluted in 4 X LDS (lithium dodecyl sulfate) sample buffer (Thermo Fisher Scientific) without the addition of reducing agents. The samples were loaded onto NuPAGE Bis-Tris gels (Thermo Fisher Scientific) that were run at 220 V for 35 min.

The gels were transferred to a nitrocellulose membrane using the iBlot dry blotting system (Thermo Fisher Scientific) according to manufacturer's instructions. The membrane was subsequently washed with iBind solution (Thermo Fisher Scientific) for 5 min and then transferred to the iBind Western device (Thermo Fisher Scientific). The iBind device was loaded with a 6 X His Tag Monoclonal primary antibody (Thermo Fisher Scientific) and Rabbit

anti-Mouse IgG HRP conjugate secondary antibody (Thermo Fisher Scientific). The antibodies were prepared in iBind buffer at dilution factors of 1:2000 (primary) and 1:4000 (secondary) respectively, and were incubated with the nitrocellulose membrane for a duration of 3 h. The Western blots were developed using the ImageQuant LAS4000 system (GE Healthcare) with an exposure time of 60 s (chemiluminescent mode). Densitometry analysis of the McjD monomer and cross-linked dimer (CLD) band intensities was performed using the ImageQuant TL Software (GE Healthcare) with the automatic peak detection mode applied. To quantify the extent of MccJ25 stimulated cross-linking of 122C, band intensities corresponding to CLD formation were recorded for each gel lane.

2.2.9. PEGylation cavity accessibility assays

Cysteine mutations for cross-linking were incorporated at the periplasmic side of the TMDs (R134C, N138C) and the cytoplasmic side of the TMDs (I287C, T298C). ISOVs of each McjD cavity mutant were prepared in a buffer containing 50 mM HEPES (pH 7.5) and 150 mM NaCl. The total protein concentration was measured using the BCA protein assay kit and ISOVs were diluted to a final concentration of 10 µg/µl. All PEGylation reactions were performed in duplicate. In the relevant conditions, ISOVs were pre-incubated with 3 mM nucleotides (AMP-PNP or ATP/sodium orthovanadate) and 3 mM $MgCl_2$ at 37° C for 30 min. The ISOVs were then treated with 1 mM methoxypolyethylene glycol maleimide 10,000 (mPEG-10k) (Sigma Aldrich) and incubated at 25° C for 1 h. For the competition assays, MccJ25 (in DMSO) was added to the reactions at a final concentration of 1 mM peptide. All reaction mixtures were quenched by addition of 2 mM *N*-ethylmaleimide, diluted in 4 X LDS sample buffer with no added reducing agents, and loaded onto NuPAGE Bis-Tris gels. Anti-His Western blots were prepared using the same methods described in section 2.2.8 and were imaged using the

ImageQuant LAS4000 system (GE Healthcare) with an exposure time of 60 s. For densitometry analysis of the competition assay blots, the band intensities were quantified for PEGylated species in the gel lanes containing mPEG-10k. Quantification was performed using the ImageQuant TL software (GE Healthcare) using the automatic peak detection mode.

2.2.10. Preparation of labelled McjD mutants for PELDOR

Cysteine mutations for PELDOR measurements were incorporated at the periplasmic side of the TMDs (L52C) and in the NBDs (C547). Expression and purification of the mutants were performed using the same methods applied to wild-type McjD-GFP-His, up to and including the reverse chromatography step (sections 2.2.1 – 2.2.3). Following collection of the flow through containing cleaved McjD, the protein was concentrated to a final volume of < 500 µl using a 100 kDa cut-off concentrator. McjD was then incubated with a 10-fold molar excess of (1-oxyl-2,2,5,5-tetramethyl-Δ3-pyrroline-3-methyl) methanethiosulfonate dye (Toronto Research Chemicals) dissolved in DMSO. The solution was placed on an elliptical roller in the dark for 3 h. To remove excess dye, the protein was injected onto a Superdex S200 10/300 gel filtration column, equilibrated in a buffer containing 100 mM TES (pH 7.5), 300 mM NaCl and 0.06% DDM, made up in D_2O. The absorbance at 280 nm was monitored using the Äkta prime system (GE Healthcare). Fractions were collected and concentrated using a 100 kDa cut-off concentrator until a concentration of 18 mg/mL was reached. The sample was flash frozen in liquid N_2 and sent to our collaborator Dr Gregor Hagelueken (University of Bonn) for PELDOR measurements.

2.2.11. ATPase assays

ATPase activity measurements were performed using the Enzcheck phosphate assay kit (Molecular Probes). The assay kit measures the production of inorganic phosphate (Pi) during the ATP hydrolysis process. The kit contains a substrate, 2-amino-6-mercapto-7-methylpurine riboside (MESG), that reacts with Pi in the presence of the enzyme purine nucleoside phosphorylase (PNP). The reaction leads to a spectrophotometric shift in absorbance from 330 nm for the substrate to 360 nm for the product. The final concentration of ATP added to the reaction components was 1 mM. The assay was carried out at 25° C in 96 well Nunc optical bottom 96-well plates (Thermo Fisher Scientific) using the SpectraMax Gemini microplate reader (Molecular Devices). Changes in absorbance at 360 nm were calculated from the linear part of the curve. A phosphate standard curve was plotted by linear regression analysis to enable conversion of absorbance values into the amount of phosphate liberated. The gradient of the phosphate standard curve was measured to be 0.0214 A_{360} units/nmole protein. The equations used to determine the rate of ATPase activity are shown below. The calculation is based on each 100 µl reaction well containing 6.5 µg McjD.

$$\frac{\text{Change in Absorbance (360 nm)}}{0.0214} = \text{Pi (nmoles)}$$

$$\frac{\text{Pi (nmoles)}}{\text{time (min)}} = \text{Pi (nmoles/min)}$$

$$\text{Pi (nmoles/min)} \ \text{x} \ \frac{1000}{6.5} = \text{Pi (nmoles/min/mg)}$$

Figure 27. Equations for calculation of McjD ATPase activity

2.2.12. Liposome reconstitution

McjD was diluted in a buffer containing 20 mM Tris, 150 mM NaCl and 0.03% DDM to a final concentration of 0.5 mg/mL in 100 µl. A 20 mg/mL solution of *E. coli* polar lipids (Avanti Polar Lipids) was prepared in ddH_2O by sonicating them in a water bath at 25° C until the solution became less hazy. 20 µl of the phospholipid solution was added to the protein and incubated on ice for 5 min. The solution was further diluted in 4 mL liposome buffer (50 mM Tris (pH 8.0), 50 mM KCl) and incubated again on ice for 5 min. Proteoliposomes were pelleted by ultracentrifugation at 100,000 *g* for 30 min and the supernatant was discarded. The pellets were then resuspended in 100 µl of liposome buffer and the final protein concentration was estimated using the BCA kit (Thermo Fisher Scientific).

2.2.13. Transport assays

The principle of the Hoeschst uptake assay is illustrated in Figure 28. Following incorporation of McjD in liposomes, uptake of the fluorescent dye Hoechst 33342 into the acidic lumen causes a quenching of the fluorescent signal and therefore a drop in the measured fluorescent units. McjD can only transport Hoechst in liposomes in the presence of ATP (Choudhury *et al*., 2014). Importantly, only McjD molecules whose NBDs are oriented to the outside of the liposome are responsive to the addition of Hoechst and nucleotides. McjD molecules whose NBDs face the inside of the liposome are unresponsive to nucleotides and Hoechst since the NBDs are buried in the lumen and therefore can no longer react to these added ligands.

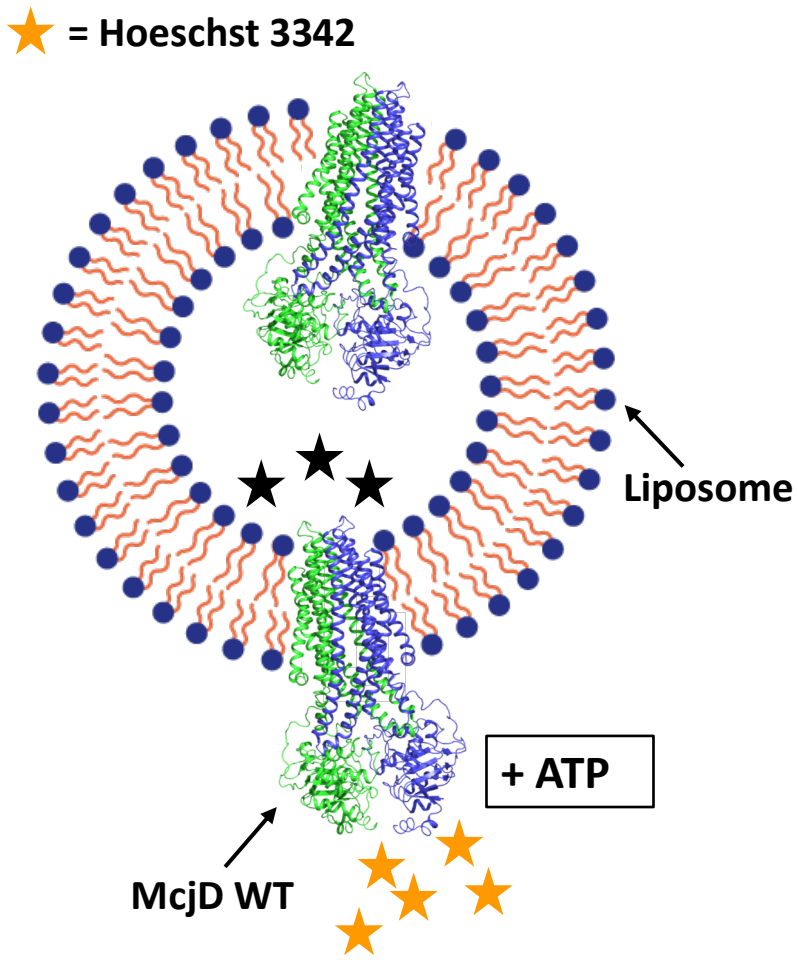


Figure 28. Hoechst 33342 uptake assay in liposomes. Wild-type McjD is depicted following incorporation into proteoliposomes. The fluorescent dye Hoechst 33342 is shown as yellow stars and in the quenched form is depicted as black stars. Only McjD molecules whose NBDs face the outside of the liposome can respond to the addition of nucleotides and Hoechst. McjD-dependent uptake of Hoechst into the acidic lumen of the liposome occurs in the presence of ATP and causes quenching of dye fluorescence, leading to a reduction in the measured fluorescent signal.

Proteoliposomes containing wild-type or L53C-McjD (5 µg in liposome buffer) were diluted 1:50 in a buffer containing 10 mM Tris (pH 7.5), 10 mM KPi, 300 mM NaCl and 5 mM $MgSO_4$. Where required, L53C incorporated liposomes were cross-linked in the presence of 2 mM $CuCl_2$ for 1 h, followed by the addition of 2 mM *N*-ethylmaleimide. Reactions were carried out in 3 mL fluorimeter cuvettes (Sigma Aldrich) at 37° C using a Cary Eclipse Fluorescence Spectrophotometer (Agilent Technologies) set at excitation and emission wavelengths of 355 nm and 457 nm respectively. Fluorescence measurements were initiated at t = 0 s with the McjD reconstituted liposomes alone to create a stable baseline signal. At t = 60 s, 0.1 µM Hoechst 33342 was added to the cuvette and allowed to equilibrate for 40s. At t = 100 s, 3 mM ATP was added to the relevant conditions, while ensuring that negative control reactions were supplemented with an equivalent volume of ddH_2O. For the cross-linked L53C reaction demonstrating existence of the outward-open state, 3 mM DTT and 3 mM ATP were added to the cuvette at t = 10 min. To demonstrate the efficiency of cross-linking, L53C reconstituted liposomes before and after $CuCl_2$ addition were treated with a 10-fold molar ratio of diethylamino-3-(4'-maleimidylphenyl)-4-methylcoumanin (CPM) dye. The samples were loaded on SDS-PAGE gels and visualised by the ImageQuant LAS4000 system (GE Healthcare) set to fluorescence mode. All transport assays were performed in duplicate with independently prepared batches of liposomes and the mean values obtained were plotted in GraphPad Prism 7 (GraphPad Software).

2.3. Results

2.3.1. Structure of McjD-ADP-VO_4

The structure of McjD-AMP-PNP was previously determined in an outward-occluded conformation and defines the ATP-bound state (Choudhury *et al*., 2014). In order to better understand the mechanism McjD uses to export MccJ25, I sought to determine the structure of McjD in a post-ATP hydrolysis intermediate state.

The Walker B motif of ABC transporters contains a catalytic glutamate residue which can acts as a general base to activate a water molecule for nucleophilic attack on the γ-phosphate of ATP (ter Beek *et al*., 2014). The ATP hydrolysis reaction proceeds *via* formation of a pentacovalent transition state intermediate (Figure 29). In the transition state, the geometry of the γ-phosphate changes from tetrahedral to trigonal bipyramidal, with three oxygen atoms at the equatorial plane, and the β/γ phosphate bridging oxygen and the water nucleophile at the axial positions (Davies and Hol, 2004).

Vanadate (VO_4^{3-}) is an inorganic phosphate analogue that acts as a potent inhibitor of many ATPases because it can mimic the transition state for the γ-phosphate of ATP during hydrolysis and stabilise the transition state conformation (Goodno and Taylor, 1982; Shimizu and Johnson, 1983). Vanadate has been shown to stably trap ADP in the NBDs of ABC transporters by occupying the position of the ATP γ-phosphate group in the catalytic site (Urbatsch *et al*., 1995; Sharma and Davidson, 2000). Among ABC exporters, the crystal structure of MsbA has been captured in the ADP-VO_4 bound state (Ward *et al*., 2007). Determining whether McjD-ADP-VO_4 can adopt an outward-open conformation like the MsbA-ADP-VO_4 structure will provide important mechanistic insights into type IV ABC transporters.

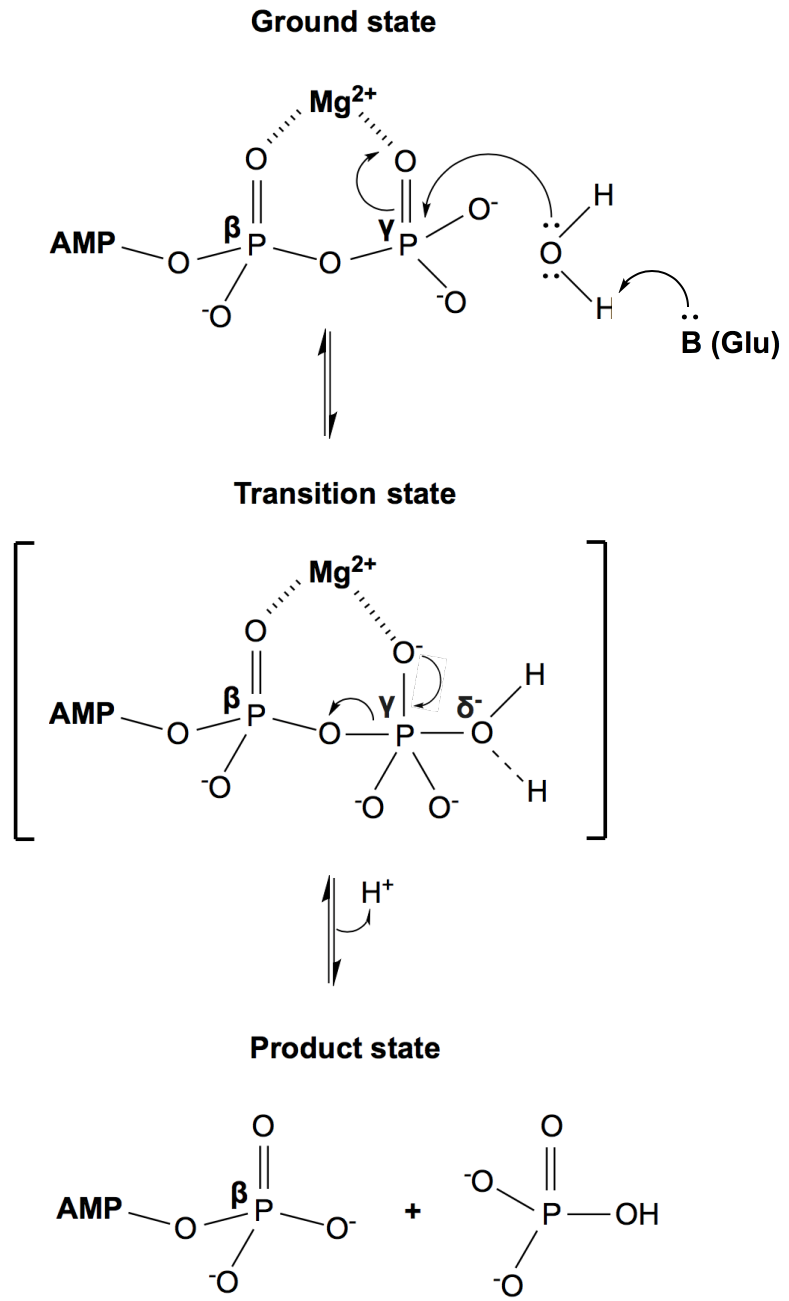


Figure 29. The stereochemistry of ATP during hydrolysis. In the ground state, the γ-phosphate of ATP displays tetrahedral geometry. A catalytic glutamate residue acts as a general base to activate a water molecule. The activated water molecule promotes nucleophilic attack at the γ-phosphate of ATP resulting in formation of a pentacovalent transition state intermediate where the γ-phosphate group switches to trigonal bipyramidal geometry. Cleavage of the scissile bond follows and generates the reaction products ADP and inorganic phosphate. Adapted from Oldham and Chen (2011b).

To facilitate structural studies, wild-type McjD was purified in 0.03% DDM using an established method (Choudhury *et al*., 2014). The McjD gel filtration profile was monodisperse with a clear peak observed at an elution volume of ~12 mL which is the expected molecular weight (Figure 30A). Furthermore, SDS-PAGE revealed a high degree of sample purity that was suitable for crystallisation trials (Figure 30B). McjD was reacted with an equimolar ratio of ATP and sodium orthovanadate prior to crystallisation in order to trap ADP-VO_4 in the NBDs. Initial crystal hits for McjD-ADP-VO_4 were obtained using the MemGold matrix screen plate (Newstead *et al*., 2008). The hits were optimised by conducting fine screens around the crystallisation condition and by lowering both the McjD and sodium orthovanadate concentrations. Following extensive screening, improvements were observed in the crystal size, and quality with conditions containing 10% PEG 4000, 0.1 M ammonium sulphate, 0.1 M HEPES (pH 7.5) and 22% glycerol (Figure 30C).

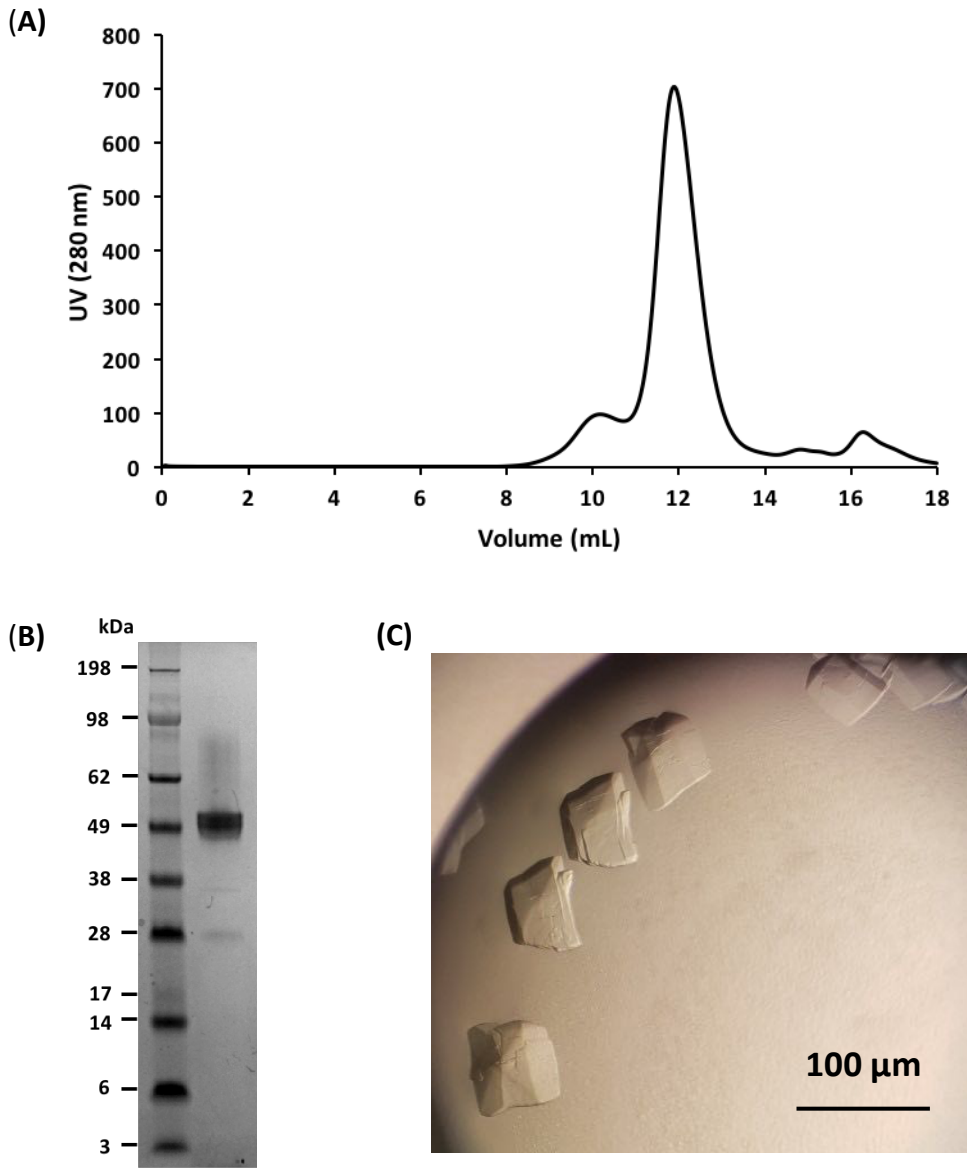


Figure 30. Purification and crystallisation of McjD. (A) Gel filtration profile of wild-type McjD showing a monodisperse peak at 12 mL. (B) SDS-PAGE of purified McjD. The band corresponding to McjD (~50 kDa) migrates slightly lower than the expected molecular weight (65 kDa) due to the masking effect of SDS on hydrophobic regions of membrane proteins. The sample displays a high degree of purity. (C) Optimised crystals of McjD-ADP-VO_4 obtained using the hanging drop vapour diffusion method at 20°C. The crystallisation condition contains 10% PEG 4000, 0.1 M ammonium sulphate, 0.1 M HEPES (pH 7.5) and 22% glycerol.

Initially, data collection was performed using the microfocus I-24 beamline at the Diamond Light Source. The McjD-ADP-VO_4 crystals demonstrated a high degree of anisotropy with the best diffraction spots observed at a resolution of ~4.5 Å. In order to verify the presence of VO_4 in the NBDs, data were collected close to the vanadium K-edge (2.26 Å). However, due to the effects of X-ray scattering from the air path, a weak anomalous signal-to-noise ratio was attained and anomalous difference maps could not be calculated. Subsequent data collection was performed close to the vanadium K-edge at the long wavelength I-23 beamline of the Diamond Light Source. The I-23 beamline utilises an in-vacuum sample environment that reduces the measured background to X-rays scattered only from the crystal and its mount (Wagner *et al*., 2016). The advantage of this setup over conventional beamlines is that the anomalous signal for vanadium is maximised, while contributions from X-ray absorption noise due to air scattering are minimised. Consequently, using the I-23 beamline, the structure of McjD-ADP-VO_4 was determined to a resolution of 3.4 Å (Figure 31).

The structure represents the transition state of a water molecule making a nucleophilic attack on γ-phosphate of ATP. The McjD-ADP-VO_4 structure was solved by molecular replacement using the McjD-AMP-PNP structure as a search model. Clear electron density was observed in the McjD NBDs for two molecules of VO_4^{3-}, ADP and Mg^{2+} (Figure 32). The quality of the data was sufficient for building of the complete McjD sequence, and the structure was refined to an R_{work} of 25.9% and an R_{free} of 26.1%. McjD-ADP-VO_4 contains an outward-occluded conformation where the TMDs are closed off to both sides of the membrane. TM2 and TM5/6 contribute to formation of the TMD dimer interface along with the equivalent TM helices from the opposite subunit. The NBDs adopt a dimerised state where the ADP-VO_4 complex is coordinated by a range of conserved motifs (described in section 1.1.4). The structure of McjD-ADP-VO_4 is almost identical to McjD-AMP-PNP, and the two structures can be superimposed with a root-mean-square deviation (rmsd) of 0.7 Å over 560 Ca atoms (Figure 33).

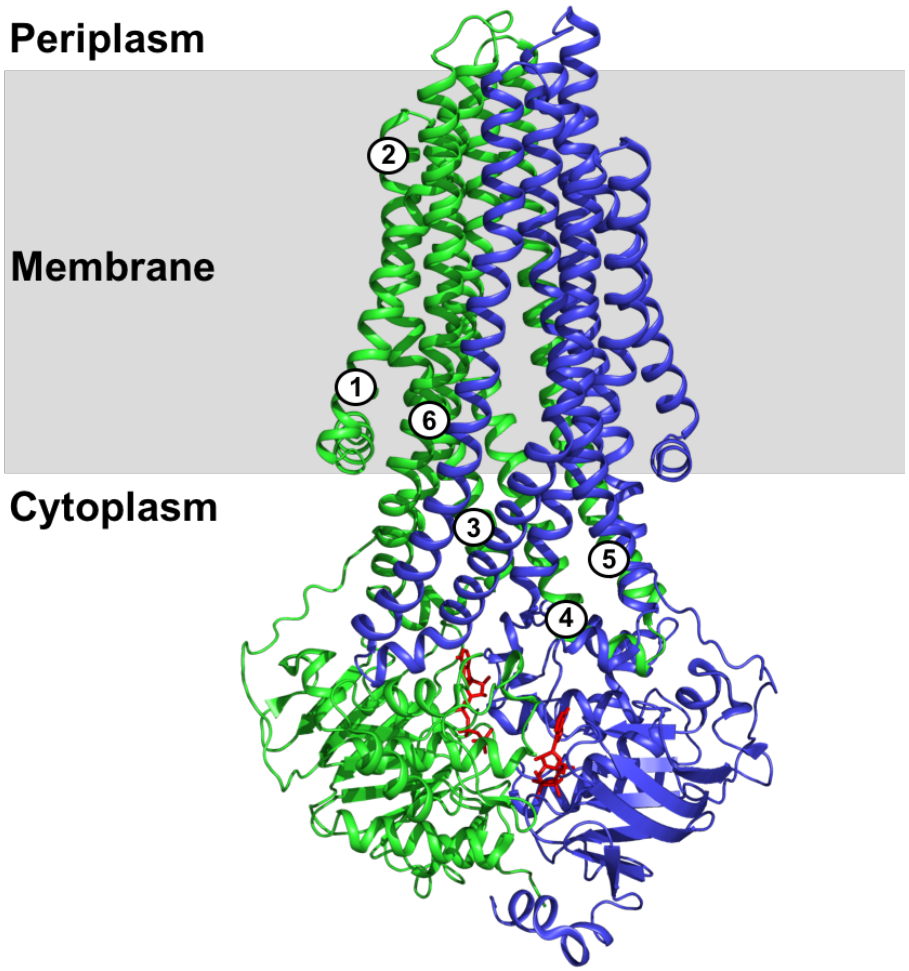


Figure 31. Structure of McjD ADP-VO_4. The McjD monomers are shown in green and blue respectively. ADP-VO_4 is depicted in red stick format. The structure of McjD-ADP-VO_4 displays an outward-occluded conformation (PDB: 5OFR) (Bountra *et al*., 2017). Two molecules of ADP-VO_4 are sandwiched between the NBDs causing them to dimerise. The TMDs are occluded from both sides of the membrane. The TMD dimer interface is formed from TMs 2, 5 and 6 from one subunit with the equivalent TMs from the opposite half of the transporter.

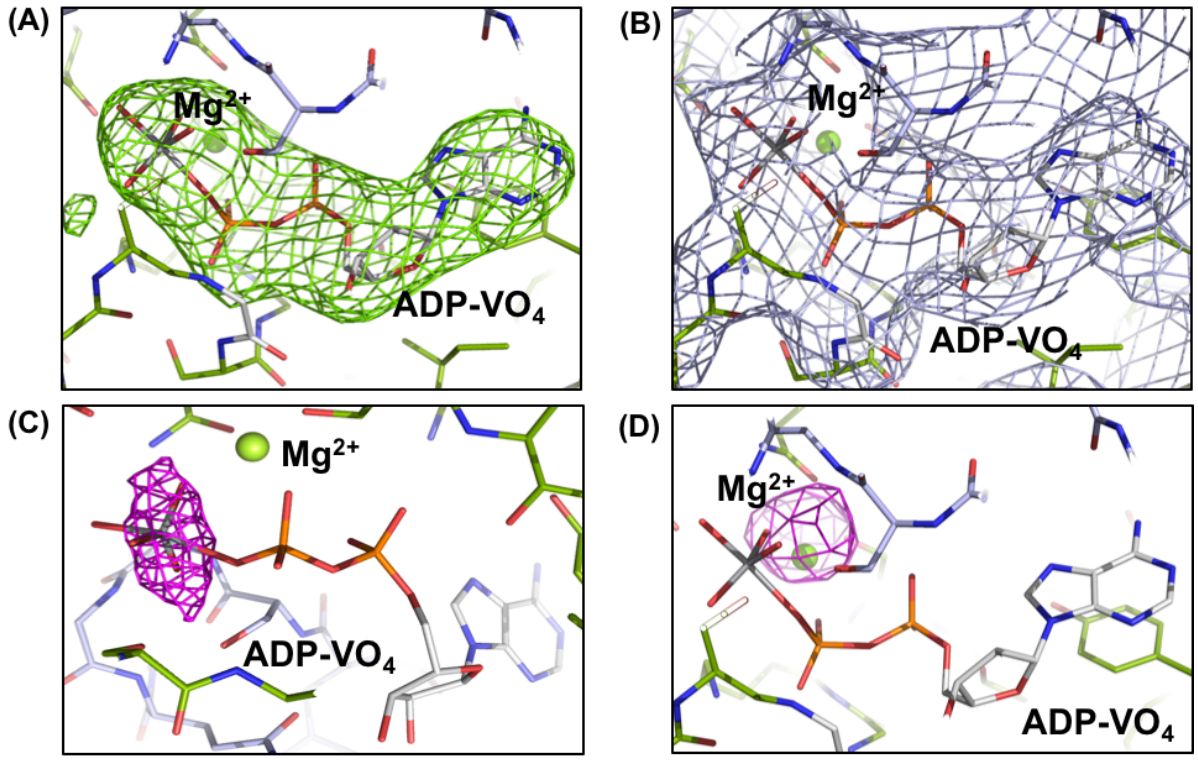


Figure 32. Electron density and anomalous difference maps for McjD ADP-VO_4. (A) F_o-F_c electron density map (green mesh contoured at 3 σ) showing clear density around the ADP-VO_4^{3-} molecule after molecular replacement. ADP-VO_4 is only shown for clarity but it was not included in the refinement. The magnesium ion is shown as a green sphere. (B) Final $2F_o$-F_c electron density map (blue mesh contoured at 1 σ) after including ADP-VO_4 in the refinement. No negative or positive electron density peaks are observed. (C) Anomalous difference electron density map (pink mesh) around the vanadate, from data collected at the vanadium edge, 2.26 Å. The map is contoured at 10 σ. ADP-VO_4 is shown as sticks. The ADP-VO_4 carbons are coloured grey, oxygens red, phosphate orange and vanadate dark grey. (D) Positive F_o-F_c electron density map (purple mesh contoured at 3 σ around Mg^{2+} after excluding it from the refinement.



Figure 33. Comparison of McjD-ADP-VO_4 structure with McjD-AMP-PNP. The top panel shows a view of McjD along the membrane and the lower panel shows a view of the McjD NBDs from the cytoplasmic side. McjD ADP-VO_4 (green) can be superimposed on McjD AMP-PNP (black) with an rmsd of 0.7 Å over 560 Ca atoms indicating the structures are almost identical. No significant conformational changes are observed in the TMDs or the NBDs.

2.3.2. Coordination of ADP-VO_4 in the NBDs

The α and β-phosphate groups of ADP form a network of hydrogen bonds with residues in the Walker A of one McjD monomer and the ABC-signature motif of the opposite monomer. In addition, the adenine ring of the ADP molecule is packed against Y354 in the A-loop *via* a π–π stacking interaction (Figure 34A). The VO_4^{3-} moiety interacts with the Walker A, the Q-loop, and the switch histidine of one NBD and the ABC-signature motif of the other NBD (Figure 34B). The Mg^{2+} ion is coordinated by the Walker A S385, the Q-loop Q426, the β-phosphate group of ADP and the VO_4^{3-} moiety, bridging these different elements together (Figure 34C).

Comparison between the ground state (McjD AMP-PNP) and the transition state (McjD-ADP-VO_4) reveals notable structural differences in the orientation of the γ-phosphate and the presence of an attacking water molecule (Figure 35). In the McjD-AMP-PNP structure, the γ-phosphate and linking oxygen of the β-phosphate are separated by a distance of 1.8 Å, which equates to formation of a covalent bond in the ground state ATP. In addition, there is no electron density for the hydrolytic water molecule in McjD-AMP-PNP, which indicates that the ground state conformation has a low affinity for the attacking water molecule. By contrast, in the McjD structure trapped with ADP-VO_4, the covalently linked oxygen atom of VO_4^{3-} mimics the attacking water. The oxygen atom is positioned 2.7 Å from E506 of the Walker B motif, resulting in formation of a hydrogen bond in the transition state. The stereochemistry is consistent with the function of glutamate in ATP hydrolysis to polarise the nucleophilic water molecule. It has previously been demonstrated that mutation of E506 to a glutamine residue mimicking the protonated form of glutamate, abolishes ATP hydrolysis, consistent with a strong base at this position being essential for hydrolysis (Choudhury *et al.*, 2014). The transition state geometry observed for the McjD-ADP-VO_4 closely resembles the organisation found in the NBDs of $MalFGK_2$-ADP-VO_4 (Oldham and Chen, 2011).

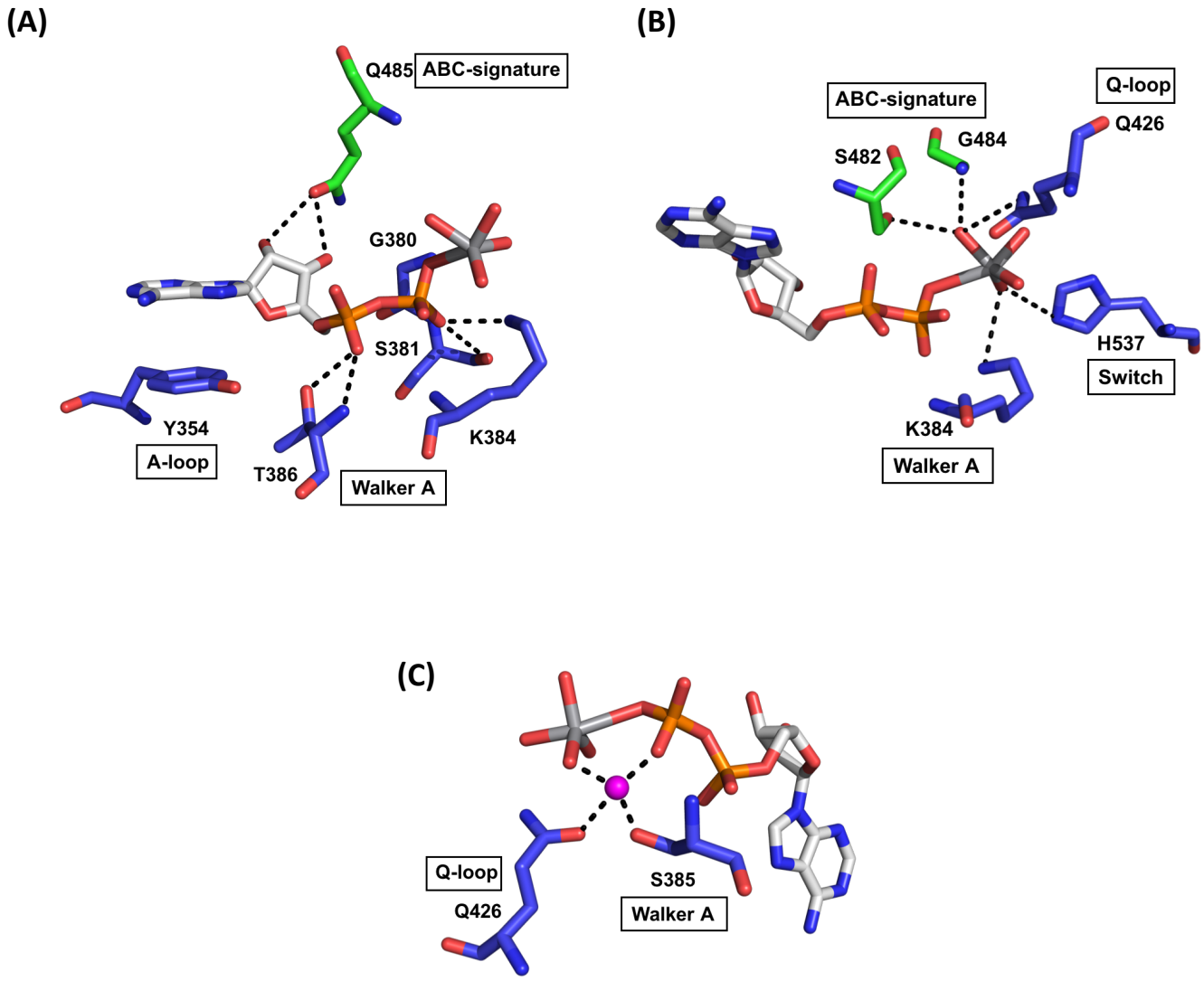


Figure 34. Coordination of ADP, VO_4^{3-} and Mg^{2+} in the McjD NBDs. Residues from the McjD monomers are coloured green and blue. The ADP-VO_4 carbons are coloured white, oxygens red, phosphate orange and vanadate dark grey. The Mg^{2+} ion is depicted as a pink sphere. Hydrogen bonds are indicated by the black dotted lines. (A) The bound ADP molecule is coordinated by hydrogen bonds to residues in the Walker A motif of one NBD (G380, S381, K384, T386) and the ABC-signature motif (Q485) of the opposite NBD. Y354 in the A-loop forms a π–π stacking interaction with the adenine ring of ADP. The Mg^{2+} ion is excluded for clarity. (B) The VO_4^{3-} molecule is coordinated by hydrogen bonds to residues in the ABC-signature (S482, G484), Q-loop (Q426), switch histidine (H537) and Walker A (K384) motifs. (C) The Mg^{2+} ion interacts with ADP, VO_4^{3-}, S385 in the Walker A motif and Q426 in the Q-loop.

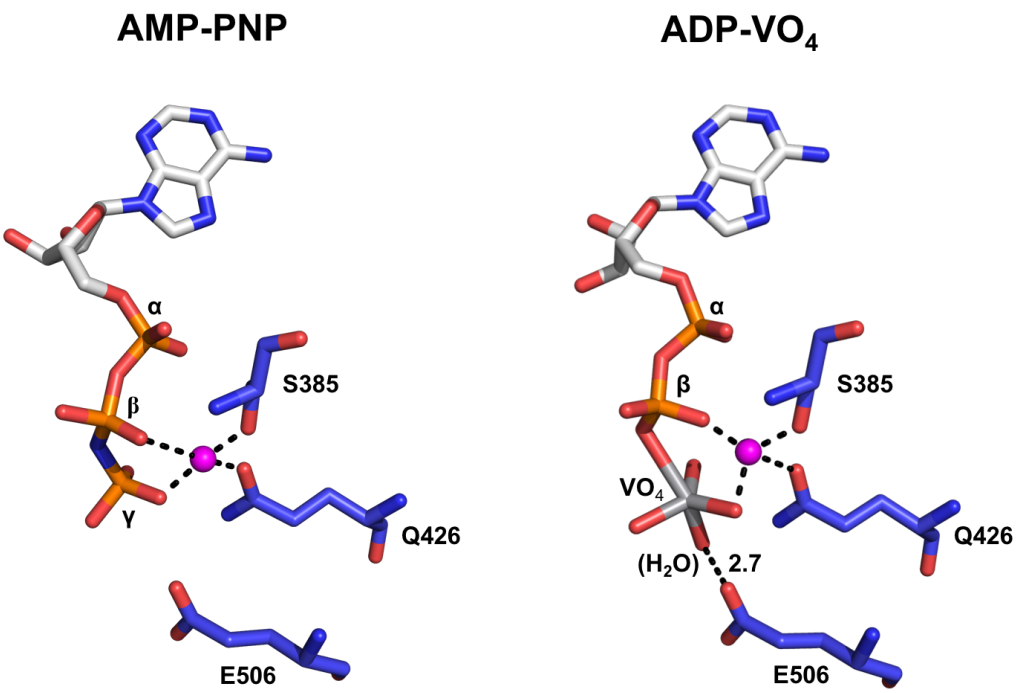


Figure 35. Comparison between the McjD ground state and transition state. The ADP-VO_4 carbons are coloured white, oxygens red, phosphate orange and vanadate dark grey. The Mg^{2+} ion is depicted as a pink sphere. Hydrogen bonds are indicated by the black dotted lines. In McjD-AMP-PNP (ground state), the nucleophilic water molecule is not present in the active site. In McjD-ADP-VO_4 (transition state), the covalently linked oxygen atom of VO_4^{3-} mimics the attacking water and forms a hydrogen bond to E506. The catalytic glutamate is correctly positioned to polarise the water nucleophile and participate in ATP hydrolysis.

2.3.3. Structure of McjD *apo*

The structure of McjD in the *apo* nucleotide free state was determined by Dr Hassanul Choudhury. McjD *apo* adopts a novel inward-occluded conformation where the TMDs are occluded from both sides of the membrane and the NBDs have disengaged from one another in a scissors-like motion. Since the McjD *apo* structure was solved in the absence of nucleotides, it provides a useful framework for comparison with the nucleotide bound structures. The structures of McjD *apo* and McjD-ADP-VO_4 can be superimposed with an rmsd of 2.1 Å over 560 Ca atoms and in the TMD alone with an rmsd of 0.7 Å over 290 Ca atoms (Figure 36). While the TMDs are almost identical in the two states, the *apo* NBDs displays conformational changes resulting in a more open configuration. The structure of McjD *apo* is compared alongside the McjD-AMP-PNP and McjD-ADP-VO_4 structures in Figure 37. The absence of conformational changes in the TMDs in all three structures suggests that the occluded TMD dimer may represent a stable feature of the McjD cavity. Compared to nucleotide bound McjD (between positions S509 and S509'), the NBDs of McjD *apo* are separated by a further 7.9 Å. This small degree of disengagement suggests that McjD is likely to undergo small conformational changes in the NBDs to facilitate formation of the closed ATP dimer which primes the transporter for ATP hydrolysis.



Figure 36. Comparison of McjD-ADP-VO_4 structure with McjD *apo*. The top panel shows a view of McjD along the membrane and the lower panel shows a view of the McjD NBDs from the cytoplasmic side. McjD ADP-VO_4 (green) can be superimposed on McjD *apo* (black) with an rmsd of 2.1 Å over 560 Ca atoms and in the TMD alone with an rmsd of 0.7 Å over 290 Ca atoms. No significant conformational changes are observed in the TMDs but the NBDs have disengaged from one another in the McjD *apo* structure.

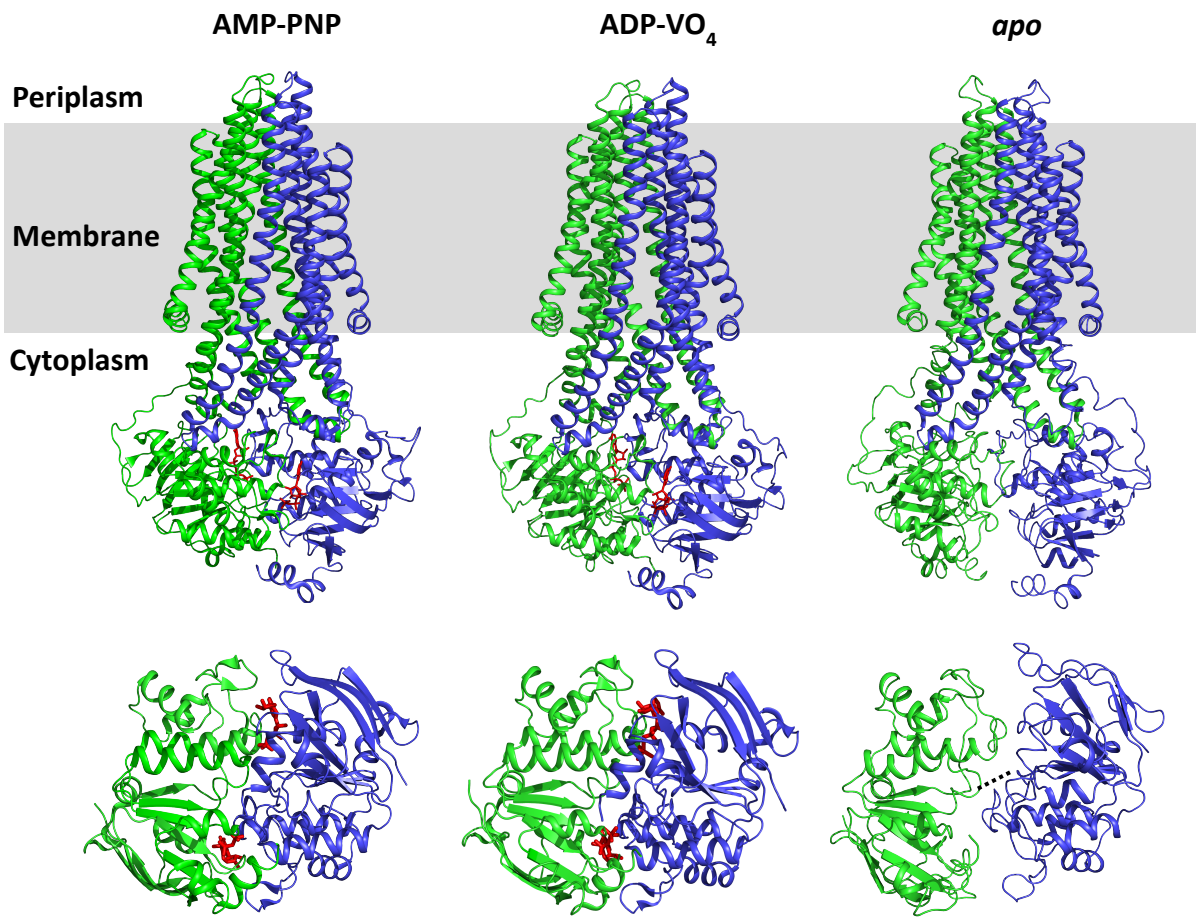


Figure 37. Comparison of McjD structures in distinct conformational states. The McjD monomers are shown in green and blue respectively. The nucleotides are shown in red stick format. In all three McjD structures the TMDs adopt an occluded conformation without access to the cytoplasmic (nucleotide bound) or periplasmic (*apo*) side of the membrane. In the nucleotide bound structures, the NBDs are in a dimerised state, whereas the NBDs in the McjD *apo* structure show a small degree of disengagement. The *apo* NBDs are separated by a further 7.9 Å at position S509 which is indicated by the black dotted line.

2.3.4. Comparison of McjD structures with other ABC exporters

Unlike the crystal structures of MsbA-ADP-VO_4 (Ward *et al*., 2007) which contains outward-open conformations due to inter-subunit twining between TMs 1-2 and TMs 3-6 in the opposite subunit, the McjD-ADP-VO_4 structure lacks inter-subunit twining and displays no opening of the TMDs to the periplasmic side (Figure 38A). In McjD-ADP-VO_4, TMs 1-2 have rotated away from TMs 3-6, giving rise to an occluded TMD interface to the periplasm.

The MsbA *apo* structure contains an inward-open conformation due to inter-subunit twining between TMs 1-3 and 6 from one subunit and TMs 4-5 of the opposite subunit (Ward *et al*., 2007). This results in formation of a transmembrane cavity that is open to the cytoplasmic side of the membrane. By contrast, the equivalent McjD *apo* structure lacks inter-subunit twining since TMs 3-5 have rotated towards the same TMs in the opposite subunit (Figure 38B). This gives rise to an inward-occluded conformation where the TMDs are inaccessible to substrate binding from the cytoplasm. The *apo* structures of the type V lipid ABC transporters ABCA1 (Qian *et al*., 2017) and ABCG5/G8 (Lee *et al*., 2016), and the type VII ABC transporter $LptB_2FG$ (Luo *et al*., 2017), also lack inter-subunit twining in their TMDs. Comparison between the NBDs of the McjD *apo* and MsbA *apo* structures reveals further differences in organisation. While the McjD NBDs (between positions S509 and S509') disengage by 7.9 Å in the absence of nucleotides, there is a much longer separation of 35 Å at the equivalent position in MsbA.

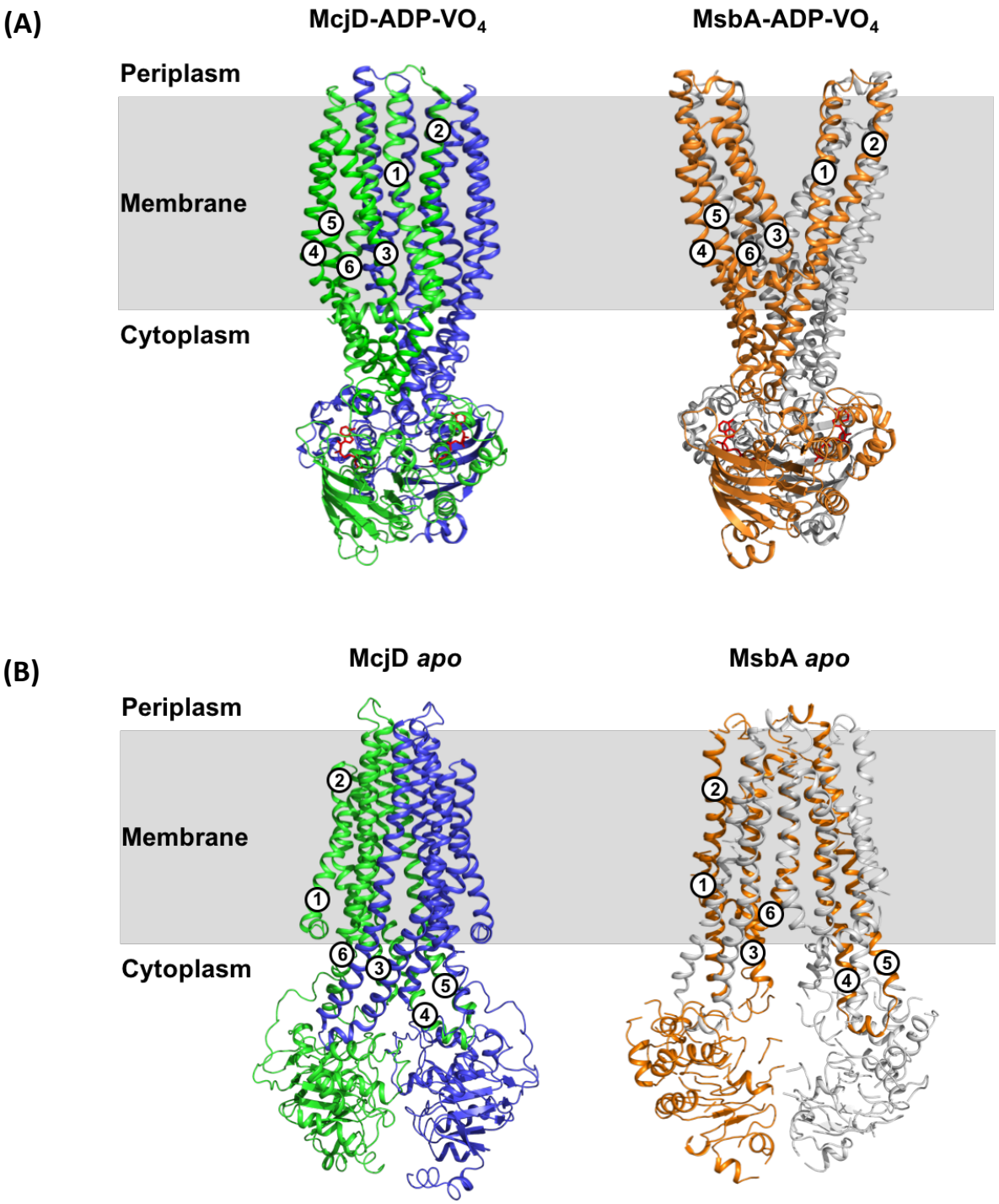


Figure 38. Structural comparison of McjD and MsbA. (A) The structure of McjD ADP-VO_4 adopts an outward-occluded conformation lacking inter-subunit twining. By comparison, MsbA-ADP-VO_4 contains an outward-open conformation due to inter-subunit twining of TM1 and TM2 with the TMs 3-6 of the opposite monomer. (B) The structure of McjD *apo* adopts an inward-occluded conformation lacking inter-subunit twining. In contrast, MsbA *apo* contains an inward-open conformation due to the movements of TM4 and TM5 towards TMs 1-3 and 6 of the opposite half of the transporter. The presence of disordered regions in the NBDs of the MsbA *apo* is attributed to weak electron density in this part of the structure.

2.3.5. Predictive cysteine cross-linking

Since the structures of McjD *apo* and McjD-ADP-VO_4 are strikingly different to the equivalent MsbA structures (~18% sequence identity), it is necessary to confirm that they are physiologically relevant conformations and can be sampled in the native *E. coli* membrane. In order to rule out the possibility of crystal or detergent artefacts, predictive cysteine cross-linking was performed at regions of the McjD structures where the conformations show divergence from MsbA. The selected regions span the periplasmic end of the TMDs (L53C), the cytoplasmic end of the TMDs (A122C) and the NBDs (S509C) (Figure 39). The cysteine mutations were designed at postions where crystal structure measurements indicated that cross-linked dimer (CLD) formation could take place between the two McjD monomers. Since disulphide bond formation requires interatomic distances < 7 Å as well as favourable stereochemistry, these requirements were satisfied by inspection of the structures in COOT (Emsley and Cowtan, 2004).

Following the incorporation of single cysteine mutations, the McjD mutants were overexpressed in *E. coli* and inside-out vesicles (ISOVs) were prepared. The membranes were not detergent-solubilised and further purified since detergent micelles do not mimic the physiological environment of McjD. Therefore, predictive cysteine cross-linking measurements were performed in ISOVs to reflect native membrane conditions. The ISOVs were pre-incubated with the reducing agent DTT in order to reduce pre-formed cysteine cross-links. To mimic the conditions required to obtain the nucleotide bound McjD structures, ISOVs were then treated with either AMP-PNP or ATP and VO_4^{3-}. The cross-linking reaction was initiated by addition of the oxidising agent $CuCl_2$ and quenched by the addition of *N*-ethylmaleimide. CLD formation was visualised by non-denaturing SDS-PAGE followed by anti-His Western blot.



Figure 39. Positions of cysteine mutations for predictive cross-linking. The McjD *apo* structure is shown. Cysteine mutations are shown in red stick format and span the periplasmic end of the TMDs (L53C), the cytoplasmic end of the TMDs (A122C) and the NBDs (S509C).

The L53 position in McjD is located at the periplasmic end of TM1 (Figure 40A). The structure of McjD-AMP-PNP indicates that rotation of TM1 and TM2 gives rise to formation of the occluded McjD cavity. In previous work, the L53C mutation was cross-linked at very high efficiency to validate the outward-occluded state of McjD in the presence of AMP-PNP (Choudhury *et al*., 2014). Since McjD-ADP-VO_4 is also outward-occluded, the ability of L53C to form cross-links was also examined in these conditions. In the presence of ATP-VO_4 and oxidising agent, McjD demonstrated CLD formation with similar efficiency to AMP-PNP, suggesting that the observed conformation of McjD-ADP-VO_4 can be adopted in the native cell membrane (Figure 40B/C). At the equivalent position of the outward-open MsbA-ADP-VO_4 structure, cross-linking would not take place as the TMDs have diverged from the periplasmic side and are too far apart to permit disulphide bond formation from taking place.

Under *apo* conditions, McjD-L53C can also be effectively cross-linked which is in agreement with the occluded periplasmic gate observed in the nucleotide free structure.

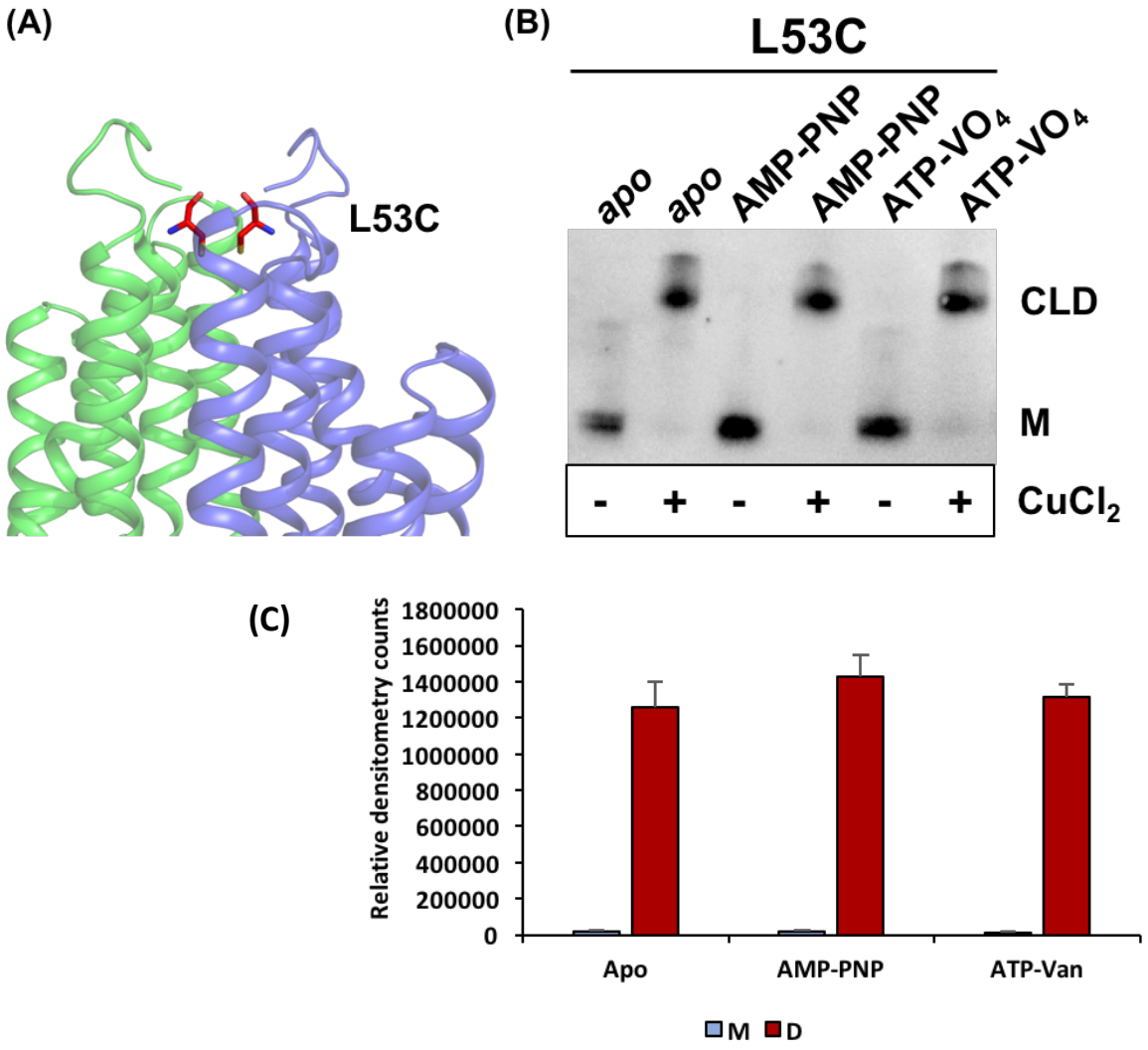


Figure 40. Predictive cysteine cross-linking of the McjD periplasmic TMDs. (A) Position of cysteine mutation (L53C) at the periplasmic end of the TMDs shown in red stick format. (B) Western blot intensities of the cross-linked dimer (CLD) and monomeric species (M) are shown for *apo* and nucleotide-trapped (AMP-PNP, ATP-VO_4) conditions after cross-linking ISOVs with 2 mM $CuCl_2$. Note that pre-incubation of McjD with ATP-VO_4 gives rise to formation of McjD-ADP-VO_4. The ability of McjD-L53C to form CLDs in the presence of ATP-VO_4 at high efficiency verifies the existence of occluded TMDs observed in the McjD-ADP-VO_4 structure. (C) Densitometry analysis of the Western blot showing mean counts of the CLD and monomeric species from three independent cross-linking experiments. Error bars are shown and represent standard deviation of the mean values.

The A122 position in McjD is located at the intracellular side of the TMDs and can monitor the opening or closure of the cytoplasmic gate (Figure 41A). Since the McjD *apo* structure contains TMDs occluded to the cytoplasm, the ability of the A122C mutant to form cross-links was examined. Under *apo* conditions in the presence of $CuCl_2$, there is clear evidence of CLD formation, suggesting that the McjD inward-occluded structure can be sampled in *E. coli* membranes (Figure 41B/C). At the equivalent position of the inward-open MsbA *apo* structure where the TMDs have diverged from the cytoplasmic side, CLD formation would not take place because the two monomers are too far apart. These data confirm that McjD is the first example of a type IV ABC transporter to display occluded TMDs to the cytoplasm in the absence of nucleotides. In the presence of AMP-PNP and ADP-VO_4, A122C displays effective CLD formation, that is consistent with the nucleotide bound crystal structures. Interestingly, cross-linking A122C in the presence of MccJ25 led to a small increase in CLD formation, suggesting that the binding of substrate is able to bring the TMDs closer together (Figure 41D/E).

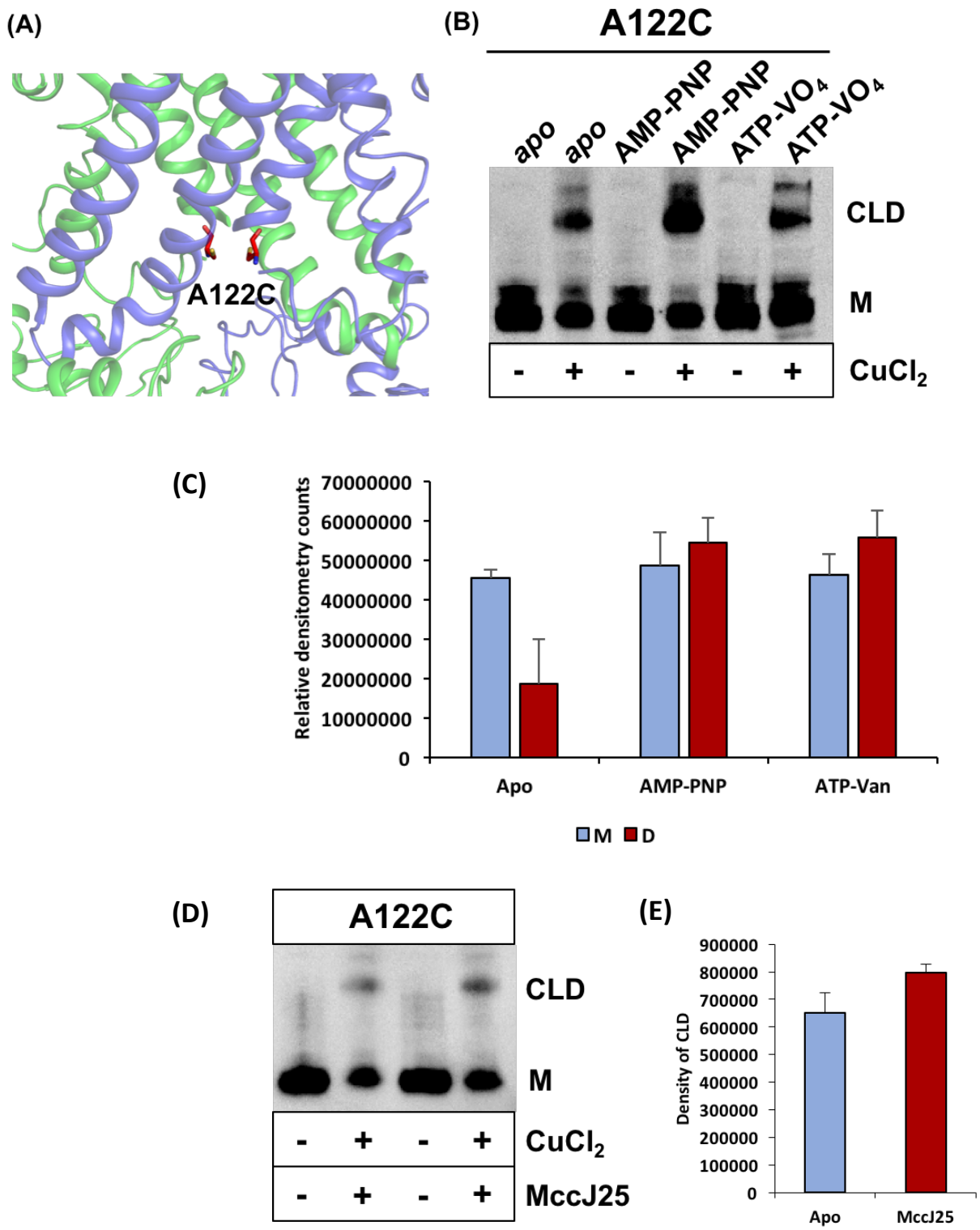


Figure 41. Predictive cysteine cross-linking of the McjD cytoplasmic TMDs. (A) The position of the cysteine mutation (A122C) at the cytoplasmic end of the TMDs is shown in red stick format. A122C-A122C' are separated by 7.9 Å (C_α-C_α) in the McjD *apo* structure (B) Western blot intensities of the cross-linked dimer and monomeric species are shown for *apo* and nucleotide-trapped (AMP-PNP, ATP-VO_4) conditions after cross-linking ISOVs with 2 mM $CuCl_2$. The inward-occluded conformation (McjD *apo*) is verified by formation of CLDs

at the cytoplasmic end of the TMDs (A122C) in the presence of $CuCl_2$. (C) Densitometry analysis of the Western blot showing mean counts of the CLD and monomeric species from three independent cross-linking experiments. Error bars are shown and represent standard deviation of the mean values. (D) Western blot intensities of the CLD and M at the cytoplasmic end of the TMDs (A122C) after addition of 1 mM MccJ25. A small increase of cross-linking in the TMDs is observed upon MccJ25 treatment, indicating that substrate binding brings the TM helices closer together. (E) Densitometry analysis showing mean counts of the CLD from three independent cross-linking experiments. Error bars are depicted as in (C).

In the absence of nucleotides, the NBDs of ABC exporters disengage but there are conflicting reports regarding the extent of NBD separation (Borbat *et al*., 2007; Zou *et al*., 2009). In the McjD *apo* structure there is only a small degree of NBD disengagement relative to the MsbA *apo* structure. To characterise the behavior of the McjD NBDs, the mutation S509C was examined (Figure 42A). In the presence of the oxidising agent $CuCl_2$ with either AMP-PNP or ADP-VO_4, strong CLD formation was observed (Figure 42B/C). This finding is in agreement with the equivalent nucleotide bound McjD crystal structures containing dimerised NBDs. Formation of CLD cross-links was also observed for *apo* S509C in the presence of $CuCl_2$. Strikingly, *apo* S509C could also be cross-linked in the absence of added oxidising agent and even after pre-treatment with the reducing agent DTT. This finding suggests that there is only a small degree of NBD separation in the absence of nucleotides, which is in agreement with the McjD *apo* crystal structure. We cannot exclude the possibility that a large population of the McjD NBDs are still associated with one another in the nucleotide free state. Taken together, the cross-linking data indicate that McjD mostly exists in an occluded conformation with its NBDs closely engaged in the *E. coli* membrane.

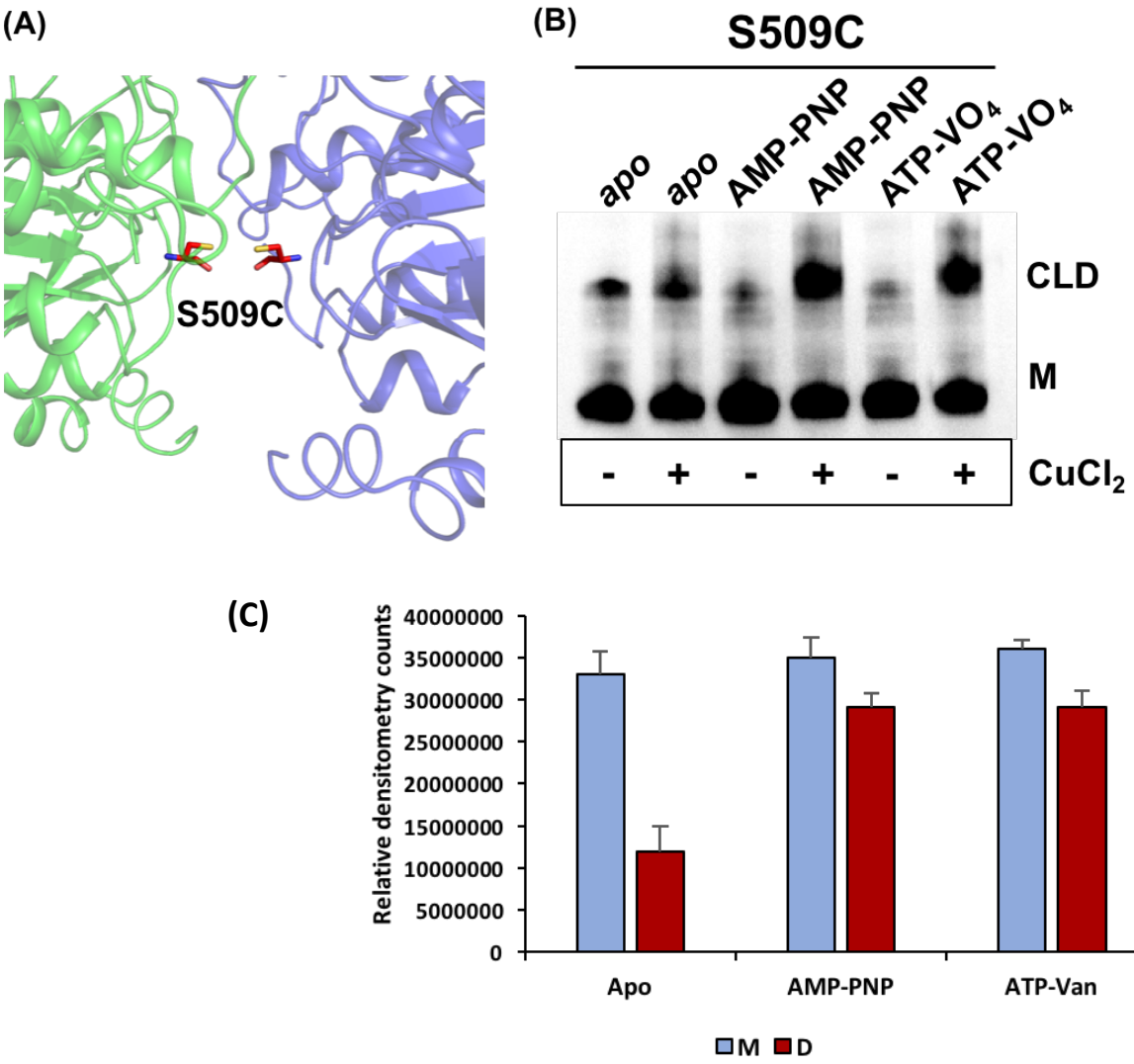


Figure 42. Predictive cysteine cross-linking of the McjD NBDs. (A) Position of cysteine mutation (S509C) at the cytoplasmic end of the TMDs shown in red stick format. S509C-S509C' are separated by 7.9 Å (C_α-C_α) in the McjD *apo* structure. (B) Western blot intensities of the cross-linked dimer and monomeric species are shown for *apo* and nucleotide-trapped (AMP-PNP, ATP-VO_4) conditions after cross-linking ISOVs with 2 mM $CuCl_2$. In the presence or absence of nucleotides, the NBDs (S509C) form CLDs, even in the absence of $CuCl_2$, suggesting a small degree of disengagement. (C) Densitometry analysis of the Western blot.

2.3.6. PEGylation cavity accessibility

Predictive cysteine cross-linking verifies that the *apo* inward-occluded state of McjD is a physiologically relevant conformation in the export cycle. However, in order for MccJ25 to enter the substrate binding site of an ABC transporter *via* the cytoplasm, an open TMD dimer is required for cavity accessibility. Since the McjD *apo* structure contains an occluded TMD interface, the ability of substrates to enter an open TMD was studied. Single cysteine mutations were designed spanning the McjD cavity from the cytoplasmic to the periplasmic sides (N134C, I138C, T298C, I287C) (Figure 43A). A maleimide-modified PEG compound was then applied in order to specifically target the McjD cavity *via* thioether linkages to cysteines (Figure 43B). As the compound is membrane impermeable and can only bind to solvent accessible cysteines, PEGylation of McjD is able to verify ligand binding from the cytoplasm. To facilitate accessibility to PEG molecules, the residues chosen for mutation were highly solvent exposed in order to prevent steric clashes. A high molecular weight PEG maleimide derivative (10 kDa) was selected in order to observe a distinct electrophoretic mobility shift by SDS-PAGE upon interaction with McjD. The long, flexible acyl chains of mPEG-10k are suitable for orientation within the large McjD binding pocket. Prior to PEGylation, the McjD cavity mutant ISOVs were pre-incubated with the relevant nucleotides. The reactions were initiated with the addition of mPEG-10k and quenched by the addition of *N*-ethylmaleimide. The formation of PEGylated species was visualised by SDS-PAGE followed by anti-His Western blot.

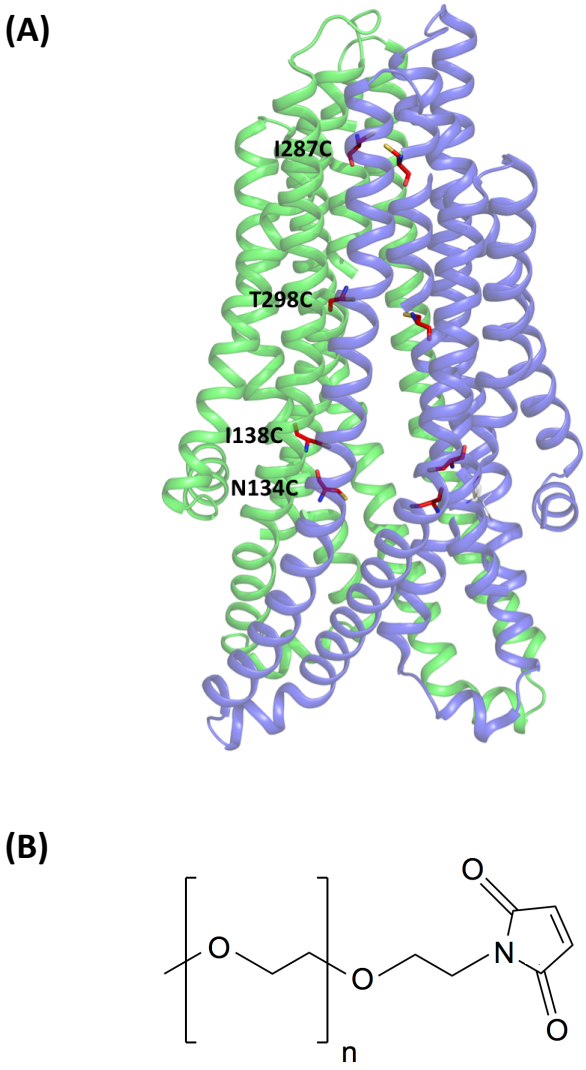


Figure 43. McjD cavity accessibility assay design. (A) Positions of cysteine mutations in the TMDs are depicted in red stick format and span the cytoplasmic to the periplasmic side of the McjD cavity. The NBDs are removed for clarity. (B) The chemical structure of methoxypolyethylene glycol maleimide (M_n = 10,000) is shown. The maleimide group can form thioether linkages to the sulfhydryl groups of cysteines.

Under *apo* conditions at different positions of the McjD cavity, gel shifts were observed corresponding to the PEGylated form of the transporter (Figure 44). This is the first direct evidence that McjD can adopt an inward-open conformation where the TMDs are accessible to substrate binding. The extent of PEGylation is highest towards the cytoplasmic end of the McjD cavity (R134C and I138C). At the periplasmic end of the cavity (T298C and I287C),

McjD is PEGylated under *apo* conditions but at a reduced level. Since the periplasmic ends of the TMDs are in closer proximity to one another, binding of one PEG molecule to one McjD monomer is likely to have reduced the accessibility of a second PEG molecule for the second half of the transporter. The observation of PEGylated species in nucleotide-containing conditions may seem counterintuitive, considering the TMDs are occluded in both the AMP-PNP and ADP-VO_4 bound structures. However, the PEGylated form of the transporter is only detected at minor levels compared to *apo* conditions, suggesting that this species actually corresponds to McjD molecules that were unresponsive to nucleotides. Since there are other ATP-dependent proteins present in ISOVs, it is likely that nucleotides are being 'consumed' by these other proteins, leaving a small population of *apo* McjD molecules that can still undergo PEGylation.

Since *apo* McjD was crystallised at pH 9 but the PEGylation experiments were performed at pH 7.5, we repeated the assay to assess whether the observed inward-opening is pH dependent. The sampling of an inward-open conformation is not affected by pH since PEGylation is similarly effective at pH 9 compared to pH 7.5, suggesting that pH is not a factor in inducing the inward-occluded conformation (Figure 45). The ability of McjD to adopt an inward-open conformation is in agreement with the *apo* structures of homodimeric ABC exporters such as MsbA (Ward *et al*., 2007) and heterodimeric ABC exporters such as TM287-288 (Hohl *et al*., 2014). McjD differs to all other ABC exporters in adopting both inward-open and inward-occluded states under *apo* conditions.

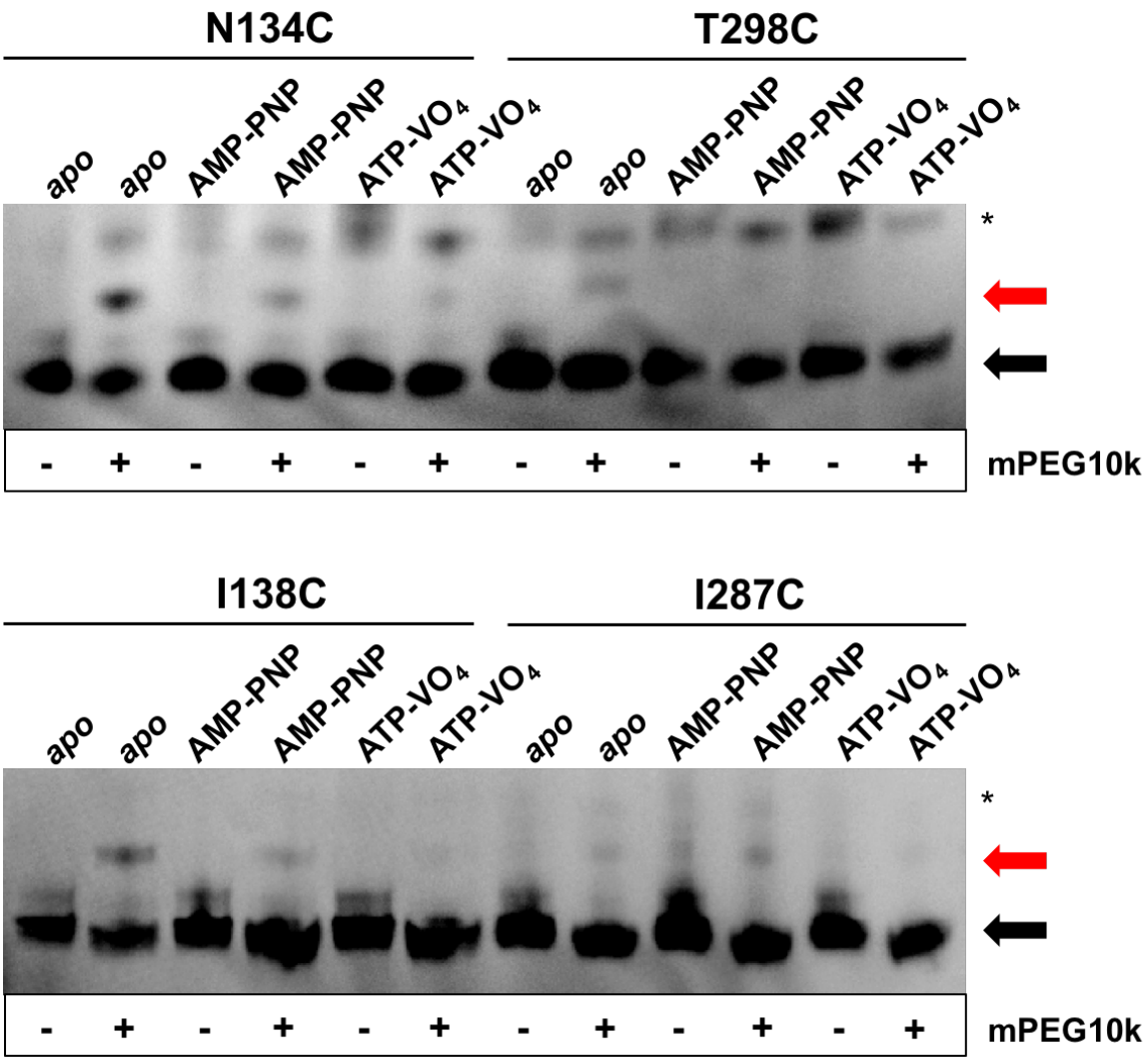


Figure 44. PEGylation of McjD at pH 7.5. Western blot intensities of the PEGylated (red arrow) and non-PEGylated (black arrow) species are shown for McjD cavity mutants in *apo* and nucleotide-trapped (AMP-PNP, ATP-VO_4) conditions after 1 h incubation with 1 mM mPEG-10k. SDS-stable dimers are denoted by the asterisk (*). Formation of a PEGylated species is visible in *apo* conditions for each McjD cavity mutant. PEGylation of the transporter verifies that McjD can adopt an inward-open conformation. In the presence of nucleotides, a degree of PEGylation can also be observed but this is probably due to the incomplete inhibition of McjD.

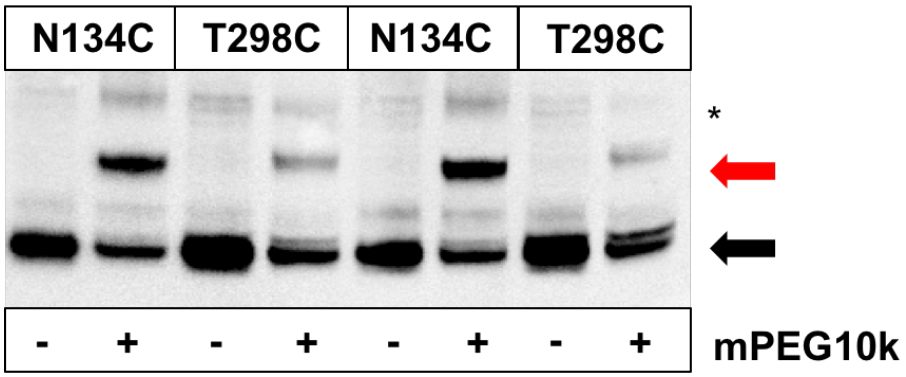


Figure 45. PEGylation of McjD at pH 9.0. Western blot intensities of the PEGylated (red arrow) and non-PEGylated (black arrow) species are shown for the McjD mutants N134C and T298C. The McjD ISOVs were treated with 1 mM mPEG-10k for 1 h. SDS-stable dimers are denoted by the asterisk (*). The level of PEGylation at pH 9.0 was similarly effective to pH 7.5, suggesting that pH does not induce the inward-open conformation.

The existing evidence for MccJ25 recognition by McjD comes from ligand-stimulated ATPase assays (Choudhury *et al*., 2014), and ligand binding studies by non-denaturing mass spectrometry (Mehmood *et al*., 2016) and microscale thermophoresis (MST) (Choudhury *et al*., 2014). While these studies have resolved the interaction between the substrate and transporter, they do not explain how MccJ25 can enter the McjD cavity. While the majority of ligands access the TMDs of ABC exporters from the cytoplasm, certain ligands have been shown to enter *via* a lateral opening in the membrane (*e.g.* LLOs in PglK) (Perez *et al*., 2015).

In order to test whether MccJ25 can enter *via* an inward-open McjD as opposed to a lateral entrance in the lipid bilayer, competition assays were performed by pre-incubating the McjD cavity mutants with 1 mM MccJ25 followed by the addition of 1 mM mPEG-10k and MccJ25 (Figure 46A). At the bottom of the TMDs (R134C), a small decrease in PEGylation was observed, suggesting that binding of MccJ25 to the cytoplasmic side of the McjD cavity is able to reduce accessibility to PEG molecules. Moving deeper in the McjD cavity towards the periplasmic side of the TMDs (I138C), MccJ25 outcompetes PEG more strongly for binding.

At the top of the TMDs (T298C), MccJ25 completely abolishes cavity accessibility to PEG molecules as demonstrated by densitometry analysis (Figure 46B). These competition data indicate that MccJ25 enters an inward-open McjD from the aqueous cytoplasmic side of the transporter rather than a lateral opening in the membrane. If MccJ25 were to enter the cavity from the membrane, mPEG-10k should not have been able to modify the cavity mutants since it is not membrane permeable and can only modify solvent accessible cysteines.

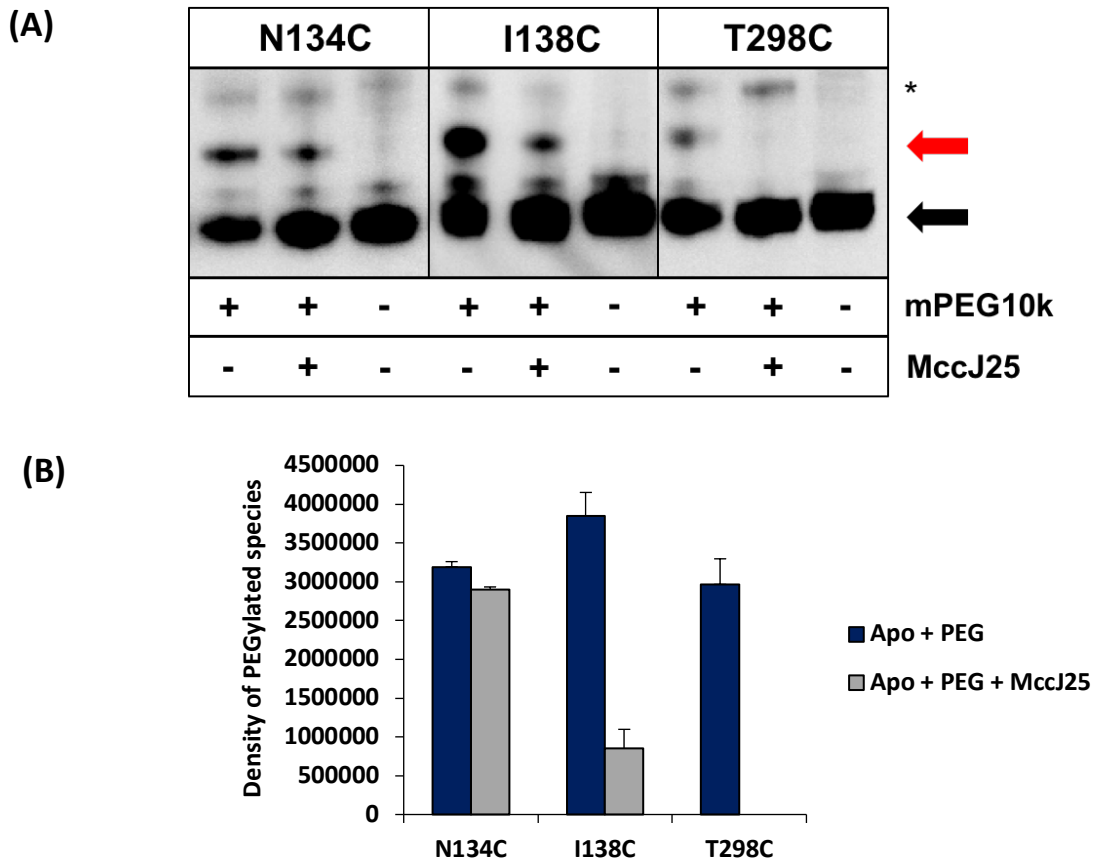


Figure 46. Competition PEGylation assay with MccJ25. (A) McjD cavity mutant ISOVs were incubated with 1 mM mPEG-10K and 1 mM MccJ25 for 1 h. Western blot intensities of the PEGylated and non-PEGylated species are shown for McjD mutants in *apo* conditions. In the presence of MccJ25, the extent of PEGylation is reduced towards the periplasmic side of the McjD cavity. (B) Densitometry analysis was performed by measuring the intensity of PEGylated species in the presence and absence of MccJ25. Error bars are shown (mean ± standard deviation; n = 3).

2.3.7. PELDOR measurements

Since both the structural and cross-linking data for McjD suggest the transporter exists in mostly occluded conformations along the transport cycle, spin-labelled McjD mutants were prepared for PELDOR analysis. The advantages of analysing McjD by PELDOR over crystallisation are as follows. First, measurements can be performed in a lipid-like environment as opposed to detergent micelles. Second, distance changes can be deduced in solution and in the absence of artificial crystal contacts. Unlike cross-linking, which monitors the sampling of conformational states, PELDOR can determine their relative distributions and provide a quantitative assessment of distance changes at a defined position.

To facilitate attachment of spin labels, single cysteine mutations were designed at the periplasmic end of the TMDs (L52C) and in the NBDs (C547) in order to monitor distance changes at both sides of the transporter (Figure 47). The TMD position L52C is ideally suited to probing by PELDOR since it is located in a soluble loop region connecting TMs 1 and 2. Such a position is regarded as a trade-off between sufficient accessibility for the spin label and rigidity of the protein backbone. Attempts to produce a cytoplasmic TMD mutant were unsuccessful as McjD could not tolerate the introduction of cysteines in this region.

During purification of L52C and C547, McjD was spin-labelled at the cysteine sites prior to the gel filtration step. Monodisperse size exclusion profiles were generated for both PELDOR mutants (Figure 48A) and SDS-PAGE analysis indicated a high level of purity (Figure 48B). To confirm that the mutants had retained their activity after spin labelling, labelled L52C and C547 in detergent were characterised by ATPase measurements. The basal and MccJ25-stimulated ATPase activity of labelled L52C and C547 in detergent were comparable to the rates determined for unlabelled wild-type protein (Figure 48C). This indicates that neither the introduction of cysteines, nor the presence of spin labels altered the activity of the mutants.

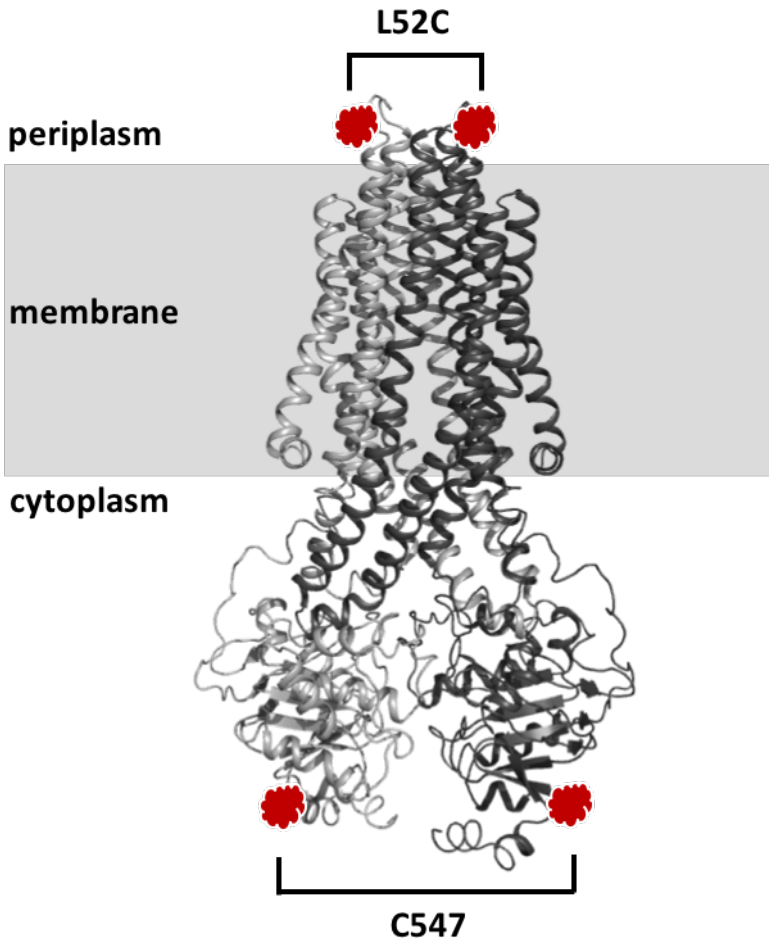


Figure 47. Positions of McjD mutations for the attachment of spin labels. The McjD monomers are coloured light grey and dark grey. The spin labels are coloured red. Cysteine mutations spanning the periplasmic end of the TMDs (L52C) and the NBDs (C547) were designed for the attachment of spin labels.

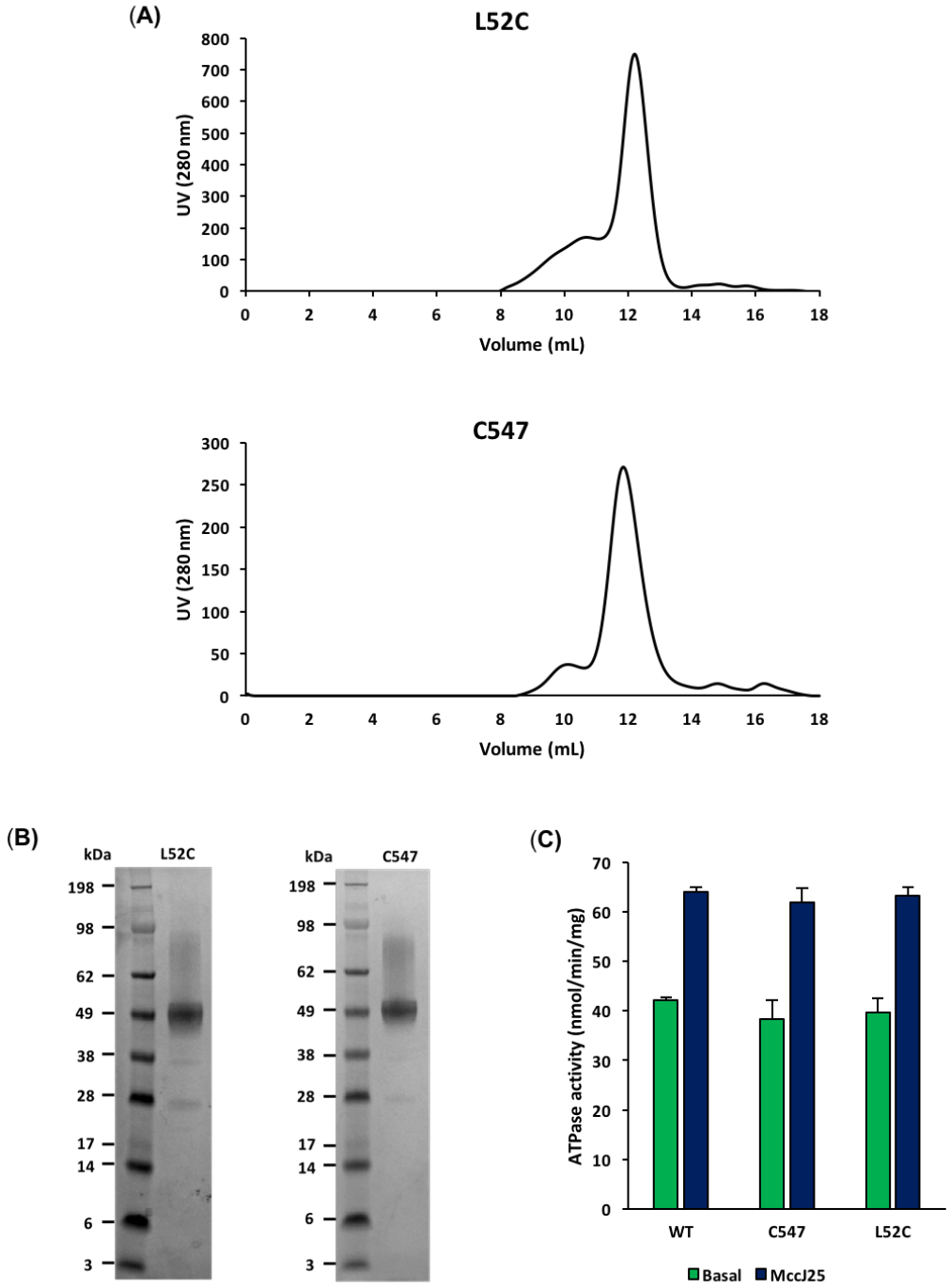


Figure 48. Characterisation of McjD-L52C and McjD-C547. (A) Gel filtration profiles for McjD-L52C and McjD-C547 demonstrating monodisperse peaks at 12 mL. The small shoulder peak observed at ~10 mL corresponds to a different oligomeric form of McjD. (B) SDS-PAGE shows that the McjD mutants display a high level of purity. (C) ATPase assay demonstrating that detergent-purified, spin-labelled McjD mutants show comparable ATPase activities to unlabelled wild-type protein. Error bars were calculated from two independent reconstitution experiments (mean ± standard deviation).

PELDOR measurements and analysis were all performed by Dr Gregor Hagelueken (University of Bonn). Under *apo* conditions, the L52C mutant produced a sharp interatomic distance peak at 28 Å and a broad range of distance distributions in the range between 40 and 60 Å (Figure 49A/B). The peak at 28 Å is in close agreement with the expected L52C-L52C' separation predicted by the McjD *apo* structure when taking into account the presence of the spin labels. In the presence of AMP-PNP and ADP-VO_4, the distance distributions were comparable to *apo* conditions, which is in agreement with the nucleotide bound crystal structures containing occluded TMDs. PELDOR measurements were also performed for L52C in the presence of ATP and MccJ25 to test whether an outward-open conformation could be detected. However, once again the distance distributions showed no change from *apo* conditions, indicating no opening up at the periplasmic end of the TMDs (Figure 49A/B). One possible explanation is that since PELDOR is only able to trap stable, highly populated states, and therefore if the outward-open state of McjD were short-lived, its existence could not be captured using this technique.

In order to test conformational changes in the NBDs, PELDOR measurements were also performed for the C547 mutant under *apo* conditions and in the presence of AMP-PNP (Figure 49A). However, no clear oscillations were observed in bicelles, indicating that the NBDs are highly dynamic at this position. The inability to record distance distributions suggests the NBDs adopt a range of different conformations in the presence and absence of nucleotides.

(A)

Condition (L52C)	Crystal structure (Å)	MtssLWizard (Å)	PELDOR (Å)
apo	12	28	28
AMP-PNP	12	26	28
ATP + VO_4^{3-}	12	26	28
ATP + MccJ25	n.d	n.d	28
Condition (C547)	**Crystal structure (Å)**	**MtssLWizard (Å)**	**PELDOR (Å)**
apo	48	62	n.d.
AMP-PNP	45	56	n.d.

(B)

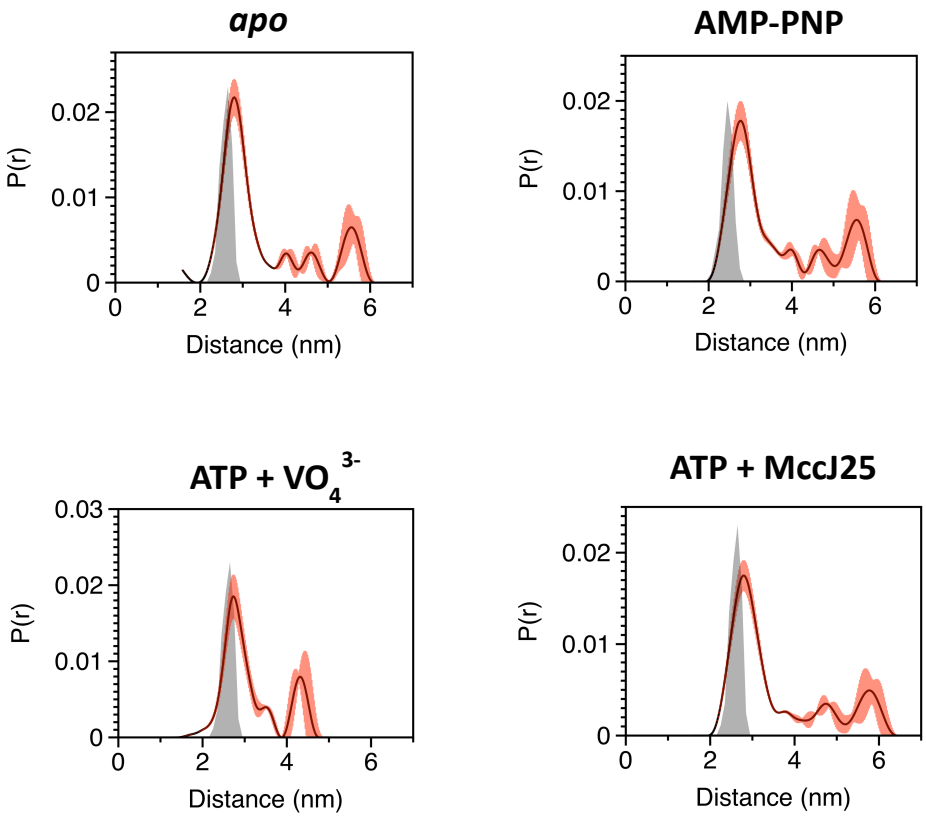


Figure 49. PELDOR analysis of McjD. (A) Table showing the calculated PELDOR distances for spin-labelled McjD-L52C in bicelles. Predicted values between the two spin-labelled positions obtained using the MtssL Wizard (Hagelueken *et al*., 2012) correlate well with the measured distances and crystal structures. PELDOR distance distributions could not be determined for McjD-C547. (B) PELDOR time traces for spin-labelled McjD-L52C in different conditions. The MtssL Wizard distance distributions are indicated by the grey shades, with error bars as calculated by DeerAnalysis2016 shown in red. In each condition, the L52C-L52C' separation was derived from the sharp interatomic distance peak observed at ~2.8 nm.

2.3.8. Fluorescence transport assays

Since a stable outward-open state could not be detected by EPR spectroscopy, we proposed that the outward-open state may only exist transiently along the transport cycle. To validate this assertion, a transport assay was performed where the McjD transport activity was tested in the presence of the fluorescent dye Hoechst 33342 (Hoechst) and MccJ25. Previously, it was demonstrated that McjD can mediate Hoechst uptake into proteoliposomes and that the ATPase activity of McjD can be stimulated by the dye at similar rates to MccJ25 (Choudhury *et al*., 2014). The transport activity of MccJ25 could not be measured directly because a radiolabelled peptide was not available for this study. In addition, a fluorescently labelled MccJ25 peptide could not be used for transport assays since it has been shown to interact non-specifically with empty liposomes.

In order to assess whether McjD can transport MccJ25 in liposomes, a competition assay was performed to determine whether Hoechst uptake can be affected by addition of the substrate MccJ25 (Figure 50). In the presence of Hoechst without ATP, the level of fluorescence remained stable indicating no uptake of the dye into liposomes. In the presence of Hoechst and ATP, there was a decrease in the level of fluorescence, indicating that Hoechst uptake into liposomes led to a quenching of the fluorescent signal. In the presence of Hoechst and a 1:1 molar ratio of MccJ25, the fluorescence returned to a stable level, indicating that MccJ25 is able to outcompete Hoechst for the McjD cavity and subsequent uptake into liposomes.

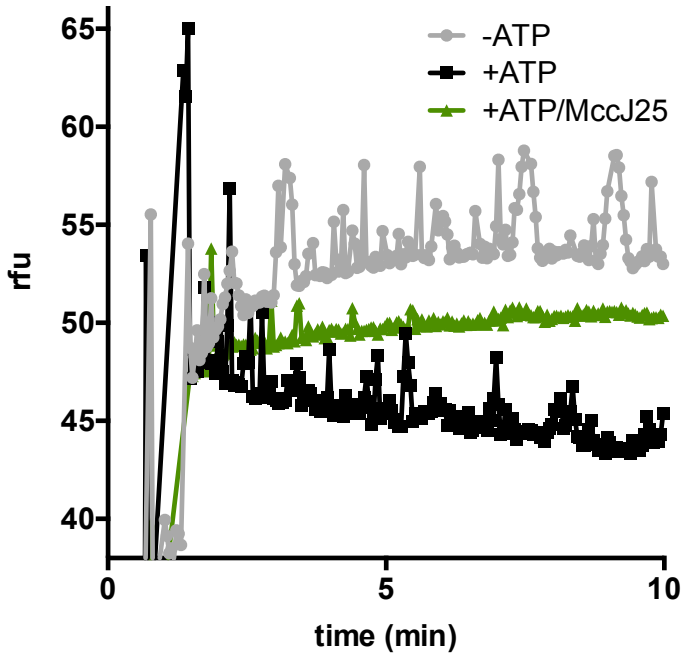


Figure 50. Competition transport assay with MccJ25. Wild-type McjD was incorporated into liposomes and its transport activity was monitored in the presence of 3 mM Hoechst 3342. The relative fluorescence units (rfu) recorded for each reaction condition are shown against time. In the absence of ATP, the level of fluorescence remains stable (grey line), indicating no Hoechst uptake in liposomes. McjD can only transport Hoechst in the presence of ATP (black line) as shown by the decrease in fluorescence. In the presence of an equimolar ratio of ATP and MccJ25, the peptide is able to outcompete Hoechst for McjD uptake, causing the fluorescent signal to return to a stable level (green line).

In order to verify whether the transport activity being observed is due to the McjD TMDs opening up in a manner similar to the MsbA-ADP-VO_4 structure (Ward *et al*., 2007), the assay was repeated with McjD containing a cysteine mutation at the periplasmic end of the TMDs (L53C) (Figure 51A). Previously, it was demonstrated that McjD could be cross-linked at position L53C with high efficiency in the presence of the oxidising agent $CuCl_2$. The Hoechst transport activity for McjD-L53C with no added cross-linking agent showed comparable behavior to wild-type protein. In the presence of ATP, the fluorescence remained stable indicating no Hoechst uptake whereas in the presence of ATP, the decrease in fluorescence reflects Hoechst transport into liposomes. Notably, in the presence of ATP and the oxidising agent $CuCl_2$, the cross-linked McjD-L53C was able to block Hoechst uptake into liposomes, suggesting that disulphide locking of the periplasmic side of the TMDs is detrimental to transport activity. The schematic diagram shown in Figure 61B demonstrates how cross-linking the transporter in liposomes inhibits McjD-dependent quenching of Hoechst.

It was then demonstrated that addition of DTT after 10 min is able to reduce the L53C disulphide bond, causing the TMDs to open up at the periplasmic side and resulting in the restoration of transport activity (Figure 51C). To confirm liposomes containing incorporated L53C were effectively cross-linked in the presence of $CuCl_2$, cross-linked and non-cross-linked samples were analysed by SDS-PAGE (Figure 52). In the presence of $CuCl_2$, L53C is only observed as a dimeric species. Moreover, after treatment of the liposomes with CPM dye, which can only bind to free cysteines, the oxidised L53C sample displayed almost no fluorescence, suggesting the near complete formation of disulphide bonds. In summary, these data provide the first evidence that McjD can sample a transient outward-open state along the transport cycle.

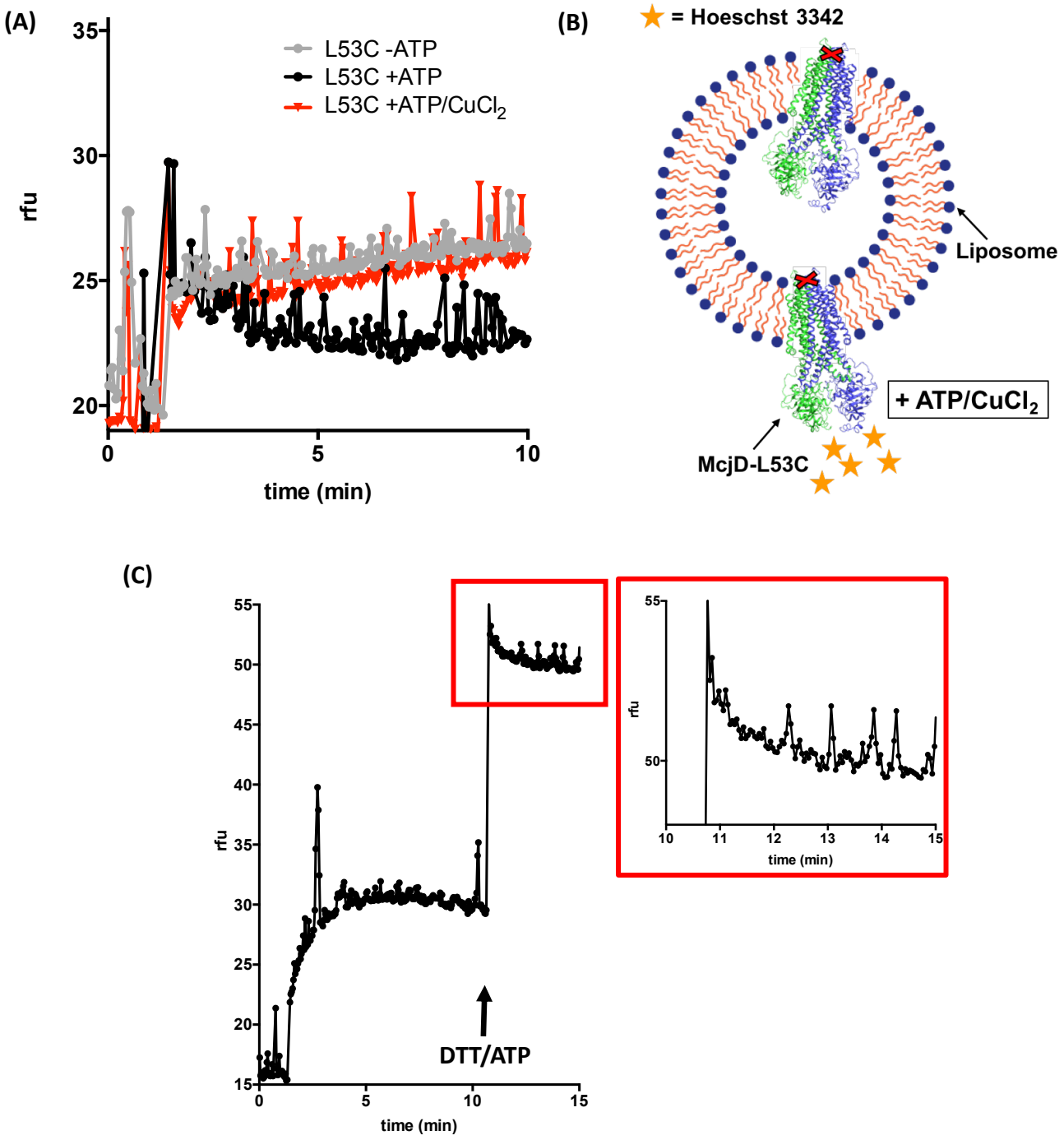


Figure 51. McjD-L53C transport assay. (A) Cross-linking McjD-L53C abolishes Hoeschst transport in the presence of ATP (red line) by blocking opening of the TMDs at the periplasmic side. In the absence of $CuCl_2$, McjD uptake is still possible as reflected by the decrease in fluorescence (black line). (B) The schematic of cross-linked McjD-L53C in liposomes after treatment with $CuCl_2$ shows that Hoechst (yellow stars) cannot be transported into liposomes even in the presence of ATP. (C) The addition of DTT in the presence of ATP (black arrow) at 10 min reduces the L53C-L53C' disulphide bond, resulting in opening of the TMDs and restoration of transport activity. The red box is a magnification of the decrease in fluorescence observed upon addition of DTT/ATP.

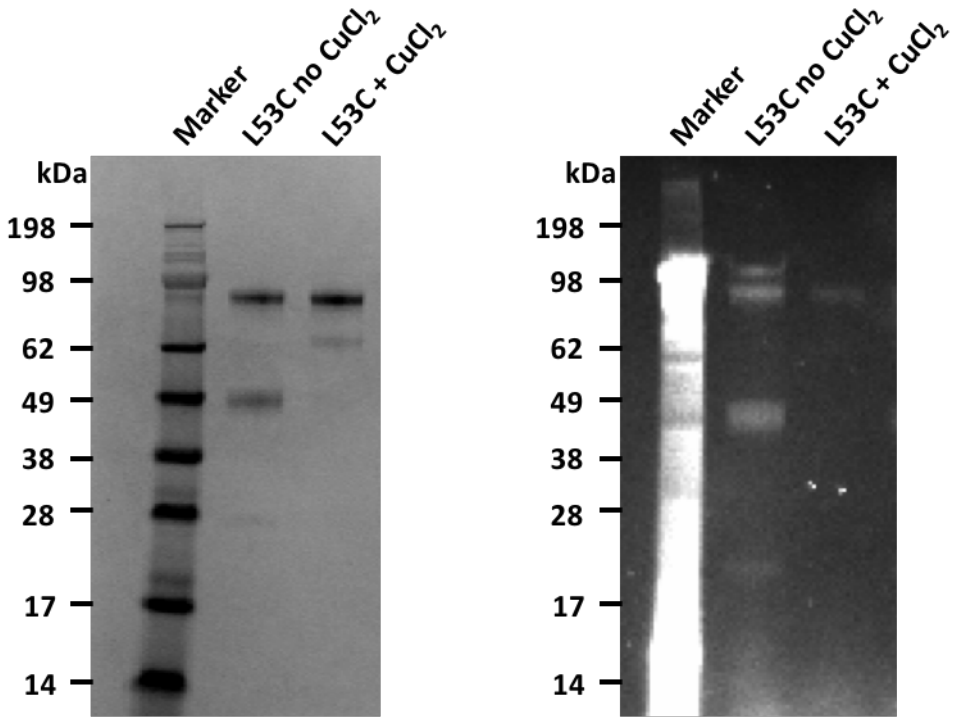


Figure 52. SDS-PAGE to show efficiency of McjD-L53C cross-linking. SDS-PAGE analysis of non-cross-linked and cross-linked McjD-L53C. In the left panel, the Coomassie stained gel shows a combination of monomeric and SDS-stable dimeric McjD-L53C (lane 1) in the absence of $CuCl_2$. In the presence of $CuCl_2$, a predominant dimeric species is observed for cross-linked L53C (lane 2). In the right panel, the same lanes have been imaged after treatment with CPM dye which becomes fluorescent upon binding to free cysteines. The strong fluorescent signal in lane 1 corresponds to non-cross-linked McjD-L53C whereas the loss of fluorescence in the presence of $CuCl_2$ (lane 2) indicates formation of CLDs. A small amount of material in lane 2 was not cross-linked since a residual fluorescent signal can still be observed at ~98 kDa.

2.4. Discussion

2.4.1. McjD ADP-VO_4 structure defines a new intermediate state

To date, structural characterisation of McjD has been limited to a single snapshot of the transporter, thus restricting our understanding of the MccJ25 efflux mechanism. In this work, structure determination of McjD-ADP-VO_4 captures the transporter at a new step of the export cycle. The structure represents an intermediate conformation between the ATP-bound and nucleotide free states, and demonstrates limited conformational changes compared to McjD-AMP-PNP (Choudhury *et al*., 2014). Taken together, the nucleotide bound McjD structures suggest that McjD cannot switch to the outward-open state in the presence of ATP alone.

The McjD-ADP-VO_4 structure containing occluded TMDs is strikingly different to MsbA-ADP-VO_4 which has a clear opening of the TMDs to the periplasmic side (Ward *et al*., 2007). The McjD structure also differs from the type I ABC importer $MalFGK_2$ captured in an ADP-VO_4 bound outward-open conformation (Oldham and Chen, 2011a). Structure solution of McjD-ADP-VO_4 was facilitated by a long wavelength beamline experiment, resulting in accurate phasing from the vanadium atom, and confirming the presence of VO_4^{3-} in the NBDs (Wagner *et al*., 2016). This method provides a rationale for solving other membrane protein structures in the vanadate-inhibited state and can be applied to a variety of primary transporters (*e.g.* ABC transporters, P-type ATPases) (Clausen *et al*., 2016).

2.4.2. The McjD TMDs are predominantly occluded

Although structures of peptide ABC exporters have previously been determined in nucleotide bound occluded states, the equivalent conformation has not been observed in the absence of

nucleotides (Choudhury *et al*., 2014; Lin *et al*., 2015; Morgan *et al*., 2017). The structure of *apo* McjD defines the first example of a peptide ABC exporter containing occluded TMDs in the nucleotide free state. This is in contrast to the type IV peptide ABC transporter PCAT, that adopts an inward-open state under *apo* conditions (Lin *et al*., 2015). In order to verify the prevalence of the occluded state, McjD was shown to form effective cross-links at both sides of the TMDs in the presence and absence of nucleotides. Furthermore, our PELDOR data support the notion that the occluded conformation is a stable feature of the McjD cavity.

2.4.3. MccJ25 enters the McjD TMDs from the cytoplasm

To demonstrate how MccJ25 enters the TMDs, PEGylation of the McjD cavity demonstrated that substrate binding occurs via a cytoplasmic opening, rather than a lateral opening in the membrane. The occluded TMDs of McjD therefore must revert to an inward-open state to facilitate MccJ25 entry in the binding pocket. Taken together, these data suggest that the inward-open and inward-occluded states exist in equilibrium, but under crystallisation conditions, the latter conformation is favoured. Our cross-linking data indicate that MccJ25 binding enhances closure of the TMDs, a finding consistent with substrate-induced changes in the MsbA TMDs (Doshi and van Veen, 2013).

2.4.4. McjD can adopt a transient outward-open state

PELDOR measurements at the periplasmic side of the TMDs are unable to detect a stable outward-open conformation of McjD, even in the presence of ATP and MccJ25. However, our transport data indicate that that the TMDs open up at the periplasmic side when both ATP and substrate are present. The stable occluded cavity of McjD can therefore open up to release

bound substrates via a transient outward-open state. Since the short lifetime of the outward-open state cannot be trapped directly by PELDOR, smFRET may be better suited to monitoring this opening. Interestingly, molecular dynamics (MD) simulations of McjD have indicated that small conformational changes at the periplasmic TMDs (between 14 Å and 20 Å) are required to release MccJ25 (Gu *et al*., 2015; Bountra *et al*., 2017). McjD distinguishes itself from homodimeric ABC exporters that require ATP binding to switch to the outward-open state and heterodimeric ABC exporters that require ATP hydrolysis for this transition (Mishra *et al*., 2014). Peptide ABC exporters such as PCAT may also adopt a transient outward-open state similar to McjD that is reset to an inward-open state after ATP hydrolysis (Lin *et al*., 2015).

2.4.5. The *apo* McjD NBDs are closely separated

The observation that the *apo* McjD NBDs can be cross-linked even in the absence of a cross-linking agent, suggests that the NBD monomers sample a conformation where they are closely separated in the nucleotide free state. The cross-linking data are consistent with the crystal structure of *apo* McjD, which indicates that the NBDs require small domain movements to form a closed NBD dimer upon ATP binding. McjD therefore differs to other type IV ABC transporters such as MsbA (Ward *et al*., 2007) and P-glycoprotein (Aller *et al*., 2009; Jin *et al*., 2012) that display wide open NBDs in the absence of nucleotides. Interestingly, the conformation of the *apo* McjD NBDs resembles type V-VI ABC transporters such as Wzm-Wzt (Bi *et al*., 2018) and $LptB_2FG$ (Luo *et al*., 2017; Dong *et al*., 2017) that maintain their NBDs in closer contact. Although accurate NBD distance distributions could not be obtained for McjD by PELDOR, this can be explained by the dynamic nature of the labelling position (C547). Since the McjD NBDs are likely to display conformational flexibility, distance changes in a native-like environment may be more amenable to smFRET (Husada *et al*., 2015).

2.4.6. MccJ25 export cycle

The combination of structural and biochemical work performed in this study enable us to propose a detailed model for translocation by the ABC exporter McjD (Figure 53). The transport model for McjD is a variation on the alternating access mechanism that reflects the nature of the transported substrate. In the presence of ATP alone, nucleotide binding to an inward-facing McjD facilitates transition to the outward-occluded state where the NBDs close and dimerise (AMP-PNP bound structure). McjD then undergoes a futile ATP hydrolysis cycle via a high energy transition intermediate (ADP-VO_4 bound structure) which resets the transporter back to an inward-facing conformation.

In the presence of MccJ25, peptide can enter the cavity via an inward-open McjD. In the *apo* state, McjD can also exist in an inward-occluded conformation (*apo* structure) where the TMDs are inaccessible from the cytoplasm. MccJ25 binding to an inward-open McjD enhances occlusion of the TMDs and is proceeded by ATP binding to the NBDs (substrate-bound outward-occluded state). McjD can then adopt a transient outward-open conformation which permits the release of MccJ25 to the periplasmic side of the membrane. After MccJ25 has left the outward-open cavity, TMs 1 and 2 rotate away from TMs 3-6 of the opposite monomer to restore the outward-occluded state (AMP-PNP bound structure) without inter-subunit twining. ATP hydrolysis (ADP-VO_4 bound structure) and dissociation of nucleotide. This in turn disrupts the NBD dimer interface and induces intertwining of TMs 1-3 and 6 from one monomer with TMs 4 and 5 from the opposite monomer. At the end of the export cycle, McjD is free again to bind a new MccJ25 molecule.

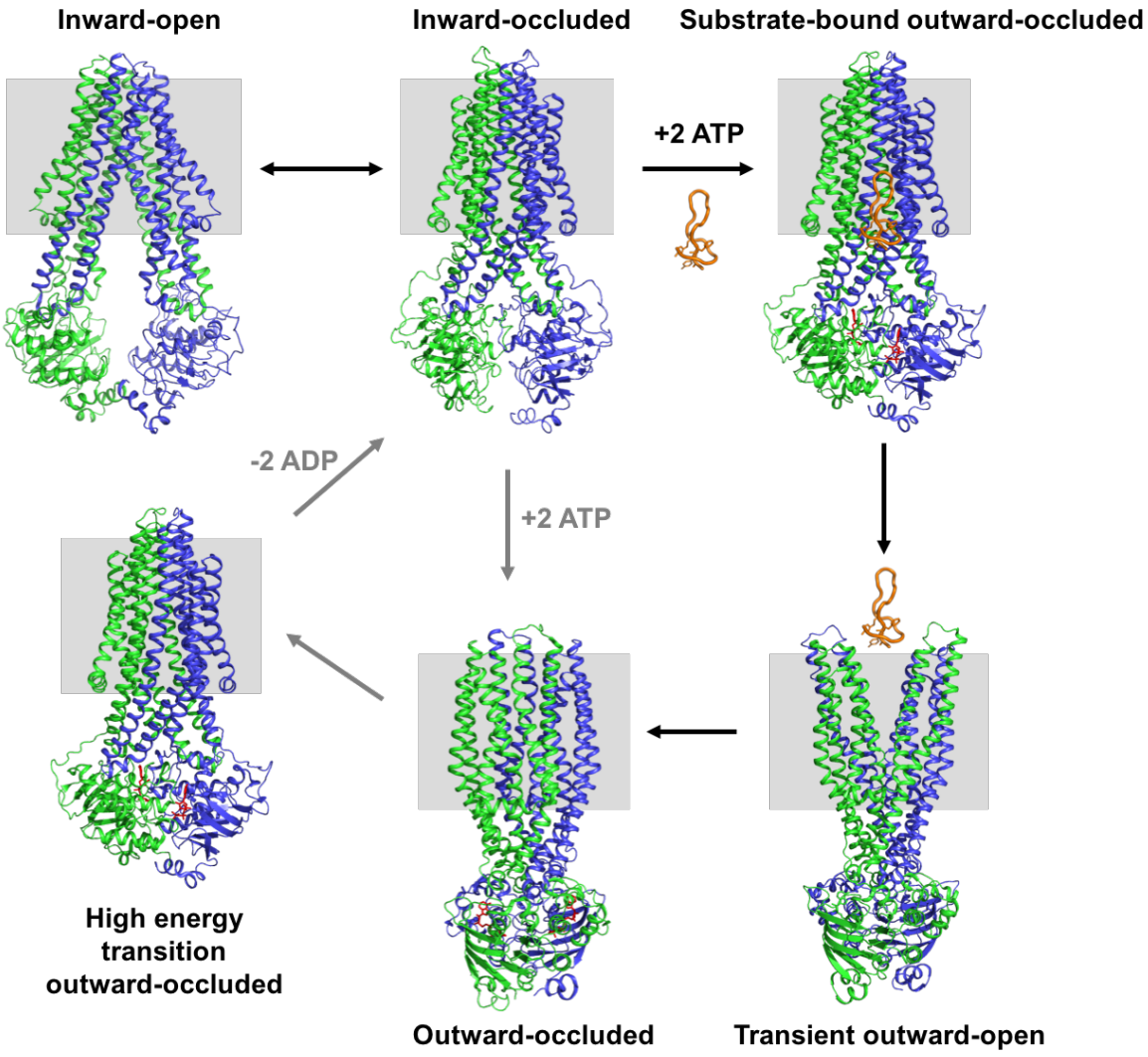


Figure 53. Mechanism of antibacterial peptide export by McjD. The inward-open (PDB: 3B5X) and outward-open (PDB: 3B60) states shown are derived from structures of MsbA. The inward-facing conformation of McjD can either be open to the cytoplasm or occluded at the TMDs. In the absence of MccJ25, McjD can undergo a futile ATP hydrolysis cycle (grey arrows) where the TMDs remain occluded. In the presence of MccJ25, the peptide enters the cavity via an inward-open McjD. Two molecules of ATP then bind to the nucleotide-binding domains causing them to dimerise. This facilitates transition to the substrate-bound outward-occluded conformation where the transporter is sealed at both ends of the membrane. Rearrangements in the TMDs induce a transient outward-open state characterised by MccJ25 release into the periplasm. McjD then returns to an outward-occluded conformation, which is followed by ATP hydrolysis via the high energy transition state intermediate. The release of nucleotide from the NBDs switches the transporter back to an inward-facing conformation.

2.4.7. Mechanism for antibacterial peptide self-immunity

Unlike other ABC exporters, which undergo large conformational changes along the export cycle, McjD exists in a mainly occluded conformation with subtle rearrangements in the NBDs and TMDs promoting the binding and release of MccJ25. The existence of McjD in an occluded conformation acts as firstly, a shielding mechanism to prevent re-uptake of exported MccJ25 and secondly as a mechanism to prime McjD, during MccJ25 biosynthesis, without building up toxic levels of the peptide. The release of MccJ25 by a transient opening of the cavity occurs without large-amplitude motions of the periplasmic TMD gate, thus minimising exposure of the TMDs to the periplasmic side. If McjD were to adopt a stable outward-open state similar to MsbA, the transporter would be vulnerable to substrate re-entry. As such, the transport model proposed for McjD provides MccJ25 producer cells with self-immunity to the peptide.

Interestingly, the type IV peptide ABC transporter TmrAB, a functional homologue of the TAP transporter, has recently been shown to adopt an occluded conformation similar to that of McjD (Barth *et al*., 2018). TAP can be trans-inhibited by high external peptide concentrations to protect the ER from stress due to the unfolded protein response (Grossman *et al*., 2014). Under transporting conditions, the occluded TmrAB represents a transient intermediate before switching to the outward-facing state for peptide release. However, trans-inhibition results in TmrAB reverting back to the occluded conformation to prevent high levels of peptide build-up (Barth *et al*., 2018). In light of these findings for TmrAB, peptide ABC transporters appear to have evolved a common mechanism to maintain self-immunity to toxic transport substrates.

Chapter 3: Single-molecule FRET of McjD

The work presented in this chapter is published in:

Husada, F[#]., **Bountra, K**[#]., Tassis, K., de Boer, M., Romano, M., Rebuffat, S., Beis, K. & Cordes, T. 2018. Conformational dynamics of the ABC transporter Mcjd seen by single-molecule FRET. *The EMBO Journal*, **37**, E100056.

[#] these authors contributed equally

3.1. Introduction

3.1.1. Application of smFRET to McjD

Single-molecule FRET has recently emerged as a novel tool to probe the conformational dynamics of ABC transporters (section 1.1.11) (Goudsmits *et al*., 2017; Yang *et al*., 2018; Liu *et al*., 2018). The advantage of smFRET over techniques such as PELDOR is that it allows individual molecules to be tracked one at a time rather than as ensemble populations (Husada *et al*., 2015). Given that ABC transporters display a wide range of conformational states, understanding their interconversion dynamics is critical to unravelling their complex transport cycles. However, to date, smFRET studies of complete ABC transporters have been restricted to the type II importer BtuCD (Goudsmits *et al*., 2017; Yang *et al*., 2018) and the archetypal type IV multidrug ABC transporter MsbA (Liu *et al*., 2018). The aim of this chapter is to provide a detailed smFRET investigation into McjD, the first example of a peptide ABC transporter analysed by this method, and to demonstrate how the architecture of McjD enables it to perform this specialised function.

In chapter 2, PELDOR measurements were carried out for McjD to monitor conformational changes in both the NBDs and TMDs (section 2.3.7). However, the results from this study were unable to validate certain aspects of the McjD transport mechanism. Specifically, the absence of clear distance distributions in the NBDs meant that conformational changes could not be accurately defined for McjD in bicelles. While cross-linking experiments and structural data support the notion of small distance changes in the McjD NBDs, such methods are unable to detect transitions between the disengaged (*apo*) and dimerised (ATP-bound) forms. In contrast, smFRET offers the resolution and sensitivity required to capture transitions in the McjD NBDs at each stage of the ATP hydrolysis cycle. We aim to apply smFRET to characterise these states

further and determine whether the NBDs display conformational dynamics in the presence and absence of nucleotides. Another advantage of smFRET is that measurements can be applied in both detergent solution and liposomes. Since specific classes of lipid provide structural stability to McjD and regulate its activity (section 1.2.9) (Mehmood *et al*., 2016), the extent to which conformational changes can be correlated in these environments will be investigated in parallel.

While PELDOR measurements in the McjD TMDs were able to define distance distributions at the periplasmic side, these data are consistent with an occluded TMD dimer that does not transition to a stable outward-open state, even in the presence of ATP and MccJ25. We have concluded that this conformation is not sufficiently populated or long-lived to be captured by the PELDOR technique, and is therefore likely to be sampled transiently along the transport cycle. In order to visualise opening of the McjD TMDs, smFRET will be performed to provide direct evidence for the transient outward-open state. The ability to trap this state by smFRET will help to validate the unconventional model proposed for MccJ25 export (section 2.4.6). A key mechanistic question to be answered is how substrate binding to the McjD TMDs is linked to the activities of ATP binding and hydrolysis in the NBDs. Using smFRET, we aim to determine whether the McjD TMDs display conformational dynamics, with the purpose of understanding how tightly coupled they are to the NBDs.

3.2. Materials and Methods

3.2.1. Design of smFRET mutants

A significant challenge in smFRET of membrane proteins is the design and production of suitable mutants. Due to the homodimeric nature of McjD, introduction of a single cysteine mutation permits maleimide-derived fluorophore labelling of the transporter at two equivalent positions. To examine conformational changes at both sides of the transporter, the McjD PELDOR mutants L52C (TMDs) and C547 (NBDs) were first investigated by smFRET (Figure 54). Position C547 was selected since the *apo* C_α-C_α distance between the two cysteines (4.8 nm) lies in the optimal region of the Förster range. In the nucleotide bound structures of McjD, at position C547, the NBDs move closer together resulting in a smaller C_a-C_a separation (4.5 nm) that can be distinguished by changes in the FRET efficiency. However, at position L52C in the TMDs, the *apo* C_α-C_α distance (1.2 nm) between the two cysteines lies outside the Förster range. Preliminary smFRET data for L52C verified that this position was not suitable to monitor conformational changes in the TMDs (section 3.3.5).

Since the McjD PELDOR mutant L52C was not amenable to smFRET, two new TMD mutations were designed containing longer C_α-C_α distances separated by 2.6 nm (Y64C) and 2.9 nm (L67C) in the *apo* McjD structure (Figure 54). In the nucleotide bound McjD structures, the distance between the labelling positions is identical since no conformational changes are observed in the TMDs. Y64C and L67C are both located in TM1 which has been proposed to shift towards the opposite McjD TMD as the transporter opens up at the periplasmic side (Choudhury *et al*., 2014; Bountra *et al*., 2018). Therefore, positions Y64C and L67C both report conformational changes in the McjD TMDs that give rise to the outward-open state.

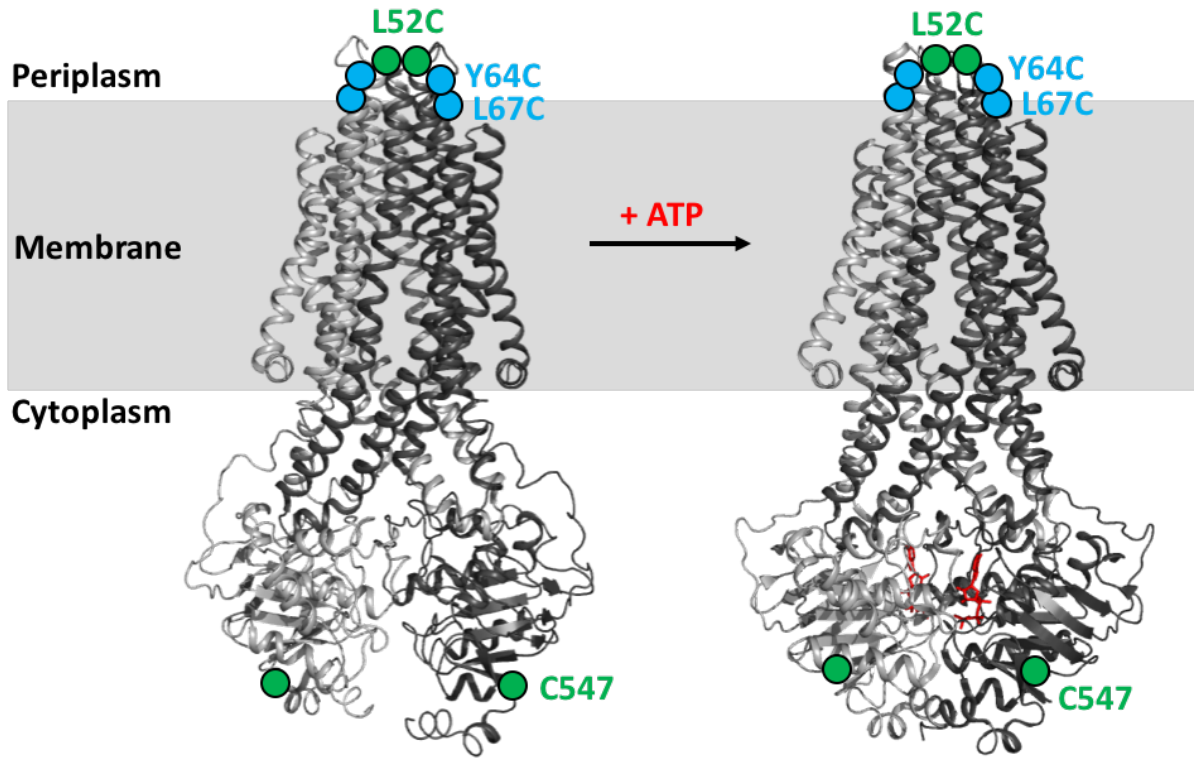
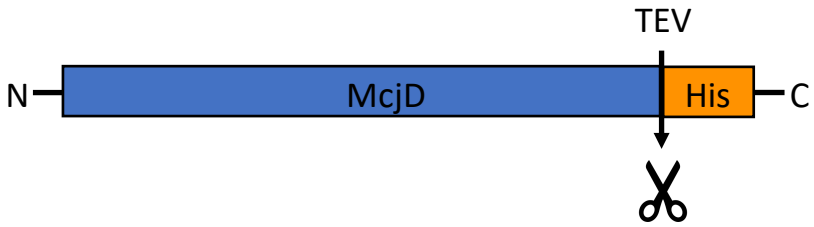


Figure 54. Positions of cysteine mutations for smFRET. The *apo* inward-occluded McjD structure (PDB: 50FP) is shown on the left hand side. The outward-occluded nucleotide bound McjD structure (PDB: 4PL0) is shown on the right hand side. The two halves of the transporter are coloured dark and light grey. AMP-PNP is highlighted red in stick format. The green coloured balls represent positions of incorporated cysteines that were examined by both PELDOR and smFRET. The blue coloured balls represent newly designed positions for smFRET.

3.2.2. Site-directed mutagenesis

The full length *mcjD* gene (accession number: Q9X2W0, residues 1-580) was previously subcloned from the *E. coli* pTUC202 vector into the pET-28b vector by Dr Konstantinos Beis. This generated a C-terminal His_8 tagged construct which was modified to create a Cys-less variant where all cysteines were substituted for alanine (Figure 55). Single cysteine mutations were introduced into the Cys-less *mcjD* template using the QuikChange Site-Directed Mutagenesis Kit (Agilent Technologies) according to manufacturer's instructions.

(A)



(B)

Mutation	Forward primer	Reverse primer
L52C	5’AATTTGACAATGAGCCAGACAG GCAATCTGTAATCTTTGCAAGAAT CAATG-3’	5’CATTGATTCTTGCAAAGATTA CAGATTGCCTGTCTGCATTGTC A-3’
Y64C	5’GGCAAGTAAAACCAGACATC ATAACTAAAATTTGACAATGAG CCAGA-3’	5’-TCTGGCTCATTGTCAAATTT TAGTTATGAATGTCTGGTTTTA CTTG CC-3’
L67C	5’-AAAACATGTATAAAGAGGC AAGGCAAACCAGATATTCATA ACTAAAATTTGACAATGAGC-3’	5'-TCTATTTCACCATTGATTCTT GCAAAGATTACAGATTTATGCT CTGGCTCATTGTCAAATTT-3'
C547	5’-CTTCATTCAATACATAAACA CA ATCGGAAGACTCCAGAAGA TTTATT-3’	5’-AATAAATCTTCTGGAGTCTT CCGATTGTGTTTATGTATTGAA TGA AG-3’

Figure 55. Generation of smFRET mutants. (A) Schematic of Cys-less McjD-TEV-His template for site-directed mutagenesis. (B) Table of primers used to incorporate single cysteine mutations for smFRET.

3.2.3. Preparation of McjD FRET mutants

Expression, membrane preparation and detergent solubilisation of the McjD-His mutants were carried out using the same techniques described for wild-type McjD-GFP-His (sections 2.2.1 - 2.2.3). Following ultracentrifugation of detergent solubilised membranes at 120,000 *g* for 30 min, the supernatant was brought to 40 mM imidazole (pH 7.5) and incubated with 7 mL of nickel-NTA superflow resin (Qiagen), stirring for 3 h. The slurry was loaded onto a glass Econo-column (Biorad) and washed with 12 X CV of 1 X PBS containing 50 mM imidazole

and 0.1% DDM. McjD-His was eluted from the column in a buffer containing 250 mM imidazole and 0.1% DDM. The protein was then dialysed overnight in 2 L of buffer containing 20 mM Tris (pH 7.5), 150 mM NaCl and 0.03% DDM. Following dialysis, McjD-His was concentrated to a final volume of < 1 mL using a 100 kDa cut-off concentrator and injected over two passes onto a Superose S200 10/300 gel filtration column (GE Healthcare) equilibrated in the dialysis buffer. The absorbance at 280 nm was monitored using the Äkta prime system and fractions were collected from the peak at ~15 mL, corresponding to McjD at the correct molecular weight. The fractions were diluted to a final concentration of 1 mg/mL and flash frozen in liquid N_2.

3.2.4. Protein labelling

For labelling, 200 μg of McjD was pre-incubated with 2 mM DTT for 30 min on ice in order to reduce the oxidised cysteines. The protein was labelled with Alexa Fluor 555 C2 Maleimide (Thermo Fisher Scientific) and Alexa Fluor 647 C2 Maleimide (Thermo Fisher Scientific) at a molar ratio of 1:4:5 (McjD: Alexa 555: Alexa 647). McjD was incubated with the fluorophores for 2 h on an elliptical roller in the dark. Excess dye was removed by injecting the protein into a Superose S200 10/300 gel filtration column (GE Healthcare), equilibrated in a buffer containing 20 mM Tris (pH 7.5), 150 mM NaCl and 0.03% DDM. Fractions were collected at an elution volume of 12 mL and reconstituted into liposomes for functional assays.

3.2.5. Preparation of biotinylated lipids

Biotinylated lipids were prepared by Konstantinos Tassis from a synthetic lipid mixture containing 67% (w/w) 1,2-dioleoyl-sn-glycero-3-phosphoethanolamine (DOPE), 23% (w/w)

1,2-dioleoyl-sn-glycero-3-phospho-(19-*rac*-glycerol) (DOPG), 7% (w/w) cardiolipin, and 3% (w/w) 1,2-dioleoyl-sn-glycero-3-phosphoethanolamine-N-(cap biotynil), short biotin-DOPE (Avanti Polar Lipids). A total of 100 µl of the lipid mixture was dissolved at 20 mg/mL in chloroform and dried under vacuum rotary evaporation at 30° C for 30 min. The lipids were subsequently hydrated in a buffer containing 20 mM Tris (pH 7.5) and 150 mM DDM to a final concentration of 20 mg/mL (w/v). The lipid mixture was then sonicated on ice for 16 cycles (15 s on, 45 s off) using an amplitude setting of 70% to form unilamellar vesicles. The vesicles were flash frozen in liquid N_2 and thawed at room temperature. The freeze-thaw cycle was repeated two further times in order to generate a homogeneous batch of liposomes.

3.2.6. Liposome incorporation

McjD was reconstituted into proteoliposomes after labelling using the rapid dilution method described in section 2.2.12. For ALEX measurements, *E. coli* polar lipid solution (20 mg/mL) (w/v) was prepared in ddH_2O by sonication in a water bath set to 25° C for 15 min. For smFRET measurements, biotinylated lipids were prepared as described in section 3.2.5. Labelled McjD was diluted in a buffer containing 20 mM Tris, 150 mM NaCl and 0.03% DDM and added at an optimised protein-to-lipid ratio of 1:1000 (v/v). For ATPase and transport assays, labelled McjD was mixed with *E. coli* polar lipids at a protein-to-lipid ratio of 1:200 (v/v). Following incubation on ice for 5 min, the solution was diluted in 4 mL liposome buffer 50 mM Tris (pH 8.0), 50 mM KCl). This step was followed by a further incubation step on ice for 5 min. Proteoliposomes were then pelleted by ultracentrifugation at 100,000 *g* for 30 min and the supernatant was discarded. The pellets were resuspended in 100 µl of liposome buffer.

3.2.7. Orientation of McjD in liposomes

To check the orientation of McjD in proteoliposomes, wild-type McjD carrying a C-terminal cleavable TEV-His tag was purified in 0.03% DDM and reconstituted into proteoliposomes. The ratio of McjD to proteoliposomes was the same as for the labelled McjD mutants used in smFRET measurements. Detergent purified McjD-His (10 µg) and liposome incorporated McjD-His (10 µg) were incubated with TEV protease-His at 25° C for 3 h using a molar ratio of 1:1 protein to TEV. Samples before and after cleavage were loaded onto an SDS-PAGE gel, and analysed by Western blot using the 6 X His Tag Monoclonal primary antibody (Thermo Fisher) and the rabbit anti-mouse IgG secondary antibody (Thermo Fisher) according to manufacturer's instructions. The Western blot was imaged using an ImageQuantLAS4000 (GE Healthcare) set to chemiluminescence mode. The orientation of McjD in liposomes (ratio of McjD-His molecules inside to outside) was calculated by measuring densitometry counts of McjD-His before and after TEV treatment. Densitometry measurements were performed using the ImageQuantTL software (GE Healthcare) and for quantification of band intensities, the automatic peak detection mode was applied. The efficiency of detergent purified McjD-His cleavage following TEV incubation was also confirmed by densitometry.

3.2.8. ATPase assays

ATPase assays with labelled McjD-His mutants reconstituted in liposomes were performed using the same methods described in section 2.2.11. MccJ25 (in DMSO) was added to the ligand-stimulated reactions at a final concentration of 0.5 mM. For each labelled McjD mutant, reactions were performed in duplicate with independently prepared batches of liposomes.

3.2.9. Transport assays

Transport assays with labelled McjD-His in liposomes were conducted using the protocol described in section 2.2.13. Wild-type McjD carrying a C-terminal His tag was purified in 0.03% DDM and incorporated into liposomes as a negative control. The reactions were performed in duplicate with independently prepared batches of liposomes. The mean values were plotted in GraphPad Prism 7 (GraphPad Software).

3.2.10. Single-molecule FRET using ALEX

Microscope cover slides (no. 1.5H precision cover slides, VWR Marienfeld) were coated with 1 mg/mL BSA for 30 s. Excess BSA was subsequently removed with the imaging buffer containing 20 mM Tris, 150 mM NaCl, 0.03% (w/w) DDM, 1 mM Trolox (Sigma Aldrich) and 10 mM cysteamine (pH 7.5) (Sigma Aldrich). Labelled McjD was further diluted in the imaging buffer to a final concentration of 25 pM. McjD was studied using a custom-built confocal FRET microscope (van der Velde *et al*., 2013) at room temperature. Excitation light at 532 and 640 nm was used in accordance with the fluorophore wavelengths (SuperK Extreme, NKT Photonics, Denmark). Alternation between the two excitation wavelengths was achieved by modulating the light at 50 s intervals.

3.2.11. Confocal scanning microscopy and analysis

The smFRET measurements in liposomes and data analysis were performed by the Cordes group. A detailed summary of the surface-immobilised smFRET setup and data processing is described in Husada *et al*. (2018). Experiments performed by the Cordes group are indicated.

3.3. Results

3.3.1. Purification and labelling of McjD mutants

In order to facilitate smFRET measurements, a rational approach was taken to select and design single cysteine point mutations for fluorophore labelling (section 3.2.1.). The McjD TMD mutant L52C was purified as described previously and only analysed in solution by ALEX measurements (section 3.3.5). The McjD TMD mutants Y64C and L67C, and the NBD mutant C547 were purified using a single nickel IMAC step followed by gel filtration in order to maintain the His tag for surface-immobilised smFRET measurements. To account for the absence of a reverse IMAC purification step, a high concentration of imidazole (45 mM) was added to the McjD supernatant during binding to the nickel resin. Furthermore, the IMAC wash buffer contained a higher imidazole concentration (50 mM) than was used previously and the number of column volume washes was increased (15 X) to minimise the carry-over of contaminant proteins. For the McjD mutants C547, Y64C and L67C, the final gel filtration profiles yielded two peaks that were poorly resolved using a Superdex S200 column. A representative SEC profile for Y64C-His is shown in Figure 56A. Interestingly, fractions from the peak observed at ~9.5 mL did not contain contaminant proteins and instead correspond to a different oligomerisation state of McjD (Figure 56B). In contrast, the peak at ~11.5 mL contains McjD fractions at the expected elution volume. One possible explanation for existence of a higher molecular weight species is that this conformation can be induced by the presence of the His-tag.

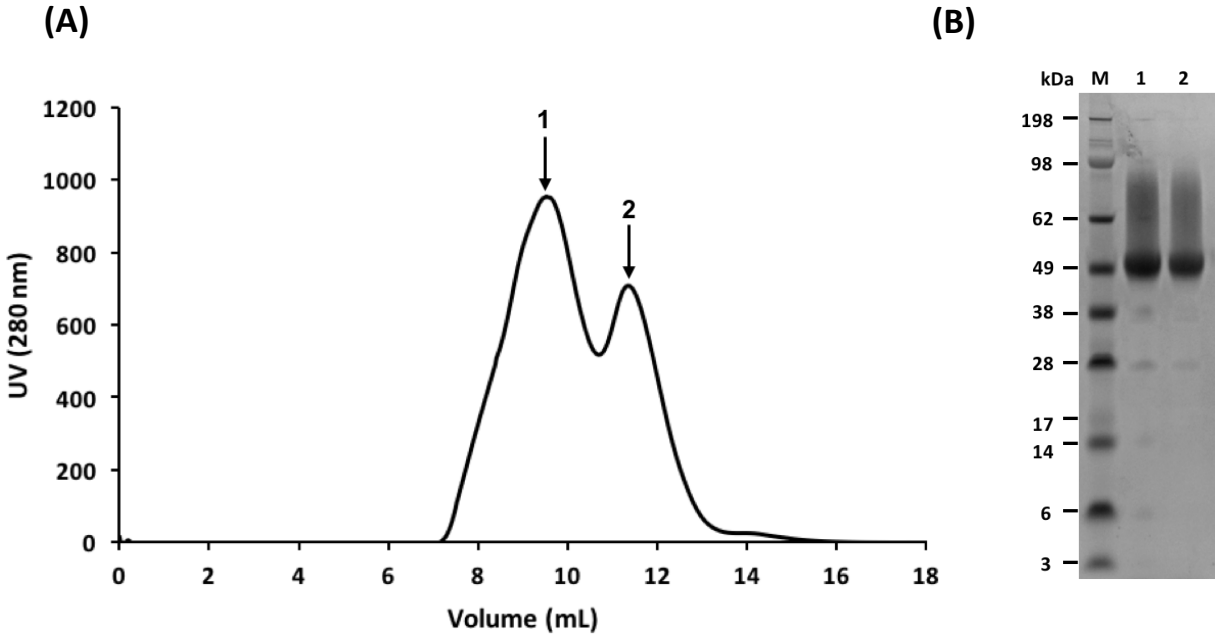


Figure 56. Purification of McjD-Y64C using a Superdex S200 column. (A) The gel filtration profile shows two peaks that are poorly resolved. Peak 1 (~9.5 mL) corresponds to an unusual oligomerisation state of McjD whereas peak 2 (~11.5 mL) corresponds to McjD at the correct molecular weight. (B) SDS-PAGE indicates that both species contain McjD at a high level of purity, verifying that neither peak has resulted from contaminant proteins.

Since the two McjD species could not be clearly separated using the Superdex column, the resulting protein preparations lacked the homogeneity required for fluorophore labelling. The McjD-His purification was therefore optimised by switching to a Superose 6 column to improve separation between the two McjD species (Figure 57). For McjD C547, there is a sharp peak observed at ~15 mL containing McjD fractions suitable for labelling. The TMD mutants Y64C and L67C both present two peaks; a broad peak at ~11.5 mL corresponding to the unusual oligomerisation state of Mcjd and a well separated peak at ~15 mL. To minimise the contribution of the McjD oligomer to FRET measurements, only fractions located in the second half of the ~15 mL peak were collected. SDS-PAGE analysis of pooled fractions for the McjD mutants indicates they all have a high degree of purity (Figure 58).

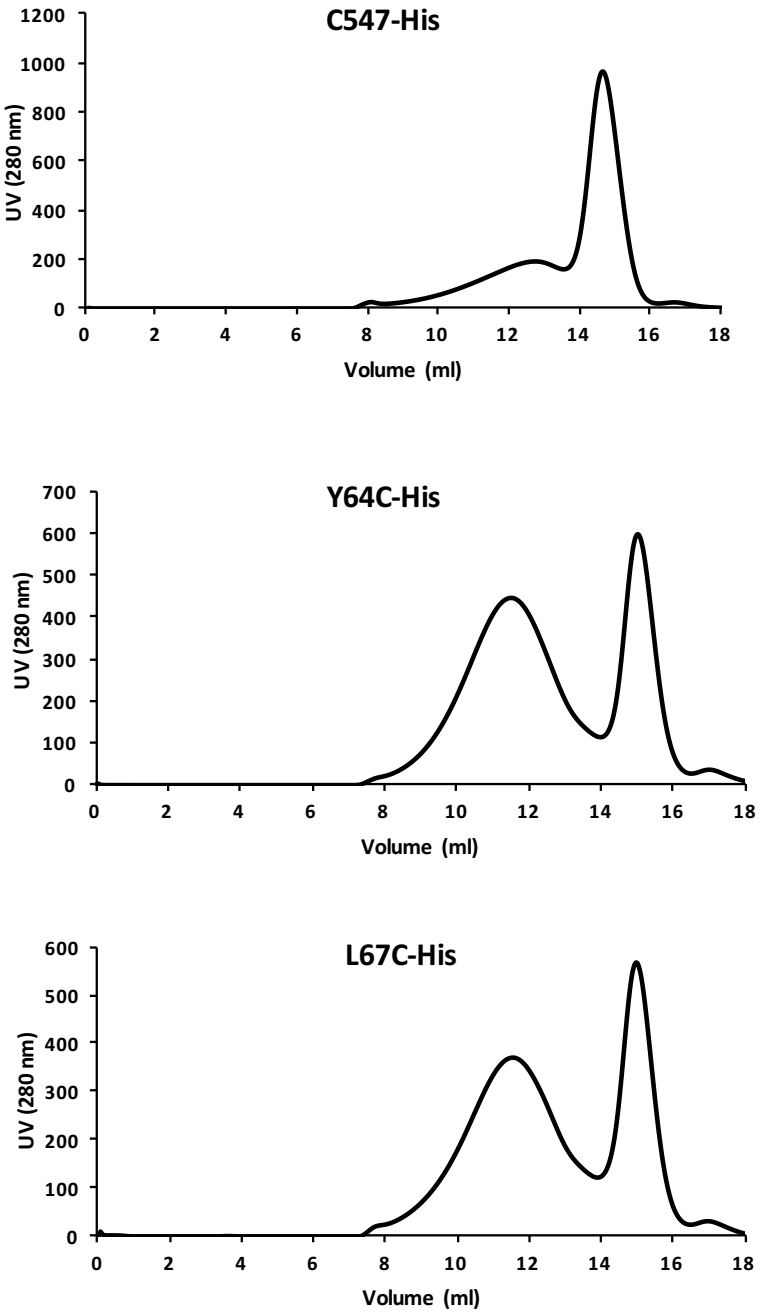


Figure 57. Optimised gel filtration profiles of McjD FRET mutants. Using the Superose 6 gel filtration column, McjD C547 generates a single monodisperse peak at an elution volume of ~15 mL. The TMD mutants Y64C-His and L67C-His both display dual peak behaviour, but the peak corresponding to the unusual oligomerisation state now elutes at ~11.5 mL. This ensures that the McjD fractions of interest at ~15 mL are well-separated and suitable for labelling.

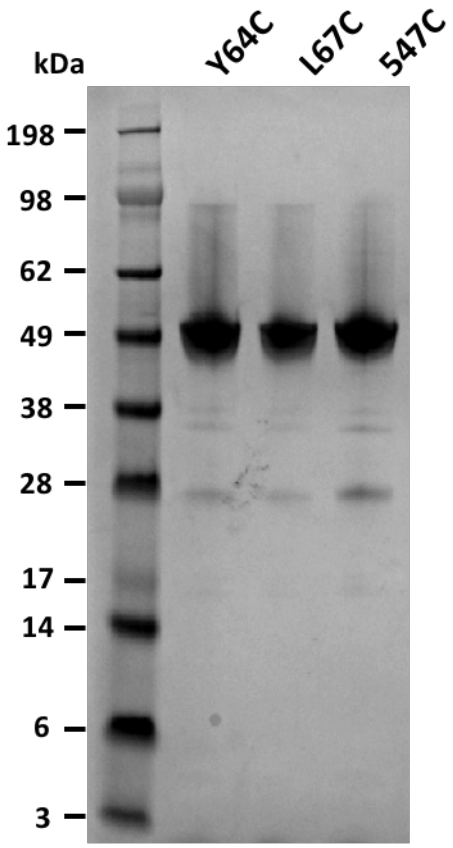


Figure 58. SDS-PAGE of McjD FRET mutants. All McjD FRET mutants were prepared to a high level of purity following the gel filtration step.

Prior to labelling, McjD was pre-incubated with DTT in order to fully reduce the oxidised cysteines. McjD was then labelled stochastically with an excess of the spectrally distinct dyes Alexa 555 and Alexa 647. The fluorophores are both linked to maleimide groups to facilitate conjugation to the thioether groups of the single cysteines. The protein-dye mixture was degassed under argon to maintain an oxygen-free environment and incubated for an optimal labelling time of 5 h. Shorter durations of dye incubation gave rise to a significant reduction in the labelling efficiency. Interestingly, the addition of DTT during McjD-His purification steps also abrogated the labelling efficiency perhaps owing to degradation of the reducing agent.

Following treatment of McjD with the fluorophores, the protein was passed through a gel filtration column to remove excess dye. McjD was observed as a monodisperse peak that demonstrated absorption at both the donor and acceptor wavelengths of 532 and 640 nm, respectively. The efficiency of fluorophore incoroporation was estimated to be ~60% for the C547 mutant, ~30% for Y64C, ~30% for L67C, and ~10% for L52C. Since the cysteine mutations in the TMDs are located close to the membrane surface, the hydrophobic fluorophores can interact directly with the lipid bilayer, resulting in a lower labelling efficiency at these positions. The incorporation of fluorophores was strongly compromised for McjD-L52C, which is surprising since the same mutant could be effectively spin-labelled for PELDOR measurements (Bountra *et al*., 2017).

3.3.2. Functional characterisation of labelled mutants

In order to test whether the labelled McjD mutants were amenable to experiments in a native-like environment, the labelled proteins were reconstituted into proteoliposomes using the rapid dilution protocol. A representative SDS-PAGE gel is shown in Figure 59 demonstrating the successful incorporation of 0.5 mg/mL labelled McjD-C547 in liposomes. Densitometry analysis indicates that > 50% of the labelled C547 mutant was reconstituted when evaluated against detergent-purified McjD aliquots at defined concentrations. The incorporation of labelled Y64C and L67C could be achieved with a similar efficiency and was reproducible for independently prepared batches of liposomes.

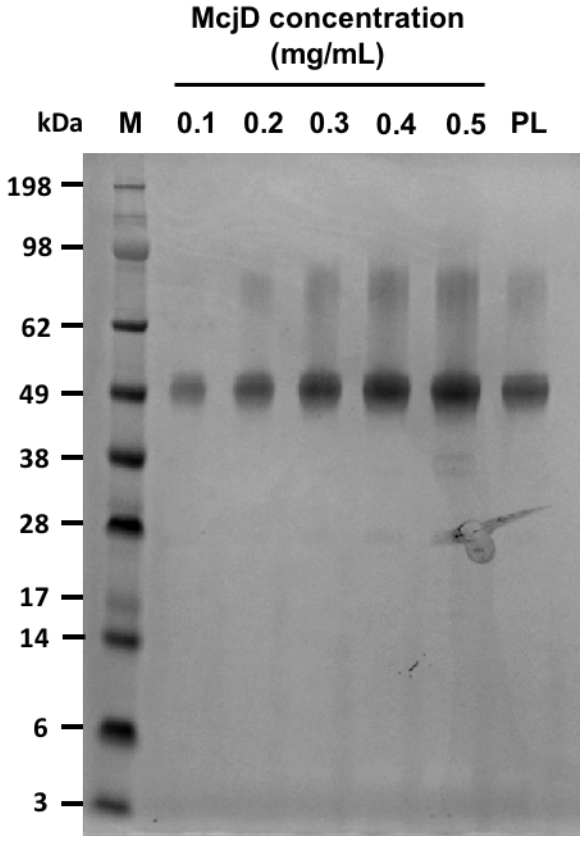


Figure 59. SDS-PAGE of labelled McjD-C547 reconstituted in proteoliposomes. The amount of protein reconstituted in proteoliposomes (PL) was evaluated against detergent-purified McjD at different concentrations.

To confirm that the labelled McjD FRET mutants retained functional activity in liposomes, ATPase measurements were performed immediately following the reconstitution step (Figure 60). Wild-type McjD-His was incorporated in liposomes as a positive control and demonstrated an ATPase activity of 49.7 nmol/min/mg protein, that is comparable to the published value (Choudhury *et al*., 2014). Upon addition of MccJ25, there was a 48.3% stimulation of ATPase activity, in accordance with previous data. The basal ATP turnover of labelled McjD 547C (64.99 nmol/min/mg protein) was slightly higher than for wild-type protein but the activity of the NBD mutant was also stimulated in the presence of MccJ25. Labelled L52C, Y64C and L67C demonstrated comparable ATPase measurements to wild-type protein in the presence or absence of MccJ25.

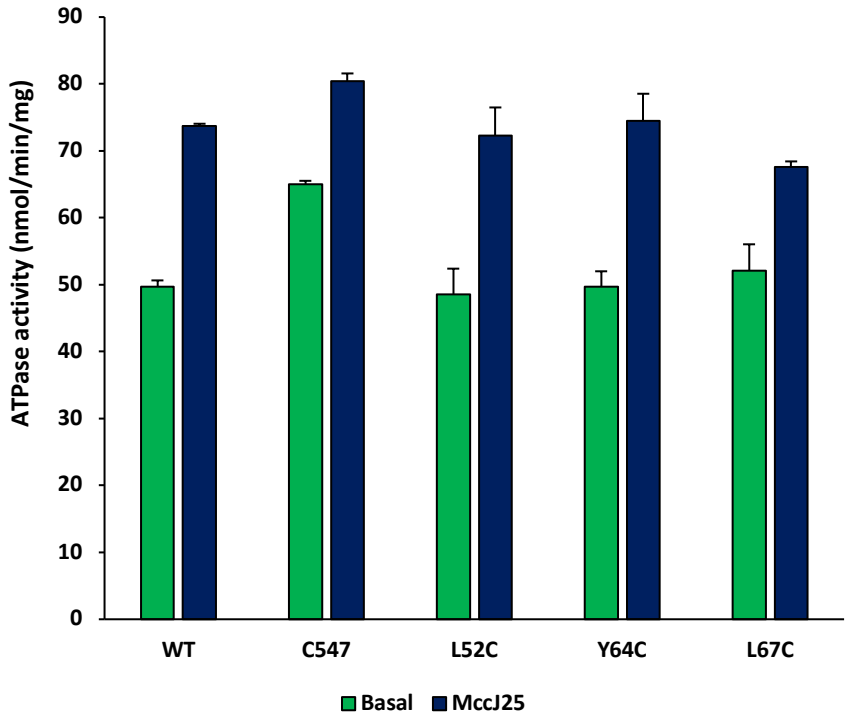


Figure 60. ATPase activity of labelled McjD FRET mutants in liposomes. The labelled McjD mutants show basal and ligand-induced ATPase activity (0.5 mM MccJ25) comparable to that of unlabelled wild-type protein in liposomes. Error bars were calculated from two independent reconstitution experiments (mean ± standard deviation).

Since the basal ATPase activity of C547 was slightly higher than the value observed for wild-type McjD, I tested whether the labelled mutant was still coupled to ATP hydrolysis using the Hoechst uptake assay in liposomes. Wild-type McjD-His was incorporated into liposomes as a control and evaluated for transport activity against the C547 mutant (Figure 61). In the absence of ATP, labelled C547 produced a stable level of fluorescence indicating no Hoechst uptake in liposomes in accordance with wild-type protein. In the presence of ATP and Hoechst, there was a drop in the measured fluorescence counts of ~15 units for C547, due to the uptake and subsequent quenching of the dye. This value is identical to the rate of transport for wild-type protein. The labelled McjD mutant is therefore transport competent and suitable for FRET analysis. In summary, these data indicate that neither the introduction of cysteines, nor the addition of fluorescent labels perturbed the actitivity of the transporter in liposomes.

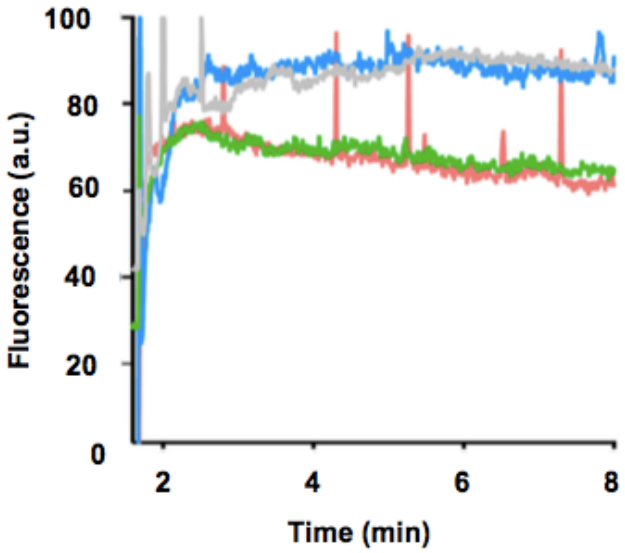


Figure 61. Hoechst uptake of labelled McjD 547C compared to wild-type protein. Wild-type McjD demonstrates uptake of Hoechst 33342 in the presence of ATP (green line) but no transport in the absence of ATP (grey line). Labelled McjD C547 demonstrates comparable transport activity to wild-type protein in the presence of ATP (orange line) and no activity when ATP is not present (blue line).

3.3.3. Visualisation of McjD mutants in detergent by ALEX

Since the labelled McjD mutants demonstrated similar behaviour to wild-type protein, they could be studied by smFRET. The initial measurements were performed with detergent-solubilised McjD in order to establish the smFRET assay and optimise the imaging conditions. Since McjD in detergent micelles diffuses freely in solution, a confocal microscope coupled to alternating-laser excitation (ALEX) was employed to monitor the conformational states for McjD under equilibrium conditions. The microscope cover slides were coated with BSA to prevent non-specific interactions with the fluorophores. Excess BSA was then removed by washing the cover slides with an imaging buffer containing the photostabilisation reagent Trolox. The addition of Trolox acts as an anti-blinking and anti-bleaching reagent (Cordes *et al*., 2009).

The ALEX setup reports emission signatures by calculating the distance-dependent FRET efficiency (E*) for D-A labelled McjD molecules and the distance-independent stoichiometry ratio (S) for all species (Kapanidis *et al*., 2004). Fluorescence-aided molecule sorting (FAMS) analysis enables single diffusing McjD molecules to be grouped according to their labelling properties (Figure 62). Although FRET does not measure absolute distances, relative distance changes can be obtained by determining the apparent FRET efficiency E^*. Comparison of the observed E^* values for McjD with respect to static dsDNA ruler structures (Ploetz *et al*., 2016) enables assessment of how well the C_α-C_α distances relate to those expected from the crystal structures. The Förster radius of Alexa555/647 is R_0 = 5.1 nm which corresponds to a theoretical FRET efficiency of 0.5. As a consequence, distances between the two fluorophore labels above this value generate smaller values of E^* whereas shorter distances are expected to show larger E^* values.

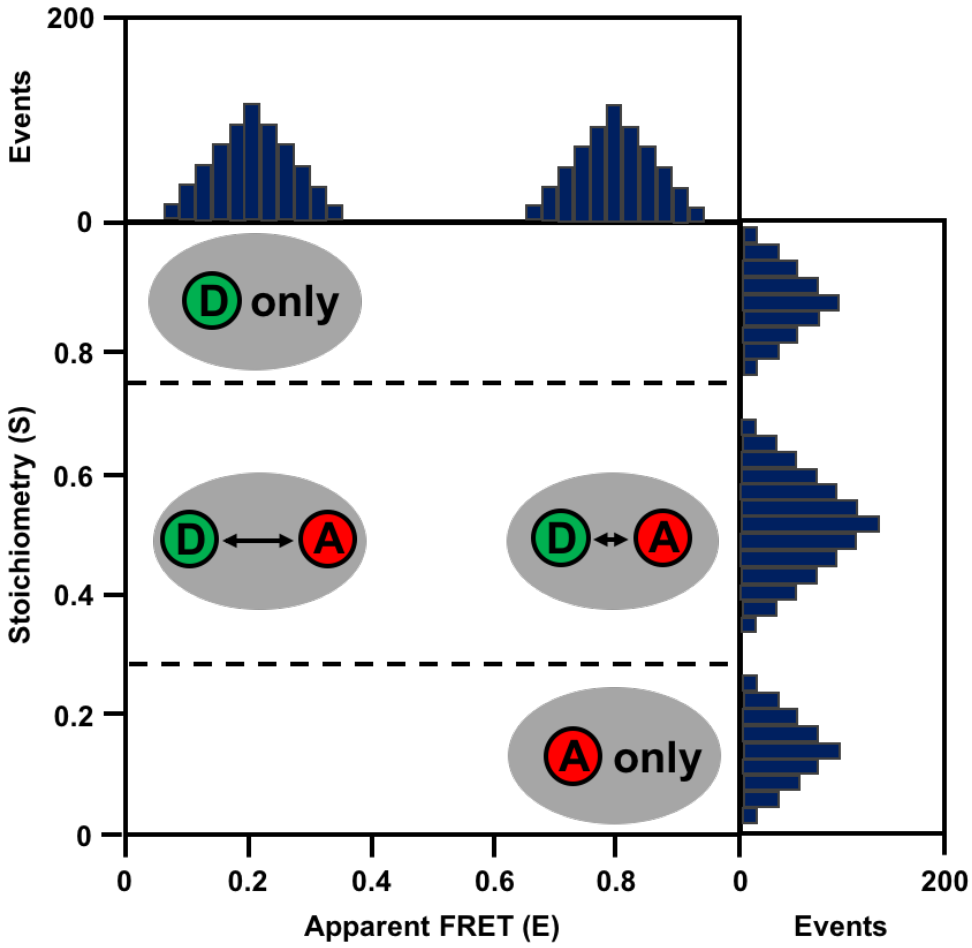


Figure 62. Schematic of smFRET using ALEX. Donor and acceptor fluorophores are shown in green and red respectively. The stochastically labelled single molecules are sorted according to their properties. Molecules labelled with either donor or acceptor fluorophores only can be filtered out, whereas molecules labelled with a single donor-acceptor dye pair are visualised in the centre of the spectrum. The panel located to the right hand side quantifies the stoichiometry of each type of labelling event (*i.e.* D, D-A, A). In this example, the D-A labelled protein adopts two conformational states so the molecules are distributed as two populations with differing FRET efficiencies. The panel located at the top indicates the relative proportions of D-A labelled single molecules adopting each state. Adapted from Kapanidis *et al.* (2004).

3.3.4. FRET observations of McjD C547 in detergent

Preliminary ALEX measurements were performed using the McjD C547 sample purified with a Superdex S200 column. Owing to the heterogeneity of this protein preparation, fluorophore labels were incorporated with low efficiency and the resulting *apo* C547 ALEX profile recorded a mixed population of McjD molecules. The profile shown in Figure 63 demonstrates a 'low FRET' species at an E^* value of ~0.3 and a 'high FRET' species that is likely to correspond to the high molecular weight oligomerisation state of McjD observed during the gel filtration step. Following optimisation of the purification however, using the Superose 6 column, the ALEX profile for *apo* C547 shows a distinct 'low FRET' species and a significant reduction in the contribution from the 'high FRET' artefact (Figure 64).

In order to establish whether the C547 mutant could undergo changes in FRET efficiency, McjD was pre-incubated with nucleotides and ALEX measurements were taken. In the presence of AMP-PNP and ATP-VO_4, the binding of nucleotide shifts the population of McjD molecules to a higher FRET state due to closure of the NBDs (Figure 64). The observation of a higher FRET efficiency in these conditions is consistent with the nucleotide bound crystal structures of McjD predicting a smaller degree of NBD separation. A 1D Gaussian fit was applied to the raw ALEX data in order to generate histograms from which mean E* values could be calculated. Representative examples of the fitted data are shown in Figure 65 alongside the mean E* values recorded for each condition. Since the NBDs display a broad range of conformations, the E* values were not converted to absolute distances. The mean E* values therefore reflect the average conformational state of the labelled position.

Apo McjD C547 generates a mean E* value of 0.31. When taking into account the added flexibility of the fluorophore linkers, this observed FRET efficiency can be correlated with the *apo* crystal structure distance of 4.8 nm at position C547. Incubation with AMP-PNP and ATP-

VO_4 both give rise to larger E* values of 0.54 and 0.56 respectively, consistent with formation of the closed NBD dimer. ATP is also able to shift the C547 mutant towards an E* value of 0.56. In contrast, the addition of ADP or vanadate alone is unable to induce conformational changes as the FRET efficiency remain unchanged from *apo* conditions. Taken together, these findings confirm that nucleotide binding triggers dimerisation of the McjD NBDs. It is only after ATP hydrolysis that disengagement of the NBDs can be observed and this opening is linked to a reset of the transporter.

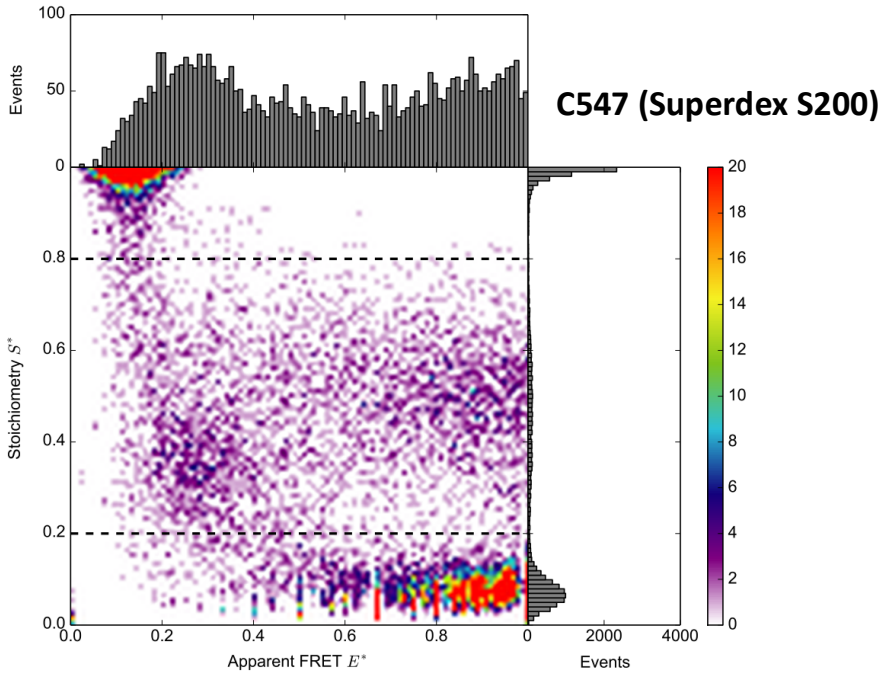


Figure 63. McjD-C547 visualisation by ALEX using a Superdex S200 column. The sample demonstrated a weak labelling efficiency with a significant fraction of McjD molecules adopting a high FRET state due to the mixed species observed during gel filtration.

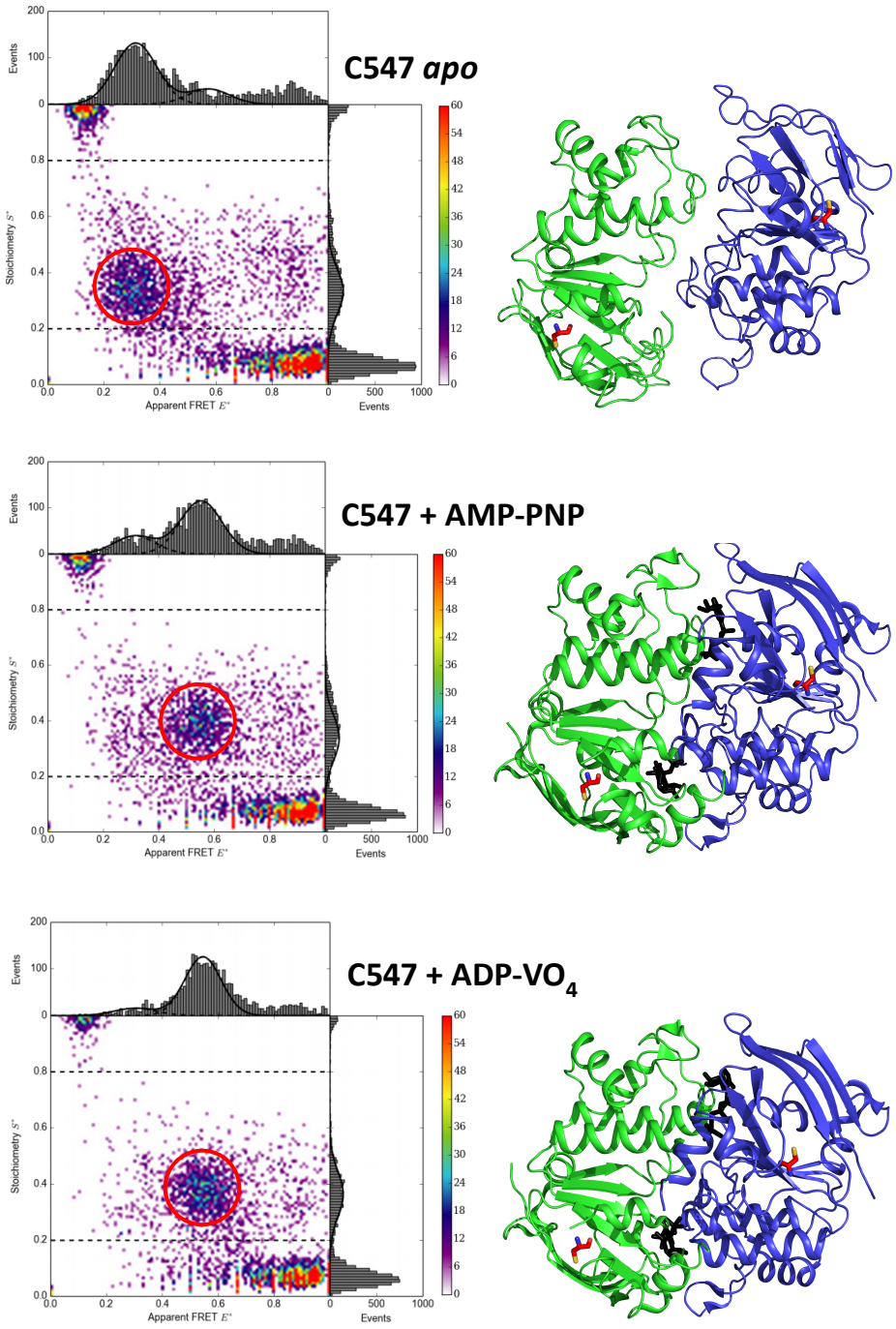
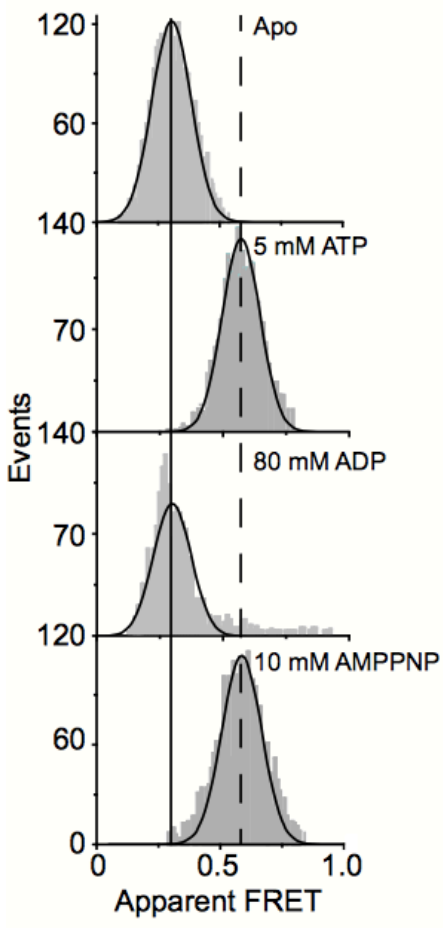


Figure 64. Conformational changes in the NBDs correlate with McjD structures. The McjD NBD monomers are coloured green and blue. AMP-PNP and ADP-VO_4 are shown in black stick format. The position of the C547 mutation is shown in red stick format. Clusters of McjD molecules with similar FRET efficiencies are indicated by the red circles. For *apo* McjD-C547, a significant population of McjD molecules are observed at FRET efficiency of ~0.3 whereas in the presence of AMP-PNP and ATP-VO_4, this population is shifted to a FRET efficiency of ~0.5.



Condition	C547 (E*)
apo	0.31
ATP	0.56
ATP + VO_4	0.56
ATP + MccJ25	n.d
ADP	0.31
ADP + VO_4	0.30 & 0.56
VO_4	0.31
AMP-PNP	0.54

Figure 65. FRET efficiency values in the McjD NBDs. The left panel shows representative examples of McjD-C547 histograms generated after a 1D Gaussian fit was applied to the raw ALEX data. The right panel shows the calculated E* values for McjD-C547 in different experimental conditions. The data indicate that the McjD NBDs transition from a low FRET state (E*= 0.31) in the absence of nucleotides to a closed dimer form (E*= 0.54/0.56) when nucleotide is trapped in the NBDs (ATP, ATP + VO_4, AMP-PNP). The addition of ADP or VO_4 alone is unable to trigger conformational changes in the NBDs.

3.3.5. FRET observations of McjD Y64C and L67C in detergent

The McjD TMD mutants were also examined in detergent solution by confocal ALEX measurements. The ALEX profiles for Y64C and L67C both produce a single population of freely diffusing McjD molecules at high FRET efficiencies (Figure 66). The FRET profiles differ when compared to the TMD mutant L52C, that displays a random distribution of FRET efficiencies that cannot be interpreted. One possible explanation is that due to the very close proximity of the two labelling positions (C_α-C_α distances of 1.2 nm), the transporter is no longer poised to exhibit meaningful changes in FRET. The L52C mutant also demonstrated a weak labelling efficiency (< 10%) compared to Y64C and L67C (~30%). This finding validates the suitability of the newly designed TMD mutants Y64C and L67C for probing by FRET.

The profiles shown in Figure 67 indicate that ATP is unable to induce conformational changes. In the presence of ATP and MccJ25 however, a small shift is observed for both Y64C and L67C, indicating movement towards a slightly lower FRET state. Due to the close separation between the labelled positions in the McjD dimer, *apo* L67C and Y64C produce high E^* values of 0.95 and 1.07 respectively (Figure 68). These high FRET E* values are in accordance with the *apo* crystal structure which predicts short C_α-C_α distances of 2.6 nm (Y64C) and 2.9 nm (L67C). Since there is a smaller separation between Y64C-Y64C' in the McjD homodimer, this TMD mutant displays a higher FRET efficiency when compared to L67C. In the presence of AMP-PNP, the observed E^* values for both TMD mutants are similar to *apo* McjD, validating the nucleotide bound crystal structure containing occluded TMDs (Choudhury *et al*., 2014). Similarly, neither the addition of ATP, nor the addition of ADP alone or ADP-VO_4 significantly altered the E* values. In the presence of ATP and MccJ25 however, the E* values for both TMD mutants are shifted to lower FRET efficiencies of 0.91 and 0.83 respectively. This result indicates that the periplasmic end of the TMDs have switched to the outward-open

state and that this opening is coupled to the binding of both ATP and MccJ25. The detergent data indicate that unlike the NBDs that can undergo conformational changes upon nucleotide binding, both nucleotide and substrate are required to switch the TMDs from an occluded state to the outward-open conformation.

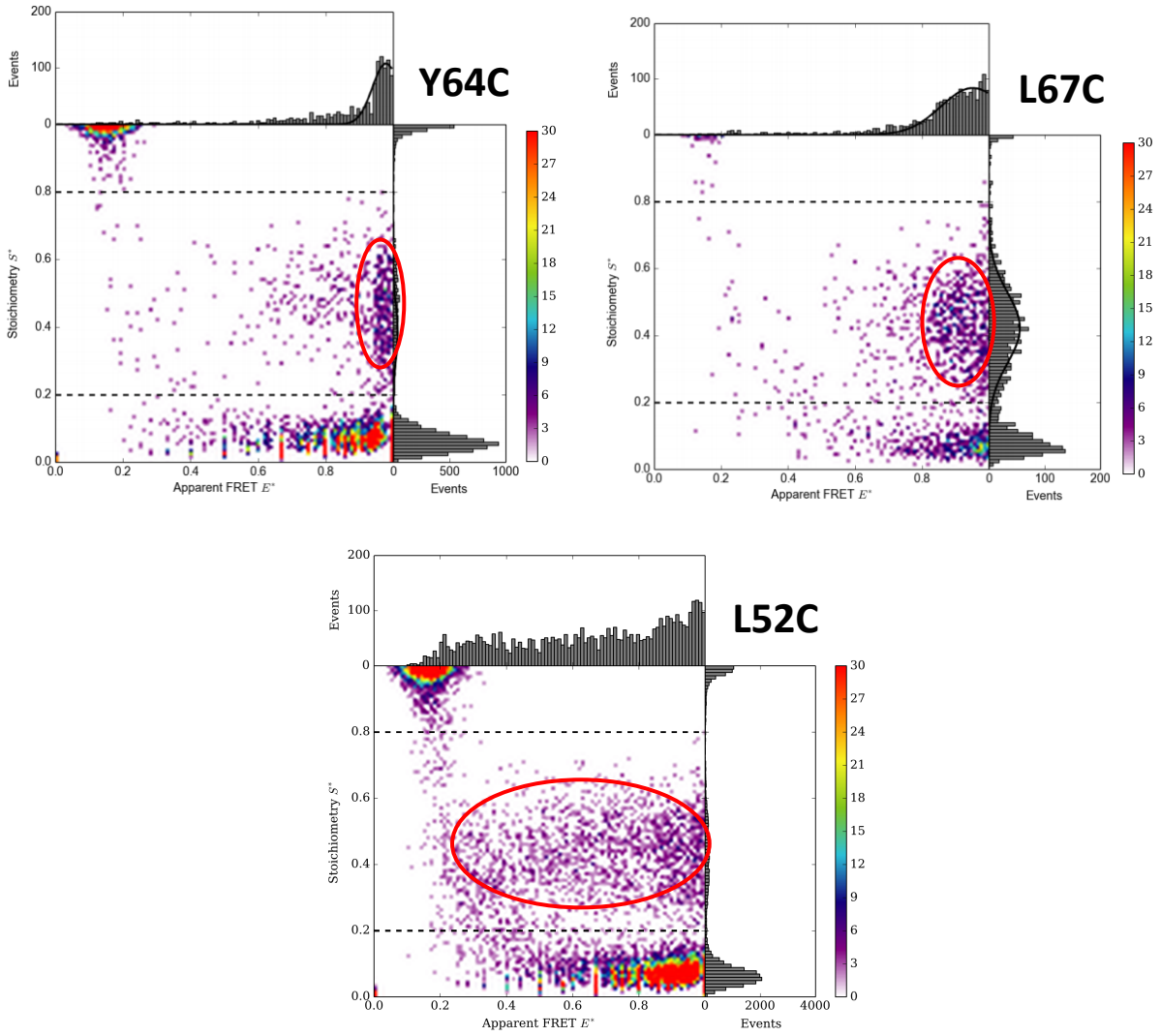


Figure 66. Distinct FRET populations observed for McjD-Y64C and McjD-L67C. The TMD mutants Y64C and L67C both demonstrate a tight population of McjD molecules that adopt high FRET states. The TMD mutant L52C by contrast is unsuitable for ALEX measurements since the individual McjD molecules show a random distribution of FRET efficiencies that cannot be interpreted to reflect distinct conformational states.

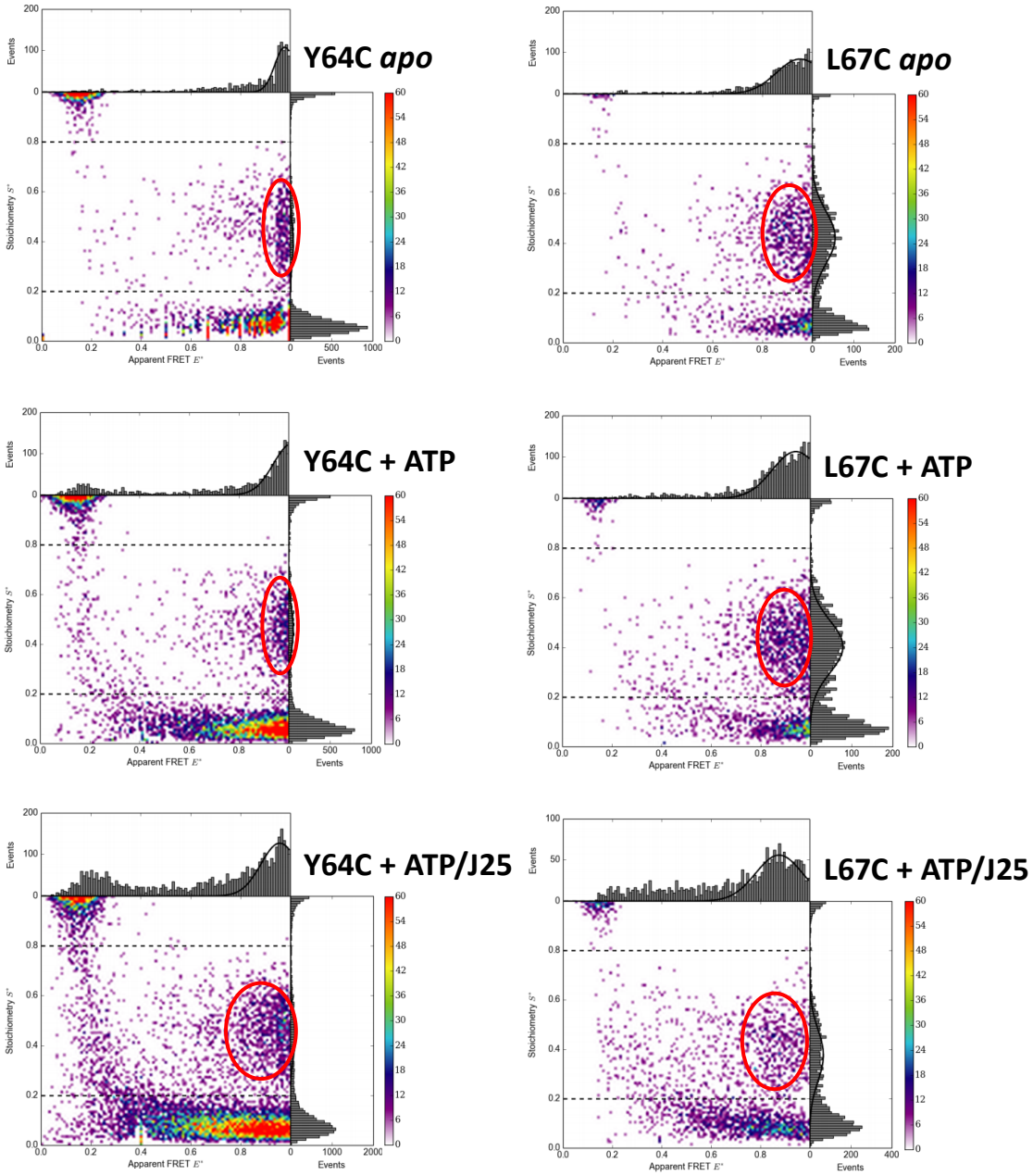
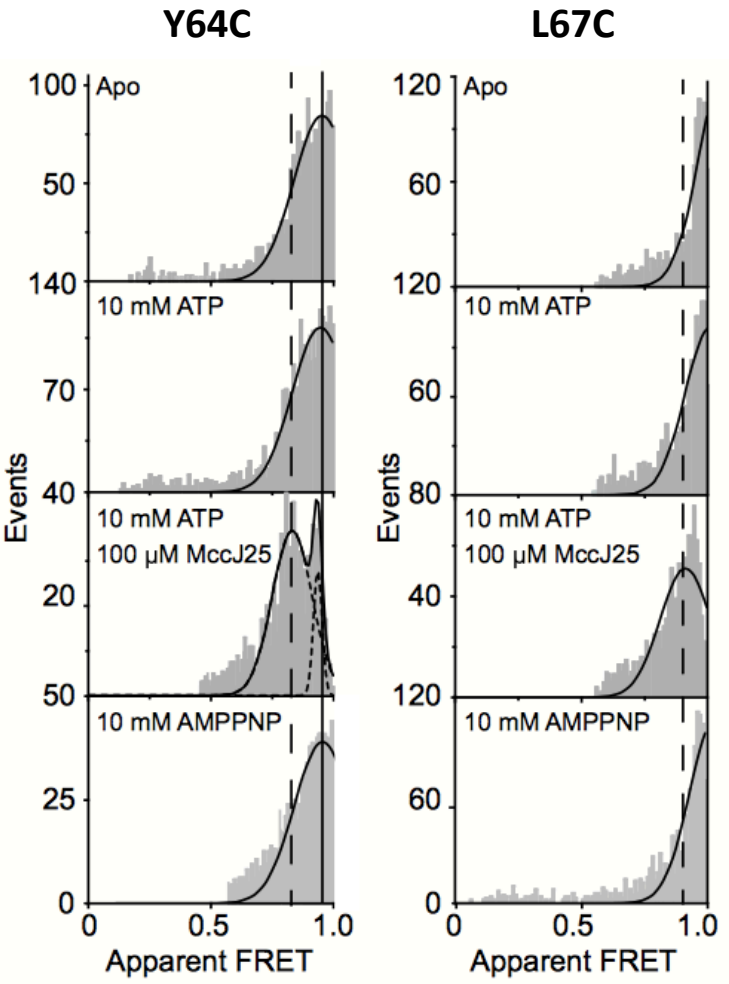


Figure 67. FRET population shifts in the TMDs upon ATP/MccJ25 treatment. The ALEX data demonstrate that in the presence of ATP there are no significant changes in the distribution of the high FRET population for Y64C or L67C compared to *apo* conditions. In the presence of ATP and MccJ25 however, the population shifts to a slightly lower FRET state, which is indicative of conformational changes at the periplasmic side of the TMDs.



Condition	Y64C (E*)	L67C (E*)
apo	1.07	0.99
ATP	1.01	0.99
ATP + VO_4	n.d	n.d
ATP + MccJ25	0.91	0.83
ADP	0.99	0.95
ADP + VO_4	0.99	0.95
VO_4	n.d	n.d
AMP-PNP	1.03	0.95

Figure 68. FRET efficiency values in the McjD TMDs. The left panel shows representative examples of McjD-Y64C and McjD-L67C histograms generated after a 1D Gaussian fit was applied to the raw ALEX data. The right panel shows the calculated E* values for the McjD TMD mutants in different experimental conditions. *Apo* Y64C and L67C demonstrate high E* values that are not altered in the presence of nucleotides alone. The addition of both ATP and MccJ25 shifts the E* values to a lower FRET state, suggesting that the outward-open state is being sampled under these conditions.

3.3.6. Orientation of McjD in proteoliposomes

Since detergent micelles represent a non-physiological environment for McjD, the impact of detergent on FRET efficiency changes requires measurements to be repeated in liposomes. The substrate-induced ATPase activity of McjD in the presence of MccJ25 is higher in liposomes than in detergent (Choudhury *et al*., 2014). Moreover, specific classes of lipid are required to modulate the activity of the transporter and these conditions can only be mimicked in a native-like environment (Mehmood *et al*., 2016). Prior to performing smFRET in liposomes, it is important to verify the random insertion of McjD molecules.

To determine the ratio of McjD molecules facing the inside of the liposomes to the proportion facing the outside, McjD containing a cleavable C-terminal His tag was reconstituted into liposomes and treated with TEV protease. Since the His tag is located at the C-terminus of the NBDs, only McjD-His molecules facing the outside of the liposomes are accessible to TEV protease. For McjD-His molecules facing the inside, the His tag is buried in the lumen and therefore no longer exposed for cleavage.

When TEV-treated and untreated McjD-His containing liposomes were analysed by anti-His Western blot, cleavage for the TEV-treated sample was incomplete, suggesting a mixed population of McjD-His orientations in liposomes (Figure 69A). In contrast, the efficiency of TEV cleavage for detergent-purified McjD-His was close to completion as indicated by the loss of signal in the Western blot. Quantification of the band intensities in liposomes before and after TEV incubation revealed that McjD molecules incorporate at a ratio of ~60:40 outside to inside (Figure 69B). Notably, two independent reconstitution experiments were able to identify a preferential orientation bias in liposomes. Since only ~60% of McjD transporters contain the correct orientation required to react with nucleotide and substrate, FRET observations in liposomes assume that a proportion of McjD molecules are unresponsive to the

addition of ATP and MccJ25. In summary, this finding enables a more detailed evaluation of McjD conformational changes to be made in liposomes.

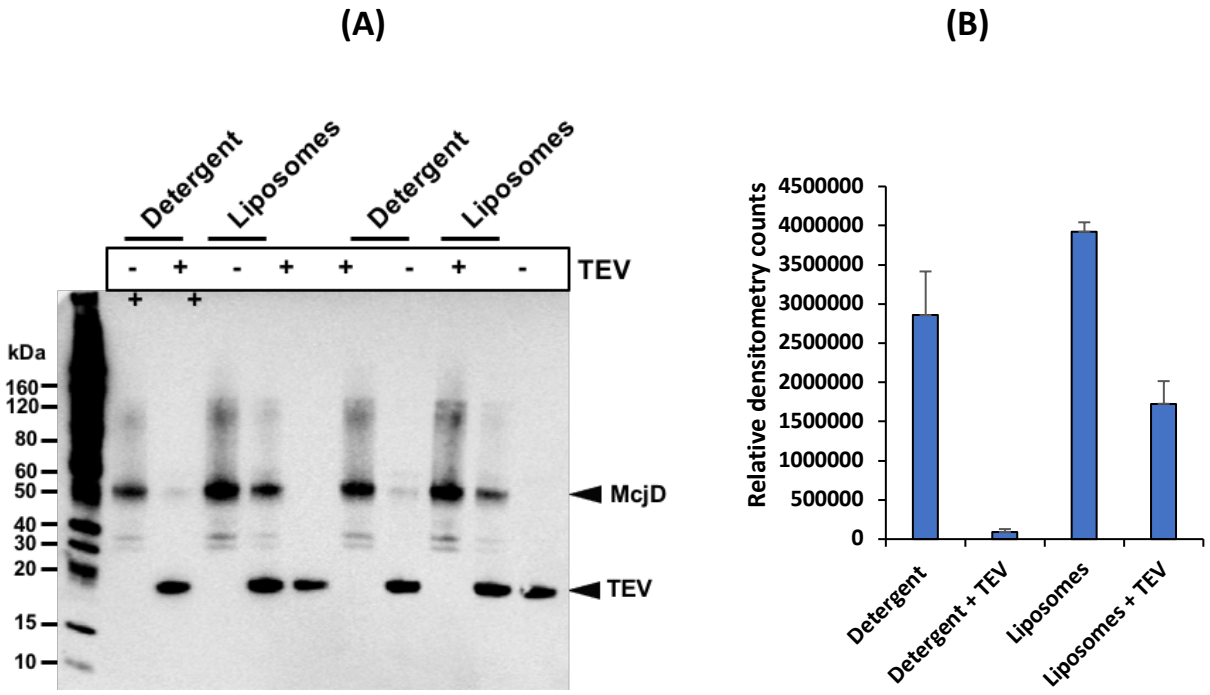


Figure 69. McjD orientiation in proteoliposomes. (A) Western blot showing the orientation of McjD in proteoliposomes. Detergent-purified McjD-His (~50 kDa) and liposome-reconstituted McjD-His were incubated with TEV protease (~20 kDa), which carries a His-tag, at a 1:1 molar ratio of protein to TEV. The reactions were visualised before and after TEV cleavage by anti-His Western blot. Bands corresponding to McjD-His and TEV protease-His are indicated. The incomplete cleavage of TEV-treated McjD in liposomes indicates that the transporter adopts both 'inside' and 'outside' facing orientations. (B) Densitometry quantification of McjD orientation. The ratio of inside to outside McjD-His in liposomes was quantified by measuring the Western blot band intensities before and after TEV protease incubation. Values represent mean densitometry counts calculated from two independent liposome preparations and indicate a proportion of 44%:56% ± 4% McjD-His inside to outside. Error bars are shown (mean ± standard deviation, n = 2).

3.3.7. Optimisation of McjD reconstitution in liposomes

Fluorophore labelled McjD was incorporated into *E. coli* polar lipids for ALEX measurements and biotin-DOPE for smFRET surface measurements. The ALEX data in liposomes give rise to cumulative histograms similar to those generated for McjD in detergent solution and allow for assessment of conformational states. The surface-immobilised measurements by contrast monitor the conformational behaviour of single McjD molecules in real time and have the added advantage of probing protein dynamics. McjD reconstituted in liposomes was immobilised in custom-made flow cells on PEGylated coverslips via liposomes containing biotin-DOPE (Figure 70).

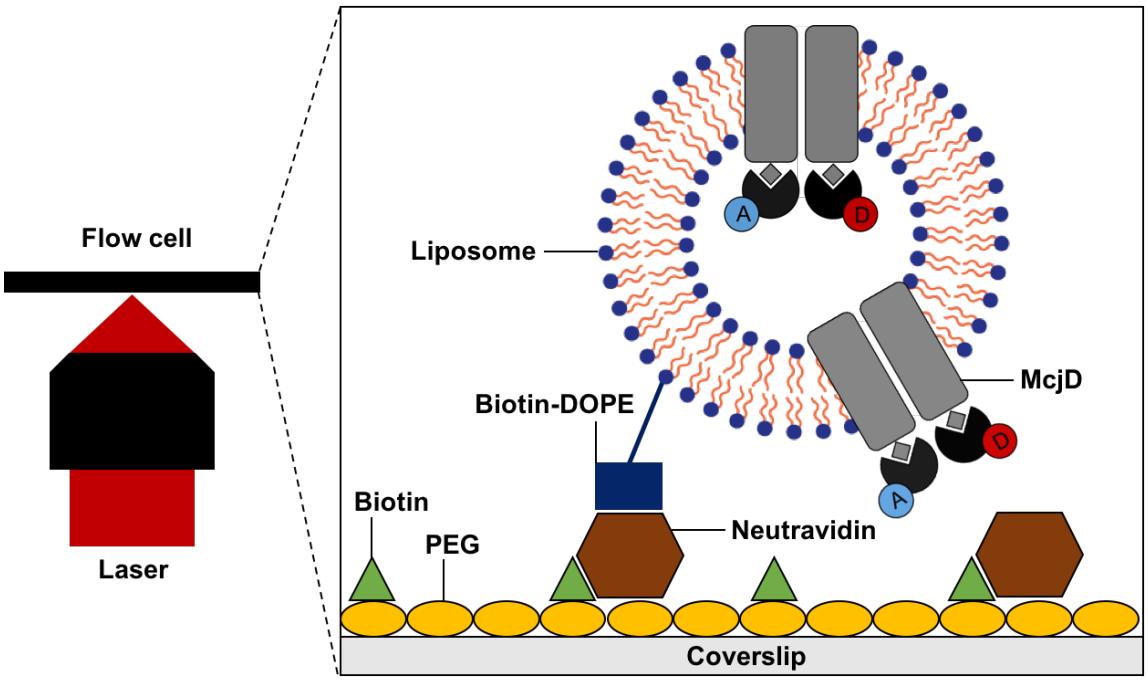


Figure 70. Experimental setup for McjD immobilised to the surface. Labelled McjD was incorporated into biotinylated DOPE lipids using the rapid dilution method. Biotinylated liposomes containing labelled McjD were immobilised to a PEG-biotin coated surface in a custom made flow cell via a neutravidin tag on the proteoliposome.

The McjD-C547 mutant was selected for optimisation of imaging conditions due to its ease of handling compared with the TMD mutants. Reconstitution of labelled McjD in proteoliposomes required optimisation of the protein-to-lipid ratio in order to facilitate detailed analysis. Following incorporation of McjD-C547 into liposomes at a protein-to-lipid ratio of 1:200, ALEX measurements identified a dominant population of McjD molecules corresponding to a low FRET state and a smaller subpopulation of McjD molecules at a high FRET efficiency (Figure 71A). The low FRET population for McjD-C547 demonstrates similarities to the state observed in our detergent data. However, visualisation of surface-immobilised McjD-C547 at a reconstitution ratio of 1:100 was complicated by (1) the incorporation of multiple McjD transporters in a single liposome and (2) the inability to identify double-labelled protein molecules on the surface. At an optimised protein-to-lipid ratio of 1:1000, a single low FRET state for McjD-C547 was observed by ALEX measurements and was accompanied by loss of the high FRET artefact (Figure 71B). Moreover, immobilisation of liposome incorporated McjD C547 (1:1000 ratio) resulted in the identification of single molecules labelled with two spectrally distinct fluorophores.

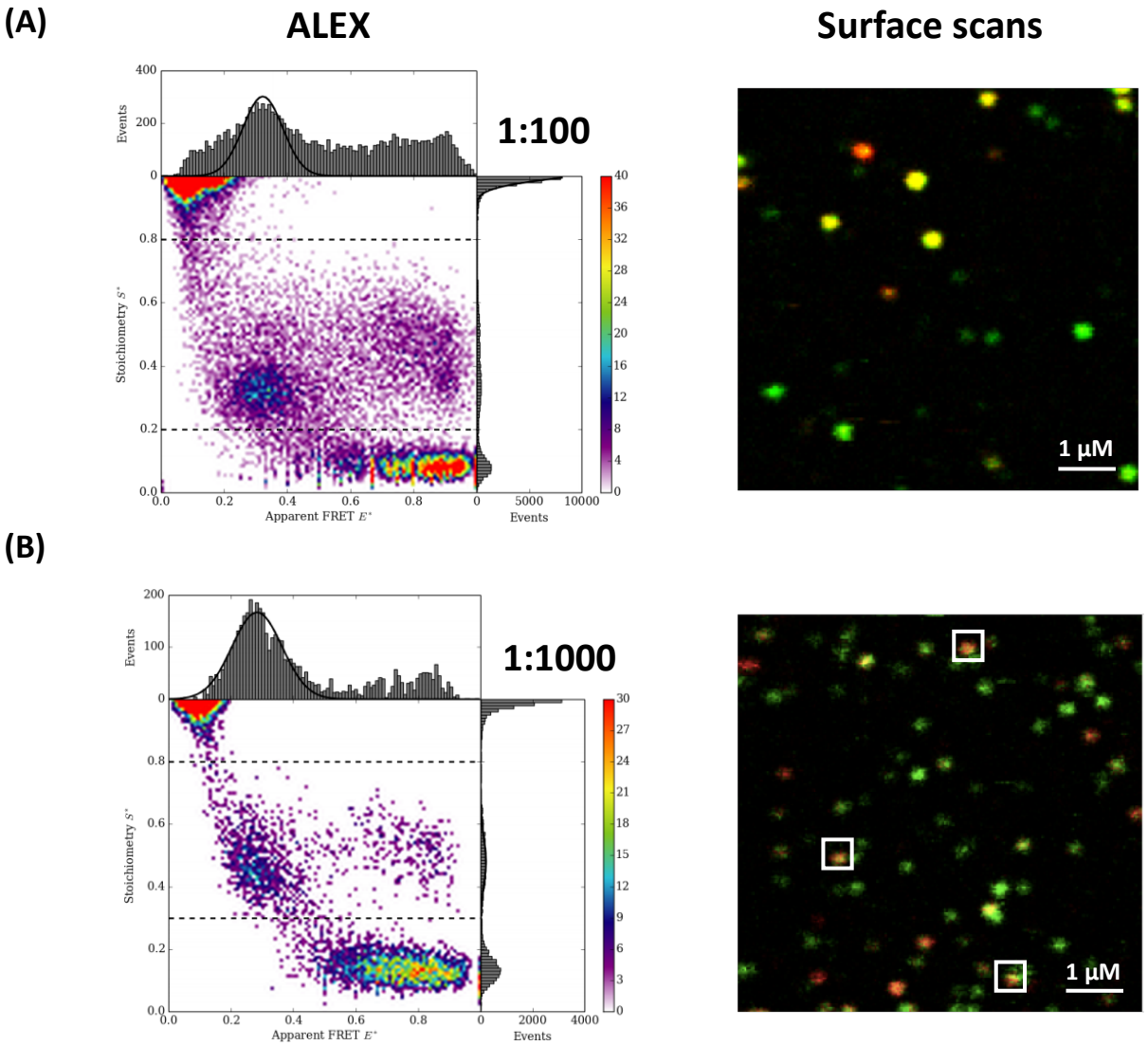


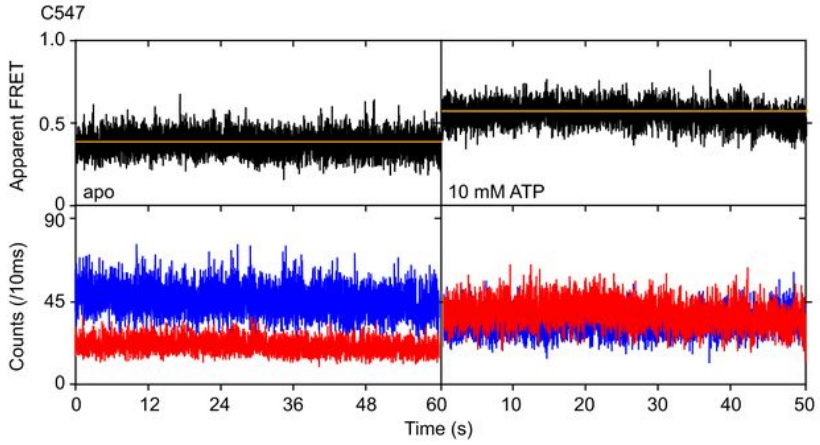
Figure 71. Optimisation of McjD liposome reconstitution for surface-immobilisation. The surface scans are shown in false-colour representation with orange, green, and red representing double-labelled McjD, McjD with donor fluorophore only, and McjD with acceptor fluorophore only. (A) Reconstitution of McjD-C547 at a protein-to-lipid ratio of 1:100. The ALEX profile shows a low FRET state at an efficiency of ~0.3 and a significant fraction of molecules adopting a higher FRET state. The surface scan indicates that few McjD molecules in liposomes were appropriately labelled with a donor-acceptor dye pair (orange). (B) Reconstitution of McjD-C547 at a protein-to-lipid ratio of 1:1000. The low FRET state predominates in the ALEX profile. The surface scan highlights double-labelled McjD molecules in white boxes, from which time traces were derived.

3.3.8. FRET observations of McjD C547 in liposomes

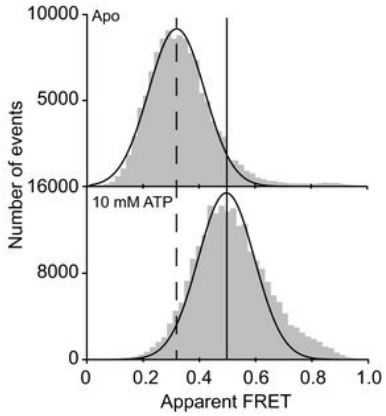
The smFRET liposome data acquisition and fitting were performed by Florence Husada, Konstantinos Tassis, Marijn de Boer and Thorben Cordes. Representative examples of single molecule time traces for the NBD mutant McjD-C547 are shown in Figure 72A. The FRET efficiencies observed with liposome incorporated McjD were comparable but not identical to the detergent data. Cumulative histograms for McjD-C547 generate average E* values of 0.32 in the absence of nucleotides and 0.50 in the presence of ATP (Figure 72B). These values are consistent with the transition between disengaged *apo* NBDs and formation of the dimerised state upon nucleotide binding. Interestingly, the FRET efficiency for the ATP-bound state is slightly lower in liposomes compared to detergent, suggesting that McjD can form a more open NBD dimer in liposomes.

Another notable finding is that McjD-C547 in the ATP-bound state does not display a bimodal distribution in the cumulative histograms. Random orientation of McjD in liposomes has been experimentally proven, and therefore only transporters whose NBDs facing the outside of the liposomes (~60%) would be expected to respond to the addition of ATP. The observation of a single population of McjD-C547 appears counterintuitive but there are two possible reasons for this discrepancy. Firstly, it is possible that a larger proportion of McjD-C547 transporters incorporate in liposomes in the 'NBD-out' orientation compared to wild-type protein. Secondly, a significant proportion of McjD-C547 molecules (~40%) were found to display very short photobleaching times that (< 1 s) that differ from the longer time traces shown in Fig. 84a. These very short time traces could all be attributed to the McjD-C547 transporters possessing the 'NBD in' orientation. Therefore, the altered photophysical properties of the fluorophores might explain why the NBD-out population dominates the cumulative histograms over the shorter traces from the NBD-in orientation that cannot react to the addition of ATP.

(A)



(B)



Condition	C547 (E*)
apo	0.32
ATP	0.50

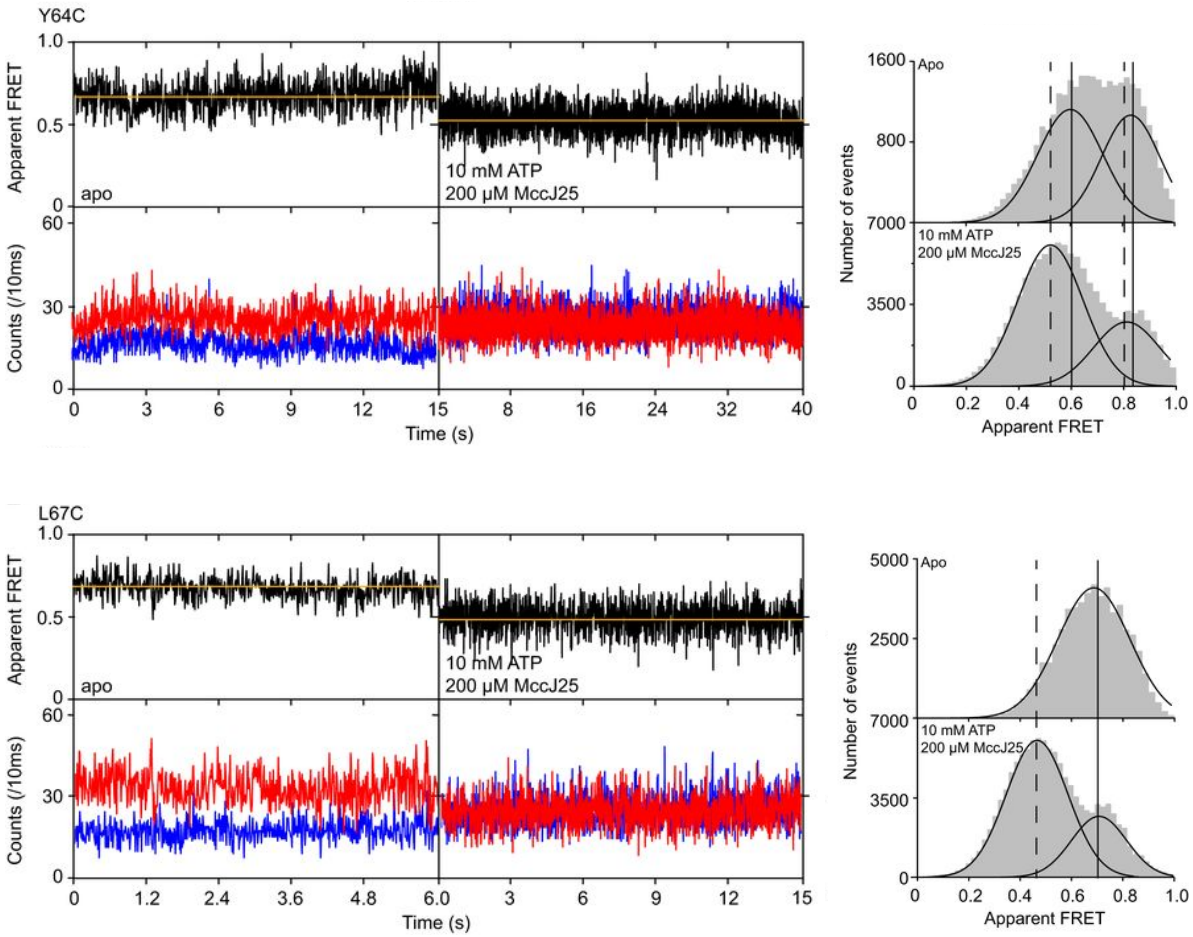
Figure 72. Conformational states of McjD-C547 in liposomes. (A) Representative single molecule fluorescence time traces (blue, donor signal; red, acceptor signal; black, FRET signal; yellow, fit) of labelled McjD-C547 in liposomes. The time traces for each condition are derived from independently examined single McjD molecules. (B) The panel to the left shows the accumulated time traces for the C547 mutant and the panel on the right shows the mean apparent FRET values (E*) for each environmental condition. The NBDs switch between a low FRET *apo* state and a high FRET ATP-bound state (Husada *et al*., 2018).

3.3.9. FRET observations of McjD Y64C and L67C in liposomes

The McjD TMD mutants were subsequently studied by smFRET measurements in liposomes. Under *apo* conditions, McjD-Y64C displays a bimodal distribution whereas the L67C mutant can be observed as a single population (Figure 73A). This finding may be due to the more dynamic nature of Y64C which is located further up TM1 that L67C and therefore less restricted in motion by the proteoliposome's lipid bilayer. Such distribution was not detected for *apo* L67C in detergent solution since the distance changes observed in this environment are small and therefore unlikely to be captured in the dynamic FRET range. The *apo* TMD mutants produce high E* values at positions Y64C (0.81) and L67C (0.69) that could be shifted to lower FRET states following the addition of ATP and MccJ25 (Figure 73B). In the presence of ATP and MccJ25, Y64C displays a lower E* value of 0.52 which is almost identical to the FRET efficiency observed for L67C (0.51). The bimodal distributions observed for this condition reflect the fact that a proportion of McjD molecules have transitioned to the outward-open state.

Interestingly, both TMD mutants display a more pronounced opening in liposomes compared to detergent micelles. These data provide the first direct evidence for a periplasmic opening of the McjD TMDs in the presence of nucleotides and substrate in a native-like environment. The cumulative FRET histograms observed for the TMD mutants are also consistent with the fact that only 60% of McjD transporters have the correct orientation (cytoplasmic NBD facing the outside of the liposome) required to react to MccJ25 and ATP, while 40% all of molecules stay in the *apo* state.

(A)



(B)

Condition	Y64C (E*)	L67C (E*)
apo	0.60 & 0.81	0.69
ATP + MccJ25	0.52 & 0.82	0.51 & 0.70

Figure 73. Conformational states of the McjD TMD mutants in liposomes. (A) The panel to the left shows representative single molecule fluorescence time traces (blue, donor signal; red, acceptor signal; black, FRET signal; yellow, fit) of labelled McjD-Y64C and L67C in liposomes. The time traces for each condition are derived from independently examined single McjD molecules. The panel to the right shows the accumulated time traces for each of the TMD mutants. (B) The mean apparent FRET values (E*) for each environmental condition indicate that the TMDs switch between a high FRET *apo* state to a lower FRET state in the presence of ATP and MccJ25 (Husada *et al*., 2018).

3.4. Discussion

3.4.1. McjD displays conformational dynamics in the NBDs

In addition to the work described in this chapter, smFRET was applied to investigate whether surface-immobilised McjD displays intrinsic conformational dynamics (Husada *et al*., 2018). In the presence and absence of nucleotides, no conformational dynamics were detected for the TMD mutants (L64C, Y67C) on timescales > 10 ms. These data indicate that the TMDs of McjD display a high level of structural rigidity under *apo* conditions.

In contrast, a significant fraction of 15% of *apo* McjD-C547 molecules generated rapid changes of FRET efficiency from the lower *apo* value of 0.3 to values > 0.5 which are comparable to those found in the presence of ATP. A representative time trace for a single McjD-C547 molecule displaying intrinsic fluctuations to the high FRET state is shown in Figure 74A. The low FRET state is shown to predominate for the majority of the trace. Among all McjD-C547 molecules displaying intrinsic FRET changes, the lifetime of the high FRET state was recorded on a timescale of ~100 ms (Figure 74B). These data support the existence of intrinsic conformational dynamics in the NBDs of McjD and may explain why McjD displays a relatively high level of basal ATPase activity in the absence of MccJ25.

The addition of ATP to McjD-C547 at concentrations similar to the K_d value, resulted in consistent transitions between the low and high FRET states on the timescale of seconds. Switching between FRET states occurred in both the low-to-high and high-to-low FRET directions (Figure 74C/D). The dynamic nature of the McjD NBDs might explain why PELDOR measurements recorded at position C547 were unable to define distance changes in the NBDs (Bountra *et al*., 2017).

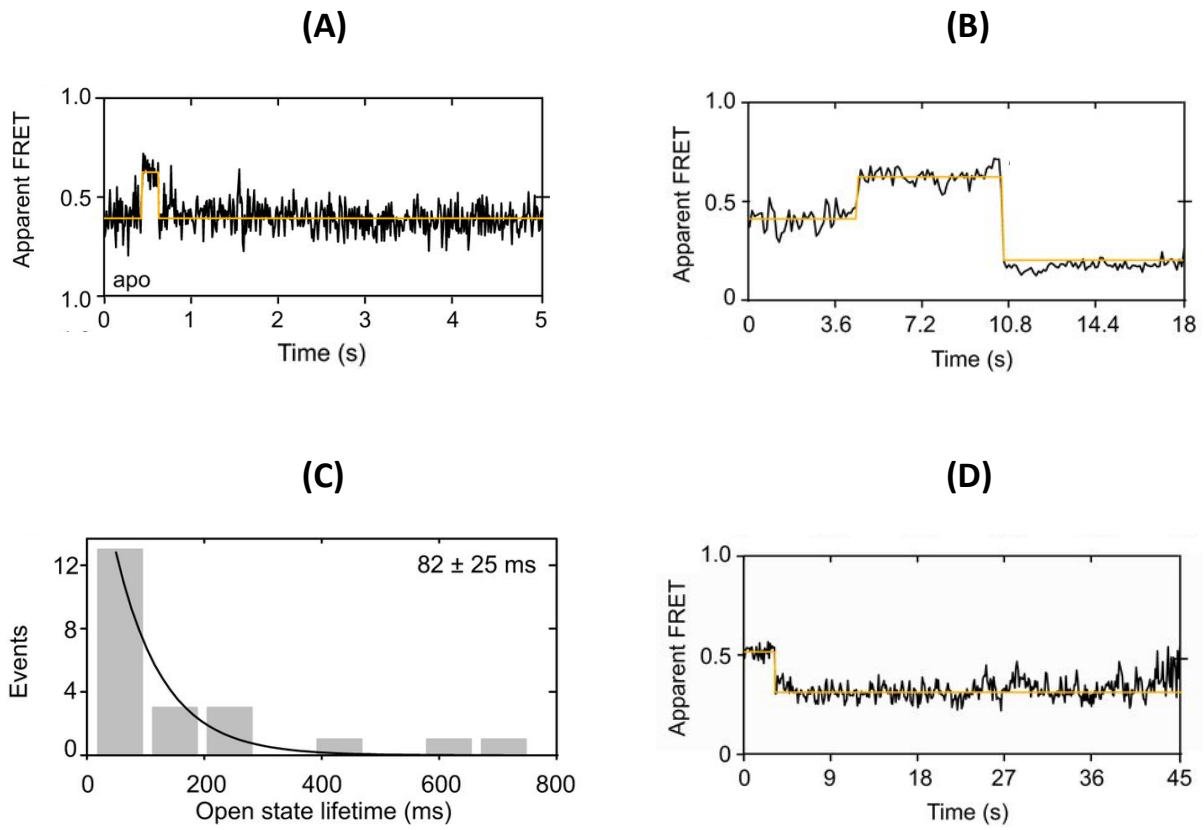


Figure 74. Conformational dynamics of the McjD NBDs. Apparent FRET changes refer to differences in E* values for single McjD C547 molecules with time. (A) Representative FRET time trace where an *apo* McjD-C547 molecule in the low FRET state (~0.3) spontaneously transitions to a high FRET state (> 0.5). (B) Among the 15% of McjD-C547 time traces showing spontaneous fluctuations (n = 80), the dwell time of the high FRET state has an average lifetime of 82 ± 25 ms. This observation indicates that the McjD NBDs can infrequently sample the dimerised state in the absence of nucleotides, a conformation that is normally associated with the nucleotide-bound state. (C) ATP-induced conformational dynamics of the McjD NBDs. A representative time trace for an McjD-C547 molecule showing switching between the ATP-loaded state (~0.3) and the ATP-free state (> 0.5) is shown. At t= 10 s, the molecule is photobleached. The duration of the ATP-loaded state is on the timescale of seconds. (D) Representative time trace for an McjD-C547 molecule switching from the ATP-free state (~0.5) to the ATP-loaded state (~0.3). Adapted from Husada *et al*. (2018).

3.4.2. NBD dynamics are a common feature of ABC transporters

The observation that a proportion of McjD molecules display intrinsic conformational dynamics, suggests that rather than ATP binding alone inducing a closed ATP dimer, the *apo* NBDs appear capable of sampling this conformation even in the absence of nucleotides. This finding is consistent with predictive cysteine cross-linking data for McjD indicating that the NBDs are in close proximity to one another (Bountra *et al*., 2017). The dynamics of the type IV ABC transporter BmrA have been previously probed by HDX (hydrogen/deuterium exchange) coupled to mass spectrometry (Mehmood *et al*., 2012). The intracellular loops of the NBDs displayed much faster HDX in the nucleotide free state compared to the nucleotide bound closed state, indicative of a high degree of flexibility in the NBDs under *apo* conditions. A molecular dynamics study of Sav1866 also reports that the NBD dimer interface becomes more mobile and hydrated in the absence of nucleotides (Becker *et al*., 2010).

3.4.3. Comparison between McjD and MsbA

The smFRET data recorded for McjD enable a detailed comparison to be made with a recent smFRET investigation MsbA (Table 7) (Liu *et al*., 2018). Unlike McjD which displays small conformational changes in the NBDs, MsbA displays large changes in FRET efficiency at the NBDs between the high and low FRET states, including an intermediate distribution in the presence of ATP-VO_4 that is likely to have a less compact NBD dimer than the high FRET state. The MsbA NBDs report E* values of ~0.2, ~0.6 and ~0.9 in liposomes corresponding to the low, intermediate and high FRET states respectively (Liu *et al*., 2018). These broad changes in FRET efficiency reflect wide conformational changes in the MsbA NBDs, consistent with PELDOR measurements that support a 20–30 Å closing motion upon nucleotide binding (Zou

et al., 2009). Intrinsic conformational dynamics have also been observed for the NBDs of MsbA on the timescale of ~200 ms, consistent with the value observed for McjD. MsbA was shown to switch between intermediate and low FRET states under *apo* conditions, whereas ATP shifted the equilibrium between intermediate and high FRET state transitions.

The smFRET efficiencies recorded in the TMD MsbA TMDs show transitions between E* values of ~0.8 and ~0.9 respectively (Liu *et al*., 2018). The lower FRET efficiency values were observed in the presence of AMP-PNP, ATP-VO_4 and ATP respectively, indicative of a small TMD opening, whereas for McjD none of these conditions induce conformational changes. The smFRET findings in the TMDs can be reconciled with PELDOR measurements reported for both MsbA and McjD (Table 7). For MsbA, a 7- to 10-Å opening motion is observed at the periplasmic side in the presence of nucleotides (Zou *et al*., 2009) whereas a stable occluded TMD dimer is detected for McjD.

3.4.4. The McjD TMDs are tightly coupled to ATP and MccJ25

The smFRET findings for McjD provide direct evidence that both ATP and MccJ25 are required for opening of the TMDs at the periplasmic side. Transition of the periplasmic TMD mutants to lower FRET efficiency states verify that the movement of TM1-2 to the opposite protomer has resulted in release of the peptide. Since conformational dynamics could not be detected in the McjD TMDs, opening of the periplasmic gate is tightly coupled to the binding of ATP and MccJ25. This mechanism of tight coupling may explain why McjD displays specificity for MccJ25 and cannot transport other substrates (Romano *et al*., 2018). McjD is likely to distinguish itself from multidrug ABC exporters such as MsbA where substrate binding is not strictly coupled to the TMDs (Table 7). In multidrug ABC exporters, the binding of ATP could facilitate promiscuous transport of ligands that have entered the transmembrane

cavity, whereas the McjD cavity can only open up in the presence of MccJ25. These functional differences in substrate coupling indicate that certain bacterial ABC exporters are likely to have evolved the function of multidrug resistance.

ABC exporter	McjD	MsbA
PELDOR of NBDs	NBDs are highly dynamic, distance distributions n.d.	Large amplitude conformational changes in the NBDs upon nucleotide binding (20–30 Å)
smFRET of NBDs (E*)	Low FRET *apo* state (0.3), high FRET ATP-bound state (0.5)	Low FRET *apo* state (0.2), intermediate state (0.6), high FRET ATP-bound state (0.9)
NBD dynamics	NBDs infrequently mimic closed ATP dimer form in the absence of nucleotides, 100 ms lifetime in the high FRET state	Transitions between low FRET apo state and intermediate state, 200 ms lifetime in the intermediate state
PELDOR of TMDs	No opening of the TMDs in the presence of nucleotides, or ATP in the presence of MccJ25	Opening at the periplasmic side of the TMDs in the presence of nucleotides (7–10 Å)
smFRET of TMDs (E*)	High FRET *apo*/nucleotide bound state (0.6-0.7), lower FRET state with added ATP + substrate (0.5)	High FRET *apo* state (0.9), lower FRET state (0.8) with added nucleotides
TMD dynamics	TMDs are static in *apo* and nucleotide bound states	n.d.
Opening of the TMDs	Tightly coupled to binding of both ATP and MccJ25	Triggered by binding of ATP alone, not coupled to substrate binding
Outward-open state	Transient outward-open state to release bound peptide	Stable outward-open state for drug efflux

Table 7. Mechanistic comparison between McjD and MsbA.

3.4.5. Refined transport model for McjD based on smFRET

Based on the smFRET data, several aspects of the McjD transport mechanism can now be clarified. The observation of intrinsic conformational dynamics in the McjD NBDs, verifies that in the absence of nucleotides, the NBDs can sample different conformations including a state that is indistinguishable from the closed NBD dimer. ATP binding leads to the NBDs becoming fully populated in the closed state, and the addition of MccJ25 further stimulates the ATPase activity of the transporter. In the presence of ATP alone, there is no opening of the TMDs and, in addition, the TMDs display no conformational dynamics. However, in the presence of ATP and MccJ25, the McjD TMDs open up as seen directly by smFRET to release the bound peptide before ATP hydrolysis restores the occluded state.

In conclusion, the work described in this chapter highlights the value of applying smFRET to investigate the mechanisms of ABC transporters. McjD provides a model system for ABC exporters to first, unravel their conformational dynamics and second, facilitate complete understanding of their transport cycles.

Chapter 4: Staphylococcal peptide ABC exporters

4.1. Introduction

4.1.1. *Staphylococcus aureus* toxins

Staphylococcus aureus is a Gram-positive pathogen responsible for hospital and community-associated infections that cause considerable morbidity on a global scale (Lowy, 1998). In healthy individuals, *S. aureus* is present on the skin and mucous membranes but for patients that are immunocompromised, *S. aureus* entry into the bloodstream results in a number of serious infections. *S. aureus* infections persist in the respiratory tract, skin and soft tissues, but can also lead to other diseases including endocarditis, osteomyelitis and toxic shock syndrome (TSS) (Lowy, 1998). Transmission of *S. aureus* can occur by direct person-to-person contact or through contaminated prosthetic medical devices. The treatment of staphylococcal infections is severely compromised by the development of bacterial antibiotic resistance, particularly in response to methicillin (Lowy, 2003). Methicillin-resistant *S. aureus* (MRSA) strains among hospital isolates are reported to exceed 50% in many countries (Cheung *et al*., 2014).

The virulence capacity of *S. aureus* is attributed to the production of a large range of toxins, either present in mobile genetic elements (MGEs) (Novick *et al*., 2001) or encoded in the core genome (Cheung *et al*., 2014). While MGE encoded toxins can be transmitted between strains through lateral gene transfer, they are typically only found in a subset of isolates (Novick *et al*., 2001). Among toxins encoded in the core genome, δ-toxin and the phenol soluble modulins (PSMs) are present in all staphylococcal strains (Cheung *et al*., 2014). Abolishing the production of *S. aureus* toxins is an attractive therapeutic strategy to combat MRSA (Oliveira *et al*., 2018).

4.1.2. Phenol soluble modulin classes

Phenol soluble modulins are a class of amphipathic, α-helical peptides (Wang *et al*., 2013). In *S. aureus*, PSMs are encoded in three regions of the genome. Four PSMα peptides (PSMα1-4) are encoded in the *psmα* operon and two PSMβ peptides (PSMβ1-2) are encoded in the *psmβ* operon. The δ-toxin meanwhile is an α-type PSM located within the coding sequence of the effector molecule RNAIII. (Kaito *et al*., 2011). Apart from *S. aureus*, the only staphylococcal species whose PSMs have been characterised is *S. epidermis* which produces PSMα, PSMβ1, PSMβ2, PSMδ, PSMε and δ-toxin (Peschel and Otto, 2013). PSMs can be grouped into two types according to the length of the corresponding amino acid sequence (Figure 75). PSMα peptides are 20-25 amino acids in length with the complete sequence forming an α-helix. PSMβ peptides are 43-45 amino acids long and only the C-terminal region of the sequence adopts α-helical topology. The PSM classes can also be distinguished on the basis of their charge properties. Within the *S. aureus and S. epidermis* subtypes, PSMα peptides are mostly net positively charged, while all PSMβ peptides contain negative charges and the δ-toxin is neutral (Peschel and Otto, 2013).

The production of PSMs is under tight control from the accessory gene regulator (Agr) quorum-sensing system (Queck *et al.*, 2008). The Agr system is comprised of two adjacent transcriptional units, RNAII and RNAIII, which are transcribed in opposite directions. Unlike most genes in the Agr regulon, which are controlled by the RNAIII locus, transcription of *psm* genes is independent of RNAIII regulation (Queck *et al*., 2008). The RNAII locus encodes a histidine kinase (*agrC*) and a response regulator (*agrA*) which together make up a two-component signal transduction system, and two further genes encoding an autoinducing peptide (AIP) precursor (*agrD*) and an AIP maturation and export protein (*agrB).* When AgrC detects critical concentrations of AIP, AgrA is activated and binds to the promoters of *psm* genes, thus

stimulating PSM production. Certain strains of *S. aureus* also produce the α-helical PSM-mec, which is not encoded in the core genome and instead is found within mobile staphylococcal cassette chromosome elements (Queck *et al*., 2009). PSM-mec contains a unique cysteine residue that is not found within the sequences of any other PSM, but forms an essential part of its secondary structure (Queck *et al*., 2009).

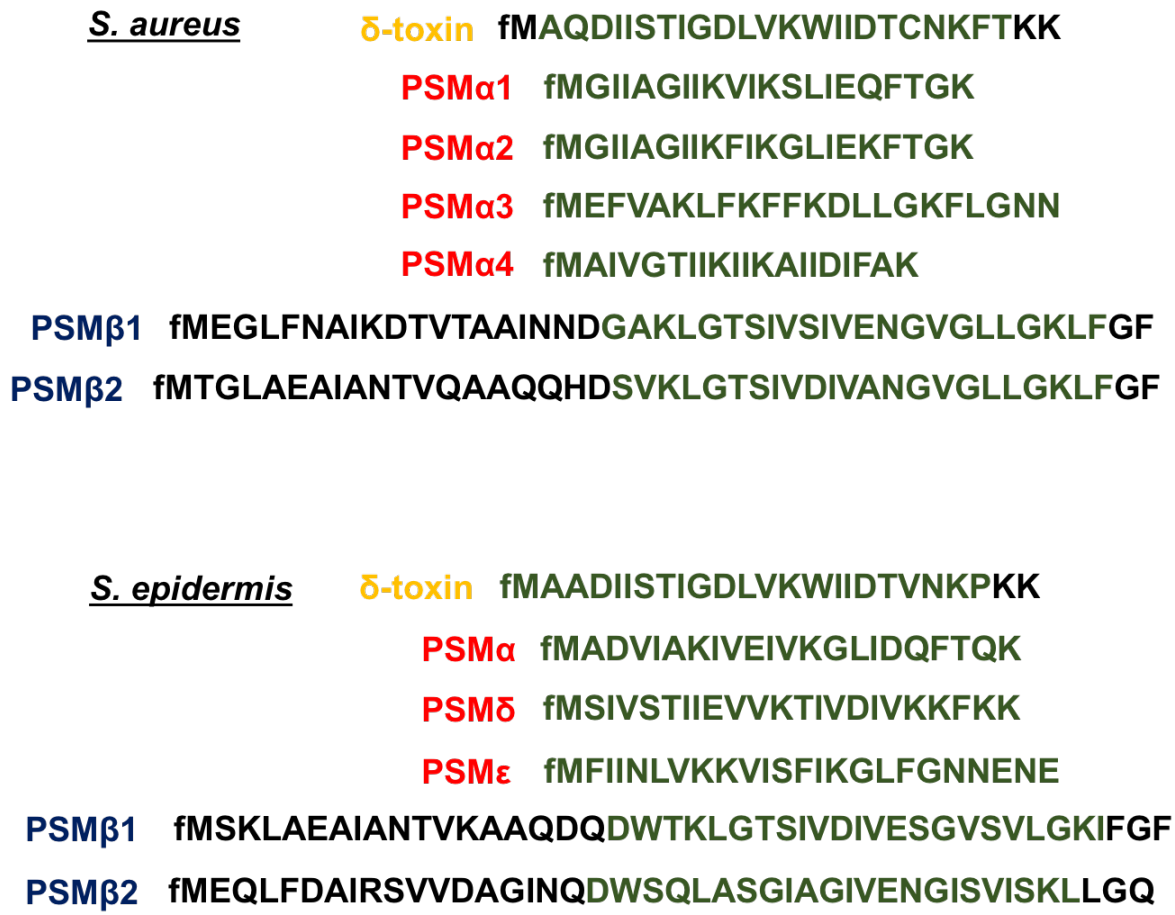


Figure 75. Sequences of gene encoded PSMs in *S. aureus* and *S. epidermis*. Amino acids forming the amphipathic α-helical domain are highlighted in green. PSM subtypes are denoted by their overall charges: neutral (yellow), positive (red), negative (blue). The amino acid sequences begin with a formylated methionine. The complete sequence of PSMα peptides forms an α-helix whereas PSMβ peptides form an α-helix towards the C-terminus. The δ-toxin is classed as an α-type PSM peptide. Adapted from Peschel and Otto (2013).

4.1.3. Phenol soluble modulin functions

PSMs play multiple key roles in the pathogenesis and infection cycle of *S. aureus* (Peschel and Otto, 2013) (Figure 76). There is mounting evidence that specific PSM classes are associated with specific disease phenotypes. PSMα peptides have strongly cytolytic properties owing to their amphipathic nature and α-helicity (Peschel and Otto, 2013). Specifically, in *S. aureus*, PSMs are responsible for the lysis of neutrophils and red blood cells. The PSMβ functions are less clear although there is evidence that they are involved in biofilm restructuring and the dissemination of biofilm-associated infections (Periasamy *et al*., 2012). However, this role does not appear to be specific to PSMβ peptides as other classes appear to contribute to biofilm development. The δ-toxin of *S. aureus* has a unique role in stimulating the degranulation of mast cells (Nakamura *et al*., 2013).

PSMs are thought to enable gliding motility in *S. aureus* due to their surfactant-like properties which enable colonisation and spreading across surfaces (Wang *et al*., 2007). They can also act as pro-inflammatory mediators, initiating chemotaxis in neutrophils and promoting the release of cytokines through activation of formyl peptide receptor 2 (FPR2) (Kretschmer *et al*., 2010; Wang *et al*., 2007). FPR2 belongs to the family of G-protein coupled receptors (GPCRs). In addition, PSMs mediate the secretion of the pro-inflammatory cytokine IL-18 from keratinocytes, which enhances inflammation in the skin (Syed *et al*., 2015). PSMs are thought to direct antimicrobial activity towards other bacterial species such as *Streptococcus pyogenes* but the mechanisms underlying this activity are yet to be determined (Cogen *et al*., 2010; Joo *et al*., 2011). Recently, it was demonstrated that PSMα3 peptides assemble into elongated, self-associating fibrils formed by the stacking of amphipathic α-helices. Cross α-fibrillation results in amyloid-like structures that contribute to cytotoxicity in *S. aureus* (Tayeb-Fligelman *et al*., 2017).

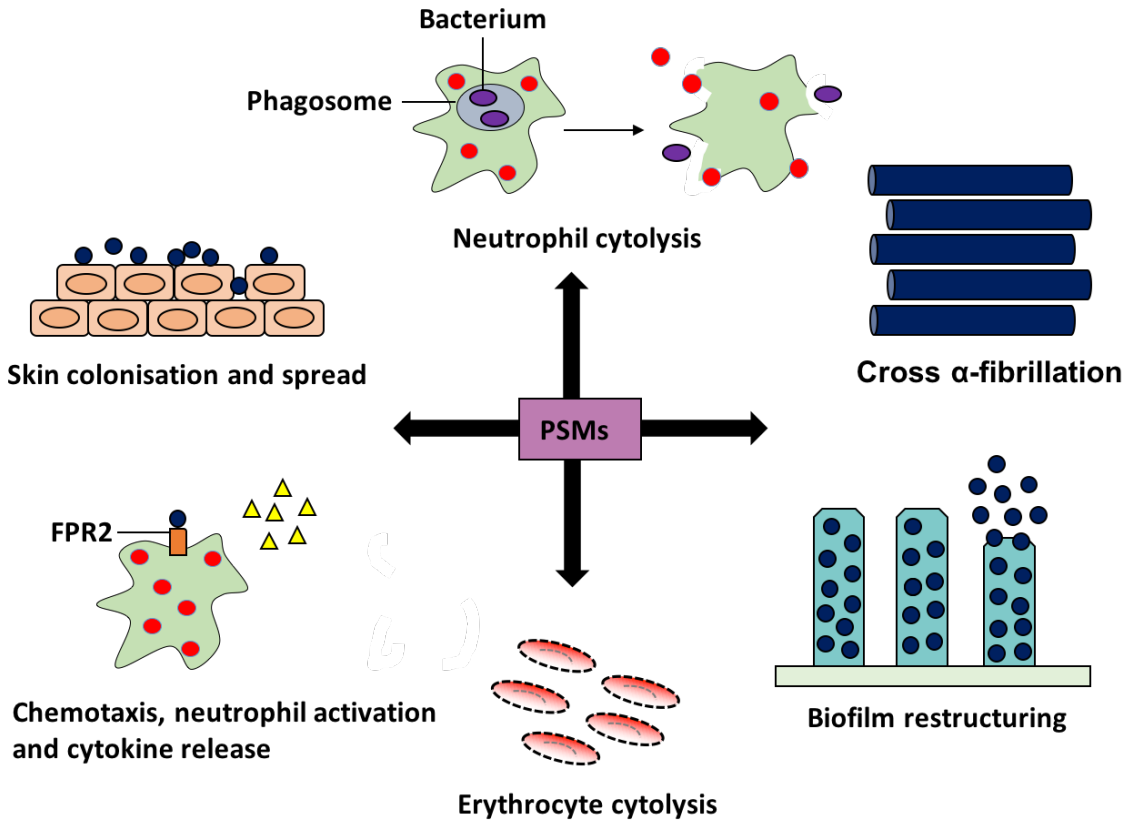


Figure 76. Summary of PSM functions in pathogenesis. PSMs are important mediators of virulence in *Staphylococci*. They are responsible for the cytolysis of neutrophils and red blood cells. PSMs also activate the GPCR, human formyl peptide receptor 2, resulting in secretion of pro-inflammatory cytokines. Other roles for PSMs include skin colonisation and spreading on surfaces due to their pronounced amphipathy, and the polymerisation of PSMs into fibrillary, amyloid-like structures. PSMs also exert antibacterial activity against other bacterial species and can regulate biofilm development. Adapted from Peschel and Otto (2013).

4.1.4. Pmt

PSMs can be secreted in the absence of a signal peptide while maintaining the N-terminal formyl methionine group. The lack of a signal peptide suggests that dedicated transport systems are required for PSM secretion. In *S. aureus*, two ABC efflux pumps have recently been identified to transport PSM peptides, designated Pmt (Chaterjee *et al*., 2013) and AbcA (Yoshikai *et al*., 2015). Pmt is a heterotetrameric ABC exporter containing two distinct NBDs (PmtA, PmtC) and two distinct TMDs (PmtB, PmtD) (Figure 77) (Chaterjee *et al*., 2013). The four genes encoding the transporter are located in the same polycistronic operon under the control of the Agr regulatory system, that is also required for the transcription of PSM encoded genes.

Chaterjee *et al*. (2013) constructed *psm* and *pmt* deletion strains, demonstrating that secretion of all PSMs is strongly dependent on Pmt in *S. aureus* and also necessary for bacterial cell survival. In the absence of *pmt*, PSM peptides accumulate in the cytosol, resulting in abnormal cell division and damage to the cytoplasmic membrane. Pmt from *S. aureus* confers producer self-immunity towards PSMs and, interestingly, also provides resistance to PSMs from *S. epidermis*. This suggests that, during host colonisation, Pmt provides a protective role against competing staphylococcal species. The Pmt-dependent virulence phenotypes include lysis of neutrophils and erythrocytes, biofilm development, and skin infection: equivalent to the sum total of all PSM effects. Since there is high divergence among PSM amino acid sequences, the α-helicity and amphipathic nature of the peptides are likely to be key determinants for Pmt recognition.

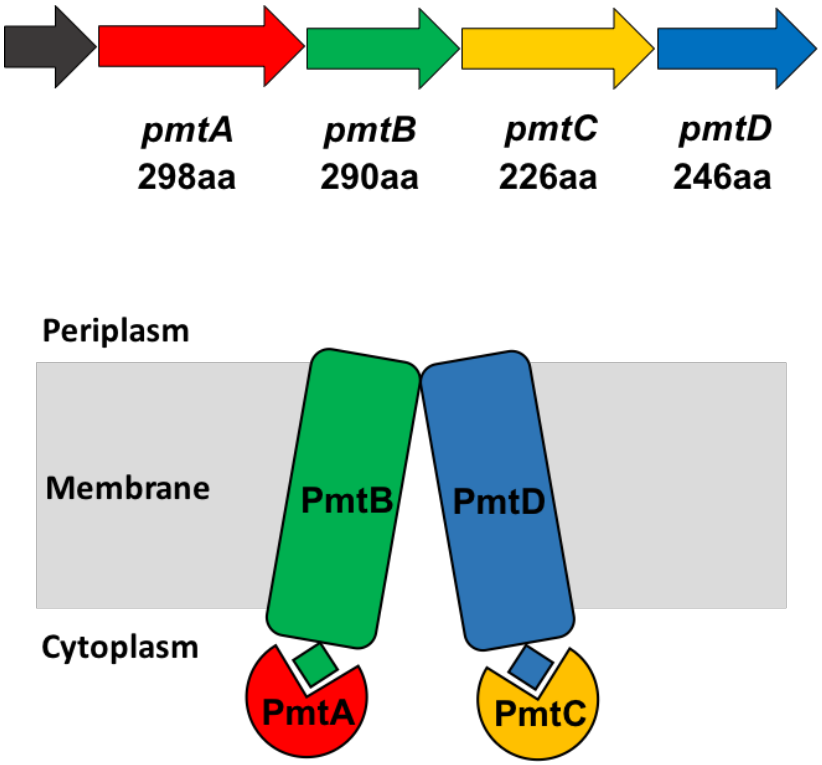


Figure 77. Gene organisation and arrangement of Pmt. The *pmt* genes are arranged in an operon. The *pmtA* and *pmtC* genes encode the NBDs while *pmtB* and *pmtD* genes encode the TMDs. In front of the *pmt* genes is a putative regulatory protein indicated by the black arrow. The heterotetrametic architecture of the complete transporter is shown.

4.1.5. AbcA

AbcA is a homodimeric ABC exporter encoded in a single polypeptide chain that is found in all staphylococcal strains. Expression of AbcA is controlled by the Agr quorum sensing system, the transcription factor NorG and the regulatory proteins MgrA, Rot, SarA and SarZ. AbcA expression levels are upregulated following antibiotic treatment and during conditions of stress where *S. aureus* virulence factors are produced (Villet *et al*., 2014). AbcA contains high sequence homology to the multidrug ABC exporters MsbA, LmrA and Sav1866 (Yoshikai *et al*., 2015). Overexpression of *abcA* results in resistance to the β-lactam antibiotics methicillin and cefotaxime, the phosphoglycolipid moenomycin, the lipopeptide antibiotic daptomycin, and dyes including rhodamine, ethidium bromide and Hoechst (Truong-Bolduc *et al*., 2007).

In addition to these roles in multidrug resistance, AbcA is also involved in the export of PSMs. Surprisingly, the amino acid sequence of AbcA displays only 14% sequence identity compared to each half of the Pmt transporter (PmtA/B, PmtC/D) (Yoshikai *et al*., 2015). However, the contribution of AbcA to PSM export is comparable to that of Pmt, as shown by the similar levels of PSMs secreted in *abcA* and *pmtC* knockouts respectively. Secretion of PSMs by AbcA occurs in a Pmt-independent manner, since a double knockout of *abcA/pmtC* abolishes PSM export at a greater rate compared with the single mutant *pmtC*. Moreover, the expression levels of Pmt and AbcA are not affected by one another (Yoshikai *et al*., 2015). Unlike *pmt* deletion strains of *S. aureus* which have impaired growth and bacterial cell death (Chaterjee *et al*., 2013), *abcA* knockouts are viable with similar growth to the wild type strain (Yoshikai *et al*., 2015). This suggests that the phenotypic consequences of PSM secretion differ in AbcA from Pmt, and could relate to the requirement of Pmt for *S. aureus* growth processes. Nonetheless, mice containing *abcA* gene knockouts display attenuated virulence which is indicative of an important role in *S. aureus* infection (Yoshikai *et al*., 2015).

4.1.6. Aims

Although there are numerous bacterial ABC exporter structures now available, the only representatives from peptide systems are McjD (Choudhury *et al*., 2014), PCAT (Lin *et al*., 2015), TmrAB (Nöll *et al*., 2017) and PrtD (Morgan *et al*., 2017). In light of the distinctive mechanism proposed for McjD, where the transporter exists in a predominantly occluded conformation (Bountra *et al*., 2017), characterising and determining structures of novel antibacterial peptide ABC exporters is likely to reveal additional features common to this subset of proteins. Given the fundamental roles of PSM peptides in *S. aureus* pathogenesis (Peschel and Otto, 2013), the dedicated secretion systems Pmt and AbcA represent important potential drug targets for intervening in PSM production. The Pmt transporter is of particular interest, owing to its unusual heterotetrameric architecture which has not been observed in structures of ABC exporters determined to date. An important first step in studying these transporters at the biochemical level is obtaining milligram quantity yields of pure protein and demonstrating activity in a native lipid environment. As such, the specific aims of this work were as follows:

- Expressing and purifying constructs of Pmt from *S. aureus*.
- Cloning, expressing and purifying AbcA from *S. aureus*.
- Measuring the ATPase activity of Pmt/AbcA in liposomes and performing crystallisation trials.

4.2. Materials and Methods

4.2.1. Cloning of Pmt

The full length *pmtA-D* genes (accession numbers: *pmtA* (A0A0D6HCS0), *pmtB* (W8U4M3), *pmtC* (X5EJW5), *pmtD* (W8TV14)) were PCR amplified from *Staphylococcus aureus* DNA and cloned into the pOPINEneo and pOPINEneo-3C-GFP vectors by the Oxford Protein Production Facility. This generated a C-terminal His_8 tagged protein containing a carboxypeptidase cleavage site and a C-terminal GFP-His_8 tagged protein containing a 3C protease cleavage site.

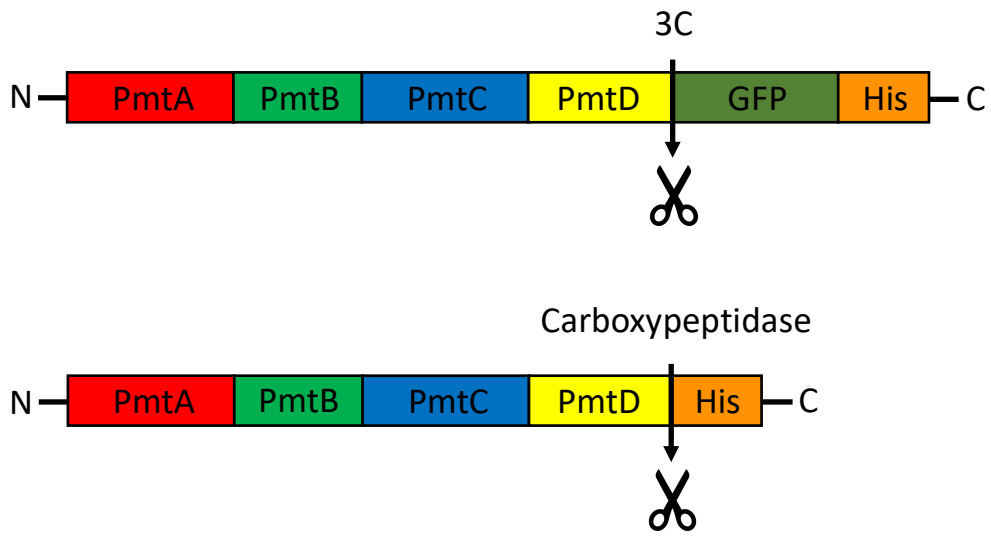


Figure 78. Schematic representation of Pmt constructs.

4.2.2. Cloning of AbcA

The full length *AbcA* gene (accession number: Q53614, residues 1-575) was PCR amplified from *S. aureus* genomic DNA and cloned into the pWaldo-GFPd vector using the restriction sites *Nde1* and *BamH1*. This resulted in a C-terminal GFP-His_8 tagged protein containing a TEV protease cleavage site. The forward primer contained the sequence 5'-CGC CAT ATG AAA CGA GAA AAT CCA TTG-3'. The reverse primer contained the sequence 5'-CGC GGA TCC ATC TGT TAA TTT TTG AGA CAC TAC-3'.

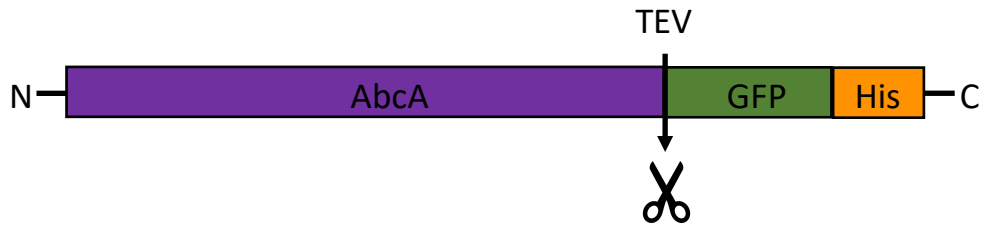


Figure 79. Schematic representation of AbcA-GFP-His construct.

4.2.3. Protein expression and membrane preparation

The Pmt constructs were transformed into the C43 (DE3) strain of *E. coli* on LB-agar plates containing ampicillin (50 µg/mL). AbcA-GFP-His_8 was transformed into C43 (DE3) cells on LB-agar plates containing kanamycin (34 µg/mL). Protein expression, membrane preparation and detergent solubilisation were performed using the same methods described for McjD (sections 2.2.1 – 2.2.3).

4.2.4. FSEC

The stability of Pmt-GFP-His_8 and AbcA-GFP-His_8 in different detergents was tested by fluorescence-detection size exclusion chromatography (FSEC). Aliquots of the ISOVs (900 µL) in 1 X PBS were first prepared in 1.5 mL microcentrifuge tubes. 100 µL of the detergent stocks below were added to the relevant membrane solutions and incubated at 4° C for 1 h on an elliptical roller with gentle shaking.

Detergent	Abbreviation	Proteins tested	Stock % (w/v)
n-Dodecyl-β-D-Maltopyranoside	DDM	Pmt and AbcA	10
Lauryl Maltose Neopentyl Glycol	LMNG	Pmt and AbcA	10
Octaethylene Glycol Monododecyl Ether	C12E8	Pmt and AbcA	10
n-Dodecyl-N,N-Dimethylamine-N-Oxide	LDAO	AbcA	10
n-Decyl-β-D-Maltopyranoside	DM	AbcA	10
6-Cyclohexyl-1-Hexyl-β-D-Maltoside	Cymal-6	AbcA	10
n-Octyl-β-D-Maltopyranoside	OM	AbcA	30
n-Octyl-β-D- Glucopyranoside	OG	AbcA	30

Table 8. List of detergents used for FSEC screening of Pmt and AbcA.

Following detergent solubilisation, the aliquots were spun in a benchtop ultracentrifuge at 150,000 *g* for 30 min for removal of unsolubilised material. The supernatant containing solubilised membranes was injected onto the Superose 6 10/300 GL Shimadzu High Performance Liquid Chromatography System, equilibrated in a buffer containing 20 mM Tris (pH 7.5), 150 mM NaCl and 0.03% DDM. The GFP fluorescence was quantified at an excitation wavelength of 470 nm and an emission wavelength of 512 nm. The resulting fluorescence traces were plotted against fraction volume.

4.2.5. Purification of Pmt-GFP-His

Pmt-GFP-His_8 was purified in 0.03% DDM using the method described in section 2.2.3 for McjD-GFP-His_8 with the following modification. After the first nickel purification step, the eluted Pmt-GFP-His_8 was treated with 3C protease (0.5 mg 3C protease per 1 mg GFP) for overnight cleavage and dialysis in a buffer containing 20 mM Tris (pH 7.5), 150 mM NaCl and 0.03% DDM. Following the reverse nickel and size exclusion steps, the protein was loaded onto Novex Tris-Glycine gels (Thermo Fisher Scientific), analysed by in-gel fluorescence and visualised using an ImageQuantLAS4000 (GE Healthcare).

4.2.6. Purification of Pmt-His

Pmt-His_8 was purified using the procedures detailed in section 2.2.3, up to and including the first nickel step, with one modification. In place of 1 X PBS, all relevant buffers were composed of 50 mM HEPES (pH 7.5) and 50 mM NaCl. The eluted Pmt-His_8 was processed in two different ways.

(1) Dialysed overnight in a buffer containing 20 mM Tris (pH 7.5), 50 mM NaCl and 0.03% DDM, concentrated to a volume of < 500 µl and injected into a Superdex S200 10/300 gel filtration column equilibrated in the same buffer.

(2) Passed through a PD-10 desalting column (Amersham Biosciences) immediately after the first nickel elution step, concentrated to a volume of < 500 µl and directly injected into the gel filtration column equilibrated in the buffer used for step 1.

4.2.7. Purification of AbcA-GFP-His

AbcA-GFP-His_8 was purified in 0.03% DDM according to the methods described in section 2.2.3 for McjD-GFP-His_8 with the following modifications. Prior to binding to nickel resin, the supernatant was brought to 30 mM imidazole (pH 8.5) and following incubation for 4 h, the resin was washed with 8 X CV of a buffer containing 40 mM imidazole (pH 8.5) and 0.1% DDM in 1 X PBS. The AbcA-GFP-His_8 fusion was eluted in a similar buffer containing 250 mM imidazole (pH 8.5). TEV protease was added (1 mg TEV per 1 mg GFP) and the protein was dialyzed overnight in a buffer containing 20 mM Tris (pH 8.5), 150 mM NaCl and 0.03% DDM. After collection of the flow through from the reverse nickel step, the cleaved protein was injected into a Superdex S200 10/300 gel filtration column equilibrated in the same buffer and fractions corresponding to AbcA at ~12 mL were pooled together and concentrated to 12 mg/mL for crystallisation trials. For crystallisation trials in C12E8 (Anatrace) and LMNG (Anatrace), the flow through from the reverse nickel step was passed through a Superdex S200 column. The gel filtration column was equilibrated in a buffer containing 20 mM Tris (pH 8.5) and 150 mM NaCl, supplemented with either 0.01% C12E8 or 0.003% LMNG. The collected fractions were pooled and concentrated to a final concentration of 12 mg/mL for crystallisation.

Purification step	Amount of AbcA
Protein expression	60 mg
Cell disruption	30 mg
Membrane preparation	26 mg
Detergent solubilisation	21 mg
Nickel IMAC elution	10 mg
Reverse IMAC elution	9 mg
Gel filtration	7 mg
Concentration to 12 mg/mL	4.5 mg

Table 9. AbcA purification table. The amount of wild-type McjD recovered at each step of purification from a typical 12 L expression is shown. Values shown up until the nickel IMAC elution step were derived by first calculating the total GFP concentration. Thereafter, the AbcA concentration was estimated by measuring the absorbance at 280 nm (ε = 7.8 M^{-1} cm^{-1}).

4.2.8. Crystallisation trials of AbcA

Crystallisation trials were performed with 12 mg/mL AbcA purified in DDM (0.03%), C12E8 (0.015%) and LMNG (0.003%) respectively. The following screen plates were tested against AbcA: MemGold1, MemGold2 and MemTrans (Molecular Dimensions). The protein and reservoir solution were mixed at a ratio of 1:1 using a Mosquito robot (TTP LabTech) set to the sitting drop method. The plates were incubated at 4° C and 20° C respectively.

4.2.9. Liposome incorporation of AbcA

E. coli polar lipid extract (Avanti Polar Lipids) and egg L-R-phosphatidylcholine (Sigma Aldrich) at 20 mg/ mL in chloroform were combined in a 1:3 ratio (w/w). Chloroform was removed by rotary evaporation under N_2 gas. The lipids were hydrated in a buffer containing 50 mM Tris (pH 7.5) and 50 mM KCl, followed by sonication in a water bath for 15 min at

25° C. Purified AbcA was added at a protein-to-lipid ratio of 1:50 (w/w) and incubated at 25° C with gentle agitation for 30 min. DDM was subsequently removed by incubation with 80 mg/mL SM2 BioBeads (BioRad) for 2 h at room temperature. BioBeads were then separated by filtration through a disposable spin filter column. The protein/lipid solution was further incubated with 8 mg/mL Biobeads at 4° C for 2 h and 16 h respectively, ensuring removal of the Biobeads after each cycle. The proteoliposomes were collected by centrifugation at 100,000 *g* for 1 h. The supernatant was discarded and the pellets were resuspended in the hydration buffer to 0.5 mg/mL for immediate use in experiments.

4.2.10. ATPase assays

ATPase assays with AbcA in detergent or reconstituted in liposomes were performed using the same methods described in section 2.2.11. The ATPase activity was not quantified due to negligible changes in absorbance at 360 nm.

4.3. Results

4.3.1. FSEC screening of Pmt-GFP-His

To facilitate purification of the intact Pmt transporter, the integrity and stability of the complex was examined by fluorescence detection size exclusion chromatography (FSEC) in solubilised crude membranes. FSEC exploits the unique fluorescence signal of GFP to assess the monodispersity and approximate molecular mass of a membrane protein without the requirement for further purification steps (Kawate and Gouaux, 2006). Accordingly, ISOVs containing the overexpressed Pmt-GFP-His construct were solubilised against a panel of detergents to assess their suitability for purification. Detergent extraction of Pmt was carried out in the presence of DDM, C12E8 and LMNG respectively (Figure 94). DDM is the most commonly used detergent during solubilisation owing to its mild properties and relatively low CMC (critical micelle concentration) value (Stetsenko and Guskov, 2017). C12E8 has been successfully used for the purification and crystallisation of several ABC transporters including Sav1866 (Dawson and Locher, 2006). LMNG has a large micelle size, that is suitable for the extraction and stabilisation of delicate membrane proteins (Stesenko and Guskov, 2017). In contrast, harsh detergents such as LDAO with compact micelle sizes tend to be conducive to the formation of stable integral membrane complexes.

Since the molecular weight of the homodimeric ABC transporter McjD (130 kDa) closely matches that of the Pmt complex (128 kDa), the profile of DDM-extracted McjD was examined by FSEC to predict the expected elution volume for Pmt. Following the detergent screen of Pmt, solubilisation by both DDM and LMNG yielded monodisperse fluorescence peaks with extraction efficiencies of 80% and 68% respectively. However, while the elution volume for DDM-extracted Pmt (~50 mL) was similar to the value observed for McjD (~49 mL), LMNG-extracted Pmt eluted at a later volume (~53 mL). One possible explanation is that following

solubilisation with LMNG, Pmt was not isolated in the heterotetrameric state, resulting in a lower molecular weight complex. The broad peak distribution observed for C12E8-extracted Pmt combined with the low efficiency of solubilisation (~30%) from membranes suggests that the transporter is not stable in C12E8. Taken together, the results from FSEC screening indicate that DDM extraction represents the best condition for large scale purification.

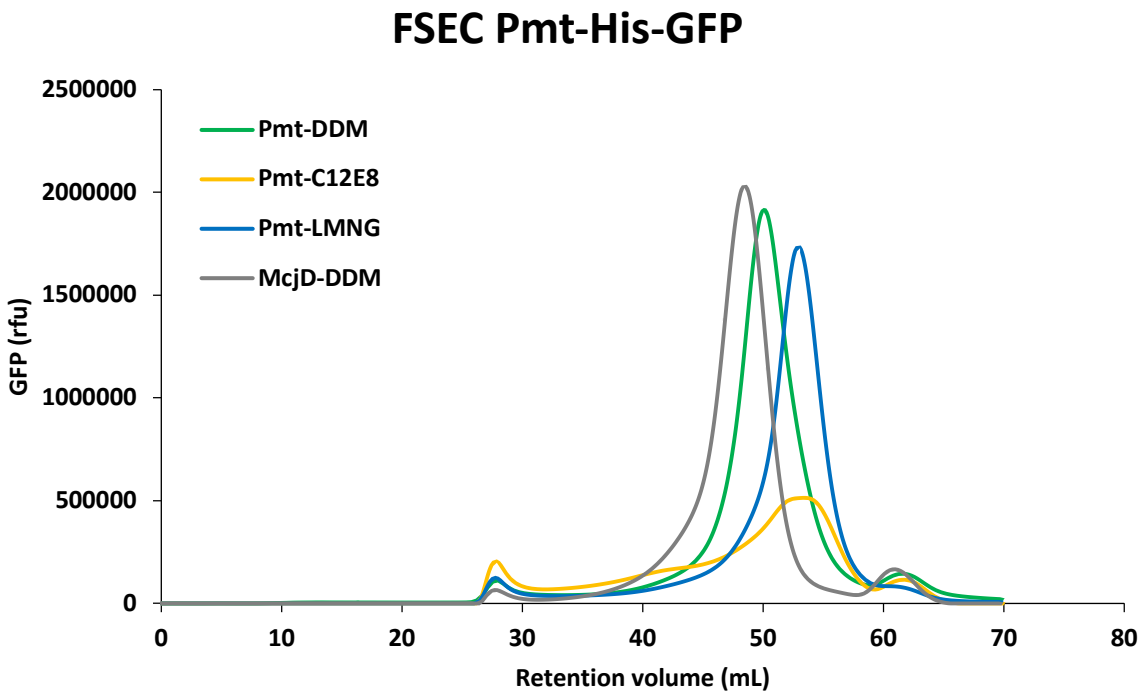


Figure 80. FSEC profile of Pmt-GFP-His in different detergents. Pmt produces monodisperse FSEC peaks following extraction in DDM and LMNG. Since the elution volume for Pmt in DDM closely matches that of McjD in the same detergent, and both proteins have similar molecular weights, this suggests that Pmt has been extracted in DDM as a heterotetramer.

4.3.2. Purification of Pmt-GFP-His

Purification of Pmt-GFP-His in DDM was initially tested using the same conditions required for purifying McjD. Although FSEC analysis indicated the transporter could be solubilised to a high level of monodispersity, further purification appeared to be disruptive to Pmt. The eluate of Pmt-GFP-His from the nickel IMAC step was examined by in-gel fluorescence, resulting in the detection of bands at ~35 kDa and ~22 kDa respectively (Figure 81). The lower molecular weight band represents free GFP, whereas the band at ~35 kDa is likely to correspond to the PmtD subunit since it is directly upstream of GFP-His in the construct. Although higher molecular weight bands were also observed with weaker intensities, the full length Pmt complex appeared to have largely degraded.

Another limitation encountered for the GFP-His construct was that cleavage with 3C protease proved ineffective. In-gel fluorescence revealed that overnight incubation of Pmt-GFP-His with a 1:1 molar ratio of 3C protease resulted in negligible cleavage of the fusion tags. Moreover, the reverse nickel IMAC step after cleavage produced no detectable protein in the flow through, whereas a 250 mM wash of imidazole led to recovery of the uncleaved Pmt fusion. The final gel filtration profile for uncleaved Pmt revealed a large aggregation peak at ~8 mL coupled to a broad peak at ~10 mL (Figure 82A). The observed aggregation could have masked the 3C cleavage site, resulting in reduced accessibility to the protease and hence no cleavage of the GFP-His moiety. In-gel fluorescence of the gel filtration fractions visualised the band migrating to a molecular weight of ~35 kDa, suggesting isolation of a dissociated component of the Pmt complex (Figure 82B).

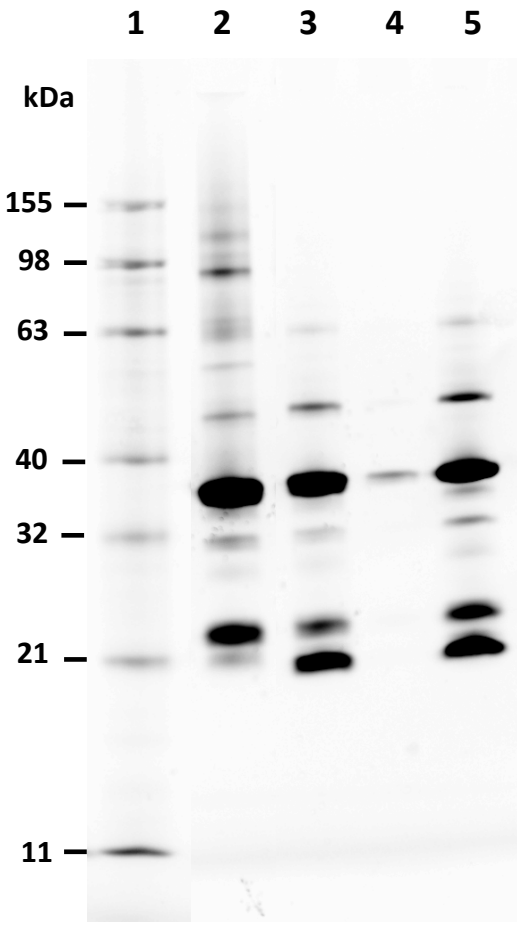


Figure 81. Nickel affinity purification of Pmt-GFP-His. In-gel fluorescence of Pmt-GFP-His following nickel affinity chromatography steps. Lane 1 corresponds to the fluorescent marker. Lane 2 contains the 250 mM imidazole elution from the first nickel affinity step. There are two prominent bands at ~35 kDa and ~22 kDa (free GFP). Lane 3 corresponds to the protein after overnight 3C protease treatment and shows strong carry-over of free GFP and the higher molecular weight band at ~35 kDa. There is also an additional band below ~20 kDa which might represent protein degradation. Lane 4 contains the flow through from the reverse nickel step which was measured at a protein concentration of < 0.05 mg/mL. Lane 5 contains the reverse nickel 250 mM imidazole wash fraction which is indistinguishable from the overnight sample (lane 3) and suggests the Pmt fusion did not cleave.

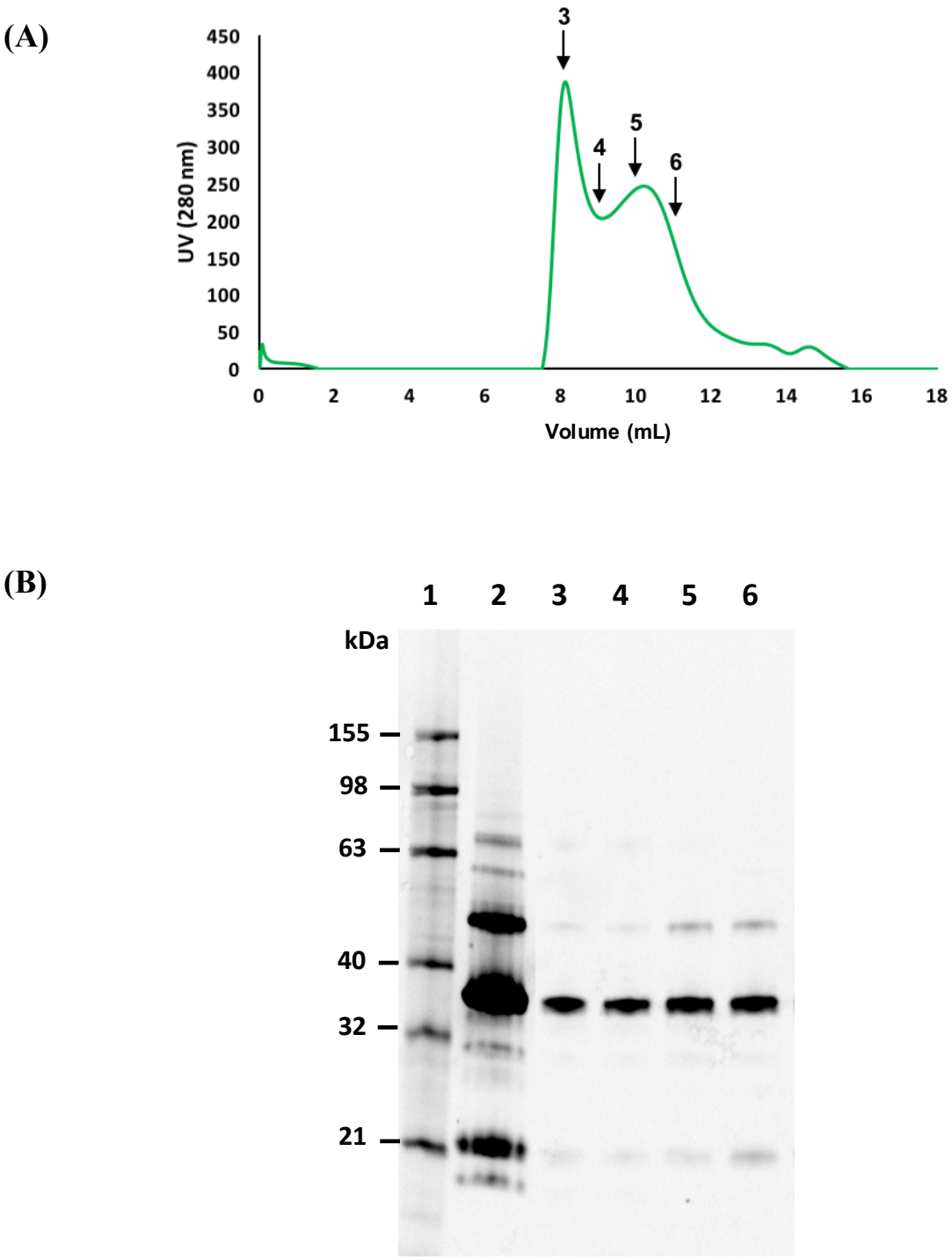


Figure 82. Gel filtration of uncleaved Pmt-GFP-His. (A) Gel filtration profile of Pmt-GFP-His. There is a significant aggregation peak at ~8 mL and a broad peak at ~10 mL. (B) In-gel fluorescence of Pmt-GFP-His after size exclusion chromatography. Lane 1 corresponds to the fluorescent marker and lane 2 represents the concentrated sample before injection into the gel filtration column. Lanes 3-6 contain fractions taken after gel filtration. A single band at ~35 kDa can be visualised that corresponds to the PmtD subunit.

4.3.3. Purification of Pmt-His

Since the Pmt-GFP-His construct was not amenable to purification, I tested whether the Pmt-His construct was more suitable for obtaining protein. In order to facilitate purification of the intact Pmt complex, the concentration of salt was reduced in the buffers. A one-step nickel IMAC purification followed by overnight dialysis and injection into a gel filtration column resulted in aggregation of the protein. A second method was applied where the nickel elution was passed through a desalting column for immediate removal of imidazole, followed by a gel filtration step. The profile demonstrates minimal aggregation and a discernible peak at ~12 mL with additional species observed at an earlier elution volume (Figure 83A). Analysis of the fractions by SDS-PAGE revealed multiple bands that could either correspond to Pmt components or contaminant proteins, since the Pmt-His did not undergo a reverse nickel IMAC step (Figure 83B).

In order to evaluate the purified sample, SDS-PAGE gel bands were extracted and submitted for mass spectrometric identification. Interestingly, the only subunit detected corresponded to the PmtD transmembrane domain which is directly in frame with the C-terminal His tag. By contrast, all other bands examined by mass spectrometry were identified as *E. coli* contaminant proteins. The fact that additional Pmt subunits are positioned upstream in the vector suggests Pmt is being correctly expressed but the complex is either dissociating or individual domains form oligomers during purification.

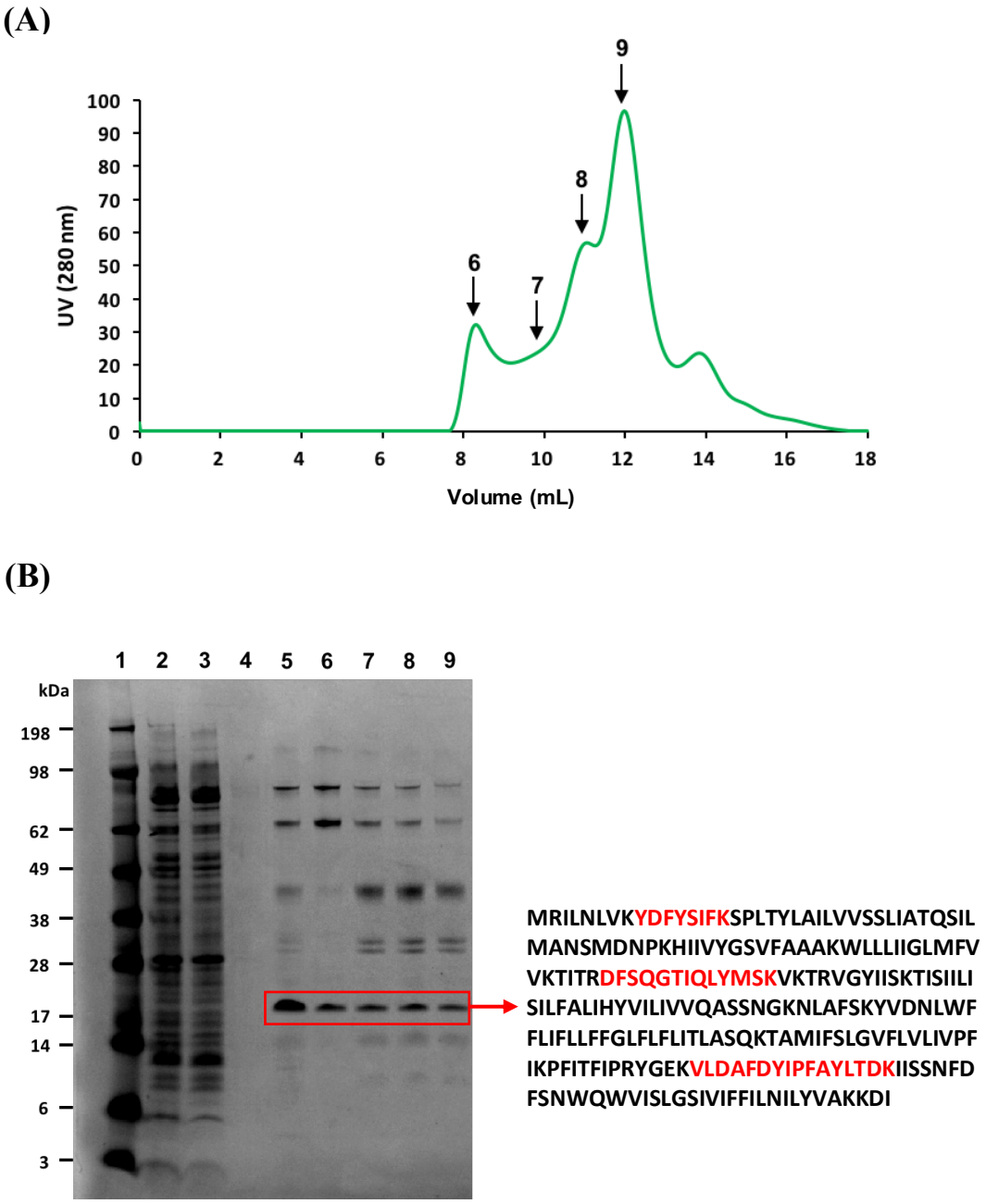


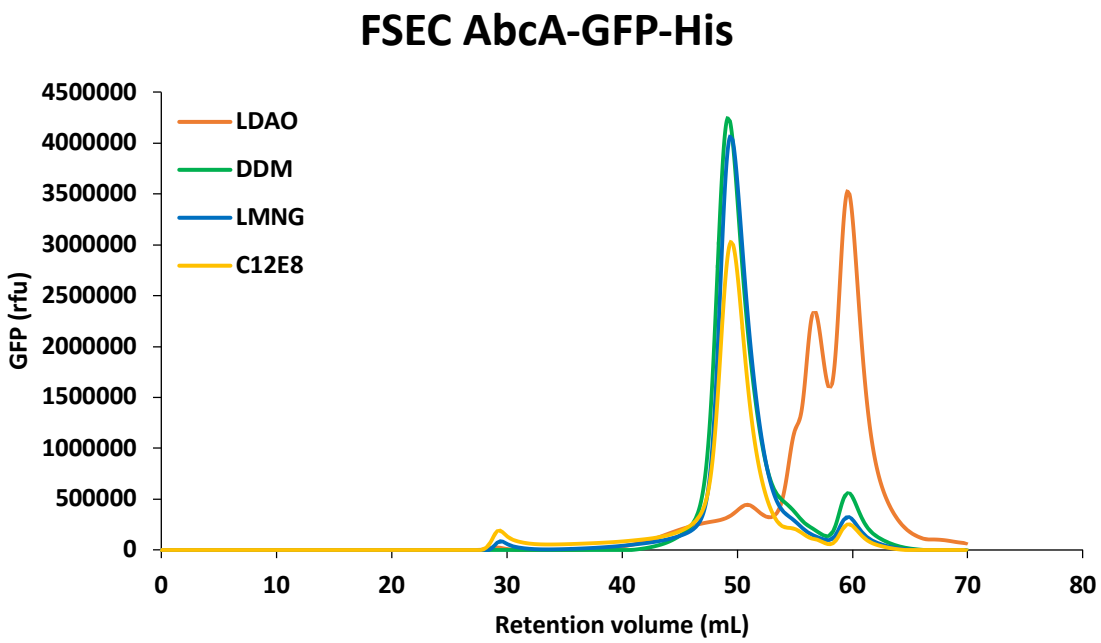
Figure 83. Purification of Pmt-His. (A) Gel filtration profile of Pmt-His. Multiple peaks were observed corresponding to different contaminants in the sample. (B) SDS-PAGE of Pmt-His. Lane 1 corresponds to the protein marker. Lane 2 represents the supernatant after detergent solubilisation. Lane 3 contains the flow through after binding to the nickel resin and lane 4 corresponds to the 30 mM imidazole wash fraction. Lane 5 contains the 250 mM imidazole nickel elution. Lanes 6-9 correspond to fractions collected after the gel filtration step. The band at ~20 kDa (red box) was identified as the PmtD subunit by mass spectrometry, but all other bands correspond to *E. coli* contaminant proteins. Peptides located in the PmtD amino acid sequence following trypsin digest are highlighted in red.

4.3.4. FSEC screening of AbcA-GFP-His

In light of the challenges faced trying to isolate full length Pmt, I switched my attention to the AbcA transporter whose subunits are encoded by a single polypeptide, hence precluding the requirement for complex formation. Extensive FSEC screening of AbcA was performed in eight different detergents with variable properties. The AbcA-GFP-His construct produced monodisperse fluorescence profiles after solubilisation in five detergents (Figure 84). Notably, the transporter can be stably extracted in alkyl maltosides (DDM, DM, Cymal-6) and, unlike Pmt, AbcA is well behaved in both C12E8 and LMNG. In contrast, harsher detergents (LDAO, OM, OG) are detrimental to homogeneous solubilisation of AbcA and therefore are unsuitable for large scale purification.

Detergent	Extraction efficiency (%)
DDM	89
LMNG	87
C12E8	59
LDAO	75
DM	90
Cymal-6	70
OM	27
OG	18

Table 10. Detergent extraction efficiencies for AbcA-GFP-His.



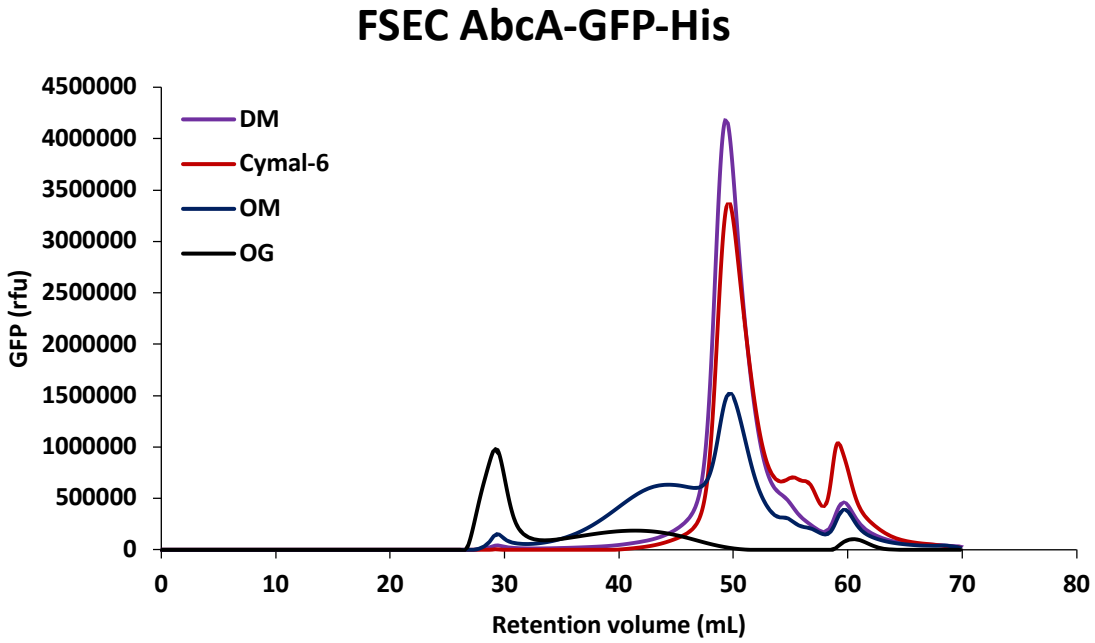


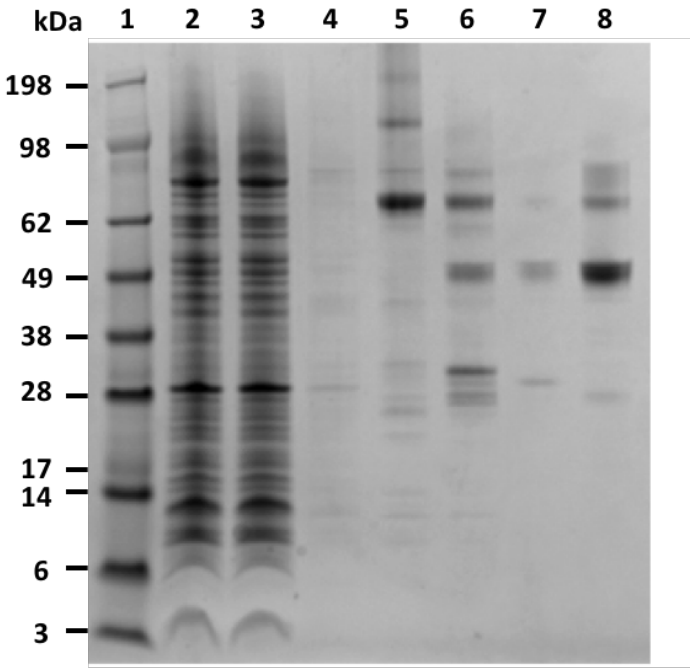
Figure 84. FSEC profile of AbcA-GFP-His in different detergents. AbcA shows stable extraction in DDM, C12E8, LMNG, DM and Cymal-6.

4.3.5. Purification and characterisation of AbcA-GFP-His

AbcA-GFP-His was purified in DDM to a high level of purity, generating a monodisperse gel filtration profile with a small shoulder adjacent to the main peak (Figure 85A/B). To characterise the activity of the protein, ATPase measurements were performed in DDM. ATP hydrolysis yields inorganic phosphate which reacts with the substrate MESG (2-amino-6-mercapto-7-methylpurine riboside) in the presence of the enzyme PNP (purine nucleoside phosphorylase) to yield a reaction product that is measured at an absorbance of 360 nm. Compared to DDM-purified McjD, AbcA was unable to stimulate ATP hydrolysis, resulting in negligible formation of the reaction product at 360 nm (Figure 86). I therefore sought to measure the activity of AbcA in other detergents identified by FSEC as suitable for purification. AbcA was exchanged into C12E8 and LMNG, yielding comparable gel filtration profiles to those obtained in DDM (Figure 87). However, the exchange of detergent was also unable to stimulate ATP turnover.

I then incorporated AbcA into proteoliposomes to test whether a lipid environment could modulate the ATPase activity. Rapid dilution of AbcA-DDM into *E. coli* polar lipids resulted in a very low efficiency of reconstitution (~10%) compared to the value measured for McjD (~60%). Since the rapid dilution method entails a harsh exchange of detergent for lipids, I then tested whether the gentler method of gradual detergent removal using Biobeads could facilitate functional incorporation of AbcA. Interestingly, the ABC transporter Sav1866 from *S. aureus* was previously reconstituted into *E. coli* polar lipids, supplemented with phosphatidylcholine using the Biobeads method (Dawson and Locher, 2007). However, upon reconstitution, AbcA once again displayed no detectable ATPase activity. Crystallisation screening of AbcA in DDM, C12E8 and LMNG also yielded no hits for optimisation.

(A)



(B)

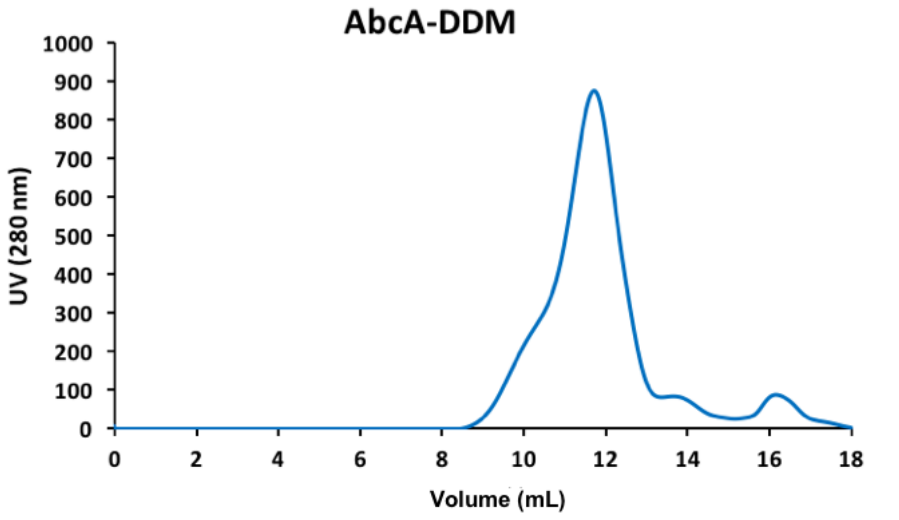


Figure 85. Purification of AbcA in DDM. (A) SDS-PAGE analysis of purified AbcA. The gel lanes correspond to the following samples: lane 1, marker; lane 2, detergent solubilised AbcA-GFP-His; lane 3, flow through from the nickel IMAC step; lane 4, 30 mM imidazole wash; lane 5, 250 mM imidazole elution; lane 6, TEV protease cleavage; lane 7, reverse nickel IMAC step flow through; lane 8, pooled gel filtration fraction after concentrating the sample. The band at ~50 kDa corresponds to AbcA while the band at ~65 kDa represents the stable SDS-dimer. (B) Gel filtration profile of AbcA in DDM.

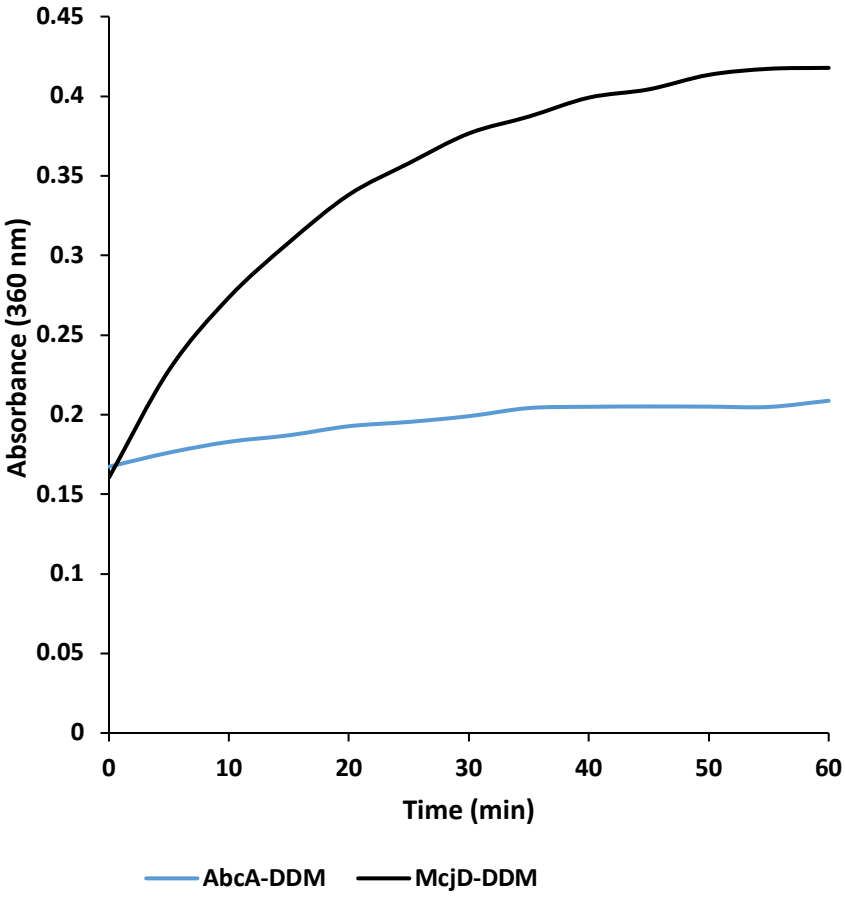


Figure 86. ATPase activity assay of AbcA in DDM. The time course demonstrates no ATPase activity for AbcA in the presence of 1 mM ATP as reflected by the negligible change in absorbance at 360 nm. The positive control of McjD by contrast shows significant basal ATPase activity levels in DDM.

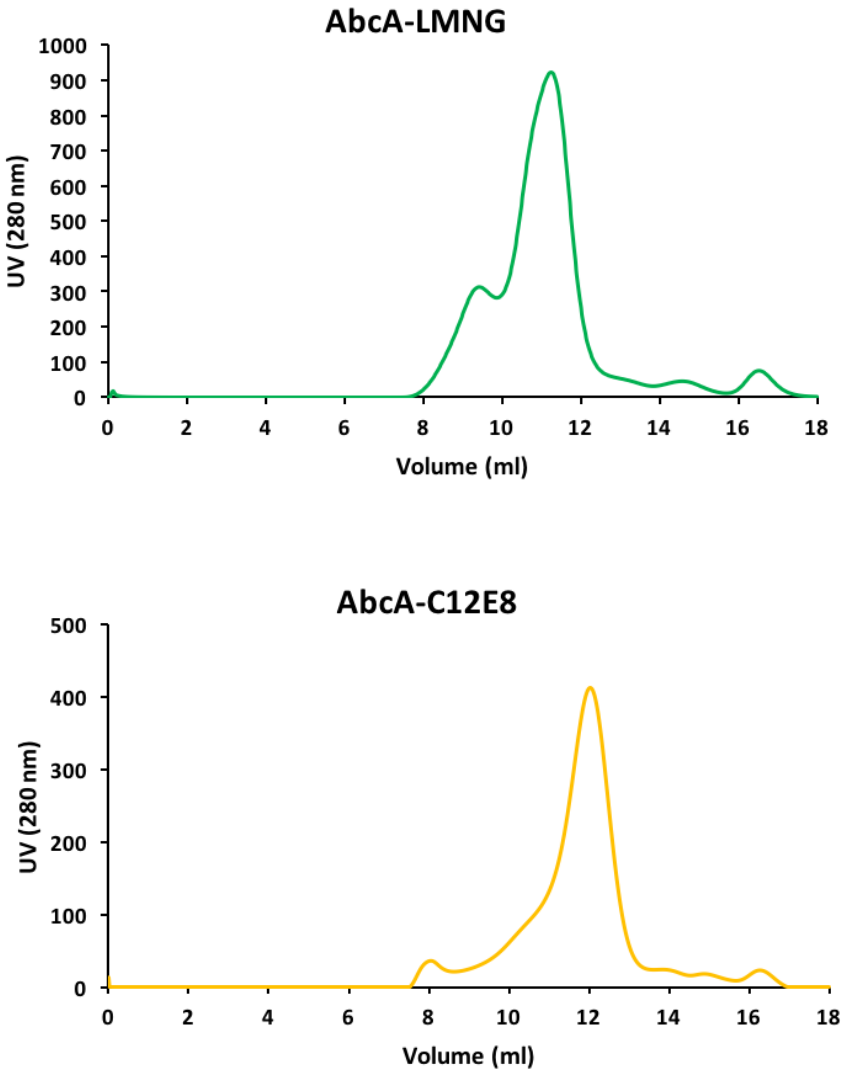


Figure 87. Gel filtration profiles for AbcA purified in different detergents. AbcA yields similar gel filtration profiles in LMNG and C12E8 when compared to DDM. For AbcA-LMNG a small shoulder peak is observed adjacent to the main peak, suggesting this could be a different oligomerisation state of the transporter.

4.4. Discussion

In this work, the phenol soluble modulin efflux pump AbcA from *S. aureus* was purified and attempts were made to reconstitute the transporter in a functionally competent state. AbcA demonstrated no ATPase activity in three detergents (DDM, C12E8, LMNG) and following incorporation into proteoliposomes. In parallel, efforts to isolate the heterotetrameric PSM transporter Pmt were unsuccessful due to dissociation of the complex during purification. In order to maintain the intact Pmt complex, further construct screening and modification will be required.

One possible explanation for the lack of ATPase activity detected for AbcA in liposomes, is that the protein was incorporated into lipids from *E. coli*, a Gram-negative bacterium. It has been demonstrated that the lipid composition and membrane organisation of Gram-positive bacteria differ to that of Gram-negative bacteria. For example, the cell membranes of Gram-negative bacteria contain a higher content of phosphatidylethanolamine (PE) and zwitterionic lipids compared to Gram-positive bacteria (Epand and Epand, 2009). Another difference is that both types of bacteria contain distinct compositions of LPS, with Gram-positive bacterial membranes enriched in lipoteichoic acids. Since the lipid composition of *S. aureus* is more likely to mimic that of other Gram-positive bacteria, a more suitable host expression platform for Pmt and AbcA may be the Gram-positive *Lactococcus lactis* system (Kunji *et al*., 2003).

The *L. lactis* system has a number of properties that makes it ideal for the expression and purification of bacterial membrane proteins (King *et al*., 2015). Growth rates of lactococci are fast, generating high cell densities and there is no requirement for aeration. In addition, promoters are tightly regulated which ensures that the gene products can be expressed in a controlled manner. Finally, membrane proteins can be readily solubilised from the *L. lactis* membrane with mild detergents and they are usually very stable due to the limited proteolytic

capability of the organism (King *et al*., 2015). The type IV ABC transporter LmrA from Gram-positive species has previously been expressed in *L. lactis*, purified to homogeneity and biochemically characterised with physiological rates of ATPase activity (Margolles *et al*., 1999). ABC transporters typically hydrolyse ATP at lower rates in detergent compared with liposomes (Choudhury *et al*., 2014; Liu *et al*., 2018). Therefore, detecting basal ATP turnover levels of AbcA in a native lipid environment is a prerequisite to further characterisation. Furthermore, incorporating AbcA in nanodiscs represents a plausible alternative system that is yet to be examined.

Assuming functional reconstitution can be achieved, future work will examine the ability of PSMs to stimulate the ATPase and transport activities of AbcA. In light of the low sequence conservation between different classes of PSMs, the mechanistic determinants for PSM selection and transport require further investigation (Peschel and Otto, 2013). It will also be of interest to evaluate whether antibiotics can stimulate the ATPase activity of AbcA. A previous study identified the antibiotics methicillin, cefotaxime and daptomycin as potential transport substrates of AbcA, suggesting a role in multidrug resistance (Truong-Bolduc *et al*., 2007). AbcA is amenable to cryo-EM analysis but the inactive protein preparations from this study are unsuitable for structure determination. Importantly, the lack of activity might explain why the existing batches of purified AbcA have resisted crystallisation.

References

Abele, R. & Tampé, R. 2011. The TAP translocation machinery in adaptive immunity and viral escape mechanisms. *Essays in Biochemistry*, **50**, 249-64.

Adelman, K., Yuzenkova, J., La Porta, A., Zenkin, N., Lee, J., Lis, J. T., Borukhov, S., Wang, M. D. & Severinov, K. 2004. Molecular mechanism of transcription inhibition by peptide antibiotic Microcin J25. *Molecular Cell*, **14**, 753-62.

Aittoniemi, J., Fotinou, C., Craig, T. J., de Wet, H., Proks, P. & Ashcroft, F. M. 2009. SUR1: a unique ATP-binding cassette protein that functions as an ion channel regulator. *Philosophical Transactions of the Royal Society*, **364**, 257-67.

Akyuz, N., Altman, R. B., Blanchard, S. C. & Boudker, O. 2013. Transport dynamics in a glutamate transporter homologue. *Nature*, **502**, 114-8.

Alam, A., Kowal, J., Broude, E., Roninson, I. & Locher, K. P. 2019. Structural insight into substrate and inhibitor discrimination by human P-glycoprotein. *Science*, **363**, 753-6.

Alam, A., Küng, R., Kowal, J., McLeod, R. A., Tremp, N., Broude, E. V., Roninson, I. B., Stahlberg, H. & Locher, K. P. 2018. Structure of a zosuquidar and UIC2-bound human-mouse chimeric ABCB1. *Proceedings of the National Academy of Sciences*, **115**, E1973-82.

Albrecht, C., McVey, J. H., Elliott, J. I., Sardini, A., Kasza, I., Mumford, A. D., Naoumova, R. P., Tuddenham, E. G., Szabo, K. & Higgins, C. F. 2005. A novel missense mutation in ABCA1 results in altered protein trafficking and reduced phosphatidylserine translocation in a patient with Scott syndrome. *Blood*, **106**, 542-9.

Aller, S. G., Yu, J., Ward, A., Weng, Y., Chittaboina, S., Zhuo, R., Harrell, P. M., Trinh, Y. T., Zhang, Q., Urbatsch, I. L. & Chang G. 2009. Structure of P-glycoprotein reveals a molecular basis for poly-specific drug binding. *Science*, **323**, 1718-22.

Baquero, F., Bouanchaud, D., Martinez-Perez, M. C. & Fernandez C. 1978. Microcin plasmids: a group of extrachromosomal elements coding for low-molecular-weight antibiotics in *Escherichia coli*. *Journal of Bacteriology*, **135**, 342-7.

Barth, K., Hank, S., Spindler, P. E., Prisner, T. F., Tampé, R. & Joseph, B. 2018. Conformational coupling and trans-inhibition in the human antigen transporter ortholog TmrAB resolved with dipolar EPR spectroscopy. *Journal of the American Chemical Society*, **140**, 4527-33.

Bauer, R. & Dicks, L. M. 2005. Mode of action of lipid II-targeting lantibiotics. 2005. *International Journal of Food Microbiology*, **101**, 201-16.

Bayro, M. J., Mukhopadhyay, J., Swapna, G. V., Huang, J. Y., Ma, L. C., Sineva, E., Dawson, P. E., Montelione, G. T. & Ebright, R. H. 2003. Structure of antibacterial peptide microcin J25: a 21-residue lariat protoknot. *Journal of the American Chemical Society*, **125**, 12382-3.

Bechara, C., Nöll, A., Morgner, N., Degiacomi, M. T., Tampé, R. & Robinson, C.V. 2015. A subset of annular lipids is linked to the flippase activity of an ABC transporter. *Nature Chemistry*, **7**, 255-62.

Becker, J. P., Van Bambeke, F., Tulkens, P. M. & Prévost, M. 2010. Dynamics and structural changes induced by ATP binding in SAV1866, a bacterial ABC exporter. *The Journal of Physical Chemistry B*, **114**, 15948-57.

Beis, K. 2015. Structural basis for the mechanism of ABC transporters. *Biochemical Society Transactions*, **43**, 889-93.

Bellomio, A., Vincent, P. A., de Arcuri, B. F., Farias, R. N. & Morero, R. D. 2007. Microcin J25 has dual and independent mechanisms of action in *Escherichia coli*: RNA polymerase inhibition and increased superoxide production. *Journal of Bacteriology*, **189**, 4180-6.

Berliner, L. J., Grunwald, J., Hankovszky, H. O. & Hideg, K. 1982. A novel reversible thiol-specific spin label: papain active site labeling and inhibition. *Analytical Biochemistry*, **119**, 450-5.

Berntsson, R. P., Smits, S. H., Schmitt, L., Slotboom, D. J. & Poolman, B. 2010. A structural classification of substrate-binding proteins. *FEBS Letters*. **584**, 2606-17.

Bi, Y., Mann, E., Whitfield, C. & Zimmer, J. 2018. Architecture of a channel-forming O-antigen polysaccharide ABC transporter. *Nature*, **553**, 361-5.

Bieler, S., Silva, F., Soto, C. & Belin, D. 2006. Bactericidal activity of both secreted and nonsecreted microcin E492 requires the mannose permease. *Journal of Bacteriology*, **188**, 7049-61.

Blanc, E., Roversi, P., Vonrhein, C., Flensburg, C., Lea, S.M. & Bricogne G. 2004. Refinement of severely incomplete structures with maximum likelihood in BUSTER-TNT. *Acta Crystallographica Section D: Biological Crystallography*, **60**, 2210-21.

Blond, A., Cheminant, M., Destoumieux-Garzón, D., Ségalas-Milazzo, I., Peduzzi, J., Goulard, C. & Rebuffat, S. 2002. Thermolysin-linearized microcin J25 retains the structured core of the native macrocyclic peptide and displays antimicrobial activity. *European Journal of Biochemistry*. **269**, 6212-22.

Borbat, P. P., Surendhran, K., Bortolus, M., Zou, P., Freed, J. H. & McHaourab HS. 2007. Conformational motion of the ABC transporter MsbA induced by ATP hydrolysis. *PLoS Biology*, **5**, e271.

Borths, E. L., Poolman, B., Hvorup, R. N., Locher, K. P. & Rees, D. C. 2005. In vitro functional characterization of BtuCD-F, the *Escherichia coli* ABC transporter for vitamin B12 uptake. *Biochemistry*, **44**, 16301-9.

Bountra, K., Hagelueken, G., Choudhury, H. G., Corradi, V., El Omari, K., Wagner, A., Mathavan, I., Zirah, S., Yuan Wahlgren, W., Tieleman, D. P., Schiemann, O., Rebuffat, S. & Beis, K. 2017. Structural basis for antibacterial peptide self-immunity by the bacterial ABC transporter McjD. *The EMBO Journal*, **36**, 3062-79.

Braffman N.R., Piscotta, F. J., Hauver, J., Campbell, E. A., Link, A. J. & Darst, S. A. 2019. Structural mechanism of transcription inhibition by lasso peptides microcin J25 and capistruin. *Proceedings of the National Academy of Sciences*, **116**, 1273-8.

Braun, V., Patzer, S. I. & Hantke, K. 2002. Ton-dependent colicins and microcins: modular design and evolution. *Biochimie*, **84**, 365-80.

Celia, H., Noinaj, N., Zakharov, S.D., Bordignon, E., Botos, I., Santamaria, M., Barnard, T. J., Cramer, W. A., Lloubes, R. & Buchanan, S. K. 2016. Structural insight into the role of the Ton complex in energy transduction. *Nature*, **538**, 60-5.

Chatterjee, S.S., Joo, H.S., Duong, A.C., Dieringer, T.D., Tan, V.Y., Song, Y., Fischer, E.R., Cheung, G.Y., Li, M. & Otto, M. 2013. Essential *Staphylococcus aureus* toxin export system. *Nature Medicine*, **19**, 364-7.

Chen, J. 2013. Molecular mechanism of the *Escherichia coli* maltose transporter. *Current Opinion in Structural Biology*, **23**, 492-8.

Chen, V. B., Arendall, W. B., Headd, J. J., Keedy, D. A., Immormino, R. M., Kapral, G. J., Murray, L. W., Richardson, J. S. & Richardson, D. C. 2010. MolProbity: all-atom structure validation for macromolecular crystallography. *Acta Crystallographica Section D: Biological Crystallography*, **66**. 12-21.

Cheung, G. Y., Joo, H. S., Chatterjee, S. S. & Otto, M. 2014. Phenol-soluble modulins – critical determinants of Staphylococcal virulence. *FEMS Microbiol Reviews*, **38**, 698-719.

Cheung, W. L., Pan, S. J. & Link, A. J. 2010. Much of the microcin J25 leader peptide is dispensable. *Journal of the American Chemical Society*, **132**, 2514-5.

Chiuchiolo, M. J., Delgado, M. A., Farias, R. N. & Salomon, R. A. 2001. Growth-phase-dependent expression of the cyclopeptide antibiotic microcin J25. *Journal of Bacteriology*, **183**, 1755-64.

Choudhury, H. G., Tong, Z., Mathavan, I., Li, Y., Iwata, S., Zirah, S., Rebuffat, S., van Veen, H. W. & Beis, K. 2014. Structure of an antibacterial peptide ATP-binding cassette transporter in a novel outward occluded state. *Proceedings of the National Academy of Sciences*, **111**, 9145-50.

Clausen, J. D., Bublitz, M., Arnou, B., Olesen, C., Andersen, J. P., Møller, J. V. & Nissen, P. 2016. Crystal Structure of the Vanadate-Inhibited Ca(2+)-ATPase. *Structure*, **24**, 617-23.

Cogen, A. L., Yamasaki, K., Sanchez, K. M., Dorschner, R. A., Lai, Y., MacLeod, D. T., Torpey, J. W., Otto, M., Nizet, V., Kim, J. E. & Gallo, R. L. 2010. Selective antimicrobial action is provided by phenol-soluble modulins derived from *Staphylococcus epidermidis*, a normal resident of the skin. *Journal of Investigative Dermatology*, **130**, 192-200.

Connell, N., Han, Z., Moreno, F. & Kolter R. 1987. An *E. coli* promoter induced by the cessation of growth. *Molecular Microbiology*, **1**, 195-201.

Corbalan, N., Runti, G., Adler, C., Covaceuszach, S., Ford, R. C., Lamba, D., Beis, K., Scocchi, M. & Vincent, P. A. 2013. Functional and structural study of the dimeric inner membrane protein SbmA. *Journal of Bacteriology*, **195**, 5352-61.

Cordes, T., Vogelsang, J. & Tinnefeld, P. 2009. On the mechanism of Trolox as antiblinking and antibleaching reagent. *Journal of the American Chemical Society*, **131**, 5018-9.

Cotter, P. D., Ross, R. P. & Hill, C. Bacteriocins - a viable alternative to antibiotics? 2013. *Nature Reviews Microbiology*, **11**, 95-105.

Coulton, J. W., Mason, P. & DuBow, M. S. 1983. Molecular cloning of the ferrichrome-iron receptor of *Escherichia coli* K-12. *Journal of Bacteriology*, **156**, 1315-21.

Crow, A., Greene, N. P., Kaplan, E. & Koronakis, V. 2017. Structure and mechanotransmission mechanism of the MacB ABC transporter superfamily. *Proceedings of the National Academy of Sciences*, **114**, 12572-7.

Cui, J. & Davidson, A. L. 2011. ABC solute importers in bacteria. *Essays in Biochemistry*, **50**, 85-99.

Cuthbertson, L., Kos, V. & Whitfield, C. 2010. ABC transporters involved in export of cell surface glycoconjugates. *Microbiology and Molecular Biology Reviews*, **74**, 341-62.

Davidson, A. L., Dassa, E., Orelle, C. & Chen, J. 2008. Structure, function and evolution of bacterial ATP-binding cassette systems. *Microbiology and Molecular Biology Reviews*, **72**, 317-64.

Davidson, A. L., Laghaeian, D. & Mannering, D. E. 1996. The maltose transport system of *Escherichia coli* displays positive cooperativity in ATP hydrolysis. *The Journal of Biological Chemistry*, **271**, 4858-63

Davies, D. R. & Hol, W. G. 2004. The power of vanadate in crystallographic investigations of phosphoryl transfer enzymes. *FEBS Letters*, **577**, 315-21.

Dawson, R. J. & Locher, K. P. 2006. Structure of a bacterial multidrug ABC transporter. *Nature*, **443**, 180-5.

Dawson, R. J. & Locher, K. P. 2007. Structure of the multidrug ABC transporter Sav1866 from *Staphylococcus aureus* in complex with AMP-PNP. *FEBS Letters*, **581**, 935-8.

de Cristobal, R. E., Solbiati, J. O., Zenoff, A. M., Vincent, P. A., Salomon, R. A., Yuzenkova, J., Severinov, K. & Farias, R. N. 2006. Microcin J25 uptake: His5 of the MccJ25 lariat ring is involved in interaction with the inner membrane MccJ25 transporter protein SbmA. *Journal of Bacteriology*, **188**, 3324-8.

Dean, M. & Annilo, T. 2005. Evolution of the ATP-binding cassette (ABC) transporter superfamily in vertebrates. *Annual Review of Genomics and Human Genetics*, **6**, 123-42.

Delgado, M. A., Rintoul, M. R., Farías, R. N. & Salomon, R. A. 2001. *Escherichia coli* RNA polymerase is the target of the cyclopeptide antibiotic microcin J25. *Journal of Bacteriology*, **183**, 4543-50.

Delgado, M. A., Vincent, P. A., Farías, R. N. & Salomon, R. A. 2005. YojI of *Escherichia coli* functions as a microcin J25 efflux pump. *Journal of Bacteriology*, **187**, 3465-70.

Dong, J., Yang, G. & McHaourab, H. S. 2005. Structural basis of energy transduction in the transport cycle of MsbA. *Science*, **308**, 1023-8.

Dong, H., Zhang, Z., Tang, X., Paterson, N. G. & Dong C. 2017. Structural and functional insights into the lipopolysaccharide ABC transporter $LptB_2FG$. *Nature Communications*, **8**, 222.

Doshi, R. & van Veen, H. W. 2013. Substrate binding stabilizes a pre-translocation intermediate in the ATP-binding cassette transport protein MsbA. *The Journal of Biological Chemistry*, **288**, 21638-47.

Doyle, D. A., Morais Cabral, J., Pfuetzner, R. A., Kuo, A., Gulbis, J. M., Cohen, S. L., Chait B. T. & MacKinnon, R. 1998. The structure of the potassium channel: molecular basis of K+ conduction and selectivity. *Science*, **280**, 69-77.

Drew, D., Lerch, M., Kunji, E., Slotboom, D. J. & de Gier, J. W. 2006. Optimization of membrane protein overexpression and purification using GFP fusions. *Nature Methods*, **3**, 303-13.

Dupuy, F. G., Chirou, M. V., de Arcuri, B. F., Minahk, C. J. & Morero, R. D. 2009. Proton motive force dissipation precludes interaction of microcin J25 with RNA polymerase, but enhances reactive oxygen species overproduction. *Biochimica et Biophysica Acta*, **1790**, 1307-13.

Duquesne, S., Destoumieux-Garzon, D., Peduzzi, J. & Rebuffat, S. 2007. Microcins, gene-encoded antibacterial peptides from enterobacteria. *Natural Product Reports,* **24,** 708-34.

Dyla, M., Terry, D. S., Kjaergaard, M., Sorensen, T. L., Lauwring Andersen, J., Andersen. J. P., Rohde Knudsen, C., Altman, R. B., Nissen, P. & Blanchard, S. C. 2017. Dynamics of P-type ATPase transport revealed by single-molecule FRET. *Nature*, **551**, 346-51.

Emsley, P. & Cowtan, K. 2004. Coot: model-building tools for molecular graphics. *Acta Crystallographica Section D: Biological Crystallography*, **60**, 2126-32.

Epand, R. M & Epand, R. F. 2009. Lipid domains in bacterial membranes and the action of antimicrobial agents. *Biochimica et Biophysica Acta Biomembranes*, **1788**, 289-94.

Erkens, G. B., Berntsson, R. P., Fulyani, F., Majsnerowska, M., Vujičić-Žagar, A., Ter Beek, J., Poolman, B., & Slotboom, D. J. 2011. The structural basis of modularity in ECF-type ABC transporters. *Nature Structural and Molecular Biology*, **18**, 755-60.

Erkens, G. B., Hänelt, I., Goudsmits, J. M., Slotboom, D. J. & van Oijen, A. M. 2013. Unsynchronised subunit motion in single trimeric sodium-coupled aspartate transporters. *Nature*, **502**, 119-23.

Ernst, R., Kueppers, P., Klein, C. M., Schwarzmueller, T., Kuchler, K. & Schmitt, L. 2008. A mutation of the H-loop selectively affects rhodamine transport by the yeast multidrug ABC transporter Pdr5. *Proceedings of the National Academy of Sciences*, **105**, 5069-74.

Ferguson, A. L., Zhang, S., Dikiy, I., Panagiotopoulos, A. Z., Debenedetti, P.G., & James Link, A. 2010. An experimental and computational investigation of spontaneous lasso formation in microcin J25. *Biophysical Journal*, **99**, 3056-65.

Fitzpatrick, A. W. P., Llabrés, S., Neuberger, A., Blaza, J. N., Bai, X. C., Okada, U., Murakami, S., van Veen, H. W., Zachariae, U., Scheres, S. H. W., Luisi, B. F. & Du, D. 2017. Structure of the MacAB-TolC ABC-type tripartite multidrug efflux pump. *Nature Microbiology*, **2**, 17070.

Fomenko, D., Veselovskii, A. & Khmel, I. 2001. Regulation of microcin C51 operon expression: the role of global regulators of transcription. *Research in Microbiology*, **152**, 469-79.

Ford, R. C. & Beis, K. 2019. Learning the ABCs one at a time: structure and mechanism of ABC transporters. *Biochemical Society Transactions*, **47**, 23-36.

Fréchet, D., Guitton, J. D., Herman, F., Faucher, D., Helynck, G., Monegier du Sorbier, B., Ridoux, J. P., James-Surcouf, E. & Vuilhorgne, M. 1994. Solution structure of RP 71955, a new 21 amino acid tricyclic peptide active against HIV-1 virus. *Biochemistry*, **33**, 42-50.

Galván, A. E., Chalón, M. C., Schurig-Briccio, L. A., Salomón, R. A., Minahk, C. J., Gennis, R. B. & Bellomio, A. 2018. Cytochromes bd-I and bo3 are essential for the bactericidal effect of microcin J25 on *Escherichia coli* cells. *Biochimica et Biophysica Acta Bioenergetics*, **1859**, 110-8.

Garcia-Bustos, J. F., Pezzi, N. & Mendez, E. 1985. Structure and mode of action of microcin 7, an antibacterial peptide produced by *Escherichia coli*. *Antimicrobial Agents and Chemotherapy*, **27**, 791-7.

Gerber, S., Comellas-Bigler, M., Goetz, B. A. & Locher, K. P. 2008. Structural basis of trans-inhibition in a molybdate/tungstate ABC transporter. *Science*. **321**, 246-50.

Ghosal, A., Vitali, A., Stach, J. E. & Nielsen, P. E. 2013. Role of SbmA in the uptake of peptide nucleic acid (PNA)-peptide conjugates in *E. coli*. *ACS Chemical Biology*, **8**, 360-7.

Glaenzer, J., Peter, M. F. & Hagelueken, G. 2018. Studying structure and function of membrane proteins with PELDOR/DEER spectroscopy - The crystallographers' perspective. *Methods*, **147**, 163-75.

Glavinas, H., Krajcsi, P., Cserepes, J. & Sarkadi, B. 2004. The role of ABC transporters in drug resistance, metabolism and toxicity. *Current Drug Delivery*, **1**, 27-42.

Goodno, C. C. & Taylor, E. W. 1982. Inhibition of actomyosin ATPase by vanadate. *Proceedings of the National Academy of Sciences*, **79**, 21-5.

Goudsmits, J. M. H., Slotboom, D. J. & van Oijen, A. M. 2017. Single-molecule visualization of conformational changes and substrate transport in the vitamin B12 ABC importer BtuCD-F. *Nature Communications*, **8**, 1652.

Gouridis, G., Schuurman-Wolters, G. K., Ploetz, E., Husada, F., Vietrov, R., de Boer, M., Cordes, T. & Poolman, B. 2015. Conformational dynamics in substrate-binding domains influences transport in the ABC importer GlnPQ. *Nature Structural and Molecular Biology*, **22**, 57-64.

Greenfield, L. K. & Whitfield, C. 2012. Synthesis of lipopolysaccharide O-antigens by ABC transporter-dependent pathways. *Carbohydrate Research*, **356**, 12-24.

Grossmann, N., Vakkasoglu, A. S., Hulpke, S., Abele, R., Gaudet, R. & Tampé, R. 2014. Mechanistic determinants of the directionality and energetics of active export by a heterodimeric ABC transporter. *Nature Communications*, **5**, 5419.

Gu, R. X., Corradi, V., Singh, G., Choudhury, H. G., Beis, K. & Tieleman, D. P. 2015. Conformational changes of the antibacterial peptide ATP binding cassette transporter McjD revealed by molecular dynamics simulations. *Biochemistry*, **54**, 5989-98.

Guijarro. J. I., González-Pastor, J. E., Baleux, F., San Millán, J. L., Castilla, M. A., Rico, M., Moreno, F. & Delepierre, M. 1995. Chemical structure and translation inhibition studies of the antibiotic microcin C7. *The Journal of Biological Chemistry*, **270**, 23520-32.

Hegemann, J. D., Zimmermann, M., Xie, X. & Marahiel, M. A. 2015. Lasso peptides: an intriguing class of bacterial natural products. *Accounts of Chemical Research*, **48**, 1909-19.

Higgins, C. F., Hiles, I. D., Salmond, G. P. C., Gill, D. R., Downie, J. A., Evans, I. J., Holland I. B., Gray, L., Buckel, S. D. & Bell, A. W. A. 1986. family of related ATP-binding subunits coupled to many distinct biological processes in bacteria. *Nature*, **323**, 448-50.

Ho, H., Miu, A., Alexander, M. K., Garcia, N. K., Oh, A., Zilberleyb, I., Reichelt, M., Austin, C. D., Tam, C., Shriver, S., Hu, H., Labadie, S. S., Liang, J., Wang, L., Wang, J., Lu, Y., Purkey, H. E., Quinn, J., Franke, Y., Clark, K., Beresini, M. H., Tan, M. W., Sellers, B. D., Maurer, T., Koehler, M. F. T., Wecksler, A. T., Kiefer, J. R., Verma, V., Xu, Y., Nishiyama, M., Payandeh, J. & Koth, C. M. 2018. Structural basis for dual-mode inhibition of the ABC transporter MsbA. *Nature*, **557**, 196-201.

Hohl, M., Hurlimann, L. M., Bohm, S., Schoppe, J., Grutter, M. G., Bordignon, E. & Seeger, M. A. 2014. Structural basis for allosteric cross-talk between the asymmetric nucleotide binding sites of a heterodimeric ABC exporter. *Proceedings of the National Academy of Sciences*, **111**, 11025-30.

Hohlbein, J, Craggs, T. D. & Cordes, T. 2014. Alternating-laser excitation: single-molecule FRET and beyond. *Chemical Society Reviews*, **43**, 1156-71.

Housden, N. G. & Kleanthous, C. 2012. Colicin translocation across the *Escherichia coli* outer membrane. *Biochemical Society Transactions*, **40**, 1475-9.

Husada, F., Bountra, K., Tassis, K., de Boer, M., Romano, M., Rebuffat, S., Beis, K. & Cordes, T. 2018. Conformational dynamics of the ABC transporter Mcjd seen by single-molecule FRET. *The EMBO Journal*, **37**, E100056.

Husada, F., Gouridis, G., Vietrov, R., Schuurman-Wolters, G. K., Ploetz, E., de Boer, M., Poolman, B. & Cordes T. 2015. Watching conformational dynamics of ABC transporters with single-molecule tools. *Biochemical Society Transactions*, **43**, 1041-7.

Hvorup, R. N., Goetz, B. A., Niederer, M., Hollenstein, K., Perozo, E. & Locher, K. P. 2007. Asymmetry in the structure of the ABC transporter-binding protein complex BtuCD-BtuF. *Science*, **317**, 1387-90.

Hyde, S.C., Emsley, P., Hartshorn, M. J., Mimmack, M. M., Gileadi, U., Pearce, S. R., Gallagher, M. P., Gill, D. R., Hubbard, R. E. & Higgins C.F. 1990. Structural and functional relationships of ATP-binding proteins associated with cystic fibrosis, multidrug resistance and bacterial transport. *Nature*, **346**, 362-5.

Jardetzky, O. 1966. Simple allosteric model for membrane pumps. *Nature*, **211**, 969-70.

Jeschke, G. & Polyhach, Y. 2007. Distance measurements on spin-labelled biomacromolecules by pulsed electron paramagnetic resonance. *Physical Chemistry Chemical Physics*, **9**, 1895-910.

Jin, M.S., Oldham, M.L., Zhang, Q. & Chen, J. 2012. Crystal structure of the multidrug transporter P-glycoprotein from *Caenorhabditis elegans*. *Nature*, **490**, 566-9.

Johnson, Z. L. & Chen, J. 2017. Structural basis of substrate recognition by the multidrug resistance protein MRP1. *Cell*, **168**, 1075-85.

Joo, H. S., Cheung, G. Y. & Otto, M. 2011. Antimicrobial activity of community-associated methicillin-resistant *Staphylococcus aureus* is caused by phenol-soluble modulin derivatives. *The Journal of Biological Chemistry*, **286**, 8933-40.

Kadaba, N. S., Kaiser, J. T., Johnson, E., Lee, A. & Rees, D. C. 2008. The high-affinity *E. coli* methionine ABC transporter: structure and allosteric regulation. *Science*, **321**, 250-3.

Kaito, C., Saito, Y., Nagano, G., Ikuo, M., Omae, Y., Hanada, Y., Han, X., Kuwahara-Arai, K., Hishinuma, T., Baba, T., Ito, T., Hiramatsu, K. & Sekimizu, K. 2011. Transcription and translation products of the cytolysin gene psm-mec on the mobile genetic element SCCmec regulate *Staphylococcus aureus* virulence. *PLoS Pathogens*, **7**, e1001267.

Kapanidis, A. N., Lee, N. K., Laurence, T. A., Doose, S., Margeat, E. & Weiss, S. 2004. Fluorescence-aided molecule sorting: analysis of structure and interactions by alternating-laser excitation of single molecules. *Proceedings of the National Academy of Sciences*, **101**, 8936-41.

Kawate, T. & Gouaux, E. 2006. Fluorescence-detection size-exclusion chromatography for precrystallization screening of integral membrane proteins. *Structure*, **14**, 673-81.

Khare, D., Oldham, M. L., Orelle, C., Davidson, A. L. & Chen J. 2009. Alternating access in maltose transporter mediated by rigid-body rotations. *Molecular Cell*, **33**, 528-36.

Killmann, H., Herrmann, C., Torun, A., Jung, G. & Braun, V. 2002. TonB of Escherichia coli activates FhuA through interaction with the β-barrel. *Microbiology,* **148**, 3497-509.

Kim, E., Lee, S., Jeon, A., Choi, J. M., Lee, H. S., Hohng, S. & Kim, H. S. 2013. A single-molecule dissection of ligand binding to a protein with intrinsic dynamics. *Nature Chemical Biology*, **9**, 313-8.

King, M. S., Boes, C. & Kunji, E. R. 2015. Membrane protein expression in *Lactococcus lactis*. *Methods in Enzymology*, **556**, 77-97.

Knappe, T. A., Linne, U., Zirah, S., Rebuffat, S., Xie, X. & Marahiel, M. A. 2008. Isolation and structural characterization of capistruin, a lasso peptide predicted from the genome sequence of *Burkholderia thailandensis* E264. *Journal of the American Chemical Society*, **130**, 11446-54.

Knappe, T. A., Manzenrieder, F., Mas-Moruno, C., Linne, U., Sasse, F., Kessler, H., Xie, X. & Marahiel, M. A. 2011. Introducing lasso peptides as molecular scaffolds for drug design: engineering of an integrin antagonist. *Angewandte Chemie International Edition*, **50**, 8714-7.

Kobayashi, N., Nishino, K. & Yamaguchi A. 2001. Novel macrolide-specific ABC-type efflux transporter in *Escherichia coli*. *Journal of Bacteriology*, **183**, 5639-44.

Korkhov, V. M., Mireku, S. A. & Locher, K. P. 2012. Structure of AMP-PNP-bound vitamin B12 transporter BtuCD-F. *Nature*, **490**, 367-72.

Korkhov, V. M., Mireku, S. A., Veprintsev, D. B. & Locher K. P. 2014. Structure of AMP-PNP-bound BtuCD and mechanism of ATP-powered vitamin B12 transport by BtuCD-F. *Nature Structural and Molecular Biology*, **21**, 1097-9.

Köster, W. 2001. ABC transporter-mediated uptake of iron, siderophores, heme and vitamin B12. *Research in Microbiology*, **152**, 291-301.

Kretschmer, D., Gleske, A. K., Rautenberg, M., Wang, R., Koberle, M., Bohn, E., Schoneberg, T., Rabiet, M. J., Boulay, F., Klebanoff, S. J., van Kessel, K. A., van Strijp, J. A., Otto, M. & Peschel, A. 2010. Human formyl peptide receptor 2 senses highly pathogenic *Staphylococcus aureus*. *Cell Host Microbe*, **7**, 463-73.

Kunji, E. R., Slotboom, D. J. & Poolman, B. 2003. *Lactococcus lactis* as host for overproduction of functional membrane proteins. *Biochimica et Biophysica Acta*, **1610**, 97-108.

Kuznedelov, K., Semenova, E., Knappe, T. A., Mukhamedyarov, D., Srivastava, A., Chatterjee, S., Ebright, R. H., Marahiel, M. A. & Severinov, K. 2011. The antibacterial threaded-lasso peptide capistruin inhibits bacterial RNA polymerase. *Journal of Molecular Biology*, **412**, 842-8.

Lagos, R., Tello, M., Mercado, G., García, V. & Monasterio, O. 2009. Antibacterial and antitumorigenic properties of microcin E492, a pore-forming bacteriocin. *Current Pharmaceutical Biotechnology*, **10**, 74-85.

Laviña, M., Pugsley, A. P. & Moreno, F. 1986. Identification, mapping, cloning and characterization of a gene (sbmA) required for microcin B17 action on *Escherichia coli* K12. *Journal of General Microbiology*, **132**, 1685-93.

Lee, J. Y., Kinch, L. N., Borek, D. M., Wang, J., Wang, J., Urbatsch, I. L., Xie, X. S., Grishin, N. V., Cohen, J. C., Otwinowski, Z., Hobbs, H. H. & Rosenbaum, D. M. 2016. Crystal structure of the human sterol transporter ABCG5/ABCG8. *Nature*, **533**, 561-4.

Lerner, E., Cordes, T., Ingargiola, A., Alhadid, Y., Chung, S., Michalet, X. & Weiss, S. 2018. Toward dynamic structural biology: Two decades of single-molecule Förster resonance energy transfer. *Science*, **359**.

LeVier, K. & Walker G. C. 2001. Genetic analysis of the *Sinorhizobium meliloti* BacA protein: differential effects of mutations on phenotypes. *Journal of Bacteriology*, **183**, 6444-53.

Lewinson O. & Livnat-Levanon. N. 2017. Mechanism of action of ABC importers: conservation, divergence, and physiological adaptations. *Journal of Molecular Biology*, **429**, 606-19.

Li, Y. M., Milne, J. C., Madison, L. L., Kolter, R. & Walsh, C. T. 1996. From peptide precursors to oxazole and thiazole-containing peptide antibiotics: microcin B17 synthase. *Science*, **274**, 1188-93.

Lin, D. Y., Huang, S. & Chen, J. 2015. Crystal structures of a polypeptide processing and secretion transporter. *Nature*, **523**, 425-30.

Liu, Y., Liu, Y., He, L., Zhao, Y. & Zhang, X. C. 2018. Single-molecule fluorescence studies on the conformational change of the ABC transporter MsbA. *Biophysics Reports*, **4**, 153-65.

Locher, K. P. 2016. Mechanistic diversity in ATP-binding cassette (ABC) transporters. *Nature Structural and Molecular Biology*, **23**, 487-93.

Locher, K. P., Rees, B., Koebnik, R., Mitschler, A., Moulinier, L., Rosenbusch, J. P. & Moras, D. 1998. Transmembrane signaling across the ligand-gated FhuA receptor: crystal structures of free and ferrichrome-bound states reveal allosteric changes. *Cell*, **95**, 771-8.

Loo T. W., Bartlett, M. C. & Clarke D. M. 2003. Substrate-induced conformational changes in the transmembrane segments of human P-glycoprotein. Direct evidence for the substrate-induced fit mechanism for drug binding. *The Journal of Biological Chemistry*, **278**, 13603-6.

Lopez, F. E., Vincent, P. A., Zenoff, A. M., Salomon, R. A. & Farias, R. N. 2007. Efficacy of microcin J25 in biomatrices and in a mouse model of Salmonella infection. *Journal of Antimicrobial Chemotherapy*, **59**, 676-80.

Lowy, F. D. 2003. Antimicrobial resistance: the example of *Staphylococcus aureus*. *Journal of Clinical Investigation*, **111**, 1265-73.

Lowy, F. D. 1998. *Staphylococcus aureus* infections. *New England Journal of Medicine*, **339**, 520-32.

Luo, Q., Yang, X., Yu, S., Shi, H., Wang, K., Xiao, L., Zhu, G., Sun, C., Li, T., Li, D., Zhang, X., Zhou, M. & Huang, Y. 2017. Structural basis for lipopolysaccharide extraction by ABC transporter $LptB_2FG$. *Nature Structural and Molecular Biology*, **24**, 469-74.

Marcoux, J., Wang, S. C., Politis, A., Reading, E., Ma, J., Biggin, P. C., Zhou, M., Tao, H., Zhang, Q., Chang, G., Morgner, N. & Robinson, C. V. 2013. Mass spectrometry reveals synergistic effects of nucleotides, lipids, and drugs binding to a multidrug resistance efflux pump. *Proceedings of the National Academy of Sciences*, **110**, 9704-9.

Margolles, A., Putman, M., van Veen, H. W. & Konings, W. N. 1999. The purified and functionally reconstituted multidrug transporter LmrA of *Lactococcus lactis* mediates the transbilayer movement of specific fluorescent phospholipids. *Biochemistry*, **38**, 16298-306.

Martínez-Mir, A., Paloma, E., Allikmets, R., Ayuso, C., del Rio, T., Dean, M., Vilageliu, L., Gonzàlez-Duarte, R. & Balcells, S. 1998. Retinitis pigmentosa caused by a homozygous mutation in the Stargardt disease gene ABCR. *Nature Genetics*, **18**, 11-2.

Mathavan, I., Zirah, S., Mehmood, S., Choudhury H. G., Goulard, C., Li, Y., Robinson, C.V., Rebuffat, S. & Beis, K. 2014. Structural basis for hijacking siderophore receptors by antimicrobial lasso peptides. *Nature Chemical Biology*, **10**, 340-2.

Mattiuzzo, M., Bandiera, A., Gennaro, R., Benincasa, M., Pacor, S., Antcheva, N. & Scocchi, M. 2007. Role of the *Escherichia coli* SbmA in the antimicrobial activity of proline-rich peptides. *Molecular Microbiology*, **66**, 151-63.

McCoy, A. J., Grosse-Kunstleve, R. W., Adams, P. D., Winn, M. D., Storoni, L. C. & Read, R. J. 2007. Phaser crystallographic software. *Journal of Applied Crystallography*, **40**, 658-74.

Mehmood, S., Corradi, V., Choudhury, H. G., Hussain, R., Becker, P., Axford, D., Zirah, S., Rebuffat, S., Tieleman, D. P., Robinson, C. V. & Beis, K. 2016. Structural and functional basis for lipid synergy on the activity of the antibacterial peptide ABC transporter McjD. *The Journal of Biological Chemistry*, **291**, 21656–68.

Mehmood, S., Domene, C., Forest, E. & Jault, J. M. 2012. Dynamics of a bacterial multidrug ABC transporter in the inward- and outward-facing conformations. *Proceedings of the National Academy of Sciences*, **109**, 10832-6.

Metlitskaya, A., Kazakov, T., Kommer, A., Pavlova, O., Praetorius-Ibba, M., Ibba, M., Krasheninnikov, I., Kolb, V., Khmel, I. & Severinov K. 2006. *The Journal of Biological Chemistry*, **281**, 18033-42.

Mi, W., Li, Y., Yoon, S. H., Ernst, R. K., Walz, T. & Liao, M. 2017. Structural basis of MsbA-mediated lipopolysaccharide transport. *Nature*, **549**, 233-7.

Mishra, S., Verhalen, B., Stein, R. A., Wen, P. C., Tajkhorshid, E. & McHaourab, H. S. 2014. Conformational dynamics of the nucleotide binding domains and the power stroke of a heterodimeric ABC transporter. *Elife*, **3**, e02740.

Mitchell, P. 1957. A general theory of membrane transport from studies of bacteria. *Nature*, **180**, 134-6.

Morgan, J. L. W., Acheson, J. F. & Zimmer, J. 2017. Structure of a type-1 secretion system ABC transporter. *Structure*, **25**, 522-9.

Mukhopadhyay, J., Sineva, E., Knight, J., Levy, R. M. & Ebright, R. H. 2004. Antibacterial peptide microcin J25 inhibits transcription by binding within and obstructing the RNA polymerase secondary channel. *Molecular Cell*, **14**, 739-51.

Murshudov, G. N., Skubak, P., Lebedev, A. A., Pannu, N. S., Steiner, R. A., Nicholls, R. A., Winn, M. D., Long, F. & Vagin, A. A. 2011. REFMAC5 for the refinement of macromolecular crystal structures. *Acta Crystallographica Section D: Biological Crystallography*, **67**, 355-67.

Nakamura, Y., Oscherwitz, J., Cease, K. B., Chan, S. M., Munoz-Planillo, R., Hasegawa, M., Villaruz, A. E., Cheung, G. Y., McGavin, M. J., Otto, M., Inohara, N. & Nunez, G. 2013. Staphylococcus δ-toxin promotes allergic skin disease by inducing mast cell degranulation. *Nature*, **503**, 397-401.

Neher, E. & Sakmann, B. 1976. Single-channel currents recorded from membrane of denervated frog muscle fibres. *Nature*, **260**, 799-802.

Newstead, S., Ferrandon, S. & Iwata, S. 2008. Rationalizing alpha-helical membrane protein crystallization. *Protein Science*, **17**, 466-72.

Nicolaou, M., Andress, E.J., Zolnerciks, J.K., Dixon, P.H., Williamson, C. & Linton, K.J. 2012. Canalicular ABC transporters and liver disease. *The Journal of Pathology*, **226**, 300-15.

Nöll, A, Thomas, C., Herbring, V., Zollmann, T., Barth, K., Mehdipour, A. R., Tomasiak, T. M., Brüchert, S., Joseph, B., Abele, R., Oliéric, V., Wang, M., Diederichs, K., Hummer, G., Stroud, R. M., Pos, K. M. & Tampé, R. 2017. Crystal structure and mechanistic basis of a functional homolog of the antigen transporter TAP. *Proceedings of the National Academy of Sciences*, **114**, E438-E447.

Novick, R. P., Schlievert, P. & Ruzin, A. 2001. Pathogenicity and resistance islands of staphylococci. *Microbes and Infection*, **3**, 585-94.

Okada, U., Yamashita, E., Neuberger, A., Morimoto, M., van Veen, H. W. & Murakami S. 2017. Crystal structure of tripartite-type ABC transporter MacB from *Acinetobacter baumannii*. *Nature Communications*, **8**, 1336.

Oldham M. L. & Chen, J. 2011a. Crystal structure of the maltose transporter in a pretranslocation intermediate state. *Science*, **332**, 1202-5.

Oldham, M. L. & Chen, J. 2011b. Snapshots of the maltose transporter during ATP hydrolysis. *Proceedings of the National Academy of Sciences*, **108**, 15152-6.

Oldham, M. L., Khare, D., Quiocho, F. A., Davidson, A. L. & Chen, J. 2007. Crystal structure of a catalytic intermediate of the maltose transporter. *Nature*, **450**, 515-21.

Oliveira, D., Borges, A. & Simoes, M. 2018. *Staphylococcus aureus* toxins and their molecular activity in infectious diseases. *Toxins*, **10**, 252.

Orelle, C., Ayvaz, T., Everly, R. M., Klug, C. S. & Davidson, A. L. 2008. Both maltose-binding protein and ATP are required for nucleotide-binding domain closure in the intact maltose ABC transporter. *Proceedings of the National Academy of Sciences*, **105**, 12837-42.

Pan, S. J. & Link, A. J. 2011. Sequence diversity in the lasso peptide framework: discovery of functional microcin J25 variants with multiple amino acid substitutions. *Journal of the American Chemical Society*, **133**, 5016-23.

Pavlova, O., Mukhopadhyay, J., Sineva, E., Ebright, R. H. & Severinov, K. 2008. Systematic structure-activity analysis of microcin J25. *The Journal of Biological Chemistry*, **283**, 25589-95.

Pawelek, P. D., Croteau, N., Ng-Thow-Hing, C., Khursigara, C. M., Moiseeva, N., Allaire, M. & Coulton, J. W. 2006. Structure of TonB in complex with FhuA, *E. coli* outer membrane receptor. *Science*, **312**, 1399-402.

Perez, C., Gerber, S., Boilevin, J., Bucher, M., Darbre, T., Aebi, M., Reymond, J.L. & Locher. K.P. 2015. Structure and mechanism of an active lipid-linked oligosaccharide flippase. *Nature*, **524**, 433-8.

Periasamy, S., Joo, H. S., Duong, A. C., Bach, T. H., Tan, V. Y., Chatterjee, S. S., Cheung, G.Y. & Otto, M. 2012. How *Staphylococcus aureus* biofilms develop their characteristic structure. *Proceedings of the National Academy of Sciences*, **109**, 1281-6.

Peschel, A, & Otto, M. 2013. Phenol-soluble modulins and staphylococcal infection. *Nature Reviews Microbiology*, **11**, 667-73.

Pierrat, O. A. & Maxwell, A. 2003. The action of the bacterial toxin microcin B17. Insight into the cleavage-religation reaction of DNA gyrase. *The Journal of Biological Chemistry*, **278**, 35016-23.

Pinkett, H. W., Lee, A. T., Lum, P., Locher, K. P. & Rees, D. C. 2007. An inward-facing conformation of a putative metal-chelate-type ABC transporter. *Science*, **315**, 373-7.

Ploetz, E., Lerner, E., Husada, F., Roelfs, M., Chung, S., Hohlbein, J., Weiss, S. & Cordes, T. 2016. Förster resonance energy transfer and protein-induced fluorescence enhancement as synergetic multi-scale molecular rulers. *Scientific Reports*, **6**, 33257.

Pomares, M. F., Delgado, M. A., Corbalan, N. S., Farias, R. N. & Vincent, P. A. 2010. Sensitization of microcin J25-resistant strains by a membrane- permeabilizing peptide. *Applied and Environmental Microbiology*, **76**, 6837-42.

Pomares, M. F., Salomón, R. A., Pavlova, O., Severinov, K., Farías, R. & Vincent, P. A. 2009. Potential applicability of chymotrypsin-susceptible microcin J25 derivatives to food preservation. *Applied and Environmental Microbiology*, **75**, 5734-8.

Pranting, M., Negrea, A., Rhen, M. & Andersson, D. I. 2008. Mechanism and fitness costs of PR-39 resistance in Salmonella enterica serovar Typhimurium LT2. *Antimicrobial Agents and Chemotherapy*, **52**, 2734-41.

Qian, H., Zhao, X., Cao, P., Lei, J., Yan, N. & Gong, X. 2017. Structure of the Human Lipid Exporter ABCA1. *Cell*, **169**, 1228-39.

Queck, S. Y., Jameson-Lee, M., Villaruz, A. E., Bach, T. H., Khan, B. A., Sturdevant, D. E., Ricklefs, S. M., Li, M. & Otto, M. 2008. RNAIII-independent target gene control by the agr quorum-sensing system: insight into the evolution of virulence regulation in *Staphylococcus aureus*. *Molecular Cell,* **32**, 150-8.

Queck, S. Y., Khan, B. A., Wang, R., Bach, T. H., Kretschmer, D., Chen, L., Kreiswirth, B. N., Peschel, A., DeLeo, F. R. & Otto, M. 2009. Mobile genetic element-encoded cytolysin connects virulence to methicillin resistance in MRSA. *PLoS Pathogens*, **5**, e1000533.

Ramos, S., Schuldiner, S & Kaback, H. R. 1976. The electrochemical gradient of protons and its relationship to active transport in Escherichia coli membrane vesicles. *Proceedings of the National Academy of Sciences*, **73**, 1892-6.

Reginsson, G. W. & Schiemann, O. 2011. Pulsed electron-electron double resonance: beyond nanometre distance measurements on biomacromolecules. *Biochemical Journal*, **434**, 353-63.

Rempel, S., Stanek, W. K. & Slotboom, D. J. 2019. Energy-Coupling Factor–Type ATP-Binding Cassette Transporters. *Annual Review of Biochemistry*, **88**, 1.

Riordan, J. R. 2008. CFTR function and prospects for therapy. *Annual Review of Biochemistry*, **77**, 701-26.

Rodionov, D. A., Hebbeln, P., Eudes, A., ter Beek, J., Rodionova, I. A., Erkens, G. B., Slotboom, D. J., Gelfand, M. S., Osterman, A. L., Hanson, A. D. & Eitinger, T. 2009. A novel class of modular transporters for vitamins in prokaryotes. *Journal of Bacteriology*, **191**, 42-51.

Rodríguez, E. & Laviña M. 2003. The proton channel is the minimal structure of ATP synthase necessary and sufficient for microcin h47 antibiotic action. *Antimicrobial Agents and Chemotherapy*, **47**, 181-7.

Romano, M., Fusco, G., Choudhury, H. G., Mehmood, S., Robinson, C. V., Zirah, S., Hegemann, J. D., Lescop, E., Marahiel, M. A., Rebuffat, S., De Simone, A. & Beis, K. 2018. Structural basis for natural product selection and export by bacterial ABC transporters. *ACS Chemical Biology*, **13**, 1598-609.

Rosengren, K. J., Blond, A., Afonso, C., Tabet, J. C., Rebuffat, S. & Craik, D. J. 2004. Structure of thermolysin cleaved microcin J25: extreme stability of a two-chain antimicrobial peptide devoid of covalent links. *Biochemistry*, **43**, 4696-702.

Rosengren, K. J., Clark, R. J., Daly, N. L., Goransson, U., Jones, A. & Craik, D. J. 2003. Microcin J25 has a threaded sidechain-to-backbone ring structure and not a head-to-tail cyclized backbone. *Journal of the American Chemical Society*, **125**, 12464-74.

Ruiz, N., Gronenberg, L.S., Kahne, D. & Silhavy, T. J. 2008. Identification of two inner-membrane proteins required for the transport of lipopolysaccharide to the outer membrane of Escherichia coli. *Proceedings of the National Academy of Sciences*, **105**, 5537-42.

Runti, G., Lopez Ruiz Mdel, C., Stoilova, T., Hussain, R., Jennions, M., Choudhury, H. G., Benincasa, M., Gennaro, R., Beis, K. & Scocchi, M. 2013. Functional characterization of SbmA, a bacterial inner membrane transporter required for importing the antimicrobial peptide Bac7(1-35). *Journal of Bacteriology*, **195**, 5343-51.

Saier Jr, M. H. 2000. Families of transmembrane transporters selective for amino acids and their derivatives. *Microbiology*, **146**, 1775-95.

Saier Jr, M. H., Reddy, V. S., Tsu, B. V., Ahmed, M. S., Li, C. & Moreno-Hagelsieb, G. 2016. The Transporter Classification Database (TCDB): recent advances. *Nucleic Acids Research*, **44**, D372-9.

Salomon, R. A. & Farias, R. N. 1992. Microcin 25, a novel antimicrobial peptide produced by *Escherichia coli*. *Journal of Bacteriology*, **174**, 7428-35.

Salomon, R. A. & Farias, R. N. 1993. The FhuA protein is involved in microcin 25 uptake. *Journal of Bacteriology*, **175**, 7741-2.

Salomon, R. A. & Farias, R. N. 1995. The peptide antibiotic microcin 25 is imported through the TonB pathway and the SbmA protein. *Journal of Bacteriology*, **177**, 3323-5.

Schneider, E. & Hunke, S. 1998. ATP-binding-cassette (ABC) transport systems: functional and structural aspects of the ATP-hydrolyzing subunits/domains. *FEMS Microbiology Reviews*, **22**, 1-20.

Seeger, M. A. & van Veen H. W. 2009. Molecular basis of multidrug transport by ABC transporters. *Biochimica et Biophysica Acta*, **1794**, 725-37.

Seo, M. H., Park, J., Kim, E., Hohng, S. & Kim, H. S. 2014. Protein conformational dynamics dictate the binding affinity for a ligand. *Nature Communications*, **5**, 3724.

Sharff, A. J., Rodseth, L. E., Spurlino, J. C. & Quiocho, FA. 1992. Crystallographic evidence of a large ligand-induced hinge-twist motion between the two domains of the maltodextrin binding protein involved in active transport and chemotaxis. *Biochemistry*, **3**, 10657-63.

Sharma, S. & Davidson, A. L. 2000. Vanadate-induced trapping of nucleotides by purified maltose transport complex requires ATP hydrolysis. *Journal of Bacteriology*, **182**, 6570-6.

Sherman, D. J., Xie, R., Taylor, R. J., George, A. H., Okuda, S., Foster, P. J., Needleman, D. J. & Kahne, D. 2018. Lipopolysaccharide is transported to the cell surface by a membrane-to-membrane protein bridge. *Science*, **359**, 798-801.

Shimizu, T. & Johnson, K. A. 1983. Presteady state kinetic analysis of vanadate-induced inhibition of the dynein ATPase. *The Journal of Biological Chemistry*, **258**, 13833-40.

Singer, S. J. & Nicolson, G. L. 1972. The fluid mosaic model of the structure of cell membranes. *Science*, **175**, 720-31.

Singh, H., Velamakanni, S., Deery, M. J., Howard, J., Wei, S. L. & van Veen, H. W. 2016. ATP-dependent substrate transport by the ABC transporter MsbA is proton-coupled. *Nature Communications*, **7**, 12387.

Smriti, Zou, P., & Mchaourab, H. S. 2009. Mapping daunorubicin-binding sites in the ATP-binding cassette transporter MsbA using site-specific quenching by spin labels. *The Journal of Biological Chemistry*, **284**, 13904-13.

Solbiati, J. O., Ciaccio, M., Farias, R. N. & Salomon, R. A. 1996. Genetic analysis of plasmid determinants for microcin J25 production and immunity. *Journal of Bacteriology*, **178**, 3661-3.

Solbiati, J. O., Ciaccio, M., Farías, R. N., González-Pastor, J. E., Moreno, F. & Salomón, R. A. 1999. Sequence analysis of the four plasmid genes required to produce the circular peptide antibiotic microcin J25. *Journal of Bacteriology*, **181**, 2659-62.

Spurlino, J. C, Lu, G. Y. & Quiocho, F. A. 1991. The 2.3- Å resolution structure of the maltose- or maltodextrin-binding protein, a primary receptor of bacterial active transport and chemotaxis. *The Journal of Biological Chemistry*, **266**, 5202-19.

Stetsenko, A. & Guskov, A. 2017. An overview of the top ten detergents used for membrane protein crystallization. *Crystals*, **7**, 197.

Swier, L. J., Guskov, A. & Slotboom, D. J. 2016. Structural insight in the toppling mechanism of an energy-coupling factor transporter. *Nature Communications*, **7**, 11072.

Syed, A. K., Reed, T. J., Clark, K. L., Boles, B. R. & Kahlenberg, J. M. 2015. *Staphlyococcus aureus* phenol-soluble modulins stimulate the release of proinflammatory cytokines from keratinocytes and are required for induction of skin inflammation. *Infection and Immunity*, **83**, 3428-37.

Tayeb-Fligelman, E., Tabachnikov, O., Moshe, A., Goldshmidt-Tran, O., Sawaya, M. R., Coquelle, N., Colletier, J. P. & Landau, M. 2017. The cytotoxic *Staphylococcus aureus* PSMα3 reveals a cross-α amyloid-like fibril. *Science*, **355**, 831-3.

Taylor, N. M. I., Manolaridis, I., Jackson, S. M., Kowal, J., Stahlberg, H. & Locher, K. P. 2017. Structure of the human multidrug transporter ABCG2. *Nature*, **546**, 504-9.

ter Beek, J., Guskov, A. & Slotboom, D. J. 2014. Structural diversity of ABC transporters. *The Journal of General Physiology*, **143**, 419-35.

Thomas, C. & Tampé, R. 2018. Multifaceted structures and functions of ABC transport systems in health and disease. *Current Opinion in Structural Biology*, **51**, 116-28.

Timachi, M. H., Hutter, C. A., Hohl, M., Assafa, T., Böhm, S., Mittal, A., Seeger, M. A. & Bordignon, E. 2017. Exploring conformational equilibria of a heterodimeric ABC transporter. *Elife*, **6**, e20236.

Trujillo, M., Rodríguez, E. & Laviña M. 2001. ATP synthase is necessary for microcin H47 antibiotic action. *Antimicrobial Agents and Chemotherapy*, **45**, 3128-31.

Truong-Bolduc, Q. C. & Hooper, D. C. 2007. The transcriptional regulators NorG and MgrA modulate resistance to both quinolones and beta-lactams in Staphylococcus aureus. *Journal of Bacteriology*, **189**, 2996-3005.

Urbatsch, I. L., Sankaran, B., Weber, J. & Senior, A. E. 1995. P-glycoprotein is stably inhibited by vanadate-induced trapping of nucleotide at a single catalytic site. *The Journal of Biological Chemistry*, **270**, 19383-90.

van der Velde, J. H., Ploetz, E., Hiermaier, M., Oelerich, J., de Vries, J. W., Roelfes, G. & Cordes, T. 2013. Mechanism of intramolecular photostabilization in self-healing cyanine fluorophores. *Chemphyschem*, **14**, 4084-93.

Verhalen, B., Ernst, S., Börsch, M. & Wilkens, S. 2012. Dynamic ligand-induced conformational rearrangements in P-glycoprotein as probed by fluorescence resonance energy transfer spectroscopy. *The Journal of Biological Chemistry*, **287**, 1112-27.

Villet, R. A., Truong-Bolduc, Q. C., Wang, Y., Estabrooks, Z., Medeiros, H. & Hooper, D. C. 2014. Regulation of expression of abcA and its response to environmental conditions. *Journal of Bacteriology*, **196**, 1532-9.

Vizán, J. L., Hernández-Chico, C., del Castillo, I. & Moreno, F. 1991. The peptide antibiotic microcin B17 induces double-strand cleavage of DNA mediated by E. coli DNA gyrase. *The EMBO Journal*, **10**, 467-76.

Vonrhein, C., Flensburg, C., Keller, P., Sharff, A., Smart, O., Paciorek, W., Womack, T. & Bricogne, G. 2011. Data processing and analysis with the autoPROC toolbox. *Acta Crystallographica Section D: Biological Crystallography*, **67**, 293-302.

Wagner, A., Duman, R., Henderson, K. & Mykhaylyk, V. 2016. In-vacuum long-wavelength macromolecular crystallography. *Acta Crystallographica Section D: Biological Crystallography*, **72**, 430-9.

Wang, R., Braughton, K. R., Kretschmer, D., Bach, T. H., Queck, S. Y., Li, M., Kennedy, A. D., Dorward, D. W., Klebanoff, S. J., Peschel, A., DeLeo, F. R. & Otto, M. 2007. Identification of novel cytolytic peptides as key virulence determinants for community-associated MRSA. *Nature Medicine*, **13**, 1510-4.

Wang, T., Fu, G., Pan, X., Wu, J., Gong, X., Wang, J. & Shi, Y. 2013. Structure of a bacterial energy-coupling factor transporter. *Nature*, **497**, 272-6.

Ward, A., Reyes, C. L., Yu, J., Roth, C. B. & Chang, G. 2007. Flexibility in the ABC transporter MsbA: Alternating access with a twist. *Proceedings of the National Academy of Sciences*, **104**, 19005-10.

Wen, P. C., Verhalen, B., Wilkens, S., Mchaourab, H. S. & Tajkhorshid, E. 2013. On the origin of large flexibility of P-glycoprotein in the inward-facing state. *The Journal of Biological Chemistry*, **288**, 19211-20.

Wilson, K. A., Kalkum, M., Ottesen, J., Yuzenkova, J., Chait, B. T., Landick, R., Muir, T., Severinov, K. & Darst, S. A. 2003. Structure of microcin J25, a peptide inhibitor of bacterial RNA polymerase, is a lassoed tail. *Journal of the American Chemical Society*, **125**, 12475-83.

Winn, M. D., Ballard, C. C., Cowtan, K. D., Dodson, E. J., Emsley, P., Evans, P. R., Keegan, R. M., Krissinel, E. B., Leslie, A. G., McCoy, A., McNicholas, S. J., Murshudov, G. N., Pannu, N. S., Potterton, E. A., Powell, H. R., Read, R. J., Vagin, A. & Wilson, K. S. 2011. Overview of the CCP4 suite and current developments. *Acta Crystallographica Section D: Biological Crystallography*, **67**, 235-42.

Woebking, B., Reuter, G., Shilling, R. A., Velamakanni, S., Shahi, S., Venter, H., Balakrishnan, L. & van Veen, H. W. 2005. Drug-lipid A interactions on the *Escherichia coli* ABC transporter MsbA. *Journal of Bacteriology*, **187**, 6363-9.

Wolfersberger, M. G. 1994. Uniporters, symporters and antiporters. *Journal of Experimental Biology*, **196**, 5-6.

Xu, K., Zhang, M., Zhao, Q., Yu, F., Guo, H., Wang, C., He, F., Ding, J. & Zhang, P. 2013. Crystal structure of a folate energy-coupling factor transporter from *Lactobacillus brevis*. *Nature*, **497**, 268-71.

Yan, K. P., Li, Y., Zirah, S., Goulard, C., Knappe, T. A., Marahiel, M. A. & Rebuffat, S. 2012. Dissecting the maturation steps of the lasso peptide microcin J25 in vitro. *ChemBioChem*, **13**, 1046-52.

Yang, C. C. & Konisky, J. 1984. Colicin V-treated Escherichia coli does not generate membrane potential. *Journal of Bacteriology*, **158**, 757-9.

Yang, M., Livnat Levanon, N., Acar, B., Aykac Fas, B., Masrati. G., Rose, J., Ben-Tal, N., Haliloglu, T., Zhao, Y. & Lewinson, O. 2018. Single-molecule probing of the conformational homogeneity of the ABC transporter BtuCD. *Nature Chemical Biology*, **14**, 715-22.

Yorgey, P., Lee, J., Kordel, J., Vivas, E., Warner, P., Jebaratnam, D. & Kolter, R. 1994. Posttranslational modifications in microcin B17 define an additional class of DNA gyrase inhibitor. *Proceedings of the National Academy of Sciences*, **91**, 4519-23.

Yoshikai, H., Kizaki, H., Saito, Y., Omae, Y., Sekimizu, K. & Kaito, C. 2016. Multidrug-resistance transporter AbcA secretes *Staphylococcus aureus* cytolytic toxins. *The Journal of Infectious Diseases*, **213**, 295-304.

Yuzenkova, J., Delgado, M., Nechaev, S., Savalia, D., Epshtein, V., Artsimovitch, I., Mooney, R. A., Landick, R., Farias, R. N., Salomon, R. & Severinov, K. 2002. Mutations of bacterial RNA polymerase leading to resistance to microcin j25. *The Journal of Biological Chemistry*, **277**, 50867-75.

Zhang, M., Bao, Z., Zhao, Q., Guo, H., Xu, K., Wang, C. & Zhang P. 2014. Structure of a pantothenate transporter and implications for ECF module sharing and energy coupling of group II ECF transporters. *Proceedings of the National Academy of Sciences*, **111**, 18560-5.

Zhang, P., Wang, J. & Shi, Y. 2010. Structure and mechanism of the S component of a bacterial ECF transporter. *Nature*, **468**, 717-20.

Zhang, Z. & Chen, J. 2016. Atomic Structure of the Cystic Fibrosis Transmembrane Conductance Regulator. *Cell*, **167**, 1586-97.

Zhao, Y., Terry, D. S., Shi, L., Quick, M., Weinstein, H., Blanchard, S. C. & Javitch, J. A. 2011. Substrate-modulated gating dynamics in a Na+-coupled neurotransmitter transporter homologue. *Nature*, **474**, 109-13.

Zhao, Y., Terry, D., Shi, L., Weinstein, H., Blanchard, S.C., & Javitch, J. A. 2010. Single-molecule dynamics of gating in a neurotransmitter transporter homologue. *Nature*, **165**, 188-93.

Zhao, Z., Orfe, L. H., Liu, J., Lu, S. Y., Besser, T. E. & Call, D.R. 2017. Microcin PDI regulation and proteolytic cleavage are unique among known microcins. *Scientific Reports*, **16**, 42529.

Zhou, Z., White, K. A., Polissi, A., Georgopoulos, C. & Raetz, C. R. 1998. Function of *Escherichia coli* MsbA, an essential ABC family transporter, in lipid A and phospholipid biosynthesis. *The Journal of Biological Chemistry*, **273**, 12466-75.

Zou, P., Bortolus, M., & McHaourab, H. S. 2009. Conformational cycle of the ABC transporter MsbA in liposomes: detailed analysis using double electron-electron resonance spectroscopy. *Journal of Molecular Biology*, **393**, 586-97.